Uniwersytet Gdański

Wydział Matematyki, Fizyki i Informatyki

Instytut Fizyki Doświadczalnej

Zakład Spektroskopii Fazy Skondensowanej

CMSD

ROZPRAWA DOKTORSKA

Optymalizacja własności optycznych jonów chromu poprzez modyfikację matrycy krystalicznej oraz zastosowanie wysokiego ciśnienia

mgr inż. Natalia Majewska

Promotor

dr hab. Sebastian Mahlik, prof. UG

Gdańsk 2023

Pracę dedykuję Rodzicom

Spis treści

Wykaz publikacji wchodzących w skład rozprawy doktorskiej

[P1] Fang, M.-H.; De Guzman, G. N.; Bao, Z.; **Majewska, N.**; Mahlik, S.; Grinberg, M.; Leniec, G.; Kaczmarek, S.; Yang, C.-W.; Lu, K.-M.; Sheu, H.-S.; Hu, S.-F.; Liu, R.-S. Ultra-High-Efficiency Near-Infrared Ga_2O_3:Cr^{3+} Phosphor and Controlling of Phytochrome. *J. Mater. Chem. C* **2020**, *8* (32), 11013-11017. https://doi.org/10.1039/D0TC02705G.

[P2] Chen, K.-C.; Fang, M.-H.; Huang, W.-T.; Kamiński, M.**; Majewska, N.**; Leśniewski, T.; Mahlik, S.; Leniec, G.; Kaczmarek, S. M.; Yang, C.-W.; Lu, K.-M.; Sheu, H.-S.; Liu, R.-S. Chemical and Mechanical Pressure-Induced Photoluminescence Tuning via Structural Evolution and Hydrostatic Pressure. *Chem. Mater.* **2021**, *33* (10), 3832-3840. https://doi.org/10.1021/acs.chemmater.1c01041.

[P3] Fang, M.-H.; Chen, K.-C.; **Majewska, N.**; Leśniewski, T.; Mahlik, S.; Leniec, G.; Kaczmarek, S. M.; Yang, C.-W.; Lu, K.-M.; Sheu, H.-S.; Liu, R.-S. Hidden Structural Evolution and Bond Valence Control in Near-Infrared Phosphors for Light-Emitting Diodes. *ACS Energy Lett.* **2021**, *6* (1), 109-114. https://doi.org/10.1021/acsenergylett.0c02373.

[P4] **Majewska, N.**; Muñoz, A.; Liu, R.-S.; Mahlik, S. Influence of Chemical and Mechanical Pressure on the Luminescence Properties of Near-Infrared Phosphors, *Chem. Mater.* **2023.** https://doi.org/10.1021/acs.chemmater.3c00203

[P5] Chang, C.-Y.; **Majewska, N.**; Chen, K.-C.; Huang, W.-T.; Leśniewski, T.; Leniec, G.; Kaczmarek, S. M.; Pang, W. K.; Peterson, V. K.; Cherng, D.-H.; Lu, K.-M.; Mahlik, S.; Liu, R.-S. Broadening Phosphor-Converted Light-Emitting Diode Emission: Controlling Disorder. *Chem. Mater.* **2022**, *34* (22), 10190-10199. https://doi.org/10.1021/acs.chemmater.2c03045.

[P6] Rajendran, V.; Fang, M.-H.; Huang, W.-T.; **Majewska, N.**; Lesniewski, T.; Mahlik, S.; Leniec, G.; Kaczmarek, S. M.; Pang, W. K.; Peterson, V. K.; Lu, K.-M.; Chang, H.; Liu, R.-S. Chromium Ion Pair Luminescence: A Strategy in Broadband Near-Infrared Light-Emitting Diode Design. *J. Am. Chem. Soc.* **2021**, *143* (45), 19058-19066. https://doi.org/10.1021/jacs.1c08334.

W publikacjach wchodzących w skład rozprawy doktorskiej, [P1] - [P3], [P5], [P6], badania strukturalne zostały przeprowadzone przez współautorów z National Taiwan University, natomiast badania własności magnetycznych zostały przeprowadzone przez współautorów z Zachodniopomorskiego Uniwersytetu Technologicznego w Szczecinie. Wszystkie badania spektroskopowe zostały zaplanowane i przeprowadzone przeze mnie, z wyjątkiem badań podstawowych przedstawionych w publikacji [P2] (widma wzbudzenia luminescencji oraz widma emisji, niektóre zależności temperaturowe). Opracowałam wszystkie wyniki pomiarów spektroskopowych oraz odegrałam znaczącą rolę w ich interpretacji. Napisałam wstępne wersje manuskryptów w częściach dotyczących własności optycznych oraz udzielałam pomocy w przygotowaniu odpowiedzi dla recenzentów.

W publikacji [P4] zaplanowałam i przeprowadziłam wszystkie badania eksperymentalne. Ponadto, samodzielnie opracowałam oraz zinterpretowałam otrzymane wyniki. Przeprowadziłam kalkulacje dotyczące stanów energetycznych, napisałam manuskrypt oraz prowadziłam korespondencję z edytorem i recenzentami. Kalkulacje dotyczące widma Ramana zostały przeprowadzone przez profesora A. Muñoza, współautora z University of La Laguna.

Wykaz skrótów używanych w rozprawie doktorskiej

NIR - *ang. Near Infrared Region,* zakres bliskiej podczerwieni

LED - *ang. Light Emitting Diode,* dioda elektroluminescencyjna

WLED - *ang. White Light Emitting Diode,* dioda elektroluminescencyjna emitująca białe światło

pc-LED - *ang. phosphor converted Light Emitting Diode,* dioda elektroluminescencyjna z luminoforem

DAC - *ang. diamond anvil cell*, komora z kowadłami diamentowymi (komora diamentowa)

FWHM - *ang. Full Width at Half Maximum,* szerokość połówkowa

CN - *ang. Coordination Number,* liczba koordynacyjna

EPR - *ang. Electron Paramagnetic Resonance*, elektronowy rezonans paramagnetyczny

p - *ang. pressure,* ciśnienie

GOC - $Ga_{1,994}O_3{:}0{,}006Cr^{3+}$

GAOC - $Ga_{1,98-x}Al_xO_3{:}0{,}02Cr^{3+}$

GSOC - $Ga_{1,994-x}Sc_xO_3{:}0{,}006Cr^{3+}$

GIOC - $Ga_{1,98-x}(Al_{0,68}In_{0,32})_xO_3{:}0{,}02Cr^{3+}$

SAGOC - $SrAl_{11,88-x}Ga_xO_{19}{:}0{,}12Cr^{3+}$

Abstract

This doctoral thesis consists of six scientific publications. The research therein focuses on the influence of the crystal matrix and high pressure on the spectroscopic properties of the Cr^{3+} ion to optimize the luminescent properties of the obtained materials for use as phosphors for infrared diode emitters (750-1100 nm). The studies were conducted on solid solutions, such as $Ga_{1.98-x}Al_xO_3:0.02Cr^{3+}$ (GAOC), $Ga_{1.994-x}Sc_xO_3:0.006Cr^{3+}$ (GSOC), $Ga_{1.98-x}(Al_{0.68}In_{0.32})_xO_3:0.02Cr^{3+}$ (GIOC), and $SrAl_{11.88-x}Ga_xO_{19}:0.12Cr^{3+}$ (SAGOC). The aim of the research included in this doctoral thesis was to determine and understand the luminescent properties of the aforementioned solid solutions, model the energy structure of the Cr^{3+} ion, and compare the influence of mechanical and chemical pressure on the luminescent properties of the Cr^{3+} ion.

In the case of GSOC material, subtle changes in the microstructure were demonstrated through luminescence measurements, while for GIOC, the influence of controlled crystal disorder on the luminescent properties was shown. Thanks to the unique technique of high-pressure spectroscopy, the position of the Cr^{3+} ion states was determined as a function of the crystal field strength, and energy diagrams were constructed as a function of pressure, taking into account the Racah parameter variation. The influence of the phase transition on the luminescent properties of the Cr^{3+} ion was demonstrated. Under high pressure in a diamond anvil cell, a new material with more favorable luminescent properties for infrared emitter applications was produced. The influence of external mechanical pressure and internal chemical pressure on the luminescent properties of Cr^{3+} was compared using the examples of GAOC and GSOC materials. These pressures were found to be equivalent for GAOC but not for GSOC. The nature of the broadband luminescence of magnetoplumbites was explained using the SAGOC as an example. The belief that this luminescence is connected to the transition from the excited state $^4T_2$ to the ground state $^4A_2$ has been unequivocally rejected. Instead, it has been established that luminescence is associated with the creation of Cr^{3+}-Cr^{3+} ion pairs.

Streszczenie

Podstawę niniejszej rozprawy doktorskiej stanowi sześć publikacji naukowych. Zawarte w nich badania koncentrują się na wpływie modyfikacji matrycy krystalicznej oraz wysokiego ciśnienia na własności spektroskopowe jonu Cr^{3+}. Badania te maiły na celu optymalizację własności luminescencyjnych otrzymanych materiałów do zastosowań jako luminofory do diodowych emiterów bliskiej podczerwieni (750-1100 nm). Przeprowadzono badania na roztworach stałych, takich jak $Ga_{1,98-x}Al_xO_3:0,02Cr^{3+}$ (GAOC), $Ga_{1,994-x}Sc_xO_3:0,006Cr^{3+}$ (GSOC), $Ga_{1,98-x}(Al_{0,68}In_{0,32})_xO_3:0,02Cr^{3+}$ (GIOC) oraz $SrAl_{11,88-x}Ga_xO_{19}:0,12Cr^{3+}$ (SAGOC). Celem prac badawczych zawartych w niniejszej rozprawie doktorskiej było określenie i zrozumienie własności luminescencyjnych ww. roztworów stałych, określenie struktury energetycznej Cr^{3+}, a także porównanie wpływu ciśnienia mechanicznego i chemicznego na luminescencje jonów Cr^{3+}.

W przypadku materiału GSOC, poprzez pomiary optyczne, udało się wykazać subtelne zmiany w mikrostrukturze krystalicznej. Natomiast dla GIOC, określono wpływ kontrolowanego nieuporządkowania kryształu na własności luminescencyjne. Dzięki unikalnej technice, jaką jest spektroskopia wysokociśnieniowa, wyznaczono położenie stanów jonu Cr^{3+} w zależności od siły pola krystalicznego oraz skonstruowano diagramy energetyczne w funkcji ciśnienia, uwzględniając zmianę parametrów Racah. Zademonstrowano wpływ przejścia fazowego na własności optyczne jonów Cr^{3+}. W komorze diamentowej pod wysokim ciśnieniem, wytworzono nowy materiał o korzystniejszych własnościach luminescencyjnych do zastosowań jako emiter podczerwieni. Na przykładzie materiałów GAOC oraz GSOC porównano wpływ zewnętrznego ciśnienia mechanicznego i wewnętrznego ciśnienia chemicznego na własności luminescencyjne jonów Cr^{3+}. Stwierdzono, że te ciśnienia są równoważne dla GAOC, jednak nie są równoważne dla GSOC. Ponadto, na przykładzie SAGOC wyjaśniono naturę szerokopasmowej luminescencji magnetoplumbitów domieszkowanych jonami chromu. Jednoznacznie odrzucono pogląd, że luminescencja ta związana jest z przejściem ze stanu wzbudzonego $^4T_2$ do stanu podstawowego $^4A_2$. Zamiast tego, ustalono, że jest ona powiązana z kreacją par jonów Cr^{3+}-Cr^{3+}.

1. Wprowadzenie

Znaczącą grupę materiałów luminescencyjnych (luminoforów) stanowią związki nieorganiczne, domieszkowane aktywnymi optycznie jonami lantanowców oraz metali przejściowych, o niewielkiej koncentracji. Te domieszki są nazywane aktywatorami lub centrami luminescencji. Nieorganiczne materiały luminescencyjne znajdują szerokie zastosowanie w produkcji laserów,[1] wyświetlaczy, pigmentów, luminoforów do diod elektroluminescencyjnych,[2] scyntylatorów[3] dozymetrów oraz warstw luminoforowych wykazujących przedłużoną luminescencję.[4,5] Jednym z najlepiej zbadanych oraz najczęściej stosowanych aktywatorów jest jon Cr^{3+}. W zależności od matrycy krystalicznej, w której się znajduje, wykazuje on luminescencję składającą się z wąskich linii lub/i szerokiego pasma, zarówno w zakresie widzialnego światła czerwonego, jak i bliskiej podczerwieni (NIR-*ang. Near Infrared Region*). Najbardziej znanym materiałem aktywowanym jonami Cr^{3+} jest kryształ Al_2O_3, znany jako rubin. To właśnie na bazie rubinu w 1960 roku skonstruowano pierwszy laser na ciele stałym.[6]

Mimo wieloletnich intensywnych badań i szeregu już istniejących zastosowań, podczerwona luminescencja jonu Cr^{3+} nadal budzi duże zainteresowanie świata nauki, przede wszystkim ze względu na pojawiające się nowe możliwości aplikacyjne. W szczególności uwagę przyciągają zastosowania biologiczne i medyczne, takie jak biosensory, markery biologiczne, analizatory składu oraz świeżości jedzenia.[7–11] Promieniowanie NIR ma zdolność do przenikania przez skórę, co pozwala na stosowanie go w diagnostyce medycznej.[12] Jednym z głównych zastosowań luminoforów emitujących promieniowanie podczerwone jest znakowanie i obrazowanie substancji wprowadzanych do wnętrza żywych organizmów. W tym celu wykorzystuje się również zjawisko przedłużonej luminescencji, czyli świecenia, które po wzbudzeniu może trwać nawet do kilkunastu godzin.[13–15] Nanocząstki wykazujące przedłużoną luminescencję podczerwoną, naładowane przez promieniowanie ultrafioletowe lub widzialne przed wstrzyknięciem do żywych organizmów, mogą emitować światło przez długi czas bez wzbudzania *in situ*, dlatego nadają się do optycznego obrazowania *in vivo*.[16–18] Luminescencja jonów Cr^{3+} w bliskiej podczerwieni jest również obiecująca w termometrii optycznej, wykorzystującej zależną od temperatury ewolucję własności optycznych, takich jak widmo, czy kinetyka luminescencji.[19–22] Luminescencja Cr^{3+} jest zlokalizowana w tzw. oknie biologicznym, które obejmuje zakres długości fal, w którym światło ma największą zdolność przenikania przez tkanki biologiczne. Dzięki temu, materiały aktywowane jonami Cr^{3+} mogą

być skutecznie wykorzystywane jako luminescencyjne markery, na przykład do zdalnego pomiaru temperatury w obiektach biologicznych. Luminescencja jonów Cr^{3+} ma również zastosowanie w manometrii optycznej, która polega na bezkontaktowym monitorowaniu i pomiarze ciśnienia za pomocą luminescencji. W ramach tych badań analizuje się wpływ ciśnienia na własności luminescencyjne jonu Cr^{3+}.[23,24]

Materiały aktywowane jonami Cr^{3+} mogą być wydajnymi emiterami bliskiej podczerwieni, charakteryzującymi się szerokopasmową luminescencją przy wzbudzeniu światłem niebieskim (np. niebieską diodą LED-*ang. Light Emitting Diode*). Emitery podczerwieni znajdują zastosowanie w spektrometrii optycznej, umożliwiając identyfikację i charakterystykę różnych substancji na podstawie ich charakterystycznych własności optycznych, takich jak widma odbicia, transmisji bądź rozpraszania światła. Obecnie stosowane źródła promieniowani podczerwonego, takie jak tradycyjne żarówki, lampy wyładowcze czy halogenowe, charakteryzują się dużymi rozmiarami oraz posiadają niską sprawność i wysoką temperaturę pracy.[25] W celu zwiększenia możliwości aplikacyjnych, konieczne jest znalezienie mniejszych i bardziej wydajnych rozwiązań, bazujących na technologii LED. Diody NIR-*pc*-LEDs (*ang. pc-phosphor converted*) to miniaturowe urządzenia podobne do powszechnie stosowanych diod emitujących światło białe WLED (*ang. White LED*). W przypadku diod WLED, na niebieską diodę nanosi się warstwę żółtego luminoforu, co pozwala na uzyskanie światła białego. Natomiast w przypadku diod NIR-*pc*-LED, na diodę nanosi się warstwę materiału, który emituje promieniowanie w zakresie podczerwonym.[26] Konstrukcja wydajnych i miniaturowych NIR-*pc*-LED pozwoli na zastosowanie ich w urządzeniach przenośnych, takich jak smartfony. Takie rozwiązania otwierają szerokie spektrum zastosowań, takich jak monitorowanie stanu zdrowia czy analizy świeżości oraz jakości jedzenia w warunkach domowych.[27] Przy użyciu smartfonów będzie możliwe monitorowanie stanu skóry, diagnozowanie składu tkanki tłuszczowej oraz ocenianie poziomu nawodnienia organizmu. W przypadku żywności, przenośne urządzenia umożliwią ocenę zawartości składników odżywczych, takich jak węglowodany, białka, tłuszcze i inne. Będzie również możliwe identyfikowanie obecności substancji niepożądanych, takich jak pestycydy czy zanieczyszczenia.

Idealny luminofor NIR, pod względem aplikacyjnym w spektrometrii, powinien charakteryzować się wysoką wydajnością kwantową, stabilnością temperaturową i pasmem emisji o dużej szerokości połówkowej (FWHM - *ang. Full Width at Half Maximum*) w zakresie

widmowym 650–1350 nm. Jednak, dotychczas opracowane materiały wciąż nie spełniają tych wymagań.[12]

Chociaż w ostatnim czasie osiągnięto znaczny postęp naukowy w tym popularnym obszarze badań, większość dotychczasowych badań skupia się na zsyntezowaniu jednego rodzaju materiału lub zmianie aktywatorów luminescencji. Brakuje natomiast systematycznego podejścia do dopasowania struktury krystalicznej i własności luminescencyjnych poprzez częściowe podstawianie kationów matrycy.[28–31] Synteza roztworów stałych, w tym częściowe podstawienie kationów matrycy, stanowi skuteczną metodę pozwalającą na dopasowanie np. widma emisji materiału do potrzeb aplikacyjnych. Mimo możliwości przewidywania własności strukturalnych oraz luminescencyjnych, wynikających z domieszkowania matrycy jonami aktywnymi optycznie, istnieje możliwość nieoczekiwanych zmian spowodowanych pewnymi lokalnymi zniekształceniami struktury lub przejściami fazowymi.

Wszystkie prace zawarte w niniejszej rozprawie doktorskiej koncentrują się na badaniu własności luminescencyjnych jonów Cr^{3+} w roztworach stałych, które mogą posłużyć jako emitery promieniowania w zakresie bliskiej podczerwieni (NIR-*pc*-LED).

Elektronowa struktura energetyczna materiałów dielektrycznych domieszkowanych jonami lantanowców lub metali przejściowych składa się zarówno ze zdelokalizowanych stanów elektronowych atomów matrycy krystalicznej (tworzących pasmo walencyjne oraz przewodnictwa), jak i ze zlokalizowanych stanów energetycznych centrów luminescencji. Struktura energetyczna swobodnego jonu jest zdeterminowana przez oddziaływanie kulombowskie elektronów z jądrem oraz wzajemnym oddziaływaniem elektronów walencyjnych jonu. Oddziaływania te są opisane odpowiednim hamiltonianem, skąd otrzymuje się siatkę stanów (termów atomowych) jonu. Umieszczenie jonu w matrycy krystalicznej skutkuje poddaniem stanów swobodnego jonu na oddziaływanie pola krystalicznego, powodującego rozszczepienie termów atomowych na poziomy pola krystalicznego (subtermy).

Powszechnie stosowany model opisujący strukturę energetyczną centrum luminescencji w matrycy krystalicznej opiera się na diagramie współrzędnych konfiguracyjnych. Wpływ matrycy krystalicznej na stany energetyczne domieszki Cr^{3+} możemy modelować jednowymiarowym kwantowym oscylatorem harmonicznym, w którym każdy stan elektronowy reprezentowany jest przez parabolę (potencjał harmoniczny odpowiedzialny za
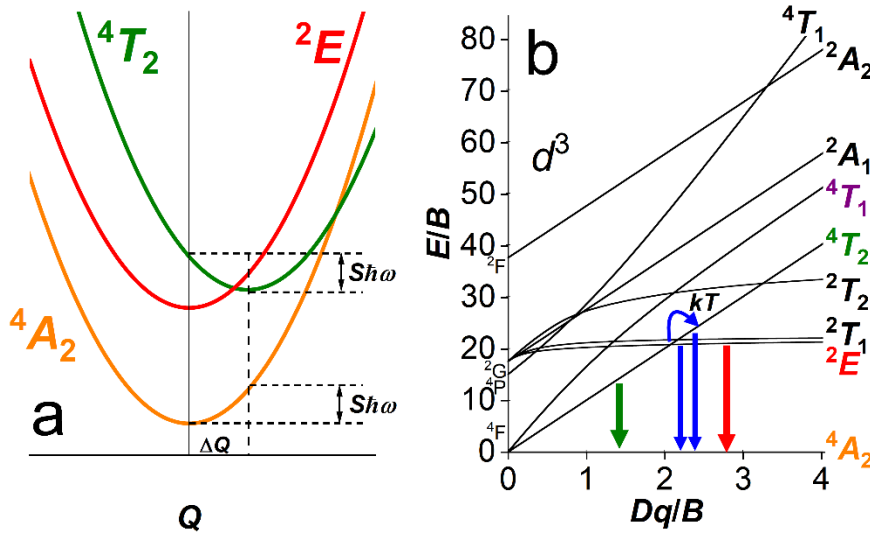
Rys. 1 Przykładowe diagramy przedstawiające jon Cr³⁺w matrycy krystalicznej **(a)** diagram konfiguracyjny **(b)** diagram Tanabe-Sugano dla jonu Cr³⁺ w otoczeniu oktaedrycznym.

drgania sieci).[32] Pomimo tego, że model ten uwzględnia tylko jeden mod oscylacji, jest on niezwykle przydatny w wyjaśnianiu wielu mechanizmów przejść promienistych i bezpromienistych. **Rys. 1 a** przedstawia przykładowy diagram konfiguracyjny dla domieszki Cr³⁺. Parabole reprezentują wybrane stany elektronowe jonu Cr³⁺. Najniżej położona parabola $^4A_2$ reprezentuje stan podstawowy, natomiast wyżej położone parabole reprezentują dwa stany wzbudzone: ^2E oraz $^4T_2$. Jednym z kluczowych aspektów opisanych przez model współrzędnych konfiguracyjnych, przedstawionym na **Rys. 1 a**, jest relaksacja sieci wywołana sprzężeniem elektron-sieć. Relaksację sieci można opisać za pomocą wartości $S\hbar\omega$, gdzie $\hbar\omega$ jest efektywną częstotliwością fononową, a S jest bezwymiarowym parametrem Huanga-Rhys, który jest miarą sprzężenia stanu elektronowego z siecią.[5,33] Znając różnicę energii między pasmem absorpcji oraz emisji (przesunięcie Stokesa), energię $S\hbar\omega$ można określić jako połowę tego przesunięcia. Ponadto zmianę minimum energii elektronowej w przestrzeni konfiguracyjnej ΔQ można obliczyć jako:

$$\Delta Q = \sqrt{\frac{2S\hbar\omega}{k}}, \tag{1}$$

gdzie k odpowiada stałej sprężystości sieci.

Jon Cr^{3+} ma trzy elektrony na powłoce d (konfiguracja $3d^3$). Typowo lokuje się on w pozycjach krystalograficznych z sześcioma najbliższymi sąsiadami w symetrii oktaedrycznej z ewentualnymi zniekształceniami obniżającymi symetrie.

Gdy jon metalu przejściowego znajduje się w sieci krystalicznej (matrycy), elektrony walencyjne domieszki oddziałują z sąsiednimi jonami matrycy (ligandami). Oddziaływanie to nazywane jest oddziaływaniem pola krystalicznego i znacząco wpływa na własności elektronowe jonu.

Dla domieszki posiadającej jeden elektron d (d^1), odziaływanie pola krystalicznego powoduje rozszczepienie stanów energetycznych domieszki, a wartość rozszczepienia pomiędzy nimi wynosi $10Dq$. Natomiast, energie stanów elektronowych jonu d^n, n > 1, są zdeterminowane poprzez parametr siły pola krystalicznego Dq oraz parametry Racah B i C, które opisują wzajemne odziaływanie elektronowe w jonach metali przejściowych. Poszczególne subtermy pola krystalicznego konfiguracji d^n są zaprezentowane na tzw. diagramie Tanabe-Sugano w funkcji Dq, przy ustalonych wartościach parametrów Racah B i C.[34–36] Oś x reprezentuje parametr siły pola krystalicznego Dq, natomiast oś y przedstawia energię stanów energetycznych jonów metali przejściowych, E. Obie wartości są znormalizowane przez parametr Racah B. Przykładowy diagram Tanabe-Sugano dla konfiguracji d^3, odpowiadającej jonom Cr^{3+} w otoczeniu oktaedrycznym przedstawiono na **Rys. 1 b**. Oznaczenia z lewej strony pokazują termy atomowe jonu swobodnego o konfiguracji d^3, które pod wpływem pola krystalicznego rozszczepiają się na subtermy pola krystalicznego. Stanem podstawowym konfiguracji d^3 w otoczeniu oktaedrycznym jest zawsze stan $^4A_2$. Zależnie od wartości parametru Dq/B najniższym stanem wzbudzonym jest stan $^4T_2$ lub ^2E. Punkt przecięcia tych stanów rozgranicza centra Cr^{3+} na słabopolowe oraz silnopolowe, w których odpowiednio najniższym stanem wzbudzonym jest stan $^4T_2$, bądź ^2E. Zwyczajowo wyróżnia się również centra luminescencyjne, które znajdują się w tzw. „pośrednim" polu krystalicznym. Tak naprawdę, to stwierdzenie odnosi się do obszaru silnego pola krystalicznego w przedziale Dq/B, który jest blisko punktu przecięcia się stanów $^4T_2$ oraz ^2E. W tym obszarze, energia termiczna w temperaturze pokojowej jest wystarczająca, aby następowało termiczne obsadzanie stanu $^4T_2$ z najniższego stanu wzbudzonego ^2E. Strzałki na **Rys. 1 b** przedstawiają przejścia elektronowe dla jonów Cr^{3+}: odpowiednio w silnym (czerwona strzałka), „pośrednim" (niebieskie strzałki) oraz słabym (zielona strzałka) polu krystalicznym.

Parametr pola krystalicznego Dq oraz parametry Racah B i C można wyznaczyć z położeń stanów ${}^4T_2$, ${}^4T_1$ i ${}^2E$. Wartość $10Dq$ jest równa energii maksimum pasma wzbudzenia luminescencji ${}^4A_2 \rightarrow {}^4T_2$. Parametry Racah można obliczyć z następujących równań:[33]

$$B = Dq \frac{\left[\frac{\Delta E}{Dq}\right]^2 - 10 \cdot \frac{\Delta E}{Dq}}{15\left(\frac{\Delta E}{Dq} - 8\right)}, \tag{2}$$

$$C = \frac{B}{3{,}05}\left\{\frac{E({}^2E - {}^4A_2)}{B} - 7{,}9 + 1{,}8\frac{B}{Dq}\right\}, \tag{3}$$

gdzie ΔE jest różnicą energii pomiędzy przejściami optycznymi ${}^4A_2 \rightarrow {}^4T_1$ i ${}^4A_2 \rightarrow {}^4T_2$. Parametry Racah dla swobodnego jonu Cr^{3+} wynoszą: $B_0 = 918$ cm^{-1} i $C_0 = 3850$ cm^{-1}.[37]

W polu krystalicznym o odpowiednio wysokiej symetrii, zgodnie z tzw. regułą Laporte'a, wszystkie przejścia elektryczne dipolowe wewnątrz konfiguracji d^n (przejścia d-d) swobodnego jonu Cr^{3+} są wzbronione. Wynika to z faktu, że funkcje falowe wszystkich stanów energetycznych w konfiguracji d^n mają tę samą parzystość. W większości przypadków reguła Laporte'a jest zniesiona ze względu na występujące w matrycy krystalicznej zaburzenia, znoszące symetrię pola krystalicznego ze względu na operację inwersji (tj. zniesienie istnienia środka symetrii układu Cr^{3+} - ligandy). Dodatkowo przejścia optyczne ze zmianą spinu są formalnie wzbronione. Jednakże, w przypadku jonów Cr^{3+}, obserwuje się przejścia ze zmianą spinu ${}^2E \rightarrow {}^4A_2$. Jest to spowodowane mieszaniem się wyższego stanu ${}^4T_2$ ze stanem ${}^2E$, na skutek oddziaływania spin-orbita.

W materiałach nieorganicznych domieszkowanych jonami Cr^{3+} istnieją trzy główne przejścia ze stanu podstawowego ${}^4A_2$ do stanów wzbudzonych: ${}^4T_2$, ${}^4T_1({}^4F)$ i ${}^4T_1$ $({}^4P)$. Najwyższe pasmo absorpcji/wzbudzenia ${}^4A_2 \rightarrow {}^4T_1({}^4P)$ znajduje się w zakresie ultrafioletu, natomiast pasma absorpcji/wzbudzenia o niższej energii związane z przejściem ${}^4A_2 \rightarrow {}^4T_2$, ${}^4T_1({}^4F)$ znajdują się zazwyczaj w zakresie widzialnym (przejście ${}^4A_2 \rightarrow {}^4T_1({}^4F)$ niekiedy w bliskim ultrafiolecie).[38] Dodatkowo, jony metali przejściowych wykazują zwykle silną szerokopasmową absorpcję w obszarze ultrafioletu. Związane jest to z przejściem absorpcyjnym z przeniesieniem ładunku między poziomami domieszki, a stanami pasmowymi.[39,40]

Ze względu na bezpromienistą relaksację, najbardziej prawdopodobne jest przejście emisyjne z najniżej położonego stanu wzbudzonego. Kiedy pole krystaliczne jest silne, najniżej położonym stanem wzbudzonym jest stan ^2E. W takim przypadku widmo emisji w temperaturze pokojowej składa się typowo z wąskich linii, w czerwonym obszarze promieniowania widzialnego, nazywanych w literaturze liniami R_1 oraz R_2.[38] Emisji tej mogą towarzyszyć pewne słabe przejścia wibracyjne (struktura fononowa). Ponieważ przejście ze stanu wzbudzonego ^2E do stanu podstawowego $^4A_2$ zachodzi ze zmianą spinu, czas zaniku luminescencji związanej z tym przejściem (odwrotnie proporcjonalny do prawdopodobieństwa przejścia) jest w zakresie milisekundowym.

Dla jonów Cr^{3+} w słabych polach krystalicznych, stan $^4T_2$ jest położony niżej niż stan ^2E.[5,33,41–43] W tym przypadku obserwuje się szerokopasmową emisję związaną z przejściem bez zmiany spinu $^4T_2 \rightarrow {}^4A_2$, typowo w zakresie NIR.[44] Takie przejście charakteryzuje się czasem zaniku w zakresie mikrosekundowym.

W niektórych związkach, mimo że stan ^2E jest niżej położonym stanem niż $^4T_2$, stan $^4T_2$ może być termicznie obsadzany przez elektrony z blisko leżącego stanu ^2E („pośrednie" pole krystaliczne).[45] W takim przypadku obserwujemy zarówno liniową, jak i szerokopasmową, emisję w temperaturze pokojowej oraz silną zależność temperaturową ich względnych intensywności. Czas zaniku luminescencji Cr^{3+} w „pośrednim" polu krystalicznym również silnie zależy od temperatury. W niskich temperaturach, kiedy głównie obserwuje się emisję liniową ze stanu ^2E, typowy czas zaniku jest w zakresie milisekundowym i wraz ze wzrostem temperatury następuje skrócenie się czasów zaniku ze względu na termiczne obsadzanie stanu $^4T_2$.

Strukturę elektronową, a co za tym idzie energię stanów ^2E oraz $^4T_2$, można zmieniać za pomocą ciśnienia hydrostatycznego, otrzymując szereg nowych informacji.[46] Poddając materiał działaniu wysokiego ciśnienia zmniejszamy jego objętość, a o wielkości tej zmiany decyduje wielkość przyłożonego ciśnienia oraz moduł sprężystości objętościowej (*ang. bulk modulus*, B_0), który jest cechą charakterystyczną materiału. Aby znacząco wpłynąć na własności ciała stałego, ze względu na duże oddziaływania międzycząsteczkowe, konieczne jest zastosowanie wysokiego ciśnienia, rzędu kilku lub nawet kilkudziesięciu GPa (1 GPa = 10 kbar). Do osiągnięcia tak wysokich ciśnień wykorzystuje się komory diamentowe (DAC - *ang. diamond anvil cell*).[47–50] Przykładając wysokie ciśnienie hydrostatyczne możemy

obserwować makroskopowe zmiany zachodzące w krysztale, które są konsekwencją zmiany objętości, takie jak: zmiana energii pasm energetycznych, zmiana fazy krystalicznej, czy też zmiana energii drgań sieci krystalicznej (fononów). Możemy również obserwować zmiany mikroskopowe, które ograniczają się do lokalnego otoczenia centrum luminescencji. Zaliczamy do nich zmianę energii stanów elektronowych centrów luminescencji, zmianę oddziaływań pomiędzy jonami, zmianę kątów, długości oraz charakteru wiązań (np. w kierunku bardziej kowalencyjnym, efekt nefeloauksetyczny)[10] oraz zmianę siły pola krystalicznego.

Przedstawione w niniejszej pracy badania skupiają się na luminescencji jonów Cr^{3+} w nieorganicznych matrycach krystalicznych typu $(Ga,Al,Sc,In)_2O_3$ (Ga_2O_3 modyfikowany przez częściowe podstawienie kationów matrycy) oraz $SrAl_{12-x}Ga_xO_{19}$. Oprócz standardowych metod spektroskopii optycznej (widma wzbudzenia i luminescencji), istotną i wiodącą metodą badawczą były pomiary luminescencji stacjonarnej oraz czasowo – rozdzielonej w wysokich ciśnieniach hydrostatycznych do 30 GPa (300 kbar).

W celu generacji wysokiego ciśnienia hydrostatycznego wykorzystano komory diamentowe typu Merrilla-Bassetta,[51] wytwarzające ciśnienia do 40 GPa (400 kbar). Sercem tego urządzenia są dwa umieszczone naprzeciw siebie i odpowiednio oszlifowane kowadła diamentowe. Rozmiar powierzchni roboczych diamentów wynosił 500 µm. Pomiędzy kowadłami umieszczano metalową uszczelkę (gasket) o grubości, po wstępnym zagnieceniu, około 70 µm. W uszczelce wywiercano otwór (obszar aktywny komory) o średnicy 200 µm, w którym umieszczano próbkę oraz czujnik ciśnienia, a następnie wypełniano substancją zapewniającą hydrostatyczność ciśnienia. Substancją przenoszącą ciśnienie był olej silikonowy - poli(dimetylosiloksan), a jako materiał referencyjny do odczytu wartości ciśnienia posłużył $KMgF_3$:0,5%Eu^{2+}.[52]

2. Omówienie celu naukowego cyklu prac składających się na rozprawę doktorską

W cyklu publikacji stanowiących podstawę rozprawy doktorskiej skoncentrowano się na dogłębnym badaniu wpływu matrycy krystalicznej oraz wysokiego ciśnienia na własności luminescencyjne jonów Cr^{3+} (inżynieria własności luminescencyjnych) za pomocą zaawansowanych metod spektroskopowych. Celem tych badań było poszukiwanie nowych materiałów, które mogą znaleźć zastosowanie jako emitery światła w zakresie bliskiej podczerwieni (750-1100 nm). **Szczegółowymi celami prac badawczych zawartymi w niniejszej rozprawie doktorskiej były:**

- **określenie własności luminescencyjnych roztworów stałych domieszkowanych jonami Cr^{3+}, takich jak: ($Ga_{1,98-x}Al_xO_3$:$0,02Cr^{3+}$; $Ga_{1,994-x}Sc_xO_3$:$0,006Cr^3$; $Ga_{1,98-x}(Al_{0,68}In_{0,32})_xO_3$:$0,02Cr^{3+}$; $SrAl_{11,88-x}Ga_xO_{19}$:$0,12Cr^{3+}$);**
- **wyznaczenie struktury energetycznej badanych układów w celu zrozumienia ich mechanizmu luminescencji;**
- **określenie prawdopodobieństw przejść promienistych i bezpromienistych, co pozwoliło na lepsze zrozumienie procesów luminescencyjnych zachodzących w tych układach;**
- **półempiryczne określenie struktury energetycznej jonów Cr^{3+} w funkcji ciśnienia chemicznego i mechanicznego, dla grupy materiałów $Ga_{1,98-x}Al_xO_3$:$0,02Cr^{3+}$;**
- **porównanie wpływu ciśnienia mechanicznego oraz chemicznego na własności luminescencyjne Cr^{3+} w matrycach ($Ga_{1,98-x}Al_xO_3$:$0,02Cr^{3+}$ oraz $Ga_{1,994-x}Sc_xO_3$:$0,006Cr^3$.**

Wszystkie materiały, będące przedmiotem rozprawy doktorskiej, zostały pozyskane w ramach współpracy z grupą prof. Ru-Shi Liu z Materials Chemistry Laboratory, Department of Chemistry, National Taiwan University. W pracy doktorskiej zaprezentowano i omówiono wyniki badań następujących materiałów:

- $Ga_{1,994}O_3:0,006Cr^{3+}$;

- $Ga_{1,98-x}Al_xO_3:0,02Cr^{3+}$ ($0 \leq x \leq 1,98$; krok 0,2);

- $Ga_{1,994-x}Sc_xO_3:0,006Cr^{3+}$ ($0 \leq x \leq 0,87$; krok 0,2);

- $Ga_{1,98-x}(Al_{0,68}In_{0,32})_xO_3:0,02Cr^{3+}$ ($0 \leq x \leq 0,8$; krok 0,1);

- $SrAl_{11,88-x}Ga_xO_{19}:0,12Cr^{3+}$ ($0 \leq x \leq 12$; krok 2).

W sumie przebadano 36 różnych materiałów, otrzymanych za pomocą syntezy w ciele stałym, charakteryzujących się wydajnością kwantową powyżej 75 %, gdzie dla większości z nich osiąga ona wartość powyżej 90 %.

Badania spektroskopowe jonu Cr^{3+} w matrycy Ga_2O_3 opisano w publikacji [P1]. Następnie, w publikacjach [P2], [P3] oraz [P5], przedstawiono wpływ modyfikacji matrycy Ga_2O_3 (współdomieszkowania jonami Al^{3+}, Sc^{3+} oraz In^{3+}) na własności luminescencyjne jonów Cr^{3+}. W szczególności skupiono się na sprawdzeniu relacji pomiędzy wewnętrznym ciśnieniem chemicznym, a zewnętrznym ciśnieniem mechanicznym, a dokładniej ich wpływem na stany elektronowe jonów Cr^{3+}. Wewnętrzne ciśnienie chemiczne powstaje wskutek oddziaływania jonu Cr^{3+} z polem krystalicznym pochodzącym od ligandów, pod wpływem modyfikacji związanej z podstawieniem kationów matrycy jonami o większym lub mniejszym promieniu jonowym. Zewnętrzne ciśnienie mechaniczne (hydrostatyczne) jest wytwarzane w wysokociśnieniowych komorach diamentowych, gdzie ściskając materiał w całej objętości zmieniamy odległości międzyatomowe. Szczegółowa analiza tego problemu została przedstawiona w publikacji [P4]. Dodatkowo, w publikacjach [P2], [P4] oraz [P5] przedstawiono wpływ przemiany fazowej indukowanej ciśnieniem chemicznym, jak i mechanicznym na luminescencję jonu Cr^{3+} w modyfikowanym związku Ga_2O_3. W publikacji [P6] pokazano szerokopasmową luminescencję związaną z kreacją par jonów Cr^{3+}-Cr^{3+} w materiałach o strukturze magnetoplumbitu. Udowodniono, że w tych materiałach szerokopasmowa luminescencja, błędnie przypisywana w literaturze przejściu optycznemu $^4T_2 \rightarrow {}^4A_2$, jest tak naprawdę luminescencją par Cr^{3+}-Cr^{3+}. Zaskakujące jest, że obserwowana luminescencja charakteryzuje się szerokopoasmową oraz wysoce wydają emisją, podczas gdy własności luminescencyjne par zwyczajowo objawiają się słabo intensywną, wąskoliniową emisją.

3. Omówienie osiągniętych wyników w cyklu prac składających się na rozprawę doktorską

3.1. Luminescencja jonu Cr^{3+} w matrycy Ga$_2$O$_3$ modyfikowanej jonami Al, Sc oraz In

3.1.1 Podstawowe własności spektroskopowe

Przedstawione w publikacji [P1] widmo wzbudzenia Ga$_{1,994}$O$_3$:0,006Cr^{3+} (GOC) ($x = 0$ na **Rys. 2 a**) jest typowe dla jonów Cr^{3+} znajdujących się w miejscach krystalograficznych o sześciokrotnej koordynacji (zdeformowany oktaedr). Widmo składa się z dwóch szerokich pasm, z maksimami przy 440 i 610 nm, przypisanym przejściom $^4A_2 \rightarrow {}^4T_1$ oraz $^4A_2 \rightarrow {}^4T_2$.

Widmo luminescencji w temperaturze pokojowej składa się z wąskich linii przy długości fali 688,8 oraz 695,5 nm oraz szerokiego pasma w zakresie 650-950 nm z maksimum przy 730 nm. Szerokie pasmo luminescencji jest związane ze spinowo dozwolonym przejściem ze stanu wzbudzonego $^4T_2$ do stanu podstawowego $^4A_2$. Emisja wąskoliniowa jest związana z przejściem ze zmianą spinu $^2E \rightarrow {}^4A_2$. Dodatkowo, zaobserwowano rozszczepienie stanu ^2E na dwa stany $E_{1/2}$ oraz $E_{3/2}$, z których przejścia do stanu podstawowego $^4A_2$ nazywa się odpowiednio liniami R_1 oraz R_2.

Podstawienie jonu Al^{3+}, o mniejszym promieniu jonowym (0,39 Å; CN = 4; 0,54 Å; CN = 6, CN - *ang. Coordination Number,* liczba koordynacyjna), w miejsce Ga^{3+} (0,47 Å, CN = 4; 0,62 Å, CN = 6)[53] powoduje zmniejszenie średniej odległości między atomami w sieci krystalicznej, zwiększając siłę pola krystalicznego wokół jonu Cr^{3+}. Zgodnie z diagramem Tanabe-Sugano (**Rys. 1 a**), zwiększenie siły pola krystalicznego (Dq) działającego na jon Cr^{3+}, prowadzi do zwiększenia energii pomiędzy stanami wzbudzonymi $^4T_1$ oraz $^4T_2$, a stanem podstawowym $^4A_2$. Domieszkowanie Ga$_2$O$_3$ jonami Al^{3+} prowadzi więc do oczekiwanego przesunięcia widma wzbudzenia luminescencji w kierunku wyższych energii (krótszych długości fal), co jest przedstawione na **Rys. 2 a** i **c** oraz w publikacji [P2] dla serii Ga$_{1,98-x}$Al$_x$O$_3$:0,02Cr^{3+} (GAOC), $x = 0 - 1,98$. Zarówno w przypadku wzbudzenia, jak i emisji, zaobserwowano nieciągłość przesunięcia widm wraz ze wzrostem x. Jest to spowodowane przemianą fazową z fazy β-Ga$_2$O$_3$ ($x < 1,6$) o strukturze jednoskośnej (grupa przestrzenna C2/m) do fazy α-Ga$_2$O$_3$, o strukturze trygonalnej (R$\overline{3}$c), obserwowaną również w dyfrakcji rentgenowskiej.
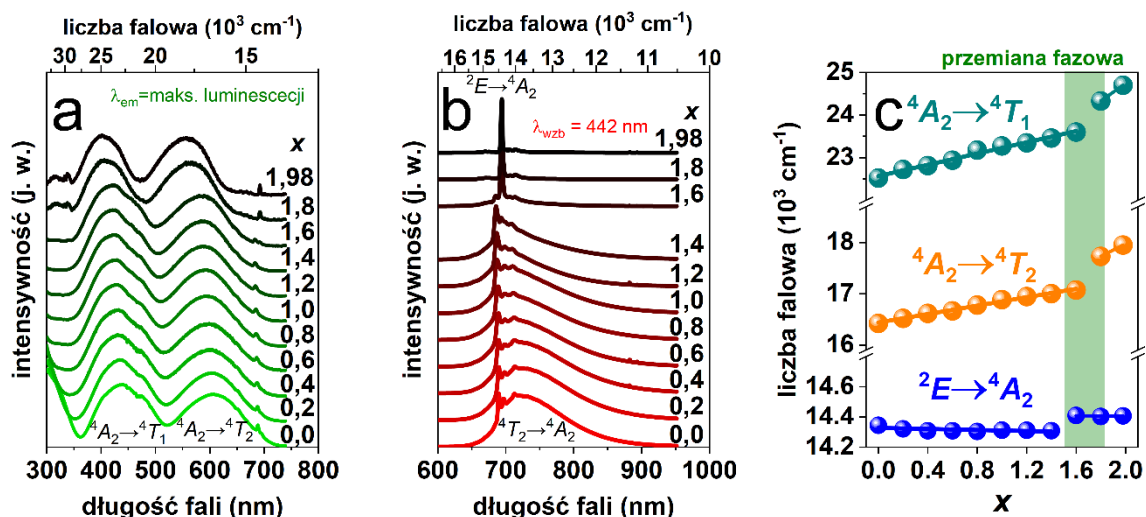
Rys. 2 (a) Widma wzbudzenia luminescencji rejestrowane dla maksimum luminescencji (λ_{em}) oraz **(b)** widma luminescencji rejestrowane przy długości fali wzbudzającej λ_{wzb} = 442 nm, dla GAOC, x = 0 - 1,98 w temperaturze pokojowej. **(c)** Wyznaczone przesunięcia maksimum pasm wzbudzenia luminescencji związanych z przejściami $^4A_2 \rightarrow {}^4T_1$ oraz $^4A_2 \rightarrow {}^4T_2$, oraz luminescencji wąskoliniowej $^2E \rightarrow {}^4A_2$.

Domieszkowanie Ga_2O_3:Cr^{3+} jonami Al^{3+} prowadzi również do wydłużenia czasów zaników wraz ze wzrostem x do x = 1,4, jak pokazano w publikacji [P2] dla serii GAOC. Wydłużenie czasów zaniku spowodowane jest mniejszym wpływem stanu $^4T_2$ na stan ^2E (wynikającym z mieszania się tych dwóch stanów poprzez odziaływanie spin-orbita), ze względu na zwiększenie energii pomiędzy tymi stanami. Dla próbek $x \geq 1,6$ nastąpiło natomiast znaczne skrócenie czasów zaników ze względu na wspomnianą już wcześniej przemianę fazową.

Odwrotne zachowanie parametrów sieci krystalicznej, niż w przypadku domieszkowania Al^{3+}, obserwujemy, gdy Ga^{3+} jest zastępowane jonami Sc^{3+}, o większym promieniu jonowym (0,745 Å; CN = 6).[53] Wraz ze wzrostem koncentracji Sc^{3+} zwiększają się odległości Cr-O, tym samym zmniejszając siłę pola krystalicznego wokół jonu Cr^{3+}. To skutkuje przesunięciem w kierunku dłuższych fal szerokopasmowej emisji oraz pasm wzbudzenia luminescencji, co pokazano w publikacji [P3] dla serii $Ga_{1,994-x}Sc_xO_3$:$0,006Cr^{3+}$ (GSOC), x = 0 - 0,87.

Podstawiając $(Al_{0,68}In_{0,32})^{3+}$ w miejsce jonu Ga^{3+} możemy wytworzyć strukturę z zaburzeniami kationowymi, o zniekształconej oraz nieuporządkowanej sieci krystalicznej. Efekt ten może wzmocnić sprzężenie elektron-fonon oraz stopień rozszczepienia stanów energetycznych, prowadząc do poszerzenia widma emisji luminoforu Ga_2O_3:Cr^{3+}.[54] Badania dla serii $Ga_{1,98-x}(Al_{0,68}In_{0,32})_xO_3$:$0,02Cr^{3+}$ (GIOC), x = 0 - 0,8, przedstawione w publikacji [P5],

pokazały poszerzenie oraz przesunięcie widm emisji w kierunku dłuższych fal przy domieszkowaniu $Al_{0,68}In_{0,32}$, zachowując niezmienną objętości kryształu (objętość sieci krystalicznej V zmienia się o mniej niż 1%).

Dodatkowo, w publikacjach [P1]-[P3] wyznaczono parametry pola krystalicznego Dq oraz parametry Racah B i C (opisane za pomocą równań (2) oraz (3)) oraz opisano położenie stanów energetycznych dla domieszki Cr^{3+} w danej matrycy krystalicznej, za pomocą diagramów konfiguracyjnych. Parametry Dq, B i C, oraz diagramy konfiguracyjne dla trzech różnych matryc: matrycy o słabym polu krystalicznym (GSOC), „pośrednim" polu krystalicznym (GOC) oraz silnym polu krystalicznym (GAOC), zostały przedstawione odpowiednio w publikacjach [P3], [P1] oraz [P2]. Dla materiału GSOC, $x = 0,87$, najniżej położonym stanem wzbudzonym jest stan $^4T_2$, natomiast dla próbki GOC, $x = 0$, stan ^2E. Wraz ze zwiększeniem siły pola krystalicznego Dq, różnica pomiędzy tymi stanami, wzrasta, co zostało zademonstrowane dla materiału GAOC, $x = 1,2$.

3.1.2   Wpływ temperatury na własności luminescencyjne

Przedstawione w publikacji [P1] badania widm emisji w funkcji temperatury materiału GOC wykazały, że całkowita intensywność luminescencji ($^2E + {}^4T_2 \rightarrow {}^4A_2$) spadła jedynie w nieznacznym stopniu wraz ze wzrostem temperatury od 10 do 400 K. Wskazuje to na wysoką stabilność temperaturową emisji w badanym zakresie temperatur. Dodatkowo, w niskich temperaturach zaobserwowano wyłącznie emisję wąskoliniową, co pokazuje, że wszystkie jony Cr^{3+} w matrycy Ga_2O_3 znajdują się w silnym polu krystalicznym.

Kolejnym interesującym zjawiskiem, które zaobserwowano, jest zależność stosunku intensywności linii R_2 do R_1 w funkcji temperatury. W niskiej temperaturze (10 K) tylko niżej położony stan wzbudzony jest obsadzony, skutkując tylko jedną linią R (R_1) w widmie emisji. Wraz ze wzrostem temperatury następuje termiczne obsadzenie wyższego stanu, co powoduje pojawienie się emisji pochodzącej od wyżej położonego stanu (linia R_2). Co ciekawe, w badanym związku lina R_2 zaczyna dominować nad R_1 przy temperaturze około 200 K. Ten nietypowy efekt jest spowodowany wysokim prawdopodobieństwem przejścia dla linii emisyjnej R_2, charakterystycznym dla jonów Cr^{3+} okupujących miejsca krystalograficzne o silnym, trygonalnym zniekształceniu.[55] Na podstawie dopasowania wyników eksperymentalnych stosunku R_2/R_1 wykazano, że energia rozszczepienia linii R_1 oraz R_2 (δ),

wynosi 162 ± 8 cm^{-1}, a prawdopodobieństwo przejścia (q) linii emisyjnej R_2 jest ok. cztery razy większe niż R_1. Dodatkowo, wyznaczono stosunek intensywności stokesowskich powtórzeń fononowych (I_{SB}) do linii $R(R_1+R_2)$ (I_R), $I_{SB}/I_R = 0{,}7$ oraz stosunek prawdopodobieństwa przejść promienistych stanów ^2E oraz $^4T_2$, $\tau_E/\tau_T = 125 \pm 40$.

W publikacji [P2] wyznaczono zależność położenia stanów $^4T_2$ od koncentracji Al^{3+}. Przyjęto, że różnica energii pomiędzy wyższym stanem $^4T_2$ a stanem ^2E stanowi energię aktywacji Δ w procesie skracania czasu zaniku pod wpływem wzrostu temperatury. Energia aktywacji Δ dla fazy β-Ga$_2$O$_3$ jest dużo mniejsza (614-602 cm^{-1}) niż dla fazy α-Ga$_2$O$_3$ (1012-1581 cm^{-1}) ze względu na większą różnicę energii pomiędzy stanami $^4T_2$ oraz ^2E dla fazy α.

Z zależności temperaturowej luminescencji wynika dodatkowo, że próbki o wyższej koncentracji Al^{3+} ($x \geq 1{,}6$) są bardziej stabilne temperaturowo, a ich energia aktywacji przejść bezpromienistych E_A wynosi 3640-4390 cm^{-1}. Dla próbek o niskim x ($x \leq 1{,}2$), E_A wynosi w przybliżeniu 2700-2870 cm^{-1}. Natomiast dla serii GIOC, energia aktywacji E_A maleje wraz ze wzrostem x (Al$_{0,68}$In$_{0,32}$)$^{3+}$, z 3760 cm^{-1} ($x = 0{,}1$) do 1700 cm^{-1} ($x = 0{,}8$) (publikacja [P5]).

3.1.3 Subtelne zmiany w mikrostrukturze krystalicznej, ujawnione za pomocą spektroskopii czasowo-rozdzielczej

W publikacji [P3], za pomocą pomiarów optycznych, pokazano subtelne zmiany w mikrostrukturze krystalicznej serii GSOC. Pomiary luminescencji rozdzielonej w czasie, w temperaturze 10 K, wykazały, że dla próbki niedomieszkowanej Sc^{3+} ($x = 0$), widma luminescencji rozdzielonej w czasie, wzięte w dwóch różnych odstępach czasowych po wzbudzeniu, są takie same. Pokazuje to, że w tym materiale występuje tylko jedno centrum luminescencji. Natomiast dla próbek $x = 0{,}2$-$0{,}6$ widmo luminescencji zmienia się znacząco w czasie. Wskazuje to na ciągły rozkład wartości siły pola krystalicznego w pobliżu przecięcia się stanów ^2E i $^4T_2$, gdzie centra luminescencji Cr^{3+} znajdują się zarówno w silnym, jak i słabym, polu krystalicznym. W związku z tym obserwujemy jednocześnie emisję szerokopasmową, jak i emisje liniową, nawet w bardzo niskich temperaturach (10 K). Dla próbek o wyższej koncentracji Sc^{3+} ($x = 0{,}8$ i $1{,}0$) wszystkie centra luminescencji Cr^{3+} znajdują się w słabym polu krystalicznym ($Dq/B < 2{,}4$). Powoduje to nakładanie się widm luminescencji o zbliżonych

czasach zaniku. Podobny efekt zaobserwowano dla serii GIOC, co zostało przedstawione w publikacji [P5].

3.1.4 Wpływ wysokiego ciśnienia na własności luminescencyjne jonów Cr^{3+}

Rys. 3 a przedstawia widma luminescencji materiału GOC w funkcji ciśnienia mechanicznego. Zgodnie z oczekiwaniami, ze względu na silną zależność przejść $^4A_2 \rightarrow ^4T_1$, $^4T_2$ od parametru Dq, emisja szerokopasmowa dla GOC, związana z przejściem $^4T_2 \rightarrow ^4A_2$, przesuwa się silnie w kierunku niebieskim (wyższych energii) wraz ze wzrostem ciśnienia. Dla pewnego ciśnienia (około 44 kbar dla $x = 0$), emisja szerokopasmowa zanika, a obserwuje się tylko emisję wąskoliniową (linie R). Jest to wywołane przesunięciem ciśnieniowym stanu $^4T_2$ w kierunku wyższych energii oraz jednoczesnym przesunięciem się stanu ^2E w kierunku niższych energii. W efekcie energia termiczna jest zbyt mała, by obsadzić stan $^4T_2$, ze stanu ^2E, który staje się jedynym emitującym stanem. Ponadto, widoczna jest znaczna zmiana widma luminescencji pomiędzy ciśnieniem 123 a 140 kbar, gdzie widoczna jest tylko jedna linia. Zmiana widma emisji jest spowodowana przejściem fazowym z β-Ga_2O_3 do α-Ga_2O_3. Warto przypomnieć, że zaobserwowano również tę samą przemianę fazową wywołaną domieszkowaniem jonami Al^{3+} (ciśnienie chemiczne) w serii GAOC.

Podobne wyniki ciśnieniowe pokazano dla GAOC ($x = 0,4$; $1,6$) w publikacji [P2], GSOC ($x = 0,87$) w publikacji [P3] oraz dla GIOC ($x = 0,1$; $0,8$) w publikacji [P5], z tym, że dla próbki GAOC, $x = 0,4$, pasmo zanika już w 18 kbar (ze względu na większą różnicę energii stanów ^2E oraz $^4T_2$ w porównaniu z próbką $x = 0$). Dla $x = 1,6$ nie obserwuje się szerokiego pasma nawet w ciśnieniu atmosferycznym. Natomiast, dla materiałów GSOC ($x = 0,87$) oraz GIOC ($x = 0,8$) szerokie pasmo zanika w dużo wyższych ciśnieniach, odpowiednio, 136 oraz 94 kbar, ze względu na większą różnicę energii stanów ^2E oraz $^4T_2$ w porównaniu do próbki $x = 0$.

Z zależności ciśnieniowej kinetyki luminescencji przedstawionej w publikacji [P1] dla GOC wynika, że zanik luminescencji jest jednowykładniczy dla wartości ciśnień do 88 kbar, podczas gdy dla wyższych ciśnień staje się niewykładniczy, gdzie zmiana ta jest wywołana przejściem fazowym. Na **Rys. 3 b** przedstawiono czasy zaniku, wyznaczone z dopasowania funkcją jednowykładniczą profili zaników do 88 kbar. Dla ciśnień powyżej tego zakresu, ze względu na niewykładniczość profili zaników, obliczono średnie czasy zaniku luminescencji. Indukowany ciśnieniem wzrost siły pola krystalicznego zwiększa różnicę energii pomiędzy

29
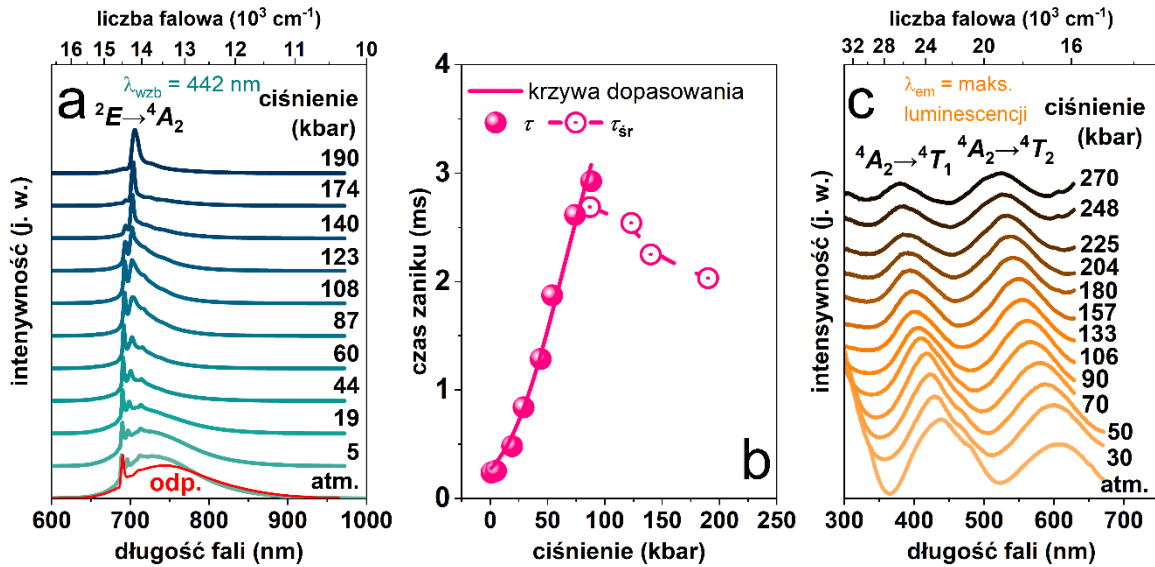
Rys. 3 (a) Widma luminescencji w funkcji ciśnienia zarejestrowane przy długości fali wzbudzającej 442 nm, dla GOC w temperaturze pokojowej. **(b)** Czasy zaniku luminescencji w funkcji ciśnienia wyznaczone z dopasowania profili zaniku funkcją jednowykładniczą do 88 kbar, oraz wyliczone średnie czasy zaniku do wyższych wartości ciśnień. **(c)** Widma wzbudzenia luminescencji w funkcji ciśnienia zarejestrowane dla maksimum luminescencji.

stanami $^4T_2$ oraz ^2E oraz zmniejsza termiczne obsadzenie wyższego stanu $^4T_2$. Biorąc pod uwagę, że przejście $^2E \rightarrow {}^4A_2$ jest przejściem ze zmianą spinu, liniowa emisja zachodzi głównie ze względu na sprzężenie spin-orbita między stanami ^2E i $^4T_2$. Sprzężenie to zmniejsza się wraz ze wzrostem ciśnienia. W konsekwencji, oba efekty prowadzą do wydłużenia się czasu zaniku luminescencji przejścia wraz ze wzrostem ciśnienia.

Jak pokazano na **Rys. 3 b** wydłużanie się czasów zaniku następuje do pewnego ciśnienia, równego 88 kbar. Powyżej tego ciśnienia, czas zaniku luminescencji skraca się ze względu na wspomnianą wcześniej przemianę fazową. Czas zaniku jonu Cr^{3+} w nowej fazie trygonalnej jest krótszy. Dla ciśnień w zakresie powyżej 88 kbar występuje mieszanina obydwu faz: β-Ga_2O_3 oraz α-Ga_2O_3. Skrócenie czasów zaniku w tym obszarze spowodowane jest wzrostem składnika fazy α-Ga_2O_3, o krótszym czasie zaniku. Z dopasowania zależności czasu zaniku od ciśnienia przed przemianą fazową (ciągła różowa linia na **Rys. 3 b**) otrzymano zmianę ciśnieniową energii aktywacji stanu $^4T_2$, $d\Delta/d\wp$ równą $10 \pm 0,5$ cm^{-1}/kbar.

W publikacji [P4] oraz na **Rys. 3 c** przedstawiono wyniki unikatowych pomiarów widm wzbudzenia luminescencji w funkcji ciśnienia dla GOC ($x = 0$). Jak się spodziewano, obydwa szerokie pasma w widmie wzbudzenia luminescencji przesuwają się w kierunku większych
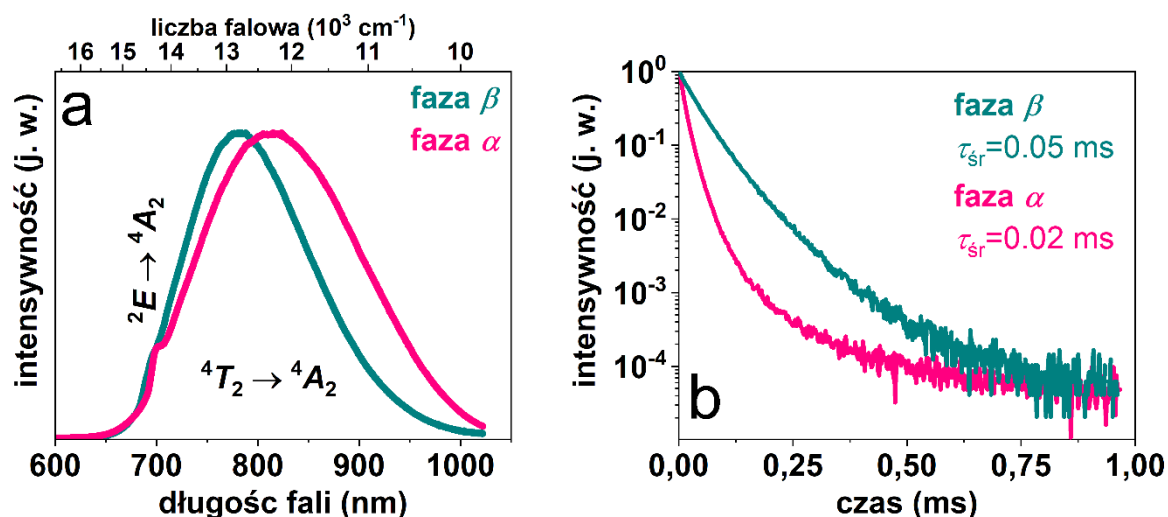
Rys. 4 (a) Widma luminescencji próbki $Ga_{1,18}Al_{0,544}In_{0,256}O_3$:$0,02Cr^{3+}$ w ciśnieniu atmosferycznym oraz temperaturze pokojowej, w fazie β (przed przemianą fazową) oraz α (po przemianie fazowej). **(b)** Profile zaniku luminescencji obserwowanej dla emisji w zakresie 750-850 nm, wraz z wyznaczonymi średnimi czasami zaniku.

energii wraz ze wzrostem ciśnienia, tak samo jak emisja szerokopasmowa, natomiast emisja wąskoliniowa (linie R) przesuwa się w kierunku mniejszych energii.

Podobne zachowanie własności optycznych w wysokich ciśnieniach obserwuje się dla próbek GAOC, GSOC oraz GIOC, pokazanych w publikacj [P2], [P4] oraz [P5].

3.1.5 *Własności luminescencyjne nowego materiału wytworzonego w komorze diamentowej pod wysokim ciśnieniem*

Jak już wcześniej wspomniano, dla przebadanych materiałów pod wpływem wysokiego ciśnienia zachodzi przemiana fazowa z fazy β- do α-Ga_2O_3. Warto jest tutaj podkreślić, że przemiana ta jest nieodwracalna. Po odpuszczeniu ciśnienia próbka pozostaje w nowej fazie α, co zostało zilustrowane na **Rys. 3 a** dla materiału GOC, gdzie obserwuje się znaczącą zmianę w widmie luminescencji (czerwona krzywa). Innymi słowy, pod wpływem wysokiego ciśnienia uzyskano nowy materiał luminescencyjny. Podobny efekt zaobserwowano również w przypadku materiału GIOC.

W publikacji [P5] przedstawiono charakterystykę spektroskopową nowego materiału, α-$Ga_{1,18}Al_{0,544}In_{0,256}O_3$:$0,02Cr^{3+}$, wytworzonego w komorze diamentowej pod wysokim ciśnieniem. Próbka w nowej fazie α wykazuje luminescencję jonu Cr^{3+}, korzystniejszą z punktu

widzenia zastosowań jako luminofor do diodowych emiterów podczerwieni. Luminescencja próbki w fazie α jest przesunięta ku czerwieni o około 30 nm oraz znacznie poszerzona o 325 cm^{-1}, w porównaniu z próbką w fazie β, jak pokazano na **Rys. 4 a**. Co więcej, jej średni czas zaniku jest znacznie krótszy (0,2 ms) niż dla próbki w fazie β (0,5 ms), co pokazano na **Rys**. **4 b**. Próbka w nowej fazie znajduje się w słabszym polu krystalicznym (Dq = 1 612 cm^{-1}) niż próbka w fazie β (Dq = 1 638 cm^{-1}).

3.1.6   *Struktura energetyczna jonu Cr^{3+} w funkcji ciśnienia*

Znajomość siły pola krystalicznego Dq oraz parametrów Racah B i C daje możliwość wygenerowania całej struktury energetycznej jonu Cr^{3+}, czyli obliczenia energii wszystkich subtermów pola krystalicznego w konfiguracji d^3 jonu Cr^{3+}. Co więcej, znajomość zachowania tych parametrów względem x oraz ciśnienia (p), przedstawionych w publikacji [P4], pozwoliła na **określenie ewolucji struktury energetycznej jonów Cr^{3+} względem ciśnienia chemicznego oraz mechanicznego, dla serii GAOC.**

Na **Rys. 5** przedstawiono wyniki obliczeń struktury energetycznej wybranych subtermów pola krystalicznego w funkcji x i p dla fazy β oraz α. Dodatkowo, przedstawiono wyniki obliczeń wykonanych przy założeniu stałości B i C w funkcji x oraz p (linie przerywane na **Rys. 5**), co jest równoważne wykresowi Tanabe-Sugano dla parametrów B i C odpowiadających danemu materiałowi w ciśnieniu atmosferycznym.

W strukturze energetycznej jonu Cr^{3+} w GAOC dla ciśnienia chemicznego (**Rys. 5 a**) obserwuje się tylko niewielką zmianę stanów energetycznych, ponieważ zmiana pola krystalicznego jest niewielka w rozpatrywanym obszarze x. W przypadku zewnętrznego ciśnienia mechanicznego zmiany te są znaczące w rozpatrywanym zakresie ciśnienia, zarówno dla fazy β (**Rys. 5 b**) oraz α (**Rys. 5 c**). Dodatkowo, obserwuje się większą zmianę ciśnieniową położeń stanów $^4T_2$, $^4T_1$ i ^2E dla fazy β, niż α (większa zmiana ciśnieniowa parametrów Dq, B oraz C, a w konsekwencji szybszą zmianę stanów elektronowych jonu Cr^{3+}). Jest to spowodowane mniejszą ściśliwością materiału α-Ga$_2$O$_3$ w porównaniu z β-Ga$_2$O$_3$. Potwierdza to wyznaczony w publikacji [P4] moduł sprężystości objętościowej (B_0) dla obu faz. B_0 dla fazy β i α wynosi odpowiednio 154,5 oraz 364,4 GPa, co zgadza się z literaturą.[56–60]
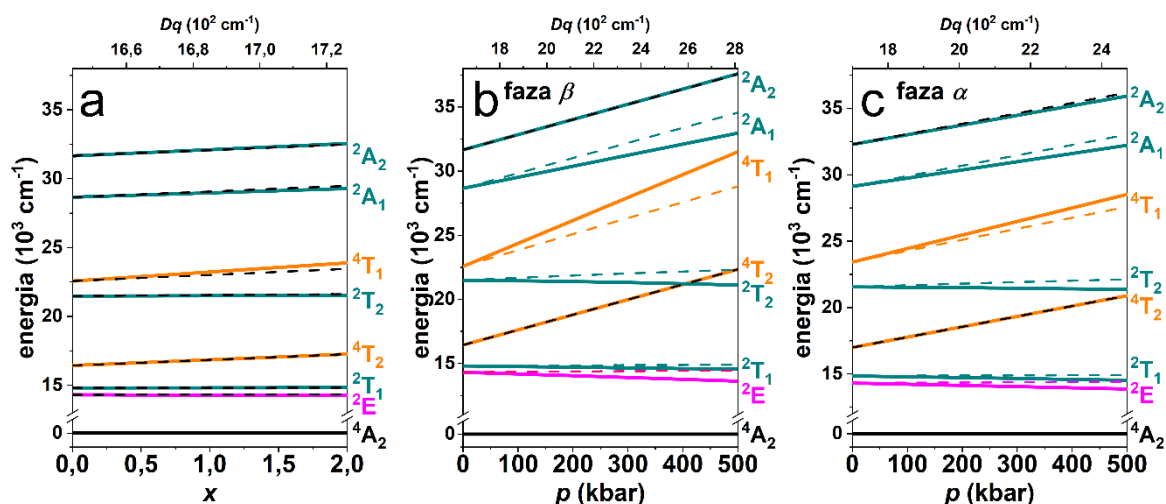
Rys. 5 Schemat struktury energetycznej wybranych subtermów konfiguracji d^3 jonu Cr^{3+} w funkcji **(a)** x dla $Ga_{1,98-x}Al_xO_3{:}0{,}02Cr^{3+}$ (GAOC) oraz p dla GOC ($x = 0$) w fazie **(b)** α i **(c)** β, wraz z obliczeniami przeprowadzonymi przy założeniu, że parametry B i C są niezależne od Dq (linie kreskowane), co jest równoważne diagramom Tanabe-Sugano dla parametrów B i C w ciśnieniu atmosferycznym.

Warto zauważyć, że przedstawione diagramy struktury energetycznej pokazują spadek energii stanów wzbudzonych należących do konfiguracji pola krystalicznego t_2^3 (^2E, $^2T_1$, $^2T_2$) wraz ze wzrostem Dq (zarówno dla p jak x). To zachowanie jest zgodne z obserwowaną zmianą energii przejścia emitującego $^2E \rightarrow {}^4A_2$. Jednakże, nie jest zgodne z przewidywanym zachowaniem na podstawie standardowego diagramu Tanabe-Sugano. Fakt ten jednoznacznie potwierdza konieczność uwzględnienia zmian parametrów Racah przy opisywaniu wyników badań spektroskopowych materiałów domieszkowanych jonami metali przejściowych w funkcji ciśnienia. Kierunek zmian stanów należących do pozostałych konfiguracji jest taki sam dla obu diagramów, jednak szybkość zmian tych stanów w zależności od ciśnienia różni się od siebie. Jedynie zmiana stanu $^4T_2$ jest identycznie opisywana przez oba sposoby we wszystkich przypadkach, ponieważ zależy on wyłącznie od wartości Dq ($10Dq = E(^4A_2 \rightarrow {}^4T_2)$).

3.1.7 *Porównanie wpływu wewnętrznego ciśnienia chemicznego z zewnętrznym ciśnieniem mechanicznym na własności optyczne jonów Cr^{3+}*

Powszechnie przyjmuje się, że oddziaływanie zewnętrznego ciśnienia mechanicznego jest równoważne oddziaływaniu wewnętrznego ciśnienia chemicznego. **Jednakże, na przykładzie własności luminescencyjnych jonów Cr^{3+} zaprezentowanych w publikacji [P4], pokazano, że wpływ ten może być zasadniczo różny.**

Rys. 6 przedstawia porównanie wpływu ciśnienia mechanicznego oraz chemicznego na własności luminescencyjne jonów Cr^{3+} w matrycy krystalicznej Ga_2O_3 modyfikowanej jonami Al^{3+}, czy Sc^{3+}. Porównano wartości parametrów Dq, C i B oraz zmiany energii stanów ^2E i $^4T_1$.

Zastępowanie jonów Ga^{3+} mniejszymi jonami Al^{3+} w materiale GAOC powoduje wzrost natężenia pola krystalicznego (zmniejszanie odległości Ga/Al-O), podobnie jak przy zastosowaniu ciśnienia mechanicznego. W publikacji [P2] pokazano, że zmiana wartości x od 0,0 do 1,6 (ciśnienie chemiczne), jest równoważna zmianie objętości komórki elementarnej z 209,7 na 192,4 $Å^3$. To odpowiada zmianie Dq o około 70 cm^{-1} (cyjanowe punkty na **Rys. 6 a**) od wartości $Dq = 1642$ cm^{-1} do 1710 cm^{-1}. Jest to równoważne zmianie ciśnienia mechanicznego z atmosferycznego do 55 kbar. To pokazuje, że w badanym materiale zmiana x o 0,1 jest równoznaczna zwiększeniu ciśnienia mechanicznego o około 3,4 kbar.

Zmiany wartości parametrów C oraz B (**Rys. 6 b**), jak również stanów $^4T_1$ oraz ^2E (**Rys. 6 c**) od Dq, nie zależą od tego, czy były wywołane ciśnieniem, czy zmianą koncentracji jonów Al^{3+} (x), co wskazuje na podobne działanie ciśnienia mechanicznego i chemicznego na własności luminescencyjne Cr^{3+} dla serii GAOC.

W przypadku zastępowania jonów Ga^{3+} większymi jonami Sc^{3+} w materiale GSOC, następuje spadek natężenia pola krystalicznego (zwiększenie odległości Ga/Sc-O), przeciwnie do zastosowania ciśnienia mechanicznego. Odwracając rozumowanie, zmiana x z 0,87 na 0,00 powoduje zmniejszenie objętości komórki elementarnej z 231,9 na 209,5 $Å^3$, czemu towarzyszy zmiana wartości Dq o około 160 cm^{-1} (cyjanowe punkty na **Rys. 6 d**). Jest to równoważne przyłożonemu ciśnieniu o wartości 110 kbar. Zmiana x o 0,1 jest więc równoważna zmianie ciśnienia o 12,6 kbar. Jest to prawie cztery razy większa zmiana ciśnienia w stosunku do x, niż w przypadku domieszkowania Al^{3+}.

Z porównania parametrów B i C (**Rys. 6 e**) oraz stanów $^4T_1$ oraz ^2E (**Rys. 6 f**) dla GSOC wynika, że zachowanie parametru C oraz stanu $^4T_1$ jest podobne zarówno dla ciśnienia chemicznego, jak i mechanicznego, podczas gdy zmiana parametru B oraz stanu ^2E jest przeciwna. W przypadku ciśnienia chemicznego mamy odwrotne do oczekiwanego zachowanie stanu ^2E wraz z domieszkowaniem Sc^{3+}. Zaskakująco, wraz ze wzrostem wartości Dq (zmniejszeniem x), obserwuje się przesunięcie stanu ^2E w kierunku wyższych energii. Zmniejszając koncentrację janów Sc^{3+} odległości między atomami maleją, ale zmienia się też

lokalne otoczenie. Ta zmiana lokalnego otoczenia silnie wpływa na zachowanie się stanu ^2E, powodując zmniejszenie efektu nefelauksetycznego, pomimo że samo zmniejszanie odległości prowadziłoby do zwiększenia tego efektu.
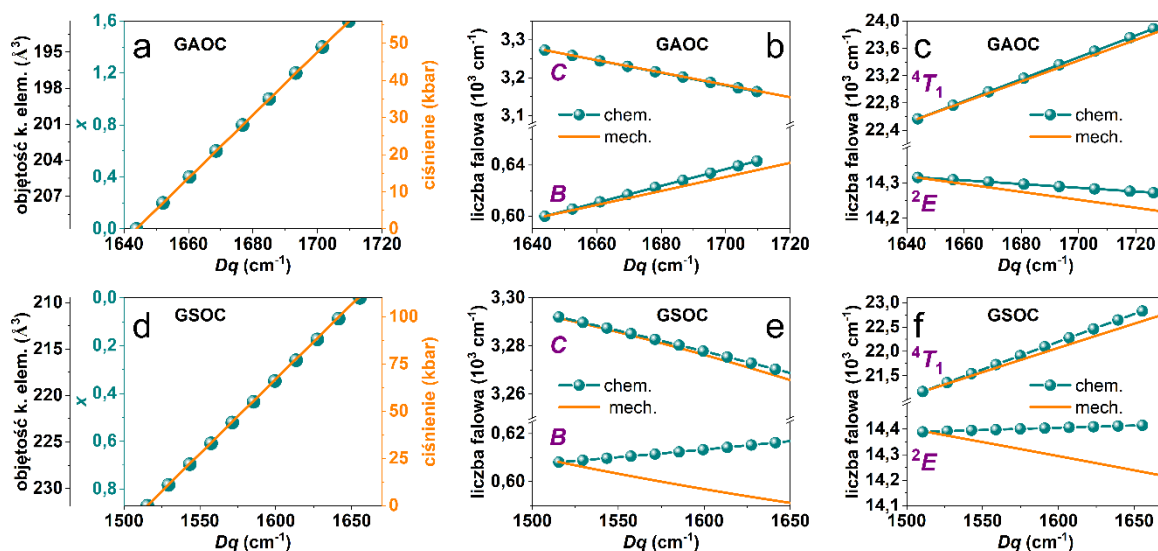
Rys. 6 Porównanie wartości parametru siły pola krystalicznego Dq, parametrów Racah B oraz C oraz stanów $^4T_1$ i ^2E dla ciśnienia zewnętrznego mechanicznego oraz wewnętrznego ciśnienia chemicznego dla serii **(a-c)** GAOC oraz **(d-f)** GSOC.

Podsumowując, dla serii GAOC wpływ ciśnienia chemicznego i mechanicznego jest równoważny, co oznacza, że modyfikacja matrycy przez jony Al^{3+} nie wpływa znacząco na kąty wiązań chemicznych. Najprawdopodobniej podstawianie jonów zachodzi w sąsiedniej komórce elementarnej, która zmienia objętość kryształów i charakter wiązania chemicznego, podobnie jak w przypadku ciśnienia mechanicznego. W przypadku próbek domieszkowanych Sc^{3+} ciśnienie mechaniczne i chemiczne nie jest równoważne. Domieszkowanie jonami Sc^{3+} zmienia lokalne otoczenie wokół jonów Cr^{3+}, co jest również potwierdzone poprzez znaczącą zmianę w widmach Ramana, przedstawionych w publikacji [P4], dla próbek o $x \geq 0,8$. Ściskając materiał GSOC, $x = 0,87$, zmniejszamy objętość komórki, ale nie możemy odwrócić zniekształceń spowodowanych domieszkowaniem. Ciśnienie mechaniczne w tym przypadku nie jest równoważne ciśnieniu chemicznemu.

### 3.2. Wydajna szerokopasmowa luminescencja par Cr^{3+}-Cr^{3+}

W opisywanych dotychczas badaniach, zawartych w niniejszej rozprawie doktorskiej, skoncentrowano się na luminescencji podczerwonej pochodzącej od izolowanych jonów Cr^{3+}. W tym podrozdziale skupiono się na luminescencji podczerwonej pochodzącej od par jonów Cr^{3+}-Cr^{3+}, która jest ciekawym i mało przebadanym dotąd zjawiskiem. Zazwyczaj, luminescencję pochodzącą od par Cr^{3+}-Cr^{3+} traktuje się jako pasożytniczą, która jest słaba i często niewykrywalna w temperaturze pokojowej.[61,62]

W materiałach o strukturze magnetoplumbitu (o wzorze sumarycznym $A[B_{12}]O_{19}$) występuje pięć niezależnych miejsc krystalograficznych dla kationu B. W tych materiałach dwa atomy M4 oraz trzy atomy M5 znajdują się blisko siebie (**Rys. 7 a**), a ich zniekształcone oktaedry połączone są ściankami (M4) lub krawędziami (M5), tworząc wielościany o odległościach M4-M4 oraz M5-M5, wynoszącymi odpowiednio 2,650 i 2,756 Å. Z tego względu tworzenie się par jonów Cr^{3+} (mogących lokować się w miejsca M4 oraz M5) w tych materiałach jest wysoce prawdopodobne.[63,64]

W publikacji [P6] przedstawiono badania spektroskopowe materiałów $SrAl_{11,88-x}Ga_xO_{19}$:0,12Cr^{3+} ($0 \leq x \leq 12$, krok 2, SAGOC) obejmujące badania widm wzbudzenia luminescencji oraz luminescencji wraz z analizą kinetyki luminescencji, widma luminescencji czasowo rozdzielone i stacjonarne w funkcji temperatury oraz ciśnienia. Próbki $x = 0$ oraz 12 odpowiadają materiałom $SrAl_{12}O_{19}$:Cr^{3+} oraz $SrGa_{12}O_{19}$:Cr^{3+}, natomiast pozostałe są roztworami stałymi tych związków.

Widmo luminescencji SAGOC (**Rys. 7 b**) składa się z wąskich linii, (Cr1) około 700 nm oraz szerokiego pasma w zakresie spektralnym od 650 do 950 nm (Cr2). Typowo, luminescencję liniową jonu Cr^{3+} przypisuje się przejściom optycznym ze zmianą spinu $^2E \rightarrow {}^4A_2$, podczas gdy emisję szerokopasmową przypisuje się przejściom bez zmiany spinu $^4T_2 \rightarrow {}^4A_2$. Zaskakująco, czas zaniku luminescencji Cr2 jest w zakresie 1,1-2,4 ms, podobnie jak w przypadku luminescencji Cr1. Luminescencja związana z przejściem optycznym $^4T_2 \rightarrow {}^4A_2$, powinna zanikać znacznie szybciej, w zakresie mikrosekundowym. Milisekundowy czas zaniku luminescencji Cr2 wskazuje na to, że luminescencja ta najprawdopodobniej nie jest związana z przejściami optycznymi bez zmiany spinu $^4T_2 \rightarrow {}^4A_2$, jak pokazano w pracach,[65–67] a z przejściami ze zmianą spinu o mniejszym prawdopodobieństwie. Podobny, milisekundowy

czas zaniku, około 2 ms, zaobserwowano dla par $Cr^{3+}-Cr^{3+}$ w materiale o strukturze perowskitu LaAlO$_3$ domieszkowanym Cr^{3+}.[68]
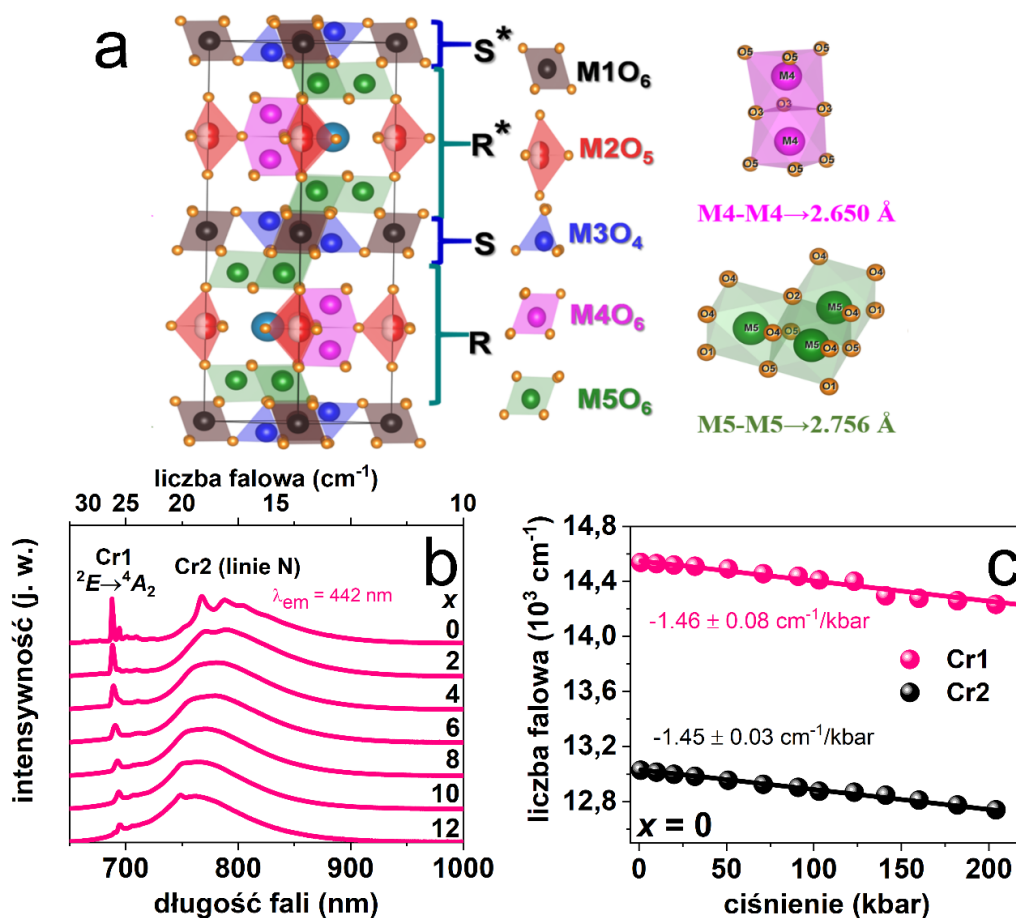
Rys. 7 (a) (po lewej) Struktura krystaliczna magnetoplumbitu. Sfery o kolarze brązowym, czerwonym, niebieskim, różowym oraz zielonym reprezentują Al, Ga odpowiednio w miejscach od M1 do M5, pomarańczowe sfery to atomy tlenu. (po prawej) Lokalna struktura miejsc krystalograficznych M4 oraz M5 w magnetoplumbitach. **(b)** Widma luminescencji wzbudzane długością fali 442 nm. **(c)** Empirycznie wyznaczone, ciśnieniowe przesunięcie luminescencji Cr1 oraz Cr2, dla $x = 0$.

Pomiary ciśnieniowe dla próbek $x = 0$, 6 i 12 przedstawione w publikacji [P6] i na **Rys. 7 c** ($x = 0$) pokazały, że we wszystkich testowanych przypadkach wzrost ciśnienia prowadził do liniowego przesunięcia emisji Cr1 i Cr2 w kierunku niższych energii (dłuższych długości fal) z przesunięciem ciśnieniowym typowym dla przejść optycznych ze zmianą spinu $^2E \rightarrow {}^4A_2$, około -1,5 cm^{-1}/kbar.[69,70] To jednoznacznie potwierdziło, że luminescencji Cr2 nie można przypisać przejściu $^4T_2 \rightarrow {}^4A_2$, które przesunęłoby się w kierunku wyższej energii w znacznie szybszym tempie.[34,35,71] Podsumowując, emisja Cr1 pochodzi od luminescencji izolowanych jonów Cr^{3+}, podczas gdy szerokopasmowa emisja Cr2 pochodzi od par jonów Cr^{3+}-Cr^{3+}.

Występowanie par jonów Cr^{3+} w materiałach o strukturze magnetoplumbitu, zostało również potwierdzone przez pomiary EPR (*ang. Electron Paramagnetic Resonance*), co przedstawiono w publikacji [P6].

W tym miejscu należy zauważyć, iż kreacja par Cr^{3+} prawdopodobnie tyczy się większości materiałów o strukturze magnetoplumbitu. *Liu i wsp.*[65,66] przypisali luminescencję szerokopasmową przejściom $^4T_2 \rightarrow \,^4A_2$ w materiale $LaMgGa_{11}O_{19}:Cr^{3+}$, mimo że w tych pracach pokazano zwiększenie się udziału szerokopasmowej luminescencji w stosunku do luminescencji linii *R*, wraz ze zwiększeniem koncentracji Cr^{3+} oraz milisekundowy czas zaniku dla szerokiego pasma. Prawdopodobnie, luminescencja ta również związana jest z kreacją par Cr^{3+}. Wraz ze zwiększeniem koncentracji Cr^{3+}, rośnie prawdopodobieństwo podwójnego obsadzenia miejsc krystalograficznych M4 oraz M5, prowadząc do zwiększonego udziału luminescencji par Cr^{3+} w stosunku do jonu izolowanego, co właściwie zostało pokazane w tych pracach.

4. Podsumowanie

Podstawę rozprawy doktorskiej stanowi sześć publikacji naukowych, w których przedstawiono wyniki badań spektroskopowych dotyczących luminescencji Cr^{3+} w roztworach stałych: $(Ga_{1,98-x}Al_xO_3:0,02Cr^{3+}$ (GAOC); $Ga_{1,994-x}Sc_xO_3:0,006Cr^3$ (GSOC); $Ga_{1,98-x}(Al_{0,68}In_{0,32})_xO_3:0,02Cr^{3+}$ (GIOC) oraz $SrAl_{11,88-x}Ga_xO_{19}:0,12Cr^{3+}$ (SAGOC)). W ramach tych badań, należy wskazać kilka kluczowych osiągnięć:

- **Pokazano subtelne zmiany w mikrostrukturze krystalicznej materiałów GSOC oraz GIOC, za pomocą badań optycznych.**

- **Określono wpływ kontrolowanego nieuporządkowania kryształu na własności luminescencyjne GIOC. Skutecznie poszerzono oraz przesunięto widma emisji ku czerwieni, przy zachowaniu niezmiennej objętości kryształu.**

- **Wyznaczono położenia stanów energetycznych jonu Cr^{3+} w zależności od siły pola krystalicznego oraz skonstruowano właściwe diagramy energetyczne w funkcji ciśnienia, uwzględniając zmianę parametrów Racah**. Diagramy struktury energetycznej przedstawione w publikacji [P4] wykazują spadek energii stanów ^2E, $^2T_1$ oraz $^2T_2$ wraz ze wzrostem Dq (czego nie demonstruje standardowy diagram Tanabe-Sugano). Takie zachowanie jest zgodne z obserwowaną doświadczalnie zmianą emisji związaną z przejściem $^2E \rightarrow {}^4A_2$. W ten sposób potwierdzono, że należy przedstawiać stany energetyczne jonu Cr^{3+} zgodnie z metodą i diagramami zaproponowanymi w publikacji [P4]. Podobną interpretację należy również zastosować dla innych metali przejściowych.

- **Określono wartości ciśnienia dla przejść fazowych oraz pokazano wpływ przejść fazowych na własności luminescencyjne jonów Cr^{3+}.** W komorze diamentowej pod wysokim ciśnieniem wytworzono nowy materiał, który wykazuje korzystniejszą (szerszą oraz przesuniętą ku czerwieni) luminescencję jonu Cr^{3+} z punktu widzenia zastosowań jako luminofor do diodowych emiterów podczerwieni. Badania te jednoznacznie dowiodły użyteczność spektroskopii wysokociśnieniowej w projektowaniu nowych materiałów luminescencyjnych. Zamiast skomplikowanej, czasochłonnej oraz drogiej syntezy wielu próbek, możliwe jest sprawdzenie własności luminescencyjnych materiałów za pomocą metod wysokociśnieniowych oraz zaproponowanie odpowiedniego materiału do późniejszej syntezy. Obecnie prowadzone są intensywne prace mające na celu zsyntezowanie tego materiału.

- **Porównano wpływ zewnętrznego ciśnienia mechanicznego i wewnętrznego ciśnienia chemicznego na własności luminescencyjne jonu Cr^{3+}.** Dla serii GAOC wpływ ciśnienia chemicznego i mechanicznego jest równoważny. W przypadku próbek GASOC wpływ ten nie jest równoważny. Domieszkowanie jonami Sc^{3+} zniekształca sieć w lokalnym otoczeniu jonu Cr^{3+}. Ściskając taki materiał można zmniejszyć objętość komórki, ale nie można odwrócić zniekształceń spowodowanych domieszkowaniem.

- **Wyjaśnieniono pochodzenie szerokopasmowej luminescencji magnetoplumbitów domieszkowanych jonami chromu poprzez badania wysokociśnieniowe.** Dzięki tym badaniom jednoznacznie odrzucono przekonanie, że luminescencja ta związana jest z przejściem ze stanu wzbudzonego $^4T_2$ do stanu podstawowego $^4A_2$. Emisję wąskoliniową przypisano luminescencji izolowanych jonów Cr^{3+} w miejscach oktaedrycznych, podczas gdy szerokopasmową emisję przypisano parom jonów Cr^{3+}-Cr^{3+}.

Materiały tlenkowe domieszkowanych jonami Cr^{3+} są obecnie bardzo intensywnie badane, ze względu na ich potencjalne możliwości aplikacyjne jako wydajne materiały luminescencyjne o określonych parametrach spektralnych do zastosowań jako emitery światła w zakresie bliskiej podczerwieni. Badane w publikacjach materiały zostały w większości wykorzystane do konstrukcji diod *pc*-LED emitujących promieniowanie podczerwone w zakresie spektralnym 750-1100 nm o wysokiej sprawności. Wszystkie diody *pc*-LED zostały wykonane w oparciu o diodę InGaN emitująca światło o długości fali 450 nm i sprawdzone przy prądzie zasilającym 350 mA. Wykorzystując materiał $Ga_{1,594}Sc_{0,4}O_3$:$0,006Cr^{3+}$ ([P3]) oraz $Ga_{1,18}(Al_{0,544}In_{0,256})O_3$:$0,02Cr^{3+}$ ([P5]), zbudowano diody charakteryzujące się mocą promieniowania równą odpowiednio 66,09 mW oraz 68,8 mW z FWHM równą 160 oraz 156 nm. Wymieszanie luminoforów $Ga_{1,594}Sc_{0,4}O_3$:$0,006Cr^{3+}$ i $Ga_{1,18}Al_{0,8}O_3$:$0,02Cr^{3+}$ ([P2]) pozwoliło na poszerzenie widma emisji o ponad 40 nm oraz zwiększenie mocy promieniowania do 118,77 mW. Natomiast, dla diody *pc*-LED z luminoforem $SrAl_{5,88}Ga_6O_{19}$:$0,12Cr^{3+}$ osiągnięto moc wyjściową 96 mW ([P6]). Dioda ta wykazuje wyższą wartość mocy promieniowania w porównaniu ze znanymi luminoforami na podczerwień domieszkowanymi jonami Cr^{3+} takimi jak $LiIn_{0,94}Si_2O_6$:$0,06Cr^{3+}$, $Sc_{0,98}BO_3$:$0,02Cr^{3+}$, $La_3Ga_{0,93}Ge_5O_{16}$:$0,07Cr^{3+}$ oraz $La_3Ga_{4,95}GeO_{14}$:$0.05Cr^{3+}$.[7,42,72,73] Otrzymane wyniki jednoznacznie dowodzą dużego potencjału aplikacyjnego materiałów przedstawionych w pracy doktorskiej jako luminoforów do diodowych emiterów podczerwieni.

5. Bibliografia

(1)   *Handbook of Laser Technology and Applications: Volume 2: Laser Design and Laser Systems*; Jones, C. W., Julian D. C., Ed.; CRC Press: Boca Raton, 2020.

(2)   Lü, W.; Lv, W.; Zhao, Q.; Jiao, M.; Shao, B.; You, H. A Novel Efficient Mn^{4+} Activated $Ca_{14}Al_{10}Zn_6O_{35}$ Phosphor: Application in Red-Emitting and White LEDs. *Inorg. Chem.* 2014, *53* (22), 11985–11990.

(3)   Mello, A. C. S. de; Santana, G. C.; Jackson, R. A.; Macedo, Z. S.; Moreira, S. G. C.; Valerio, M. E. G. Optical Properties of Pure and Cr^{3+} Doped BGO Ceramic Scintillators. *Phys. Status Solidi C* 2007, *4* (3), 980–983.

(4)   Dai, Z.; Boiko, V.; Grzeszkiewicz, K.; Markowska, M.; Ursi, F.; Hölsä, J.; Saladino, M. L.; Hreniak, D. Effect of Annealing Temperature on Persistent Luminescence of $Y_3Al_2Ga_3O_{12}$:Cr^{3+} Co-Doped with Ce^{3+} and Pr^{3+}. *Opt. Mater.* 2021, *111*, 110522.

(5)   *Phosphor Handbook*; Shionoya, S., Yen, W. M., Ed.; CRC Press: Boca Raton, 1999.

(6)   Maiman, T. H. Stimulated Optical Radiation in Ruby. *Nature* 1960, *187* (4736), 493–494.

(7)   Rajendran, V.; Fang, M.-H.; Guzman, G. N. D.; Lesniewski, T.; Mahlik, S.; Grinberg, M.; Leniec, G.; Kaczmarek, S. M.; Lin, Y.-S.; Lu, K.-M.; Lin, C.-M.; Chang, H.; Hu, S.-F.; Liu, R.-S. Super Broadband Near-Infrared Phosphors with High Radiant Flux as Future Light Sources for Spectroscopy Applications. *ACS Energy Lett.* 2018, *3* (11), 2679–2684.

(8)   Fang, Y.; Shang, J.; Liu, D.; Shi, W.; Li, X.; Ma, H. Design, Synthesis, and Application of a Small Molecular NIR-II Fluorophore with Maximal Emission beyond 1200 Nm. *J. Am. Chem. Soc.* 2020, *142* (36), 15271–15275.

(9)   Huang, L.; Li, Z.; Zhao, Y.; Yang, J.; Yang, Y.; Pendharkar, A. I.; Zhang, Y.; Kelmar, S.; Chen, L.; Wu, W.; Zhao, J.; Han, G. Enhancing Photodynamic Therapy through Resonance Energy Transfer Constructed Near-Infrared Photosensitized Nanoparticles. *Adv. Mater.* 2017, *29* (28), 1604789.

(10)   *Phosphor Handbook: Experimental Methods for Phosphor Evaluation and Characterization*, 3rd ed.; Wang, R.-S. L., Xiaojun, Ed.; CRC Press: Boca Raton, 2022.

(11)   *Phosphor Handbook: Novel Phosphors, Synthesis, and Applications*, 3rd ed.; Wang, R.-S. L., Xiaojun, Ed.; CRC Press: Boca Raton, 2022.

(12)   Smith, A. M.; Mancini, M. C.; Nie, S. Second Window for in Vivo Imaging. *Nat. Nanotechnol.* 2009, *4* (11), 710–711.

(13) Xu, J.; Tanabe, S. Persistent Luminescence Instead of Phosphorescence: History, Mechanism, and Perspective. *J. Lumin.* 2019, *205*, 581–620.

(14) Basavaraju, N.; Sharma, S.; Bessière, A.; Viana, B.; Gourier, D.; Priolkar, K. R. Red Persistent Luminescence in $MgGa_2O_4 : Cr^{3+}$; a New Phosphor for in Vivo Imaging. *J. Phys. Appl. Phys.* 2013, *46* (37), 375401.

(15) Van den Eeckhout, K.; Smet, P. F.; Poelman, D. Persistent Luminescence in Eu2+-Doped Compounds: A Review. *Materials* 2010, *3* (4), 2536–2566.

(16) Li, Y.; Gecevicius, M.; Qiu, J. Long Persistent Phosphors - from Fundamentals to Applications. *Chem. Soc. Rev.* 2016, *45* (8), 2090–2136.

(17) Lécuyer, T.; Teston, E.; Ramirez-Garcia, G.; Maldiney, T.; Viana, B.; Seguin, J.; Mignet, N.; Scherman, D.; Richard, C. Chemically Engineered Persistent Luminescence Nanoprobes for Bioimaging. *Theranostics* 2016, *6* (13), 2488–2524.

(18) le Masne de Chermont, Q.; Chanéac, C.; Seguin, J.; Pellé, F.; Maîtrejean, S.; Jolivet, J.-P.; Gourier, D.; Bessodes, M.; Scherman, D. Nanoprobes with Near-Infrared Persistent Luminescence for in Vivo Imaging. *Proc. Natl. Acad. Sci.* 2007, *104* (22), 9266–9271.

(19) Ueda, J.; Back, M.; Brik, M. G.; Zhuang, Y.; Grinberg, M.; Tanabe, S. Ratiometric Optical Thermometry Using Deep Red Luminescence from $^4T_2$ and ^2E States of Cr^{3+} in $ZnGa_2O_4$ Host. *Opt. Mater.* 2018, *85*, 510–516.

(20) Back, M.; Ueda, J.; Brik, M. G.; Lesniewski, T.; Grinberg, M.; Tanabe, S. Revisiting Cr^{3+}-Doped $Bi_2Ga_4O_9$ Spectroscopy: Crystal Field Effect and Optical Thermometric Behavior of Near-Infrared-Emitting Singly-Activated Phosphors. *ACS Appl. Mater. Interfaces* 2018, *10* (48), 41512–41524.

(21) S. Brites, C. D.; P. Lima, P.; O. Silva, N. J.; Millán, A.; S. Amaral, V.; Palacio, F.; D. Carlos, L. Thermometry at the Nanoscale. *Nanoscale* 2012, *4* (16), 4799–4829.

(22) Jaque, D.; Vetrone, F. Luminescence Nanothermometry. *Nanoscale* 2012, *4* (15), 4301–4326.

(23) Szymczak, M.; Woźny, P.; Runowski, M.; Pieprz, M.; Lavín, V.; Marciniak, L. Temperature Invariant Ratiometric Luminescence Manometer Based on Cr^{3+} Ions Emission. *Chem. Eng. J.* 2023, *453*, 139632.

(24) Szymczak, M.; Runowski, M.; Lavín, V.; Marciniak, L. Highly Pressure-Sensitive, Temperature Independent Luminescence Ratiometric Manometer Based on $MgO:Cr^{3+}$ Nanoparticles. *Laser Photonics Rev.* 2023, *17* (4), 2200801.

(25) Hayashi, D.; van Dongen, A. M.; Boerekamp, J.; Spoor, S.; Lucassen, G.; Schleipen, J. A Broadband LED Source in Visible to Short-Wave-Infrared Wavelengths for Spectral Tumor Diagnostics. *Appl. Phys. Lett.* 2017, *110* (23), 233701.

(26) De Guzman, G. N. A.; Fang, M.-H.; Liang, C.-H.; Bao, Z.; Hu, S.-F.; Liu, R.-S. [INVITED] Near-Infrared Phosphors and Their Full Potential: A Review on Practical Applications and Future Perspectives. *J. Lumin.* 2020, *219*, 116944.

(27) Huang, W.; Luo, S.; Yang, D.; Zhang, S. Applications of Smartphone-Based near-Infrared (NIR) Imaging, Measurement, and Spectroscopy Technologies to Point-of-Care (POC) Diagnostics. *J. Zhejiang Univ. Sci. B* 2021, *22* (3), 171–189.

(28) Jia, Z.; Yuan, C.; Liu, Y.; Wang, X.-J.; Sun, P.; Wang, L.; Jiang, H.; Jiang, J. Strategies to Approach High Performance in Cr^{3+} -Doped Phosphors for High-Power NIR-LED Light Sources. *Light Sci. Appl.* 2020, *9* (1), 86.

(29) Pan, Z.; Lu, Y.-Y.; Liu, F. Sunlight-Activated Long-Persistent Luminescence in the near-Infrared from Cr^{3+}-Doped Zinc Gallogermanates. *Nat. Mater.* 2011, *11* (1), 58–63.

(30) He, S.; Zhang, L.; Wu, H.; Wu, H.; Pan, G.; Hao, Z.; Zhang, X.; Zhang, L.; Zhang, H.; Zhang, J. Efficient Super Broadband NIR $Ca_2LuZr_2Al_3O_{12}$:Cr^{3+},Yb^{3+} Garnet Phosphor for Pc-LED Light Source toward NIR Spectroscopy Applications. *Adv. Opt. Mater.* 2020, *8* (6), 1901684.

(31) Bai, B.; Dang, P.; Huang, D.; Lian, H.; Lin, J. Broadband Near-Infrared Emitting $Ca_2LuScGa_2Ge_2O_{12}$:Cr^{3+} Phosphors: Luminescence Properties and Application in Light-Emitting Diodes. *Inorg. Chem.* 2020, *59* (18), 13481–13488.

(32) Kittel, C. *Introduction to Solid State Physics*, 8th ed.; Wiley: Hoboken, NJ, 2005.

(33) Henderson, B.; Imbusch, G. F. *Optical Spectroscopy of Inorganic Solids*; Monographs on the Physics and Chemistry of Materials; Oxford University Press: Oxford, New York, 2006.

(34) Tanabe, Y.; Sugano, S. On the Absorption Spectra of Complex Ions. I. *J. Phys. Soc. Jpn.* 1954, *9* (5), 753–766.

(35) Tanabe, Y.; Sugano, S. On the Absorption Spectra of Complex Ions II. *J. Phys. Soc. Jpn.* 1954, *9* (5), 766–779.

(36) Sugano, S.; Tanabe, Y.; Kamimura, H. Multiplets of Transition-Metal Ions in Crystals. *Academic Press* 1970.

(37) Griffith, J. S. *The Theory of Transition-Metal Ions*; Cambridge University Press, 1961.

(38) Aoki, Y.; My, N. T.; Yamamoto, S.; Naramoto, H. Luminescence of Sapphire and Ruby Induced by He and Ar Ion Irradiation. *Nucl. Instrum. Methods Phys. Res. Sect. B Beam Interact. Mater. At.* 1996, *114* (3), 276–280.

(39) Chao, C.-C. Charge-Transfer Luminescence of Cr^{3+} in Magnesium Oxide. *J. Phys. Chem. Solids* 1971, *32* (11), 2517–2528.

(40) Blasse, G.; Grabmaier, B. C. *Luminescent Materials*; Springer: Berlin, Heidelberg, 1994.

(41) Campochiaro, C.; McClure, D. S. Absorption and Emission Fine Structure in $ScBO_3$: Cr^{3+}. *Tunable Solid State Lasers* 1987, TuD21 Optica Publishing Group.

(42) Shao, Q.; Ding, H.; Yao, L.; Xu, J.; Liang, C.; Jiang, J. Photoluminescence Properties of a $ScBO_3:Cr^{3+}$ Phosphor and Its Applications for Broadband near-Infrared LEDs. *RSC Adv.* 2018, *8* (22), 12035–12042.

(43) Zhao, F.; Song, Z.; Liu, Q. Advances in Chromium-Activated Phosphors for Near-Infrared Light Sources. *Laser Photonics Rev.* 2022, *16* (11), 2200380.

(44) *Phosphor Handbook: Fundamentals of Luminescence*, 3rd ed.; Wang, R.-S. L., Xiaojun, Ed.; CRC Press: Boca Raton, 2022.

(45) Walsh, C. G.; Donegan, J. F.; Glynn, T. J.; Morgan, G. P.; Imbusch, G. F.; Remeika, J. P. Luminescence from β-$Ga_2O_3:Cr^{3+}$. *J. Lumin.* 1988, *40–41*, 103–104.

(46) Bray, K. L. High Pressure Probes of Electronic Structure and Luminescence Properties of Transition Metal and Lanthanide Systems. In *Transition Metal and Rare Earth Compounds: Excited States, Transitions, Interactions I*; Yersin, H., Ed.; Topics in Current Chemistry; Springer: Berlin, Heidelberg, 2001; pp 1–94.

(47) Dunstan, D. J.; Spain, I. L. Technology of Diamond Anvil High-Pressure Cells: I. Principles, Design and Construction. *J. Phys. E* 1989, *22* (11), 913–923.

(48) Holzapfel, W. B.; Isaacs, N. S. *High Pressure Techniques in Chemistry and Physics: A Practical Approach*; Oxford University Press, 1997.

(49) Jayaraman, A. Diamond Anvil Cell and High-Pressure Physical Investigations. *Rev. Mod. Phys.* 1983, *55* (1), 65–108.

(50) Sherman, W. F.; Stadtmuller, A. A. *Experimental Techniques in High-Pressure Research*; Chichester West Sussex ; New York, 1987.

(51) Merrill, L.; Bassett, W. A. Miniature Diamond Anvil Pressure Cell for Single Crystal X-ray Diffraction Studies. *Rev. Sci. Instrum.* 1974, *45* (2), 290–294.

(52)   Barzowska, J.; Lesniewski, T.; Mahlik, S.; Seo, H. J.; Grinberg, M. $KMgF_3:Eu^{2+}$ as a New Fluorescence-Based Pressure Sensor for Diamond Anvil Cell Experiments. *Opt. Mater.* 2018, *84*, 99–102.

(53)   Shannon, R. D. Revised Effective Ionic Radii and Systematic Studies of Interatomic Distances in Halides and Chalcogenides. *Acta Crystallogr. A* 1976, *32* (5), 751–767.

(54)   Wen, D.; Liu, H.; Guo, Y.; Zeng, Q.; Wu, M.; Liu, R. S. Disorder–Order Conversion-Induced Enhancement of Thermal Stability of Pyroxene Near-Infrared Phosphors for Light-Emitting Diodes. *Angew. Chem. Int. Ed.* 2022, *61* (28), e202204411.

(55)   Chang, T. S.; Holzrichter, J. F.; Imbusch, G. F.; Schawlow, A. L. Polarized Fluorescence Study of Cr^{3+} through a Stress-Induced Phase Transition in $SrTiO_3$. *Solid State Commun.* 1970, *8* (15), 1179–1181.

(56)   Yoshioka, S.; Hayashi, H.; Kuwabara, A.; Oba, F.; Matsunaga, K.; Tanaka, I. Structures and Energetics of Ga_2O_3 Polymorphs. *J. Phys. Condens. Matter* 2007, *19* (34), 346211.

(57)   Luan, S.; Dong, L.; Jia, R. Analysis of the Structural, Anisotropic Elastic and Electronic Properties of β-Ga_2O_3 with Various Pressures. *J. Cryst. Growth* 2019, *505*, 74–81.

(58)   Varley, J. B.; Weber, J. R.; Janotti, A.; Van de Walle, C. G. Oxygen Vacancies and Donor Impurities in β-Ga_2O_3. *Appl. Phys. Lett.* 2010, *97* (14), 142106.

(59)   Caracas, R.; Cohen, R. E. Post-Perovskite Phase in Selected Sesquioxides from Density-Functional Calculations. *Phys. Rev. B* 2007, *76* (18), 184101.

(60)   Wang, H.; He, Y.; Chen, W.; Zeng, Y. W.; Stahl, K.; Kikegawa, T.; Jiang, J. Z. High-Pressure Behavior of β-Ga_2O_3 Nanocrystals. *J. Appl. Phys.* 2010, *107* (3), 033520.

(61)   Derkosch, J.; Mikenda, W.; Preisinger, A. N-Lines and Chromium-Pairs in the Luminescence Spectra of the Spinels $ZnAl_2O_4:Cr^{3+}$ and $MgAl_2O_4:Cr^{3+}$. *J. Solid State Chem.* 1977, *22* (2), 127–133.

(62)   Vink, A. P.; Meijerink, A. Electron–Phonon Coupling of Cr^{3+}-Pairs and Isolated Sites in α-Al_2O_3 and MgO. *Spectrochim. Acta. A. Mol. Biomol. Spectrosc.* 1998, *54* (11), 1755–1761.

(63)   Holtstam, D.; Hålenius, U. Nomenclature of the Magnetoplumbite Group. *Mineral. Mag.* 2020, *84* (3), 376–380.

(64)   Li, J.; Medina, E. A.; Stalick, J. K.; Sleight, A. W.; Subramanian, M. A. Structural Studies of $CaAl_{12}O_{19}$, $SrAl_{12}O_{19}$, $La_{2/3+\delta}Al_{12-\Delta}O_{19}$, and $CaAl_{10}NiTiO_{19}$ with the Hibonite Structure; Indications of an Unusual Type of Ferroelectricity. *Z. Für Naturforschung B* 2016, *71* (5), 475–484.

(65)   Liu, S.; Wang, Z.; Cai, H.; Song, Z.; Liu, Q. Highly Efficient Near-Infrared Phosphor LaMgGa$_{11}$O$_{19}$:Cr^{3+}. *Inorg. Chem. Front.* 2020, *7* (6), 1467–1473.

(66)   Liu, S.; Cai, H.; Zhang, S.; Song, Z.; Xia, Z.; Liu, Q. Site Engineering Strategy toward Enhanced Luminescence Thermostability of a Cr^{3+}-Doped Broadband NIR Phosphor and Its Application. *Mater. Chem. Front.* 2021, *5* (10), 3841–3849.

(67)   Xu, J.; Chen, D.; Yu, Y.; Zhu, W.; Zhou, J.; Wang, Y. Cr^{3+}:SrGa$_{12}$O$_{19}$: A Broadband Near-Infrared Long-Persistent Phosphor. *Chem. – Asian J.* 2014, *9* (4), 1020–1025.

(68)   Vink, A.; Bruin, M.; Roke, S.; Peijzel, P.; Meijerink, A. Luminescence of Exchange Coupled Pairs of Transition Metal Ions. *J. Electrochem. Soc.* 2001, *148*.

(69)   Grinberg, M.; Barzowska, J.; Shen, Y.; Bray, K. L. Inhomogeneous Broadening of Cr^{3+} Luminescence in Doped LiTaO$_3$. *Phys. Rev. B* 2001, *63* (21), 214104.

(70)   Grinberg, M.; Barzowska, J.; Shen, Y. R.; Bray, K. L.; Dereń, P.; Hanuza, J. High-Pressure Spectroscopy Characterisation of LiSc(WO$_4$)$_2$ Crystals Doped with Trivalent Chromium. *J. Lumin.* 2003, *102–103*, 699–704.

(71)   Galanciak, D.; Perlin, P.; Grinberg, M.; Suchocki, A. High Pressure Spectroscopy of LLGG Doped with Cr^{3+}. *J. Lumin.* 1994, *60–61*, 223–226.

(72)   Xu, X.; Shao, Q.; Yao, L.; Dong, Y.; Jiang, J. Highly Efficient and Thermally Stable Cr^{3+}-Activated Silicate Phosphors for Broadband near-Infrared LED Applications. *Chem. Eng. J.* 2020, *383*, 123108.

(73)   Rajendran, V.; Lesniewski, T.; Mahlik, S.; Grinberg, M.; Leniec, G.; Kaczmarek, S. M.; Pang, W.-K.; Lin, Y.-S.; Lu, K.-M.; Lin, C.-M.; Chang, H.; Hu, S.-F.; Liu, R.-S. Ultra-Broadband Phosphors Converted Near-Infrared Light Emitting Diode with Efficient Radiant Power for Spectroscopy Applications. *ACS Photonics* 2019, *6* (12), 3215–3224.

6. Osiągnięcia naukowe

Wykaz publikacji nie wchodzących w skład rozprawy doktorskiej

i. Satpathy, A.; Huang, W.-T.; Chan, M.-H.; Su, T.-Y.; Kamiński, M.; **Majewska, N.**; Mahlik, S.; Leniec, G.; Kaczmarek, S. M.; Hsiao, M.; Liu, R.-S. Near-Infrared I/II Nanophosphors with Cr^{3+}/Ni^{2+} Energy Transfer for Bioimaging. *Adv. Opt. Mater.* **2023**, 2300321.
https://doi.org/10.1002/adom.202300321.

ii. Hsu, J.-Y.; Chung, R.-J.; Kuo, Y.-L.; Lin, C. C.; **Majewska, N.**; Kreft, D.; Mahlik, S.; Fang, M.-H. Concentration-Induced Hetero-Valent Partial-Inverse Occupation of Infrared Phosphor. *Adv. Opt. Mater.* **2023**, 2300121.
https://doi.org/10.1002/adom.202300121.

iii. Szczodrowski, K.; Behrendt, M.; Barzowska, J.; Górecka, N.; **Majewska, N.**; Leśniewski, T.; Łapiński, M.; Mahlik, S. Lanthanide Ions (Eu^{3+}, Er^{3+}, Pr^{3+}) as Luminescence and Charge Carrier Centers in Sr_2TiO_4. *Dalton Trans.* **2023**, *52* (14), 4329-4335.
https://doi.org/10.1039/D2DT04177D.

iv. Gorbenko, V.; Zorenko, T.; Shakhno, A.; Popielarski, P.; Osvet, A.; Batentschuk, M.; Fedorov, A.; Mahlik, S.; Leśniewski, T.; **Majewska, N.**; Zorenko, Y. Single Crystalline Films of Ce^{3+}-Doped $Y_3Mg_xSi_yAl_{5-x-y}O_{12}$ Garnets: Crystallization, Optical, and Photocurrent Properties. *Materials* **2023**, *16* (5), 1869 (16pp).
https://doi.org/10.3390/ma16051869.

v. Hsu, J.-Y.; Chung, R.-J.; **Majewska, N.**; Kreft, D.; Sheu, H.-S.; Lee, J.-F.; Mahlik, S.; Fang, M.-H. Probing Local Structural Changes by Sharp Luminescent Infrared Nanophosphor for Application in Light-Emitting Diodes. *Chem. Mater.* **2022**, *34* (24), 11093-11100.
https://doi.org/10.1021/acs.chemmater.2c03224.

vi. Tsai, Y.-T.; Huang, Y.; **Majewska, N.**; Mahlik, S.; Muchlis, A.; Huang, Y.-K.; Huang, Y.; Lin, B.-H.; Su, C.; Lin, C. Shielding Effect and Compensation Defect Study on $Na_3Sc_2(PO_4)_y$:$Eu^{2+,3+}$ (y = 2.6-3.0) Phosphor by Anion-Group-Induced Phase Transition. *J. Mater. Chem. C* **2022**, *10* (40), 15044-15050.
https://doi.org/10.1039/D2TC03172H.

vii. Szczodrowski, K.; Górecka, N.; Tojek, M.; Lazarowska, A.; **Majewska, N.**; Mahlik, S. Energetic Structure of Sm^{3+} Luminescence Centers in Sr_2TiO_4. *Dalton Trans.* **2022**, *51* (9), 3713-3720.

https://doi.org/10.1039/D1DT04382J.

viii. Barzowska, J.; **Majewska, N.**; Jankowski, D.; Grzegorczyk, M.; Mahlik, S.; Michalik, D.; Sopicka-Lizer, M.; Aleshkevych, P.; Zhydachevskyy, Y.; Suchocki, A. Mechanism of the Luminescence Enhancement of $SrSi_2N_2O_2$:Eu^{2+} Phosphor via Manganese Addition. *J. Phys. Chem. C* **2022**, *126* (11), 5292-5301.

https://doi.org/10.1021/acs.jpcc.2c00055.

ix. Chen, Y.-S.; Bao, Z.; Huang, W.-T.; Lazarowska, A.; **Majewska, N.**; Mahlik, S.; Leniec, G.; Kaczmarek, S. M.; Huang, H.-Y.; Wu, C.-I.; Huang, D.-J.; Liu, R.-S. Effect of Temperature and Pressure on Structural and Optical Properties of Organic–Inorganic Hybrid Manganese Halides. *Inorg. Chem.* **2022**, *61* (5), 2595-2602.

https://doi.org/10.1021/acs.inorgchem.1c03630.

x. Fang, M.-H.; Hsueh, H.-P.; Vasudevan, T.; Huang, W.-T.; Bao, Z.; **Majewska, N.**; Mahlik, S.; Sheu, H.-S.; Liu, R.-S. Dual-Emission Eu-Doped $Ca_{2-x}Sr_xPN_3$ Nitridophosphate Phosphors Prepared by Hot Isostatic Press. *J. Mater. Chem. C* **2021**, *9* (26), 8158-8162.

https://doi.org/10.1039/D1TC01207J.

xi. Mahlik, S.; Barzowska, J.; Szczodrowski, K.; **Majewska, N.**; Grinberg, M.; Michalik, D.; Adamczyk, B. J.; Pawlik, T.; Rzychoń, T.; Adamczyk, A.; Sopicka-Lizer, M. Enhancement of $SrSi_2O_2N_2$:Eu^{2+} Phosphor by Means of Oxygen to Nitrogen Control. *J. Alloys Compd.* **2021**, *884*, 161047 (14pp).

https://doi.org/10.1016/j.jallcom.2021.161047.

xii. Bao, Z.; Hsiu, C.-Y.; Fang, M.-H.; **Majewska, N.**; Sun, W.; Huang, S.-J.; Yuan, E. C.-Y.; Chang, Y.-C.; Chan, J. C. C.; Mahlik, S.; Zhou, W.; Yang, C.-W.; Lu, K.-M.; Liu, R.-S. Formation and Near-Infrared Emission of $CsPbI_3$ Nanoparticles Embedded in Cs_4PbI_6 Crystals. *ACS Appl.Mater. Interfaces* **2021**, *13* (29), 34742-34751.

https://doi.org/10.1021/acsami.1c08920.

xiii. Jendrzejewski, R.; **Majewska, N.**; Majumdar, S.; Sawczak, M.; Ryl, J.; Śliwiński, G. Rubrene Thin Films with Viably Enhanced Charge Transport Fabricated by Cryo-Matrix-Assisted Laser Evaporation. *Materials* **2021**, *14* (16), 4413 (15pp).

https://doi.org/10.3390/ma14164413.

xiv.   Fang, M.-H.; Lin, J.-C.; Huang, W.-T.; **Majewska, N.**; Barzowska, J.; Mahlik, S.; Pang, W. K.; Lee, J.-F.; Sheu, H.-S.; Liu, R.-S. Linking Macro- and Micro-Structural Analysis with Luminescence Control in Oxynitride Phosphors for Light-Emitting Diodes. *Chem. Mater.* **2021**, *33* (19), 7897-7904.
https://doi.org/10.1021/acs.chemmater.1c02990.

xv.   Fang, M.-H.; Li, T.-Y.; Huang, W.-T.; Cheng, C.-L.; Bao, Z.; **Majewska, N.**; Mahlik, S.; Yang, C.-W.; Lu, K.-M.; Leniec, G.; Kaczmarek, S. M.; Sheu, H.-S.; Liu, R.-S. Surface-Protected High-Efficiency Nanophosphors via Space-Limited Ship-in-a-Bottle Synthesis for Broadband Near-Infrared Mini-Light-Emitting Diodes. *ACS Energy Lett.* **2021**, *6* (2), 659-664.
https://doi.org/10.1021/acsenergylett.1c00024.

xvi.   Hsueh, H.-P.; Fang, M.-H.; Vasudevan, T.; Huang, W.-T.; **Majewska, N.**; Lazarowska, A.; Mahlik, S.; Sheu, H.-S.; Lee, J.-F.; Liu, R.-S. Synergetic Effect-Triggered Performance Promotion of $Sr_{3-x}Ba_xP_5N_{10}Cl:Eu^{2+}$ Phosphors. *J. Mater. Chem. C* **2021**, *9* (36), 12063-12067.
https://doi.org/10.1039/D1TC03357C.

xvii.   **Majewska, N.**; Lesniewski, T.; Mahlik, S.; Grinberg, M.; Kulesza, D.; Ueda, J.; Zych, E. Properties of Charge Carrier Traps in $Lu_2O_3:Tb,Hf$ Ceramic Storage Phosphors Observed by High-Pressure Spectroscopy and Photoconductivity. *J. Phys. Chem. C* **2020**, *124* (37), 20340-20349.
https://doi.org/10.1021/acs.jpcc.0c04056.

xviii.   Fang, M.-H.; Chen, P.-Y.; Bao, Z.; **Majewska, N.**; Leśniewski, T.; Mahlik, S.; Grinberg, M.; Sheu, H.-S.; Lee, J.-F.; Liu, R.-S. Broadband $NaK_2Li[Li_3SiO_4]_4:Ce$ Alkali Lithosilicate Blue Phosphors. *J. Phys. Chem. Lett.* **2020**, *11* (16), 6621-6625.
https://doi.org/10.1021/acs.jpclett.0c02064.

xix.   **Majewska, N.**; Leśniewski, T.; Mahlik, S.; Grinberg, M.; Chruścińska, A.; Michalik, D.; Sopicka-Lizer, M. Study of Persistent Luminescence and Thermoluminescence in $SrSi_2N_2O_2:Eu^{2+},M^{3+}$ (M = Ce, Dy, and Nd). *Phys. Chem. Chem. Phys.* **2020**, *22* (30), 17152-17159.
https://doi.org/10.1039/D0CP01739F.

xx.   Fang, M.-H.; Huang, P.-Y.; Bao, Z.; **Majewska, N.**; Leśniewski, T.; Mahlik, S.; Grinberg, M.; Leniec, G.; Kaczmarek, S. M.; Yang, C.-W.; Lu, K.-M.; Sheu, H.-S.; Liu, R.-S. Penetrating Biological Tissue Using Light-Emitting Diodes with a Highly Efficient Near-Infrared $ScBO_3:Cr^{3+}$ Phosphor. *Chem. Mater.* **2020**, *32* (5), 2166-2171.

https://doi.org/10.1021/acs.chemmater.0c00101.

xxi. Fang, M.-H.; Meng, S.-Y.; **Majewska, N.**; Leśniewski, T.; Mahlik, S.; Grinberg, M.; Sheu, H.-S.; Liu, R.-S. Chemical Control of $SrLi(Al_{1−x}Ga_x)_3N_4:Eu^{2+}$ Red Phosphors at Extreme Conditions for Application in Light-Emitting Diodes. *Chem. Mater.* **2019**, *31* (12), 4614-4618.

https://doi.org/10.1021/acs.chemmater.9b01783.

xxii. **Majewska, N.**; Gazda, M.; Jendrzejewski, R.; Majumdar, S.; Sawczak, M.; Śliwiński, G. Organic Semiconductor Rubrene Thin Films Deposited by Pulsed Laser Evaporation of Solidified Solutions. *Third International Conference AOP*; International Society for Optics and Photonics, **2017**; Vol. 10453, p 104532H.

https://doi.org/10.1117/12.2276250.

Prezentacje na konferencjach naukowych

i. 12-15/07/2022 **plakat** w ramach konferencji The 7th International Workshop on Advance Spectroscopy and Optical Materials (IWASOM), *The NIR emission from Cr^{3+} ions in modified Ga_2O_3 matrix*, Gdańsk, Polska.

ii. 24-29/06/2022 **plakat** w ramach konferencji CimTec 9th Forum on New Materials, *The Broadband Emission from Cr^{3+} Ion in Near-Infrared Phosphors for Light-emitting Diodes* Perugia, Włochy.

iii. 12-17/09/2021 **prezentacja** w ramach konferencji 11th International Conference on Luminescent Detectors and Transformers of Ionizing Radiation, *The broadband IR emission from Cr^{3+} ions in Magnetoplumbite*, Bydgoszcz, Polska

iv. 4-6/09/2019 **plakat** w ramach 8th International Workshop on Photoluminescence in Rare Earths: Photonic Materials and Devices, *Study of persistent luminescence in $SrSi_2N_2O_2:Eu^{2+}$, M (M=Ce, Cr, Er, Dy, Nd)*, Nicea, Francja.

v. 9-14/06/2019 **plakat** w ramach 8th International Symposium on Optical Materials, *Study of optically stimulated luminescence in $Lu_2O_3:Tb$, Hf ceramic*, Wrocław, Polska.

vi. 16-18/05/2018 **plakat** w ramach International Conference on Rare Earth Materials (REMAT), *Photoluminescence properties of Narrow-Band Red-Emitting $(Sr_{0.98}Eu_{0.02})LiAl_{3-x}Ga_xN_4$ Phosphor*, Wrocław, Polska.

vii. 8-12/05/2017 **plakat** w ramach International Conference on Applications in Optics and Photonics (AOP), *Organic semiconductor rubrene thin films prepared by matrix-assisted pulsed laser evaporation*, Faro, Portugalia.

viii. 16-18/12/2016 **prezentacja** w ramach Konferencji studentów Fizyki i Astronomii, *Synteza i badanie właściwości fizycznych związku Cu_xMoO_3*, Karpacz, Polska.

ix. 18-21/11/2016 **plakat** w ramach Konferencji Studentów Fizyki, *Synteza i badanie właściwości fizycznych związku Cu_xMoO_3*, Poznań, Poland.

x. 11-17/08/2016 **plakat** w ramach International Conference of Physics Students, *Synthesis and physical properties of Cu_xMoO_3*, Malta.

xi. 25-27/05/2016 **plakat** w ramach COST HINT Training School „Functional Hybrid Materials: Structure Elucidation from Molecular to Macroscopic Level", *Organic semiconductor rubrene thin films for spintronics prepared from cryogenically cooled solutions*, Sztokholm, Szwecja.

Uczestnictwo w projektach badawczych

i. **Kierownik**: Projekt badawczy NCN Preludium 21, *Analiza mechanizmu wygaszania luminescencji w tlenkach aktywowanych jonami Cr^{3+} z wykorzystaniem pomiarów temperaturowej zależności fotoprzewodnictwa*, nr UMO-2022/45/N/ST3/00576.

ii. **Kierownik**: Projekt badawczy UG Grant na Start, *Zerowymiarowe materiały do zastosowań w nowoczesnych źródłach światła podczerwonego. Badania właściwości luminescencyjnych nanokrystalicznego perowskitu $CsPbI_3$ osadzonego w mikrokryształach Cs_4PbI_6*, nr 539-K200-B922-21.

iii. **Kierownik**: Projekt badawczy służący rozwojowi młodych naukowców oraz uczestników studiów doktoranckich na Wydziale Matematyki, Fizyki i Informatyki Uniwersytetu Gdańskiego, *Badania wpływu współdomieszkowania jonami metali przejściowych oraz jonami lantanowców na zjawisko przedłużonej luminescencji związków $SrSi_2N_2O_2:Eu^{2+}$, Ln/M (Ln-Dy, Ce, Er, Nd; M-Cr)*, nr 539-5200-B344-19.

iv. **Wykonawca/stypendysta:** Projekt badawczy NCN OPUS 17, *Inżynieria poziomu Fermiego w cienkich warstwach dielektryków z domieszkami donorowymi i akceptorowym,* nr UMO-2019/33/B/ST3/00406.

v. **Wykonawca/stypendysta:** Projekt badawczy NCN OPUS 12, *Procesy lokalizacji/ delokalizacji nośników w luminoforach aktywowanych jonami lantanowców*, nr UMO-2016/23/B/ST3/03911.

vi. **Wykonawca:** Projekt NCBiR w ósmym konkursie na wspólne projekty bilateralne w ramach współpracy polsko-tajwańskiej, *Perovskite and Broadband Infrared Phosphors for Lighting-Emitting Diode Applications (Perowskity i szerokopasmowe*

luminofory na podczerwień do diod świecących), akronim PBIPL, nr PL-TW/VIII/1/2021.

vii. **Wykonawca:** Projekt NCBiR w piątym konkursie na wspólne projekty bilateralne w ramach współpracy polsko-tajwańskiej, *Narrow Band Phosphors for the Application in Lighting and Backlighting of Light-emitting Diodes,* (*Emitujące w wąskich pasmach luminofory do diod świecących do oświetleń i podświetleń*), akronim NBBPL, nr PL-TW/V/1/2018.

viii. **Wykonawca:** Cost Action MP 1202 HINT - Rational Design of Hybrid Interfaces,

ix. **Wykonawca:** Cost Action CA 15128 MOLSPIN - Molecular Spintronics.

x. **Wykonawca:** (F.R.S.-FNRS) - PAN Bilateral Scientific Cooperation Project 2015-17: Nanostructuration and properties of spin switching thermochromic and photochromic thin films.

Uczestnictwo w stażach zagranicznych oraz krajowych

i. 12-30/04/2023 **wyjazd naukowy:** National Taiwan University, Department of Chemistry, prof. Ru-Shi Liu, Taipei, Tajwan.

ii. 1/09-30/11/2022 **staż naukowy:** University of Hawai'i at Manoa, Institute of Geophysics and Planetology, prof. Przemysław Dera, Honolulu, Stany Zjednoczone.

iii. 31/01-21/02/2022 **wyjazd badawczy:** University of La Laguna, prof. Alfonso Muñoz, Teneryfa, Hiszpania.

iv. 1/07-31/08/2019 **staż naukowy:** Utrecht University, Debye Institute for Nanomaterials Science Condensed Matter and Interfaces, prof. A. Meijerink, Utrecht, Holandia.

v. 15/07-05/08/2018 **praktyki studenckie:** Zjednoczony Instytut Badań Jądrowych (Joint Institute for Nuclear Research, JINR), Dubna, Rosja.

vi. 07-14/04/2017 **wyjazd badawczy:** Aalto University, Department of Applied Physics, Helsinki, Finlandia.

vii. 01/10/2016-30/06/2017 **staż naukowy:** Instytut Maszyn Przepływowych Polskiej Akademii Nauk, Zakład Fotofizyki, Gdańsk, Polska.

viii. 24-29/10/2016 **wyjazd naukowy:** Instytut Materii Skondensowanej i Nanonauki (Institute of Condensed Matter and Nanosciences Université catholique de Louvain) (UCL), Louvain-La-Neuve, Belgia.

ix. 1-30/09/2015 **staż naukowy:** Instytut Niskich Temperatur i Badań Strukturalnych Polskiej Akademii Nauk, praktyki studenckie, Wrocław, Polska.

Patenty

i.   **Patent**: „Dwu-fazowy tlenoazotkowy luminofor o wzmocnionej i wydłużonej luminescencji oraz sposób jego wytwarzania", numer patentu: 238800.

Nagrody i wyróżnienia

i.   **Nagroda** Rektora Uniwersytetu Gdańskiego II-ego stopnia za rok akademicki 2021/2022.

ii.   **Nagroda** Rektora Uniwersytetu Gdańskiego I-ego stopnia za rok akademicki 2020/2021.

ii.   **Nagroda** Rektora Uniwersytetu Gdańskiego I-ego stopnia za rok akademicki 2019/2020.

iii.   **Nagroda** za najlepszy poster na konferencji IWASOM 2022.

iv.   **Wyróżnienie** w dwudziestym siódmym Ogólnopolskim Konkursie im. Profesora Adama Smolińskiego na najlepsze prace dyplomowe z zakresu optoelektroniki, Komitetu Optoelektroniki SEP (stowarzyszenie Elektryków Polskich).

v.   **Ukończenie studiów drugiego stopnia z wyróżnieniem:** Nanoszenie cienkich warstw półprzewodnika organicznego przy użyciu laserowego odparowania w warunkach kriogenicznych, Promotor: dr hab. Rafał Jendrzejewski.

7. Kopie publikacji wchodzących w skład rozprawy doktorskiej

[P1]

Fang, M.-H.; De Guzman, G. N.; Bao, Z.; **Majewska, N.**; Mahlik, S.; Grinberg, M.; Leniec, G.; Kaczmarek, S.; Yang, C.-W.; Lu, K.-M.; Sheu, H.-S.; Hu, S.-F.; Liu, R.-S. Ultra-High-Efficiency Near-Infrared Ga_2O_3:Cr^{3+} Phosphor and Controlling of Phytochrome. *J. Mater. Chem. C* **2020**, *8* (32), 11013-11017.

https://doi.org/10.1039/D0TC02705G

Check for updates

Ultra-high-efficiency near-infrared Ga$_2$O$_3$:Cr^{3+} phosphor and controlling of phytochrome†

Mu-Huai Fang, [a] Gabriel Nicolo A. De Guzman, [b] Zhen Bao, [a] Natalia Majewska, [c] Sebastian Mahlik, [cd] Marek Grinberg, [c] Grzegorz Leniec, [e] Slawomir M. Kaczmarek, [e] Chia-Wei Yang, [f] Kuang-Mao Lu, [f] Hwo-Shuenn Sheu, [g] Shu-Fen Hu *[b] and Ru-Shi Liu *[a]

Phosphor-converted light-emitting diodes (LEDs) have recently become a promising candidate for next-generation devices used in agriculture and horticulture. In principle, they can overcome the limitations of regular daily sunshine. Here, the principle of LED-promoted plant growth was demonstrated by using the Ga$_2$O$_3$:Cr^{3+} phosphor with an extremely high quantum yield of 92.4%. The detailed structural and luminescent properties were characterized using X-ray diffraction, temperature-dependent photoluminescence, and pressure-dependent photoluminescence. The results reveal the unique two electronic spin-forbidden transition emissions (R1 and R2) of the Ga$_2$O$_3$:Cr^{3+} phosphor. Plant growth experiments were also conducted to evaluate the practical applications of the as-prepared phosphors, showing that they exhibit obvious positive effects on plants. This work reveals the important role of LEDs in agriculture and horticulture, as well as their potential practical applications.

1. Introduction

Light is a key component of most ecosystems. One of the important light sources, phosphor-converted light-emitting diodes (LEDs), has been utilized in many different fields, such as lighting, backlighting, and medical treatment.[1–4] One of the emerging applications of LEDs is in the field of plant cultivation.[5–8] Given the global weather change, the frequency of natural disasters, such as drought or hurricanes, has increased. These environmental phenomena destroy plants. Thus, plant cultivation has been proposed to overcome the effects of weather changes. However, finding a proper lighting source that simultaneously satisfies all requirements, such as sufficient lighting intensity and specific luminescent wavelength, remains a challenge. To solve this problem, the interaction between light and plants, including phototropism and photosynthesis, which could affect the growth rhythms of plants, should be understood. The four important biological pigments in plants are chlorophyll A, chlorophyll B,[9] red/phytochrome (P$_R$) and far-red/phytochrome (P$_{FR}$).[10] Each pigment possesses a specific absorption region, as shown in Fig. 1a. Chlorophyll helps to harvest the red and blue light to drive photosynthetic reactions, resulting in the fixation of carbon dioxide and the production of adenosine triphosphate.[11] The absorption peak of chlorophyll A is at 439 and 667 nm, and that of chlorophyll B is at 469 and 642 nm.[12] Phytochrome is a photoreceptor sensitive to red and far-red light and is classified as P$_R$ and P$_{FR}$. The ground state, P$_R$, has a strong absorption at approximately 660 nm red light, whereas the active state, P$_{FR}$, has a strong absorption peak at approximately 730 nm far-red light, as shown in Fig. 1b. When the plant is short, most of the sunlight will be blocked by other leaves except for the far-red light. Once
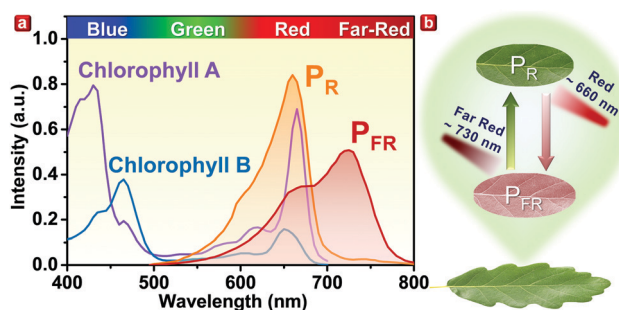
a Department of Chemistry, National Taiwan University, Taipei 106, Taiwan.
 E-mail: rsliu@ntu.edu.tw

b Department of Physics, National Taiwan Normal University, Taipei 116, Taiwan.
 E-mail: sfhu.hu@gmail.com

c Institute of Experimental Physics, Faculty of Mathematic, Physics and Informatics, Gdańsk University, Wita Stwosza 57, 80-308 Gdańsk, Poland

d Graduate School of Human and Environmental Studies, Kyoto University, Kyoto 606-8501, Japan

e Faculty of Mechanical Engineering and Mechatronics, West Pomeranian University of Technology, Szczecin, Al. Piastow 19, 70-311 Szczecin, Poland

f Everlight Electronics Co., Ltd., New Taipei City 238, Taiwan

g National Synchrotron Radiation Research Center, Hsinchu 300, Taiwan

† Electronic supplementary information (ESI) available: Experimental methods and refinement tables. See DOI: 10.1039/d0tc02705g

Fig. 1 (a) Absorption curves of chlorophyll A, chlorophyll B, PR, and PFR. (b) Scheme of the interaction between PR and PFR.

This journal is © The Royal Society of Chemistry 2020

J. Mater. Chem. C, 2020, **8**, 11013–11017 | **11013**

the plants are illuminated by the far-red light, P_{FR} will then absorb the light and transform itself into P_R. As such, plant growth is stimulated, allowing it to harvest more sunlight. Consequently, the height of the plant can be controlled by tuning the ratio of the red/far-red light illumination to the plant. In 2016, Agarwal et al.[11] systematically studied the effect of LEDs on plant biomass, height, leaf length, photosynthetic rate, and stem girth. However, a combination of different colors of LED chips, rather than the phosphor-converted LED, was used. Zhong and Zhou et al.[13–15] developed red to infrared phosphors and introduced their potential effects on plant growth. Nevertheless, practical experiments are lacking, and the quantum efficiency is not high enough. The light source for chlorophyll could be provided by the blue LED chip, whereas the one for P_{FR} is rare and should be urgently developed.

In the present study, the near-infrared (NIR) Ga_2O_3:Cr^{3+} phosphor with an extremely high internal quantum efficiency (IQE) of 92.4% is successfully synthesized. The detailed structural and luminescent properties were characterized using X-ray diffraction (XRD), temperature-dependent photoluminescence (PL), and decay curves. The unique R1 and R2 emissions of the Ga_2O_3:Cr^{3+} phosphor under different temperatures and pressures were analyzed. The positive effects of the Ga_2O_3:Cr^{3+} phosphor on plants were demonstrated through plant growth experiments with an LED packaged with Ga_2O_3:Cr^{3+} phosphor. The aim of this work is to introduce highly efficient Ga_2O_3:Cr^{3+} NIR phosphors that can promote plant growth.

2. Results and discussion

The XRD patterns of the $Ga_{2-x}O_3$:xCr^{3+} phosphor synthesized with different Cr^{3+} concentrations are shown in Fig. S1 (ESI†). The pure phase was successfully obtained for all the as-prepared compounds. Ga_2O_3 belongs to the monoclinic structure with the space group of $C2/m$. The two kinds of Ga-coordinated environments are the octahedral one, coordinated by six oxygen ions, and the tetrahedral one, coordinated by four oxygen ions, as shown in Fig. 2a. Given the similar ionic radii of Ga^{3+} (0.62 Å; CN = 6) and Cr^{3+} (0.615 Å; CN = 6), Cr^{3+} can incorporate into the octahedrally-coordinated Ga^{3+} site causing distortion, which could lead to a lowering of the local symmetry. To determine the best compound for further analysis, the IQE of all the as-prepared samples was measured and the results are collected in Table S1 (ESI†). The extremely high IQE of 92.4% for $x = 0.006$ was revealed; therefore, $Ga_{1.994}O_3$:$0.006Cr^{3+}$ was chosen for the following characterization. The Rietveld refinement utilizing synchrotron XRD was used to determine the structural information, as shown in Fig. 2b and Tables S2, S3 (ESI†). The morphology of $Ga_{1.994}O_3$:$0.006Cr^{3+}$ was determined using scanning electron microscopy (SEM). Most of the primary particle sizes of $Ga_{1.994}O_3$:$0.006Cr^{3+}$ are smaller than 2 μm, as shown in Fig. S2a (ESI†). Transmission electron microscopy (TEM) and high-resolution TEM (HRTEM) were used to elucidate the crystal structure from another perspective, as shown in Fig. S2b and c (ESI†). The (001) and (110)
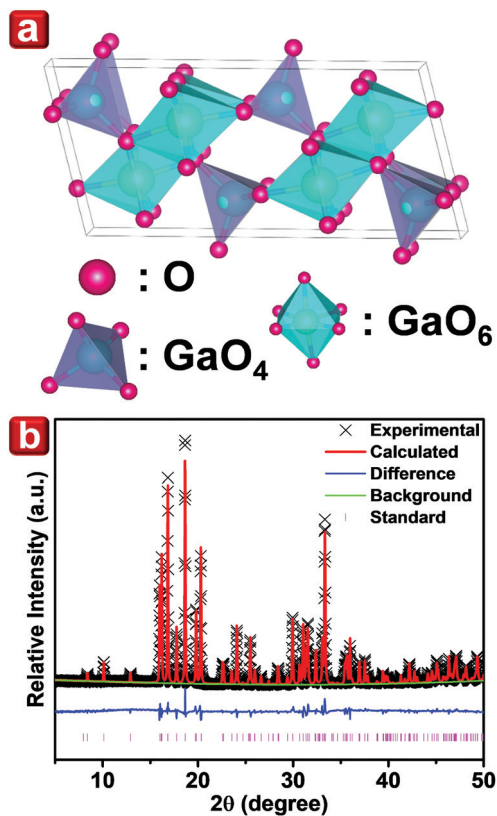

Fig. 2 (a) Crystal structure of Ga_2O_3. (b) Rietveld refinement of $Ga_{1.994}O_3$:$0.006Cr^{3+}$.

diffraction patterns can be clearly observed. The calculated d-spacing between (001) and (110) is 5.67 and 3.04 Å, which is close to the theoretical value of 5.64 and 2.95 Å, as shown in Table S4 (ESI†).

To realize the preliminarily luminescent behavior, the room-temperature PL and PL excitation (PLE) were determined (Fig. 3a). The PLE spectrum is composed of two excitation bands, with the maximum at 440 and 608 nm, typical for Cr^{3+} ions in sixfold coordination (distorted octahedral). The high energy band (440 nm) corresponds to the $^4A_2 \rightarrow {}^4T_1$, whereas the low energy band (610 nm) corresponds to the $^4A_2 \rightarrow {}^4T_2$ electronic spin-allowed transitions of Cr^{3+} ions. Upon excitation at 442 nm, the narrow-line emission and broadband emission of Cr^{3+} were observed simultaneously. The line emissions at 695.5 and 688.8 nm correspond to the $^2E \rightarrow {}^4A_2$ electronic spin-forbidden transition, R_1 and R_2 lines, respectively. The broadband emission extending from 650 nm to 950 nm corresponds to the $^4T_2 \rightarrow {}^4A_2$ electronic spin-allowed transition of Cr^{3+} ions.[16] From the discussion above, the PL spectrum can be well fitted with the absorption band of P_{FR}. On the basis of the presented spectral characteristics, the configurational coordinate diagram can be constructed. Such a diagram is important for the advanced analysis of luminescent properties. The $S\hbar\omega$ quantity was calculated using the energy of the emission band related to the $^4T_2 \leftrightarrow {}^4A_2$ transition, thereby allowing the estimated location of the zero-phonon lines for these
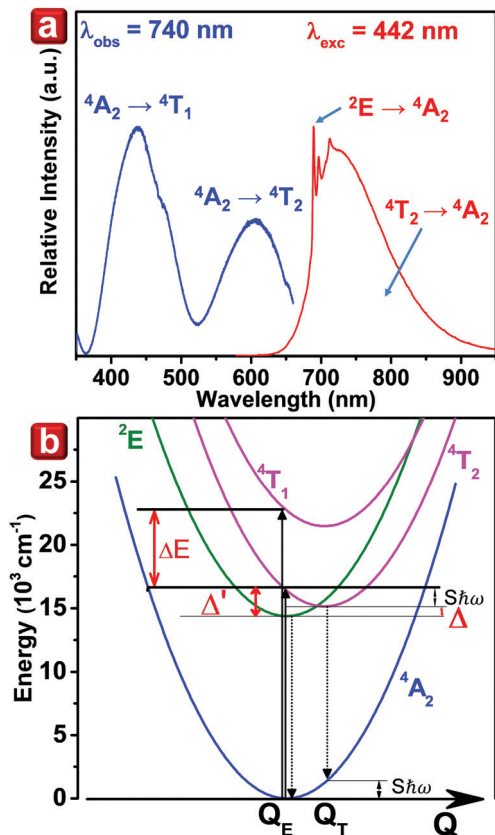
Fig. 3 (a) PL upon excitation at 442 nm and PLE upon the observation at 740 nm of $Ga_{1.994}O_3$:$0.006Cr^{3+}$. (b) Configurational coordinate diagram of the Ga_2O_3:Cr^{3+} system.

transitions. The Racah parameters (B and C) can be calculated from the following equations:[5]

$$B = Dq \frac{\left[\frac{\Delta E}{Dq}\right]^2 - 10 \cdot \frac{\Delta E}{Dq}}{15\left(\frac{\Delta E}{Dq} - 8\right)} \qquad (1)$$

$$C = \frac{B}{3.05}\left\{\frac{E(^2E)}{B} - 7.9 + 1.8\frac{B}{Dq}\right\} \qquad (2)$$

where the crystal field strength $10\ Dq = E(^4A_2 - ^4T_2)$, ΔE is the difference between the energy of the $^4T_1$ and $^4T_2$ states, S is the Huang–Rhys parameter, and $\hbar\omega$ is the phonon energy. All the obtained data are listed in Table S5 (ESI†). The configurational coordinate diagram is presented in Fig. 3b. Energy Δ' (energetic distance between the R_1 line and a maximum of the $^4A_2 \rightarrow ^4T_2$ band in the PLE spectrum) is equal to 2165 cm^{-1}. The Δ' value is crucial for determining the luminescence lifetime at low temperatures.[17] The energetic distance between the zero-vibrational states of $^4T_2$ and ^2E electronic manifolds $\Delta = \Delta' - S\hbar\omega$. The Δ value determines the thermal occupation of the $^4T_2$ state. The spectroscopic data yield $\Delta = 770 \pm 100$ cm^{-1}, which agrees with the value received for the single crystal.[16] The energy Δ' is estimated with better accuracy than Δ and $S\hbar\omega$. As a

result, these data are considered constant, whereas Δ and $S\hbar\omega$ are fitted.

Given the above information, the advanced characterization of $Ga_{1.994}O_3$:$0.006Cr^{3+}$ can be determined on the basis of the temperature-dependent PL (TDPL) excited at 442 nm at the temperature range from 10 K to 400 K (Fig. 4a). The emission consists of four features directly related to the energetic structure and the symmetry site of the Cr^{3+} ion. The first two are the R_1 and R_2 lines related to the splitting of the ^2E state into the low $E_{1/2}$ and the high $E_{3/2}$. This phenomenon is caused by the second-order effect of the spin–orbit interaction and the trigonal crystal field.[18] The intensity ratio of the high excited state R_2 to the low excited state R_1 is given as

$$\frac{I_{R_2}}{I_{R_1}} = q \cdot e^{\frac{-\delta}{kT}} \qquad (3)$$

where δ is the R_1–R_2 line splitting energy and q is the ratio of radiative transition probabilities. The experimental data are presented in Fig. S3a (ESI†). Fitting using relation (3) yields the value of $\delta = 162 \pm 8$ cm^{-1} and $q = 4.01 \pm 0.17$, suggesting that the probability of radiative transition of the R_2 line is four times that of R_1.
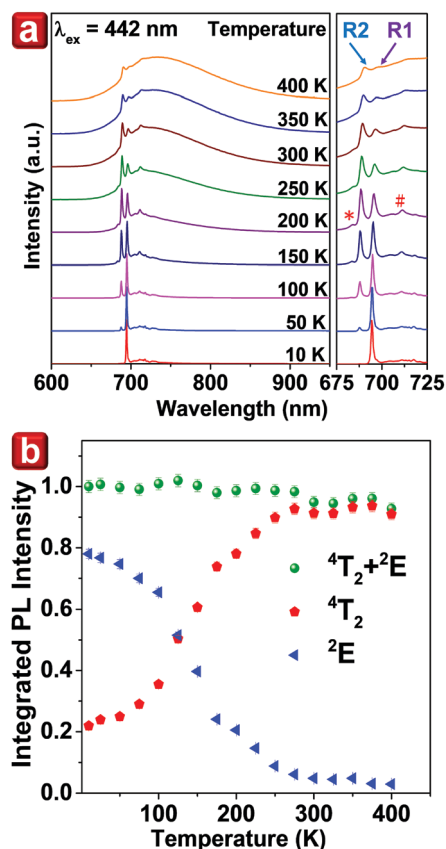

Fig. 4 (a) TDPL spectra of $Ga_{1.994}O_3$:$0.006Cr^{3+}$ upon excitation at 442 nm normalized to the maximum emission. (b) Integrated PL intensity of $^4T_2 + ^2E \rightarrow ^4A_2$, $^4T_2 \rightarrow ^4A_2$, and $^2E \rightarrow ^4A_2$ transitions of TDPL spectra. The Stokes band and anti-Stokes band are denoted as # and *, respectively.

This journal is © The Royal Society of Chemistry 2020

J. Mater. Chem. C, 2020, 8, 11013–11017 | 11015

Communication

The experimental PL spectra of $^4T_2 \rightarrow {}^4A_2$ and $^2E \rightarrow {}^4A_2$ transitions were deconvoluted for all temperatures into separate $^4T_2 \rightarrow {}^4A_2$ (broadband emission) and $^2E \rightarrow {}^4A_2$ (line emission). Thus, the integrated PL intensity spectra of $^2E + {}^4T_2 \rightarrow {}^4A_2$, $^4T_2 \rightarrow {}^4A_2$, and $^2E \rightarrow {}^4A_2$ transitions extend from 600 nm to 950 nm (16 700–10 500 cm^{-1}) and the temperature range from 10 K to 400 K can be plotted as a function of temperature as shown in Fig. 4b. The total emission ($^2E + {}^4T_2 \rightarrow {}^4A_2$) decreased slightly with increasing temperature. The integrated intensity of spin-allowed $^4T_2 \rightarrow {}^4A_2$ transition increased strongly with increasing temperature up to 300 K and remained stable from 300 K to 400 K. The integrated intensity of the spin-forbidden $^2E \rightarrow {}^4A_2$ transition decreases and is close to 0 for temperatures above 300 K. This situation can occur when the spin-forbidden ^2E state is the first excited state in Cr^{3+} and the spin-allowed $^4T_2$ state is a higher state. Given the thermal occupation of the higher excited state $^4T_2$, the intensity of this transition (broadband emission) increases strongly with increasing temperature.

The third feature is the sharp-line sideband consisting of the Stokes band and a considerably weaker anti-Stokes band. This is related to the interaction of electrons at the ^2E state with odd parity lattice modes. In Fig. 4a, only the Stokes band is well seen. For simplification, all odd modes were replaced with a single effective mode with energy $\hbar\omega_{odd} = 400$ nm. $\frac{I_{SB}}{I_R}$ is the ratio of the intensities of the sharp line sideband, I_{SB}, to the intensity of the R lines, I_R, is considered as a sum of $I(R_1)$ and $I(R_2)$. At low temperatures in our case $\frac{I_{SB}}{I_R} = 0.7$. Due to the strong overlapping of the $^4T_2 \rightarrow {}^4A_2$ broadband emission to narrow line $^2E \rightarrow {}^4A_2$ emission, it is not possible to analyze the temperature dependence of this ratio; however, typically the ratio $\frac{I_{SB}}{I_R}$ increases when the temperature increases.[17]

Given that the $^2E \rightarrow {}^4A_2$ transition is spin forbidden, the radiative transition is possible due to the spin–orbit coupling between the ^2E and the $^4T_2$ states. Consequently, the temperature dependence of the PL intensity ratio of the $^4T_2 \rightarrow {}^4A_2$ to $^2E \rightarrow {}^4A_2$ transitions was analyzed, as shown in Fig. S3b (ESI†). The simplified approach following the approximate relationship between $\frac{1}{\tau_E}$ and $\frac{1}{\tau_T}$ can be attributed to the following equation:[17]

$$\frac{1}{\tau_E} = \frac{1}{\tau_T}\left\{\frac{V_{s-o}}{\Delta'}\right\}^2 \qquad (4)$$

where V_{s-o} is the effective spin–orbit coupling constant, which mixes the ^2E and the $^4T_2$ electronic manifolds; $\frac{1}{\tau_E}$ and $\frac{1}{\tau_T}$ are the probabilities of the radiative transitions from the ^2E and the $^4T_2$ states, respectively. The PL intensities ratio, I_T/I_E, related to the $^4T_2 \rightarrow {}^4A_2$ and $^2E \rightarrow {}^4A_2$ transitions can be written as follows:

$$\frac{I_T}{I_E} = \frac{\tau_E}{\tau_T}3\exp\left(\frac{-\Delta}{kT}\right) = \left\{\frac{\Delta'}{V_{s-o}}\right\}^2 3\exp\left(\frac{-\Delta}{kT}\right) \qquad (5)$$

Fitting the data under assumption $\Delta' = \Delta + S\hbar\omega = 2165$ cm^{-1} for fitted $\Delta = 700 \pm 100$ cm^{-1} and $V_{s-o} = 195 \pm 60$ cm^{-1}, as shown in Fig. S3b (ESI†), eqn (4) yields $\frac{\tau_E}{\tau_T} = \left\{\frac{\Delta'}{V_{s-o}}\right\}^2 = 125 \pm 40$. Given the co-existence of the sharp-line emission and broadband emission, the intermediate crystal field strength and the similar transition energy of $^4T_2 \rightarrow {}^4A_2$ and $^2E \rightarrow {}^4A_2$ can be expected. The photoluminescent properties will significantly change when the crystal field strength is tuned by physically adjusting the pressure of the phosphor. The pressure-dependent PL analysis, chemical stability, and Cr^{3+}
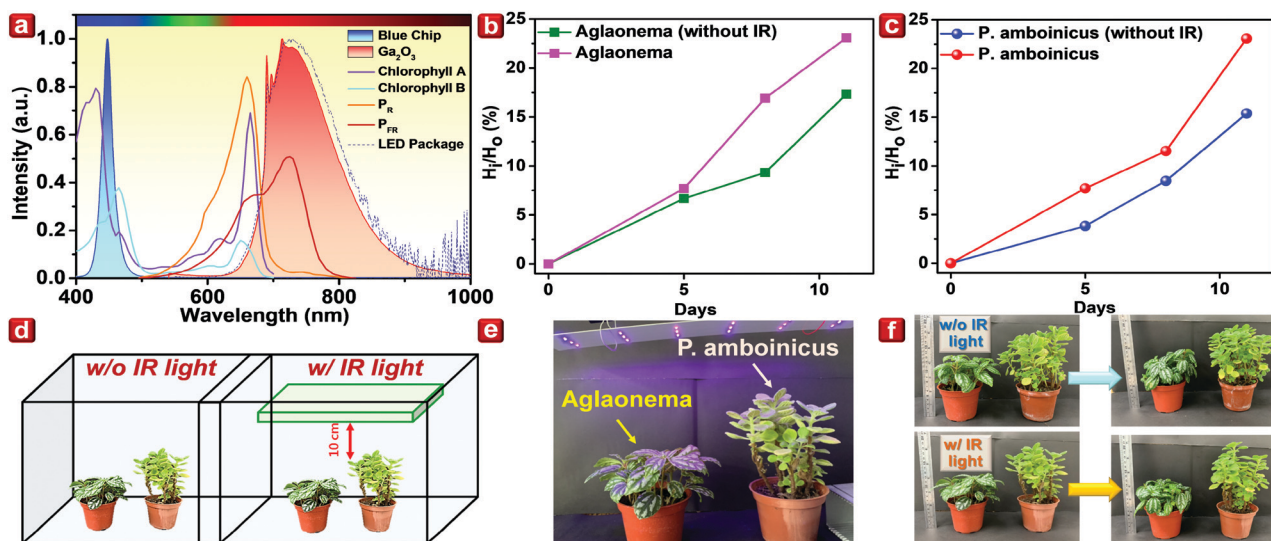

Fig. 5 (a) Infrared part of the LED package spectrum with the absorption curve of chlorophyll A, chlorophyll B, P$_R$, and P$_{FR}$. Percentage of the plant growth with and without the illumination of the IR LED in (b) *Aglaonema* and (c) *P. amboinicus*. (d) Scheme of the plant growth experiment. (e) Picture of *Aglaonema* and *P. amboinicus*. (f) Pictures of the plants before and after the illumination of the IR LED. The Infrared part of the LED package spectrum, Ga$_2$O$_3$:Cr^{3+} curve, and blue chip curve are normalized in (a).

11016 | *J. Mater. Chem. C*, 2020, **8**, 11013–11017

This journal is © The Royal Society of Chemistry 2020

electron paramagnetic resonance are discussed in detail in the ESI.†

To completely analyze the potential of $Ga_{1.994}O_3:0.006Cr^{3+}$ for practical applications, the plant growth experiment was executed. The 453 nm blue LED chip with $Ga_{1.994}O_3:0.006Cr^{3+}$ IR phosphor was used as the lighting source, as shown in Fig. 5a. The luminescent spectrum from the whole NIR LED can be well-fitted with the absorption curve of P_{FR} and chlorophyll. Afterward, two kinds of plants, *Aglaonema* and *Plectranthus amboinicus* (Fig. 5e) were divided into two groups and used as targets for evaluating the effects of the fabricated NIR LED. Both groups were illuminated with sunlight during the day-time. Only one group was additionally illuminated during the night with a NIR LED for 12 h, as shown in Fig. 5d. After 11 days of illumination, both groups grew taller, as shown in Fig. 5f. However, the *Aglaonema* and *P. amboinicus* plants illuminated with the NIR LED exhibited 5% and 8% higher growth, respectively, than those that were not illuminated (Fig. 5b and c). In general, this experiment provides a preliminary foundation for light-enhancement analysis in the artificial plant growth research field. The present study may be improved through advanced experiments with a longer observation period and an increased number of plants.

3. Conclusions

In conclusion, a series of $Ga_2O_3:Cr^{3+}$ near-infrared phosphors have been successfully synthesized with an extremely high IQE of 92.4% that well fits the absorption curve of the P_{FR} of the plant. The detailed structural and morphological information were examined using synchrotron XRD with Rietveld refinement, SEM, and HRTEM analysis. The pure phase and well-crystallized powder was obtained. TDPL was also characterized to understand the relationship between the electronic spin-allowed transition ($^4T_2 \rightarrow {}^4A_2$) and the spin-forbidden transition ($^2E \rightarrow {}^4A_2$). The configurational coordinate diagram was constructed based on the value calculated from the optical measurements. The luminescent behavior under different crystal field strength levels was revealed through pressure-dependent PL. Finally, the LED package with $Ga_2O_3:Cr^{3+}$ phosphors and the plant growth experiment was implemented to evaluate the potential of $Ga_2O_3:Cr^{3+}$. The plants illuminated with the fabricated NIR LED grew taller than the non-illuminated ones. The results indicate that the NIR light can significantly transform P_{IR} into P_R, whereas the blue light can be absorbed by chlorophyll. This study provides insights into the Cr^{3+}-doped NIR phosphor and sheds light on the practical applications of IR LEDs in agriculture and horticulture.

Conflicts of interest

There are no conflicts to declare.

Acknowledgements

References

1 P. Pust, P. J. Schmidt and W. Schnick, *Nat. Mater.*, 2015, **14**, 454.
2 Z. Xia and Q. Liu, *Prog. Mater. Sci.*, 2016, **84**, 59–117.
3 Y. Liu, S. Liu, P. Sun, Y. Du, S. Lin, R.-J. Xie, R. Dong, J. Jiang and H. Jiang, *ACS Appl. Mater. Interfaces*, 2019, **11**, 21697–21701.
4 S. Li, R.-J. Xie, T. Takeda and N. Hirosaki, *ECS J. Solid State Sci. Technol.*, 2018, **7**, R3064–R3078.
5 B. Henderson and G. F. Imbusch, *Optical Spectroscopy of Inorganic Solids*, Oxford University Press, 2006.
6 O. Avercheva, Y. A. Berkovich, S. Smolyanina, E. Bassarskaya, S. Pogosyan, V. Ptushenko, A. Erokhin and T. Zhigalova, *Adv. Space Res.*, 2014, **53**, 1574–1581.
7 R. Hernández and C. Kubota, *Environ. Exp. Bot.*, 2016, **121**, 66–74.
8 X.-L. Chen, W.-Z. Guo, X.-Z. Xue, L.-C. Wang and X.-J. Qiao, *Sci. Hortic.*, 2014, **172**, 168–175.
9 D. Von Wettstein, S. Gough and C. G. Kannangara, *Plant Cell*, 1995, **7**, 1039.
10 R. A. Sharrock, *Genome Biol.*, 2008, **9**, 230.
11 A. Agarwal and S. D. Gupta, *Curr. Biotechnol.*, 2016, **5**, 28–43.
12 V. Fattori, J. G. Williams, L. Murphy, M. Cocchi and J. Kalinowski, *Photonics Nanostruct.*, 2008, **6**, 225–230.
13 Y. Zhong, N. Zhou, M. Xia, Y. Zhou, H. Chen and Z. Zhou, *Ceram. Int.*, 2019, **45**, 23528–23539.
14 Y. Zhong, S. Gai, M. Xia, S. Gu, Y. Zhang, X. Wu, J. Wang, N. Zhou and Z. Zhou, *Chem. Eng. J.*, 2019, **374**, 381–391.
15 N. Zhou, L. Liu, Z. Zhou, Y. Zhang, M. Li, C. Zhou, M. Xia and Z. Zhou, *J. Am. Ceram. Soc.*, 2020, **103**, 1798–1808.
16 D. Vivien, B. Viana, A. Revcolevschi, J. Barrie, B. Dunn, P. Nelson and O. Stafsudd, *J. Lumin.*, 1987, **39**, 29–33.
17 M. Grinberg, T. Lesniewski, S. Mahlik and R. S. Liu, *Opt. Mater.*, 2017, **74**, 93–100.
18 R. M. Macfarlane, *J. Chem. Phys.*, 1963, **39**, 3118–3126.

SUPPORTING INFORMATION

Ultra-High-Efficiency Near-Infrared Ga$_2$O$_3$:Cr^{3+} Phosphor and Controlling of Phytochrome

Mu-Huai Fang,[a] Gabriel Nicolo A. De Guzman,[b] Zhen Bao,[a] Natalia Majewska,[c] Sebastian Mahlik,[c,d] Marek Grinberg,[c] Grzegorz Leniec,[e] Slawomir M. Kaczmarek,[e] Chia-Wei Yang,[f] Kuang-Mao Lu,[f] Hwo-Shuenn Sheu,[g] Shu-Fen Hu,[b,*] and Ru-Shi Liu[a,*]

[a]Department of Chemistry, National Taiwan University, Taipei 106, Taiwan

[b]Department of Physics, National Taiwan Normal University, Taipei 116, Taiwan

[c]Institute of Experimental Physics, Faculty of Mathematic, Physics and Informatics, Gdańsk University, Wita Stwosza 57, 80-308 Gdańsk, Poland

[d]Graduate School of Human and Environmental Studies, Kyoto University, Kyoto 606-8501, Japan

[e]Faculty of Mechanical Engineering and Mechatronics, West Pomeranian University of Technology, Szczecin, al. Piastow 19, 70-311 Szczecin, Poland

[f]Everlight Electronics Co., Ltd., New Taipei City 238, Taiwan

[g]National Synchrotron Radiation Research Center, Hsinchu 300, Taiwan

EXPERIMENTAL METHODS

Synthesis of Ga$_{2-x}$O$_3$:xCr^{3+}. Gallium oxide (Ga$_2$O$_3$, Gredmann, 99.99%), chromium oxide (Cr$_2$O$_3$, Merck, 99.9%) were acquired from chemical distributors and were directly utilized for a solid-state reaction method. The starting precursors were stoichiometrically weighed, mixed and carefully grounded in an agate mortar for 30 minutes. The finely grounded precursors were transferred into an alumina crucible and moved into a muffle furnace for the sintering process. The samples were sintered to 1200 $^{\circ}$C at a rate of 5 $^{\circ}$C for 5 hours and afterward cooled to room temperature. The detailed characterization is listed in the Supporting Information.

Plant growth experiment. The 450 nm blue LED was used with the Ga$_2$O$_3$:Cr^{3+} IR phosphors with a driving current of 300 mA. The output of the IR region was 17.5 mW. 18 pieces of LEDs are used and the illuminated area was 631.67 mm x 446.41 mm. The plants were divided into two groups and each group had Aglaonema and P. amboinicus. Both of the groups were illuminated by the sunlight for 12 hours from 08:00 a.m. to 08:00 p.m. The experimental group was further illuminated by our phosphor-converted IR LED for 12 hours from 08:00 p.m. to 08:00 a.m. The control group wasn't illuminated by the IR LED at the night. The height of the plant was calculated from the stem over the soil to the highest leaf.

Characterization. The phase and purity of the as-prepared powder samples were examined by X-ray diffraction (XRD) analysis using a D2 PHASER diffractometer (Bruker) with CuKα radiation source (λ = 1.5418 Å). Synchrotron powder X-ray diffraction pattern of Ga$_2$O$_3$:Cr^{3+} was acquired from the National Synchrotron Radiation Research Center (NSRRC, Taiwan) BL01C2 beamline with the wavelength of 0.82657 Å at room temperature using Debye - Scherrer camera. The pattern then proceeded for Rietveld analysis using Total Pattern Analysis Solutions software (TOPAS 4.2). Room temperature (RT) photoluminescence excitation (PLE) spectra were measured with a FluoroMax-4P spectrofluorometer (Horiba) equipped with a 150 W xenon lamp as an excitation light source and an R928 Hamamatsu photomultiplier as a detector which records PL and PLE spectra in the spectral range of 250 – 850 nm. The temperature dependence photoluminescence spectra (PDPL) and pressure dependence of photoluminescence spectra (PDPL) were measured using an Andor SR-750-D1 spectrometer equipped with a CCD camera (DU420A-OE) with the following laser sources: He-Cd laser with 325 and 442 nm, second harmonic Nd:YAG laser with 532 nm and He-Ne laser with 629 nm. The decay profiles were measured via apparatus for time-resolved spectroscopy which consists of a PG 401/SH optical parametric generator pumped by a PL2251A pulsed YAG:Nd laser (EKSPLA), while the detection part consisted of a 2501S grating spectrometer (Bruker Optics) combined with a C4334-01 streak camera (Hamamatsu). Data were recorded in the form of the streak

images on a 640 by 480 pixel CCD array. Results were transformed into a 2D matrix of streak image using software based on the photon counting algorithm. Decay profiles of luminescence were acquired by integrating the streak image over specified spectral windows. Emission spectra were evaluated by integrating the streak image over time. The high-pressure luminescence measurements were performed in a screw-driven Merrill-Bassett type diamond anvil cell (DAC) with a culets diameter of 0.5 mm. The $KMgF_3$:0.5%Eu^{2+} was used as a pressure sensor and polydimethylsiloxane oil was used as a pressure transmitting medium between the gaskets. High-pressure luminescence excitation spectra were acquired using a self-made spectrofluorometer. The excitation part of the device consists of a 150W xenon lamp, an SPM2 monochromator (Carl Zeiss Jena) and an R928P photomultiplier for lamp reference measurement. Besides, the detection part consists of an SPM2 monochromator and an R928P photomultiplier as a signal detector. Scanning electron microscopy was conducted on the ΣIGMA 300 Essential scanning electron microscope (ZEISS, Graduate Institute of Manufacturing Technology, National Taipei University of Technology) along with the attached energy dispersive X-ray spectrometer (Bruker). IR − LED was fabricated by mixing UV gel (Norland optical adhesive 61, LOT 392; Norland product, Inc. Cranbury, NJ 08512) with $Ga_{0.994}O_3$:0.006Cr^{3+} phosphor and smearing the mixed gel onto the 450 nm blue chip. Subsequently, the gel was solidified by irradiating 365 nm UV light. The internal quantum efficiency measurement was done using UV to NIR absolute PL quantum yield spectrometer (C1534 − 12; Hamamatsu photonics K.K.) equipped with NIR PL measurement unit (C13684 − 01; Hamamatsu photonics K.K.) using High power Xe lamp unit (L13685 − 01; Hamamatsu photonics K.K.) together with 475 nm filter for excitation (A13686 − 475). The first derivative of the absorption EPR spectrum was recorded as a function of the applied magnetic field in the range B = 10 − 1400 mT on a conventional X-band Bruker ELEXSYS E 500 CW-spectrometer operating at 9.5 GHz with 100 kHz magnetic field modulation. The temperature dependence of the EPR spectrum was analyzed using nitrogen-flow cryostat Oxford Instruments ESP at the nitrogen temperature range.   EPR/NMR program was used to find spin-Hamiltonian parameters and local symmetry of chromium ions. Optimization and normalization of the parameters were performed using the root-mean-squared deviation method.
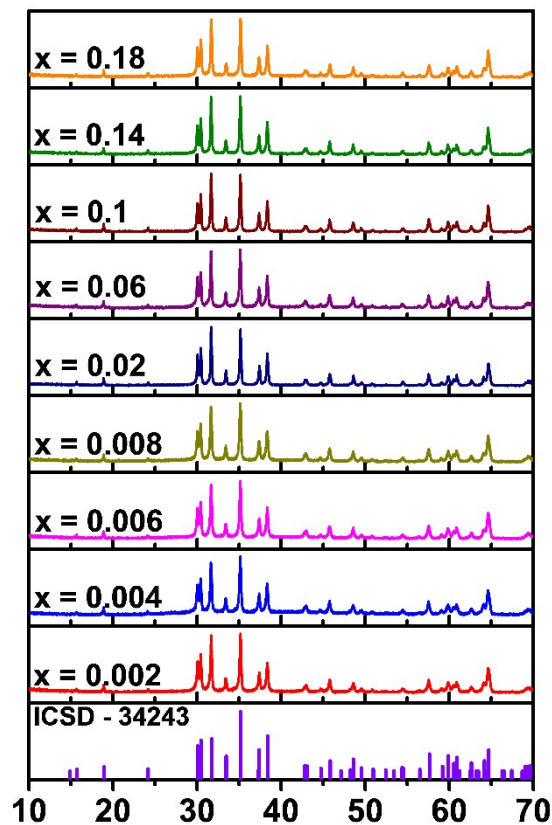
Figure S1. XRD of the $Ga_{2-x}O_3$:xCr^{3+} (x = 0 − 0.18).

Table S1. IQE of the $Ga_{2-x}O_3$:xCr^{3+} (x = 0 − 0.18).

x =	0.002	0.004	0.006	0.008	0.02	0.06	0.1	0.14	0.18
Quantum Efficiency (%)	72.1 (0.1)	88.3 (0.2)	92.4 (0.1)	86.4 (0.06)	73.0 (0.08)	59.1 (0.06)	14.2 (0.01)	3.9 (0.02)	1.7 (0.07)

Table S2. Refinement parameter of $Ga_{1.994}O_3$:$0.006Cr^{3+}$.

Crystal system	Monoclinic
Space group	$C2/m$
Rwp	1.65%
Rp	1.19%
χ^2	2.31

Table S3. Lattice parameter of $Ga_{1.994}O_3{:}0.006Cr^{3+}$.

Atoms	x	y	z	Occ	Beq ($Å^2$)
Ga1	0.08988(12)	0	0.79457(33)	1	0.033(53)
Ga2	0.34118(11)	0	0.68562(32)	1	0.022(52)
O1	0.16045(49)	0	0.1028(13)	1	0.11(19)
O2	0.49497(48)	0	0.2584(10)	1	0.03(17)
O3	0.82585(47)	0	0.4259(13)	1	0.03(15)

a	12.23328(24) Å
b	3.040145(57) Å
c	5.80791(12) Å
β	103.8331(15) °
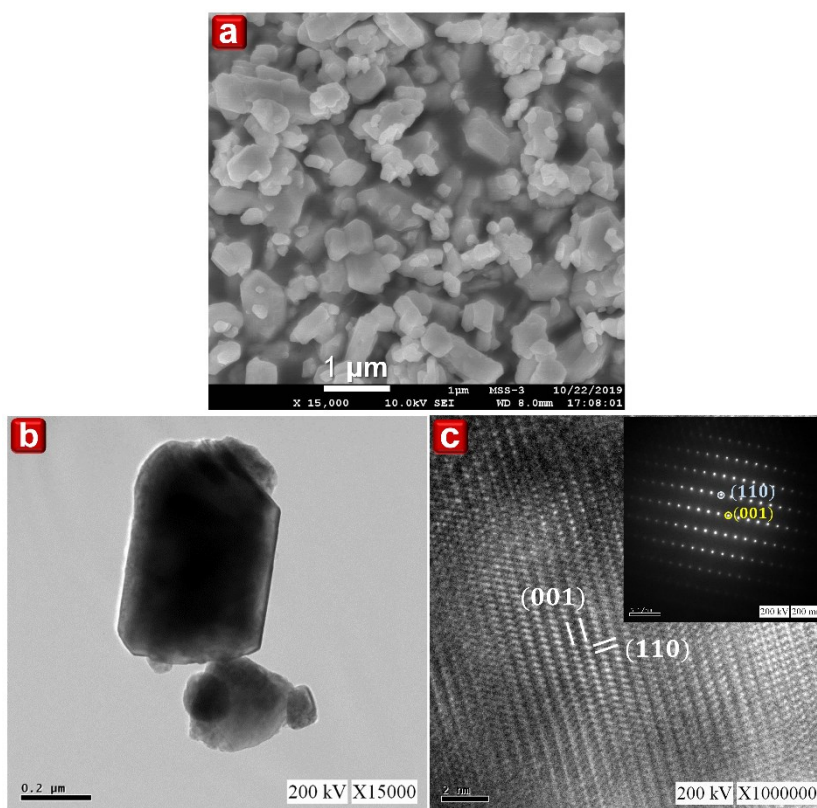
Figure S2. (a) SEM image of $Ga_{1.994}O_3{:}0.006Cr^{3+}$. (b) TEM of the $Ga_{1.994}O_3{:}0.006Cr^{3+}$. (c) HRTEM image of $Ga_{1.994}O_3{:}0.006Cr^{3+}$ (the inset figure is the SAED pattern).

Table S4. Calculated and theoretical d-spacing of [001] and [110] from HRTEM.

	$[001]$	$[110]$	Interplane angle
Experimental	5.67 Å	3.04 Å	87.0
Theoretical	5.64 Å	2.95 Å	86.6

Table S5. Values of energy levels at ambient pressure and parameters of the crystal field model for Ga_2O_3:Cr^{3+}.

Parameters	$^4A_2 \rightarrow {}^4T_2$	$^4A_2 \rightarrow {}^4T_1$	$^2E \rightarrow {}^4A_2$ (R1) $E({}^2E)$	ΔE (cm^{-1})	Dq (cm^{-1})	B (cm^{-1})	C (cm^{-1})	Δ' (cm^{-1})	$S\hbar\omega$ (cm^{-1})
Values	16530 cm^{-1} (605 nm)	22826 cm^{-1} (438.1 nm)	14345 cm^{-1} (697.1 nm)	6296	1653	620	3235	2185	1416
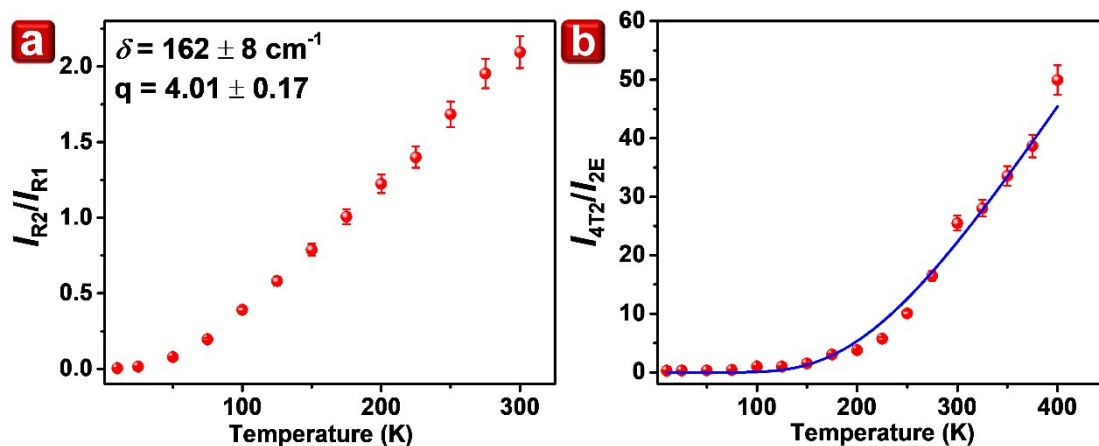
Figure S3. Temperature-dependent intensity ratio of R_2 and R_1 line emission and (b) the TDPL intensity ratio of the $^4T_2 \rightarrow {}^4A_2$ and $^2E \rightarrow {}^4A_2$ transitions of $Ga_{1.994}O_3$:0.006Cr^{3+}.

Pressure dependence of luminescence

Room-temperature pressure-dependent PL spectra of Ga_2O_3:Cr^{3+} up to 190 kbar upon excitation at 442 nm are shown in Figure S4a. The shift of the maximum of broadband ($^4T_2 \rightarrow {}^4A_2$) emission spectra towards lower wavelength is observed for low pressure, while broadband emission disappears and only line emission is observed above 44 kbar. This is interpreted as the result of the pressure-induced shift of the $^4T_2$ level towards higher energies. In effect, the thermal energy is too low at room temperature to induce the emission from $^4T_2$ level, and ^2E state becomes the only emitting state. The change of relative intensity between R_1 and R_2 lines (Figure S4a) is observed. The R2 line is no longer observed for pressure higher than 140 kbars.

Furthermore, the significant change of emission spectra between 123 and 140 kbars is observed and only one line is observed at the pressure above. Such phenomena are probably caused by the phase transition from β-Ga_2O_3 to α-Ga_2O_3, which was previously calculated at around 95 kbar.[1] Moreover, the experiment shows that for nanostructured material, this transition begins at 60 kbar and the nanocrystalline phase is a combination of both phases of gallium oxide for pressure between 60 and 150 kbar.[2] Energies of the R_1 and R_2 lines versus pressure are presented in Figure S4b. When pressure increases, the R-lines emission is shifted towards a higher wavelength. The values of pressure shifts were estimated for R-line emission, which is -0.81 ± 0.04 cm^{-1}/kbar for R_2 emission up to 124 kbar, -1.8 ± 0.1 cm^{-1}/kbar for R_1 emission up to 90 kbar, and -0.82 cm^{-1}/kbar from 90 to 190 kbar. The pressure-dependent decay profiles taken from the whole emission range up to 190 kbars, as shown in Figure S4c. The decay remain to be single exponential for lower pressure up to 88 kbar, while it becomes nonexponential for higher pressure. The decay curves for lower pressures ware fitted using for the following equation:

$$I(t) = I_0 e^{-\frac{t}{\tau}}$$

(s1)

where $I(t)$ is emission intensity at time t, I_0 is the initial intensity, and τ is the decay time of the luminescence. The obtained decay time increases almost linearly and is 0.26 ms for 5 kbar and 2.90 ms for 88 kbar. According to the model presented the previous study, luminescence lifetime of octahedrally coordinated intermediate field Cr^{3+} system, where the ^2E state is located slightly below the $^4T_2$, can be approximated by following formula:[3]

$$\tau = \frac{\left\{1 + exp(-\frac{\delta}{kT}) + 3exp\left(\frac{-\Delta}{kT}\right)\right\}}{\left[\frac{1 + q \cdot \exp\left(-\frac{\delta}{kT}\right)}{\tau_E} + \frac{1}{\tau_T}3exp\left(\frac{-\Delta}{kT}\right)\right]}$$

(s2)

When pressure increases, the crystal field strength increases. As a result, the energy of $^4T_2$ state increases, whereas the energy of ^2E slightly diminishes with pressure.[4,5] Besides, the energies Δ and Δ' increase with pressure by quantities $\frac{d\Delta}{dp}$ and $\frac{d\Delta'}{dp}$, respective. Pressure can change the quantity of $S\hbar\omega$ depending on the lattice and dopant. $S\hbar\omega$ can increase or decrease with increasing pressure.[6] Since we have no

information on the pressure-induced changes of electron lattice coupling $S\hbar\omega$, we can assume that it is constant. Then, we assume that $\dfrac{d\Delta}{dp} = \dfrac{d\Delta'}{dp}$. We can modify equation (s2) to reproduce the pressure dependence of PL lifetime.

$$\tau = \tau_T \left[\dfrac{1 + exp(-\dfrac{\delta}{kT}) + 3\exp\left(-\dfrac{\Delta + \dfrac{d\Delta}{dp}}{kT}\right)}{\left\{\dfrac{V_{s-o}}{\Delta' + \dfrac{d\Delta}{dp}}\right\}^2 [1 + q \cdot \exp\left(-\dfrac{\delta}{kT}\right)] + 3\exp\left(-\dfrac{\Delta + \dfrac{d\Delta}{dp}}{kT}\right)} \right]$$

(s3)

To obtain relation (s3), we have assumed that spin-orbit interaction weakly depends on pressure. We performed the fitting to obtain the solid and dashed red curve, as shown in Figure S4d. The fitted values for the red dashed curve were $\dfrac{d\Delta}{dp}$ =13.0V cm^{-1}/kbar obtained for τ_T = 0.027 ms, Δ = 630 cm^{-1}, $\dfrac{\tau_E}{\tau_T} = \left\{\dfrac{\Delta'}{V_{s-o}}\right\}^2 = 125,$ δ = 162 cm^{-1}, and q = 4. On the other hand, the best fit for the red solid curve, it has been obtained for δ = 162 cm^{-1}, q = 4 $\dfrac{\tau_E}{\tau_T} = \left\{\dfrac{\Delta'}{V_{s-o}}\right\}^2 = 125$, and τ_T = 0.027ms, where fitting parameters were $\dfrac{d\Delta}{dp}$ =10 ± 0.5 cm^{-1}/kbar and Δ = 880 ± 30 cm^{-1}.
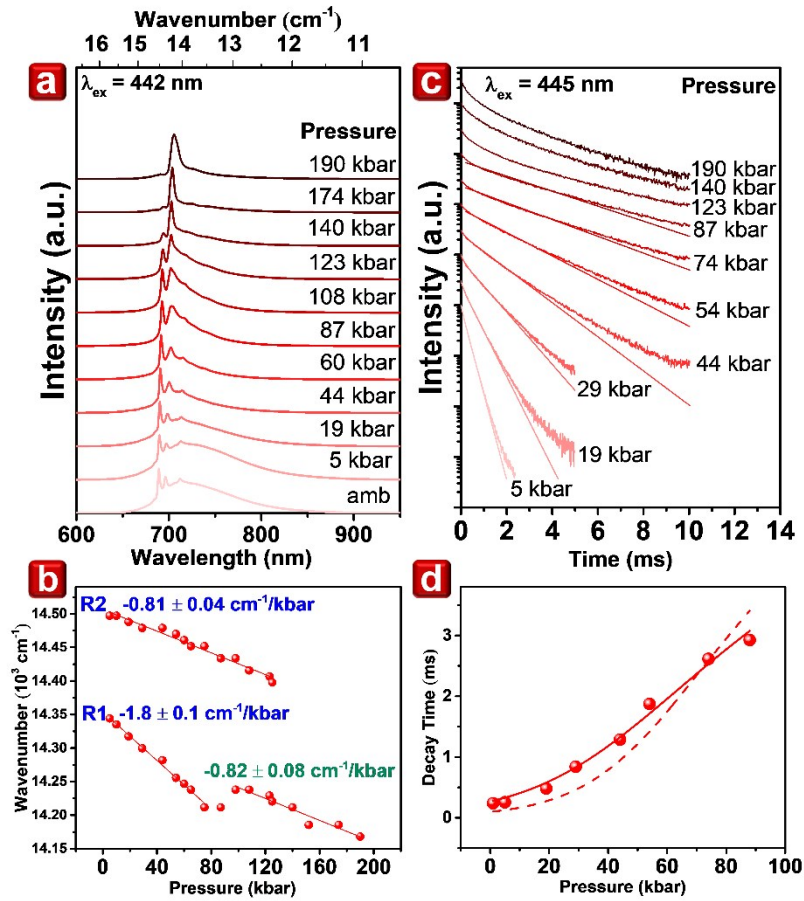
Figure S4. Pressure-dependent (a) emission spectra upon excitation at 442 nm, (b) pressure shift of the R_1 line and R_2 line vs. pressure in wavenumber scale, (c) pressure-dependent decay profiles upon excitation at 445 nm and (d) calculated decay times of Ga$_2$O$_3$:Cr^{3+}. The dashed curve is convoluted by using relation S3 and Δ = 630 and $\frac{d\Delta}{dp}$ =13.0 cm^{-1}/kbar, and solid curve by using 880 cm^{-1} and $\frac{d\Delta}{dp}$ =10.0 cm^{-1}/kbar.

Electron Paramagnetic Resonance

The EPR technique allows determining the nearest surroundings of paramagnetic ions. The EPR spectrum from chromium ions is observed in the positions g ~ 4 and g ~ 2, depending on the crystal field surrounding these ions. The signal is observed in strong magnetic inductions region (g ~ 2) in weaker crystal fields, while it is observed in weaker magnetic inductions (g ~ 4) in strong crystal fields. Cr^{3+} ions have an electron spin S = 3/2, so powder compounds can be characterized by many EPR lines depending on the symmetry of these ions and the nearest environment (interactions between chromium ions). Here, we observe the signal in the entire range of magnetic induction

from 10 mT to 550 mT. Several transitions in strong (g = 5.54,5.01), medium (g = 2.46) and weak (g = 1.57) magnetic induction are clearly observed, as shown in Figure S5.
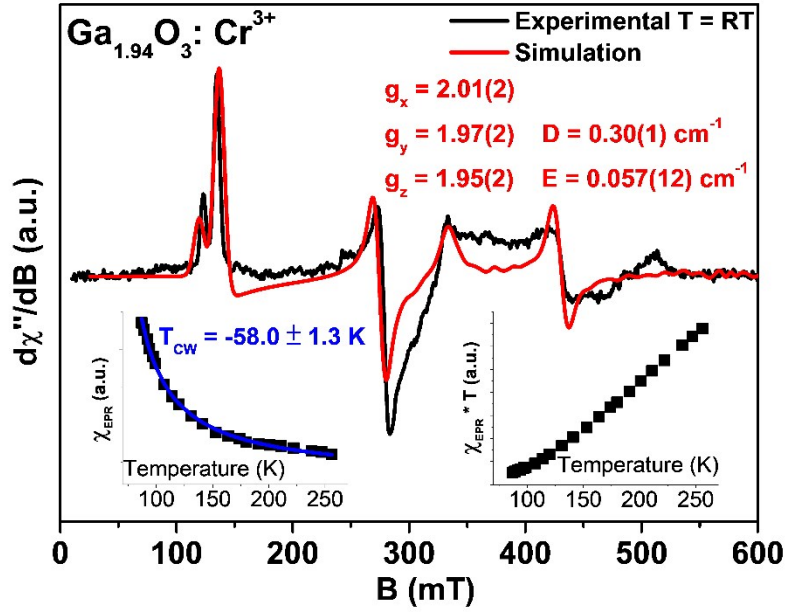

Figure S5. Experimental and simulated EPR spectrum of Ga_2O_3:Cr^{3+} at room temperature. The inset shows the dependence of magnetic susceptibility, Curie-Weiss parameters (left side), and magnetic moment (right side) on temperature.

Based on the experimental data, the parameters of spin Hamiltonian (SH) were determined from the following equation, consisting the Zeeman (Z) and Zero Field Splitting (ZFS) terms:

$$H = H_Z + H_{ZFS} = \mu_B B \cdot g \cdot S + D\left(S_z^2 - \frac{1}{3}S(S+1)\right) + E\left(S_x^2 + S_y^2\right)$$

where μ_B – Bohr magneton, B – induction of magnetic field, g – effective spectroscopic splitting factor, S – electron spin, D – axial and E – rhombic distortions of octahedral. We have obtained the following values of the Zeeman parameters g_x = 1.95(2), g_y = 1.97(2), g_z = 2.01(2) ($g_x \approx g_y \neq g_z$), indicating an axial symmetry of the chromium ion environment. The zero-field splitting (ZFS) parameters, D = 0.30(1) cm^{-1}, E = 0.057(12) cm^{-1} indicate significant axial distortion of the C_4 symmetry.   The results of the fitting of SH parameters by using the least square's method are shown in Figure S5.

Temperature dependence of the integrated EPR intensity is presented in the inset of Figure S5. The EPR integrated intensity, χ_{EPR}, is defined as an area under the absorption EPR spectrum and is proportional to the magnetic susceptibility of the

investigated spin system. For many paramagnetic ions, the temperature dependence of the integrated intensity is accurately described by the Curie-Weiss law, $\chi_{EPR}(T) = C/(T-T_{CW})$, where T_{CW} is the Curie-Weiss constant. The Curie-Weiss law appears to be valid at the entire temperature range. The least-square fitting of the experimental points to the Curie-Weiss law produced $T_{CW} = -58$ K. The negative sign and a large value of the Curie-Weiss temperature indicate a strong antiferromagnetic interaction between chromium ions. The temperature dependence of the product of temperature and integrated intensity, $T \cdot \chi_{EPR}$, is depicted in the inset of Figure S5. In general, this product is proportional to the square of an effective magnetic moment. For $Ga_2O_3:Cr^{3+}$, the magnetic moment decreases with temperature in the entire temperature range, which is in line with our expectation. This confirms the strong antiferromagnetic interactions between the chromium ions.

Chemical Stability

The luminescent degradation is also an important issue to evaluate its potential for the practical application. To understand the chemical stability of $Ga_2O_3:Cr^{3+}$, the relative quantum efficiency is measured by putting the powder in the oven with the temperature and humidity of 85 °C and 85%, respectively, as shown in Figure S6. $Ga_2O_3:Cr^{3+}$ can maintain 95% of its original quantum efficiency after 7 days, revealing its good stability toward the moisture and the great potential for the practical application.
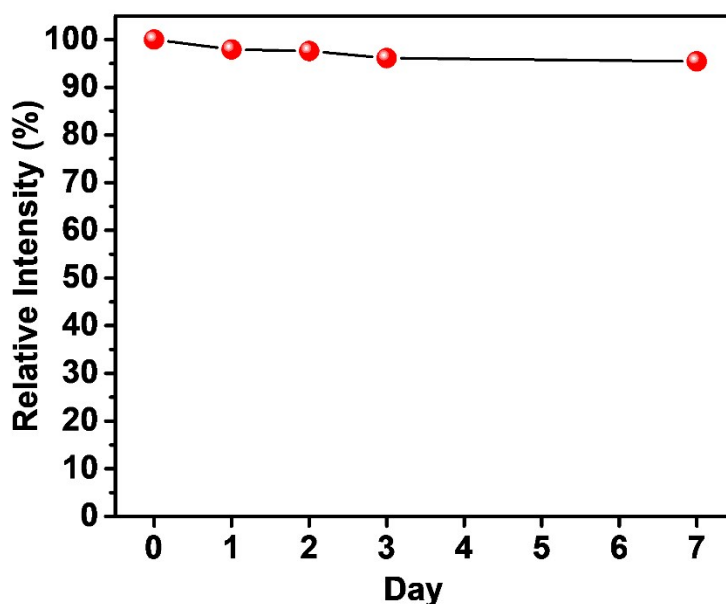
Figure S6. Relative quantum efficiency of Ga_2O_3:Cr^{3+} under the condition of 85 °C and 85% humidity.

References

1. H. He, R. Orlando, M. A. Blanco, R. Pandey, E. Amzallag, I. Baraille and M. Rérat, *Phys. Rev. B*, 2006, **74**, 195123.
2. K. Lipinska-Kalita, B. Chen, M. Kruger, Y. Ohki, J. Murowchick and E. Gogol, *Phys. Rev. B*, 2003, **68**, 035209.
3. M. Grinberg, T. Lesniewski, S. Mahlik and R. S. Liu, *Opt. Mater.*, 2017, **74**, 93-100.
4. M. Grinberg and A. Suchocki, *J. Lumin.*, 2007, **125**, 97-103.
5. Z. Zhang, K. T. Grattan and A. W. Palmer, *Phys. Rev. B*, 1993, **48**, 7772.
6. M. Grinberg, J. Barzowska, Y. Shen, R. S. Meltzer and K. L. Bray, *Phys. Rev. B*, 2004, **69**, 205101.

[P2]

Chen, K.-C.; Fang, M.-H.; Huang, W.-T.; Kamiński, **M.; Majewska**, N.; Leśniewski, T.; Mahlik, S.; Leniec, G.; Kaczmarek, S. M.; Yang, C.-W.; Lu, K.-M.; Sheu, H.-S.; Liu, R.-S. Chemical and Mechanical Pressure-Induced Photoluminescence Tuning via Structural Evolution and Hydrostatic Pressure. *Chem. Mater.* **2021**, 33 (10), 3832-3840.

https://doi.org/10.1021/acs.chemmater.1c01041

Article

Chemical and Mechanical Pressure-Induced Photoluminescence Tuning via Structural Evolution and Hydrostatic Pressure

Kuan-Chun Chen, Mu-Huai Fang, Wen-Tse Huang, Mikołaj Kamiński, Natalia Majewska, Tadeusz Leśniewski, Sebastian Mahlik,* Grzegorz Leniec, Sławomir M. Kaczmarek, Chia-Wei Yang, Kuang-Mao Lu, Hwo-Shuenn Sheu, and Ru-Shi Liu*

Read Online

| ACCESS | Metrics & More | Article Recommendations | Supporting Information |

ABSTRACT: A chemical and mechanical pressure-induced photoluminescence tuning method was developed through the structural evolution and hydrostatic pressure involving phase transition. A series of $Ga_{1.98-x}Al_xO_3$:$0.02Cr^{3+}$ phosphors were synthesized. Structural evolution reveals a crystal phase change with the incorporation of Al ions. The luminescent analysis shows the broad-to-sharp emission process with a high internal quantum efficiency value (>90%). The high-pressure study reveals the emission from the exchange-coupled Cr^{3+} pairs and the phase transition under high pressure. Electron paramagnetic resonance indicates the distortion in the microstructures of the emission center. Finally, an ultra-broadband phosphor-converted light-emitting diode is achieved by utilizing the mixture of $Ga_{1.18}Al_{0.8}O_3$:$0.02Cr^{3+}$ and $Ga_{1.18}Sc_{0.8}O_3$:$0.02Cr^{3+}$ phosphors with a bandwidth of 209 nm and an output power of 119 mW. This study provides insights into the effect of chemical and mechanical pressure on the Cr^{3+}-doped materials and the development of high-quality near-infrared luminescent materials.
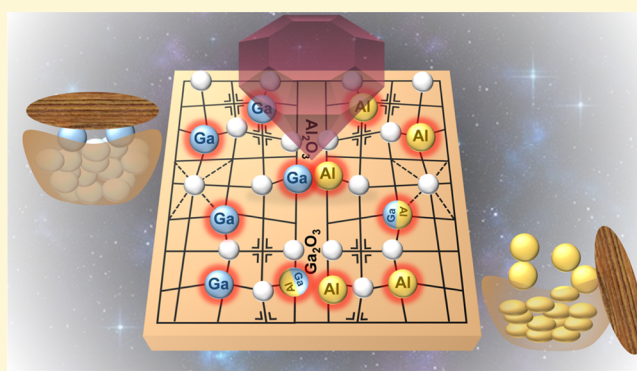
INTRODUCTION

Near-infrared (NIR) spectroscopy with noninvasive and real-time monitoring has been widely utilized in food analysis, medical diagnostics, and plant cultivation.[1−6] In combining NIR spectroscopy with a smartphone or other portable devices, compact NIR light sources with broadband emission are indispensable because traditional NIR light sources such as halogen lamps are bulky and energy-inefficient.[7] Although NIR light-emitting diodes (LEDs) have the advantages of high efficiency and small size, their full width at half-maximum (FWHM) is too narrow (<50 nm) to meet the requirements for multifunction light sources.[8] With the maturity of blue LED chips, phosphor-converted LEDs (pc-LEDs) with broadband emission have been recently proposed as a suitable and efficient NIR light source in portable devices.[9]

The Cr^{3+} ion is a unique and ideal NIR luminescence activator. Depending on the crystal field strength of the host lattices, it can provide narrowband emission (700 nm) from the spin-forbidden $^2E \rightarrow {}^4A_2$ transition or the broadband emission (650−1200 nm) ascribed to the spin-allowed $^4T_2 \rightarrow {}^4A_2$ transition. Distortions of the crystal structure or crystal phase change may cause unanticipated photoluminescent properties. Hence, adjusting the host lattices through a solid−solution method can effectively and systematically tune the crystal field strength and luminescent wavelength. Various

Cr^{3+}-doped NIR phosphors are featured with the broadband emission for LED applications, including $ScBO_3$:Cr^{3+}, $La_3Ga_5GeO_{14}$:Cr^{3+}, and $Mg_3Ga_2GeO_8$:Cr^{3+}.[3,6,10] In general, Cr^{3+} strongly prefers to occupy the octahedral sites. However, research focusing on the tuning of host lattices in NIR phosphor and the chemical and mechanical pressure-induced photoluminescent properties remains rare. In this study, a series of $Ga_{1.98-x}Al_xO_3$:$0.02Cr^{3+}$ phosphors were synthesized, and their unique structures and luminescence properties were characterized. A LED package was fabricated to verify its high potential in NIR-LED applications.

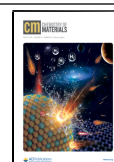## RESULTS AND DISCUSSION

Structural Analysis. The X-ray diffraction (XRD) patterns of $Ga_{1.98-x}Al_xO_3$:$0.02Cr^{3+}$ phosphors with different Al^{3+} contents ($0 \leq x \leq 1.98$) are shown in Figure 1a. The system of this phosphor can be divided into three parts, namely, β-Ga_2O_3 phase, mixed phase, and Al_2O_3 phase. The first part is

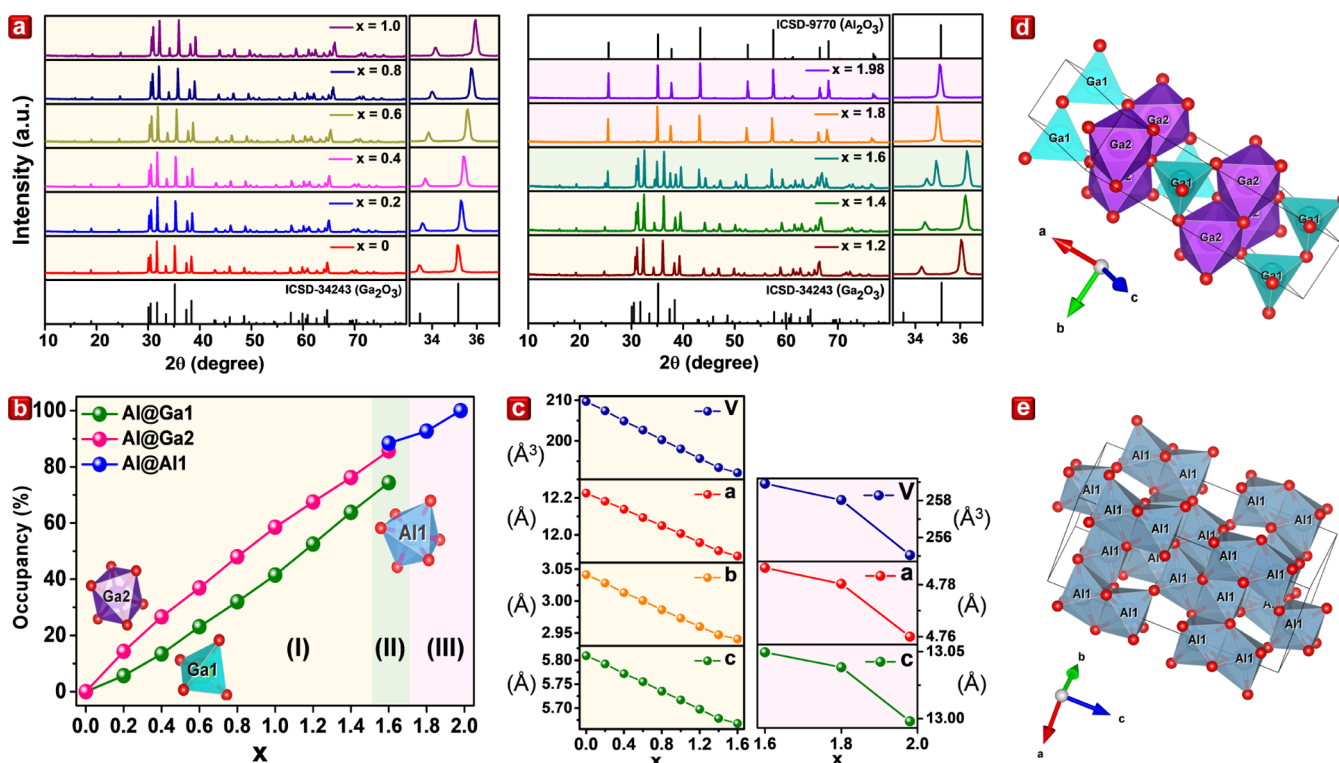**Figure 1.** Structural analysis of $Ga_{1.98-x}Al_xO_3$:0.02Cr^{3+} (x = 0, 0.2, 0.4, 0.6, 0.8, 1, 1.2, 1.4, 1.6, 1.8, and 1.98). (a) Powder XRD patterns for x = 0−1.98, (b) occupancy of Al^{3+} in Ga1, Ga2, and Al1 sites, (c) refined lattice parameter of x = 0−1.6 and 1.6−1.98 in β-Ga_2O_3 and Al_2O_3 phases, respectively, and crystal structures of (d) β-Ga_2O_3 and (e) Al_2O_3.

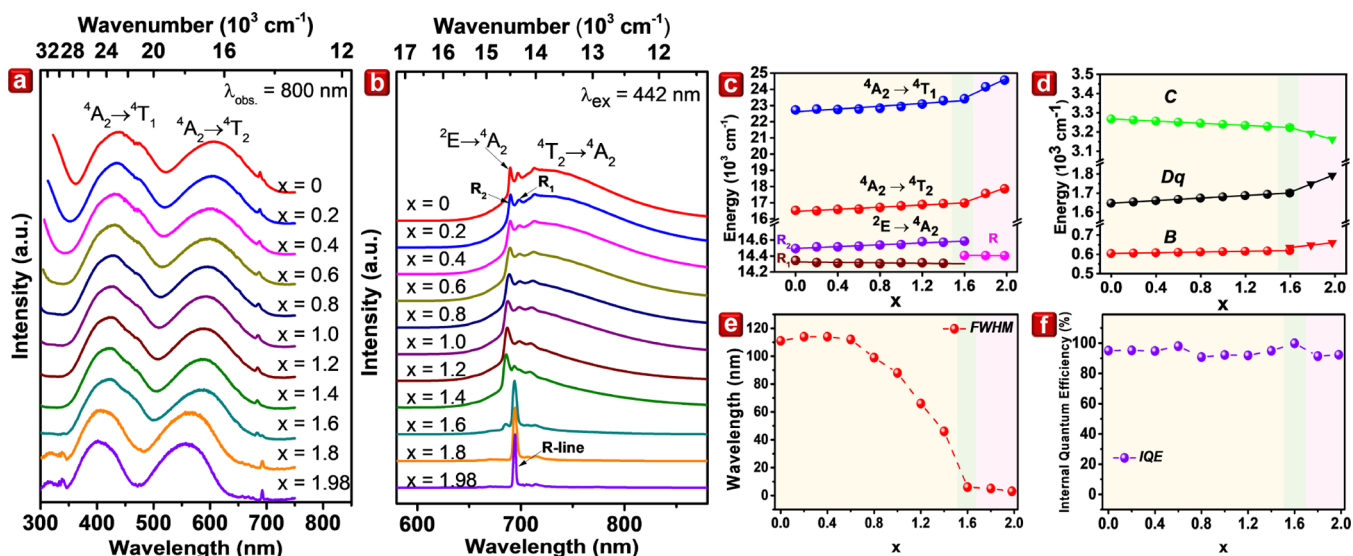**Figure 2.** RT luminescence properties of $Ga_{1.98-x}Al_xO_3$:0.02Cr^{3+} (x = 0, 0.2, 0.4, 0.6, 0.8, 1, 1.2, 1.4, 1.6, 1.8, and 1.98). (a) Excitation spectra observed at 800 nm, (b) emission spectra under 442 nm excitation, (c) transition energy values depending on Al^{3+} contents, (d) Dq, B, and C values depending on Al^{3+} contents, (e) FWHM of emission spectra, and (f) IQE.

composed of x = 0−1.4; the second only contains x = 1.6; and the third consists of x = 1.8 and 1.98. The crystal phase change from Ga_2O_3 to Al_2O_3 occurs at x = 1.6, in which the mixed phases can be observed. The diffraction patterns shift toward the high angles with the increment of Al^{3+} ions because Al^{3+} has a smaller ionic radius (0.39 Å; CN = 4, 0.54 Å; CN = 6) than Ga^{3+} (0.47 Å; CN = 4, 0.62 Å; CN = 6) (CN denotes coordinated number).[11]

Rietveld refinements of $Ga_{1.98-x}Al_xO_3$:0.02Cr^{3+} were conducted to further define this property, and the results are shown in Figure S1 and Tables S1 and S2.[12] The lattice parameters of the Ga_2O_3 and Al_2O_3 phases exhibit a linear decrease for x = 0−1.4 and x = 1.8−1.98, respectively, as shown in Figure 1c. The octahedral environment does not possess severe distortions when increasing the Al^{3+} content, and the distortion indexes of $Ga_{1.98-x}Al_xO_3$:0.02Cr^{3+} are shown in Table S3. Therefore, the decrease in the lattice parameter
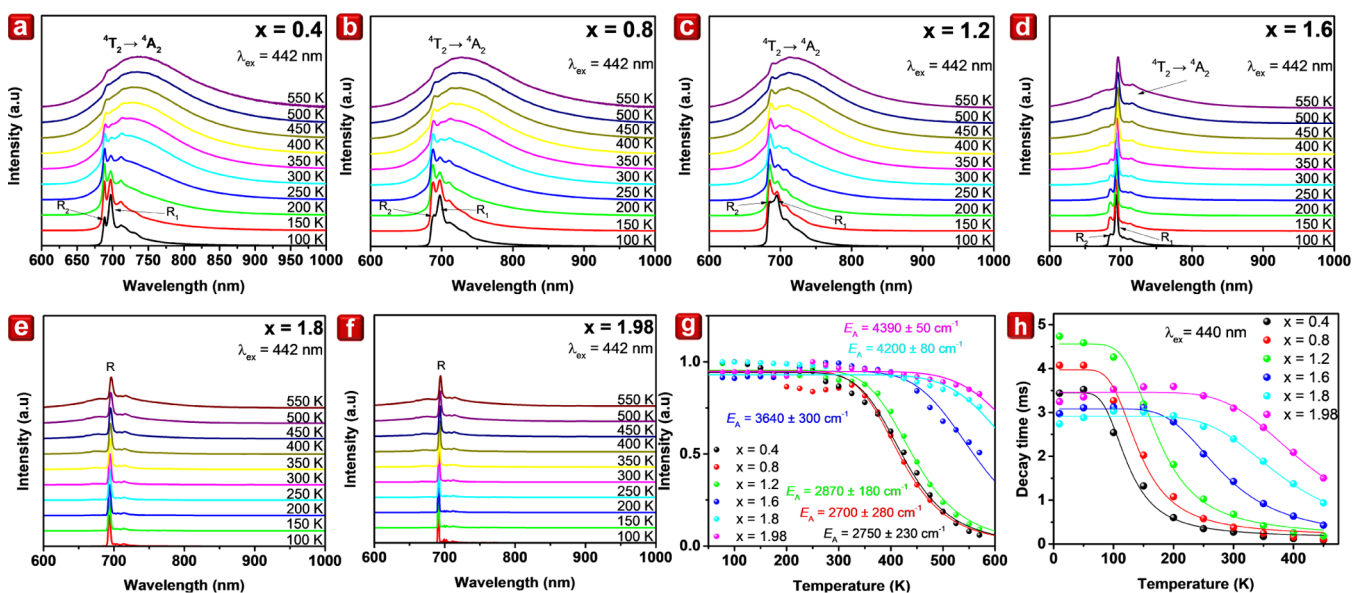
Figure 3. Temperature-dependent photoluminescent properties for samples of different Al^{3+} concentrations. (a) $x = 0.4$, (b) $x = 0.8$, (c) $x = 1.2$, (d) $x = 1.6$, (e) $x = 1.8$, (f) $x = 1.98$, (g) the integrated intensity, and (h) calculated decay time values of $Ga_{1.98-x}Al_xO_3:0.02Cr^{3+}$ for $x = 0.4, 0.8, 1.2, 1.6, 1.8,$ and 1.98 as a function of temperature.

can be attributed to the shrink caused by the chemical pressure. However, the lattice parameters deviate from linearity at $x = 1.6$ in Ga_2O_3 and Al_2O_3 phases. For further clarification, the crystal structure and locally coordinated environment of Ga_2O_3 and Al_2O_3 must be inspected in detail. Ga_2O_3 has a monoclinic structure with a space group of $C2/m$. Two different Ga^{3+} sites, namely, Ga1 and Ga2, can be found in this structure. Ga1 is coordinated by four O^{2-}-forming tetrahedrons, and Ga2 is coordinated by six O^{2-}-forming octahedrons (Figure 1d). By contrast, Al_2O_3 possesses a trigonal structure with a space group of $R\bar{3}c$ with a single Al1 site. Al1 is coordinated by six O^{2-}-forming octahedron (Figure 1e). Owing to the similar ionic radius of Ga2 (0.62 Å; CN = 6) and Cr^{3+} (0.615 Å; CN = 6), Cr^{3+} will be incorporated into Ga2 sites. When Al^{3+} is added into the Ga_2O_3 structure, no preferred occupation of Al^{3+} is observed, and the Al^{3+} ions can occupy Ga1 and Ga2 sites as calculated from Rietveld refinements (Figures 1b and S1). When the Al^{3+} concentration increases in the structure, the host lattices shrink.

Photoluminescence. The room-temperature (RT) photoluminescence excitation (PLE) spectra of $Ga_{1.98-x}Al_xO_3:0.02Cr^{3+}$ for $x = 0-1.98$ were analyzed with the observed wavelength at 800 nm to explain the relationship between the local structure and photoluminescent properties (Figure 2a). The PLE spectrum is composed of two excitation bands typical for Cr^{3+} ions in octahedral coordination (Ga2 and Al1 sites). The high-energy band in the range of 350−500 nm corresponds to $^4A_2 \rightarrow {^4T_1}$, and the other one in the 500−700 nm region corresponds to the $^4A_2 \rightarrow {^4T_2}$ spin-allowed transitions of Cr^{3+} ions. With the increment of Al^{3+} concentration, both bands shift to a short wavelength (high energy). Hence, the energy of maxima was determined and is shown in Figure 2c (blue and red dots). When the Al^{3+} content increases, the locations of $^4A_2 \rightarrow {^4T_1}$ and $^4A_2 \rightarrow {^4T_2}$ bands shift linearly to short wavelengths (high energy). However, the sample of $x = 1.6$ shows a sudden increase in the shift rate, which coincides with the crystal phase change from the Ga_2O_3 to Al_2O_3 phase, as indicated by the XRD results. This shift

would be interpreted based on the crystal field theory and assuming that the small Al^{3+} substitution for Ga^{3+} ions enhances the crystal field strength (Dq) in the vicinity of Cr^{3+} ions and increases the energy of $^4T_1$ and $^4T_2$ states for the ground state $^4A_2$. Meanwhile, the RT PL spectra of $Ga_{1.98-x}Al_xO_3:0.02Cr^{3+}$ were obtained under 442 nm excitation, as shown in Figure 2b. The line and broadband emissions of Cr^{3+} ions were observed for samples with low Al^{3+} contents. The line emission at approximately 690 nm corresponds to the $^2E \rightarrow {^4A_2}$ double-split emission line (R_1 and R_2 lines) accompanied by a weak phonon interaction, and the broadband emission extending from 650 to 950 nm corresponds to the transition from the $^4T_2$ state to the ground $^4A_2$ state. The energy shifts of R_1 and R_2 with respect to x are much lower in magnitude than the shifts of $^4T_1$ and $^4T_2$ states (Table S4). The lower component of the $^2E \rightarrow {^4A_2}$ emission (R_1 line) shifts linearly to long wavelengths (low energy), while the R_2 line shifts to high energy. Naturally, this indicates the increase of R_1 and R_2 lines splitting caused by the low-symmetry component of the crystal field, which is accompanied by a change in the relative intensity of R_1 and R_2 lines (Figure 3). For the sample of $x = 1.6$, a sharp change of $^2E \rightarrow {^4A_2}$ emission occurs due to the crystal phase change, as shown in Figure 2c (wine, purple, and pink dots). With further increases in the Al^{3+} concentration, the $^2E \rightarrow {^4A_2}$ line emission becomes highly prominent, and the $^4T_2 \rightarrow {^4A_2}$ broadband emission finally disappears. The splitting of the $^2E \rightarrow {^4A_2}$ emission is no longer observed and the observed emission line is denoted as the R-line. The presence of ^2E in the emission spectra of all samples indicates that the $^4T_2$ state has a higher energy than the ^2E state, and its presence in the emission spectra is due to thermal occupation. This conclusion is justified by the fact that the radiative transition probability of the $^2E \rightarrow {^4A_2}$ transition is much lower than that of $^4T_2 \rightarrow {^4A_2}$ (spin-forbidden compared with spin-allowed transitions). Therefore, the $^2E \rightarrow {^4A_2}$ transition will not occur at any substantial rate unless the relative occupation of ^2E is much higher than that of $^4T_2$ (i.e., it is the lowest excited state). An

increment in the Al^{3+} content enhances the $^4T_2$ state energy relative to the ^2E state and depopulating the $^4T_2$ state by increasing the Boltzmann activation barrier $\Delta_S = E(^4T_2) - E(^2E)$ between the two states, as shown in Figure S2b,c. This effect is consistent with the decrease in FWHM, as shown in Figure 2e. At the sample of $x = 1.6$, the FWHM drops dramatically because the crystal phase change from Ga_2O_3 to Al_2O_3 leads to the R-lines from Al1 sites dominating the emission.

With the known location of $^4T_2$, $^4T_1$, and ^2E states, calculations can be performed for the crystal field parameter (Dq), describing an interaction of 3d electrons and ligand ions and the Racah parameters (B and C) describing the interaction between 3d electrons in Cr^{3+}.[13] The energy of the excitation band maximum of the $^4A_2 \rightarrow {}^4T_2$ transition is equal to 10Dq, and the detailed calculation can be found in the Supporting Information. Figure 2d shows the value of these parameters for different Al^{3+} contents of all samples. The Dq parameter increases with the Al^{3+} concentration, indicating the increase of the crystal field strength responsible for the shift of the $^4T_2$ and $^4T_1$ energies toward a higher energy. The Racah parameter B increases with the Al^{3+} content, whereas C decreases. However, the observed changes are very small. This indicates that the nephelauxetic shift of the location of the ^2E state with the Al^{3+} content is small, in agreement with the observed shift of the ^2E emission in both phases.

X-ray Absorption Spectra. Cr K-edge X-ray absorption near-edge structure (XANES) was conducted in the fluorescence mode to confirm the oxidation state of the Cr ions (Figure S4). The pre- and post-edge absorption spectra of $Ga_{1.98-x}Al_xO_3$:$0.02Cr^{3+}$ phosphors were measured and normalized to 0 and 1, respectively. The dominant absorption peak in Cr K-edge XANES spectra of $Ga_{1.98-x}Al_xO_3$:$0.02Cr^{3+}$ ascribed to the $1s \rightarrow 4p$ photoelectronic transition of Cr^{3+} is located at approximately 6010 eV.[14] This absorption peak indicates that the oxidation state of Cr ions maintains around 3+ with the incorporation of Al^{3+} ions. This result stays in agreement with the observed luminescent properties mentioned above. The internal quantum efficiency (IQE) of $Ga_{1.98-x}Al_xO_3$:$0.02Cr^{3+}$ ($x = 0-1.98$) is also collected, as shown in Figure 2f. The IQE values for all samples are higher than 90%, revealing that $Ga_{1.98-x}Al_xO_3$:$0.02Cr^{3+}$ phosphors possess promising potential in practical applications.

Thermal Properties. To investigate thermal properties further, this work focuses on a detailed analysis of selected samples consisting of Al^{3+} and Ga^{3+} ions: $x = 0.4, 0.8, 1.2, 1.6, 1.8,$ and 1.98 because luminescence properties of Cr^{3+} in Ga_2O_3 ($x = 0$) have been well explained and described.[1,7] Temperature-dependent normalized PL spectra in the temperature range of 100−550 K for different Al^{3+} contents are shown in Figure 3a−f. The dominant R_1 and the thermally occupied R_2 line and phonon sidebands are observed for all samples at a temperature of 100 K. In samples of $x = 0.4, 0.8,$ and 1.2, the broadband emission extending from 650 to 950 nm appear in high temperature (above 150 K for $x = 0.4$ and 0.8 and above 250 K for $x = 1.2$). With the increasing temperature, the intensity of the R_2 emission also increases compared with that of R_1. The thermal occupation of the high R_2 state increases up to a point, and the R_2 emission starts to dominate over the R_1 emission at high temperatures (150−200 K). This highly unusual effect is interpreted as the result of the high radiative transition probability for the R_2 emission line characteristic for Cr^{3+} sites with a strong trigonal distortion.[15] However, the

higher intensity of the R_2 line than that of R_1 does not indicate a population inversion between R_2 and R_1 states. For a sample of $x = 1.6$ at 100 K, only R_1 and R_2 lines are visibly positioned at 693 and 685 nm, respectively. The broadband emission starts to appear above 400 K, but its intensity is low even at 500 K. Moreover, the R_2/R_1 intensity ratio exhibits the opposite temperature dependence, with R_2 emission diminishing with temperature. For $x = 1.8$ and 1.98, only the R-line is observed over the entire range of temperatures. The visible low-temperature narrow lines of $^2E \rightarrow {}^4A_2$ transition in these samples proved that they are under high crystal field strength, as shown in the Tanabe−Sugano diagram (Figure S2a). For samples of $x = 0.4-1.2$, the R-line emission broadens when the Al^{3+} concentration increases. This phenomenon may have resulted from the splitting of the ^2E state due to the distortion of octahedral sites for Cr^{3+} ions. With increasing temperature, the $^4T_2 \rightarrow {}^4A_2$ transition becomes highly probable, leading to the appearance of the broadband emission. Under no exception, the energy difference of the $^4T_2$ and ^2E states is smaller for samples with low Al^{3+} contents compared with that for samples with high Al^{3+} contents. Therefore, the thermal occupancy of the $^4T_2$ state occurs at lower temperatures for samples with a high Ga^{3+} content than those for the samples with high Al^{3+} content. Figure 3g shows the temperature-dependent emission intensity obtained from the whole emission range of samples for $x = 0.4, 0.8, 1.2, 1.6, 1.8,$ and 1.98 in the temperature range of 100−570 K. The intensity is stable up to 300 K for $x = 0.4, 0.8,$ and 1.2 samples and is stable up to 400 K for $x = 1.6$ and 500 K for $x = 1.8$ and 1.98 starts to decrease at high temperatures, indicating the nonradiative quenching of luminescence. For each set of the data point, an intensity plot was fitted using the following equation

$$I(t) = \frac{I(0)}{1 + A \exp\left(-\frac{E_A}{kT}\right)} \tag{1}$$

where $I(0)$ is the arbitrary intensity at 0 K, E_A is the activation energy for nonradiative transition, A is the ratio of nonradiative transition probability (p_{nr}) to radiative transition probability (p_r), and E_A values are presented in Figure 3g. E_A is approximately 2700−2900 cm^{-1} for samples of $x = 0.4, 0.8,$ and 1.2 and is larger for $x = 1.6$ (i.e., $E_A = 3640$ cm^{-1}) and $x = 1.98$ is the largest, 4390 cm^{-1}. The p_{nr} value for all samples is approximately 3×10^6 s^{-1}.

The decay curves in temperatures ranging from 10 to 450 K for samples of $x = 0.4, 0.8, 1.2, 1.6, 1.8,$ and 1.98 are depicted in Figures S6a−f, respectively. Decay time as a function of temperature for different Al^{3+} concentrations was calculated, and the results are shown in Figure 3h. Decay curves become shortened with the increase in temperature. All decay curves are single-exponential at low temperatures but deviate from the single-exponentiality at high temperatures, especially for the sample of $x = 1.6$ where mixed phase occurs. Despite the minimal deviation from single-exponentiality, decay time values (τ) can be obtained by applying the following formula

$$I(t) = I_0 \exp\left(-\frac{t}{\tau}\right) \tag{2}$$

where $I(t)$ is the emission intensity at a time (t), I_0 is the initial intensity, and τ is the decay time of the luminescence. For all samples, the decay time is stable from 10 K up to the threshold temperature (within the 50−200 K range, increasing with Al^{3+}
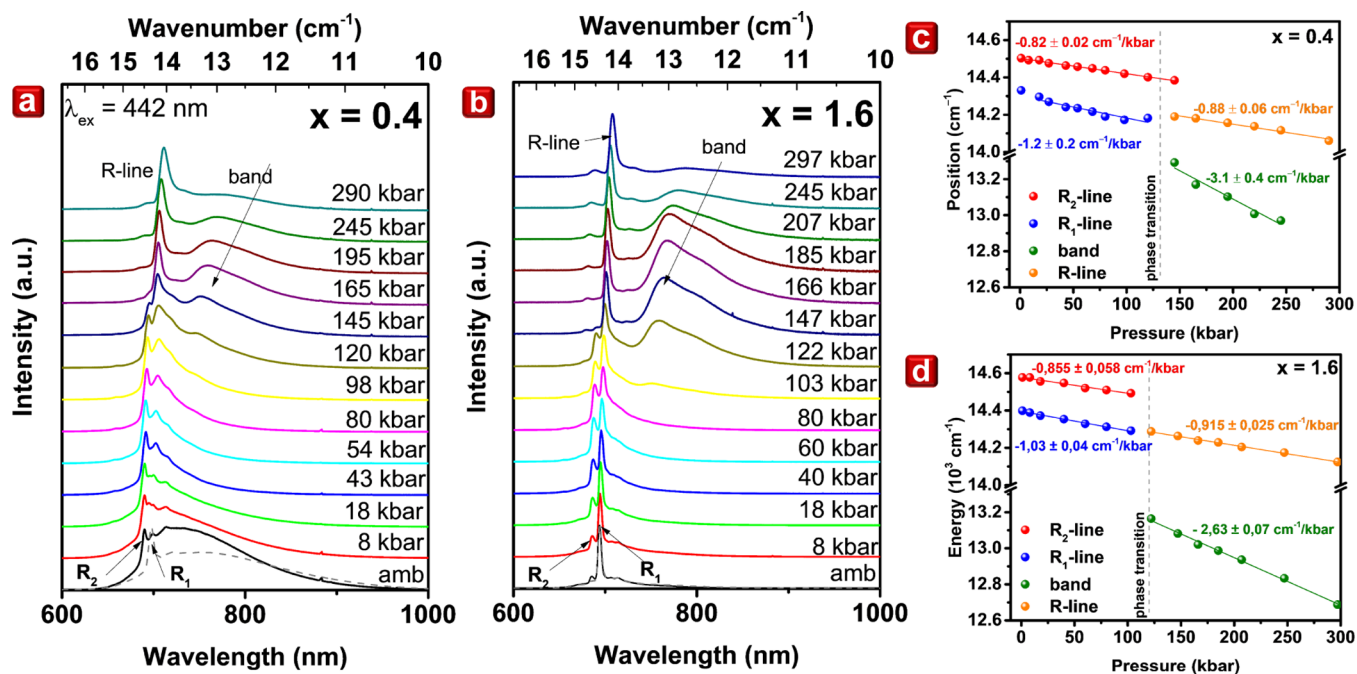
Figure 4. Pressure-dependent PL spectra for $Ga_{1.98-x}Al_xO_3$:$0.02Cr^{3+}$. (a) $x = 0.4$ and (b) $x = 1.6$. Position of the R-line emission and the maximum of the new band as a function of pressure for (c) $x = 0.4$ and (d) $x = 1.6$.

contents), above which the decay time diminishes. At 10 K, the radiative lifetime values of the $^2E \rightarrow {}^4A_2$ transition (denoted as τ_0) are unaffected by the thermal occupation of $^4T_2$ and can correspond to the radiative lifetime of the $^2E \rightarrow {}^4A_2$ transition. However, the $^2E \rightarrow {}^4A_2$ transition probability is still influenced by the presence of the $^4T_2$ state due to the quantum-mechanical mixing of the ^2E and $^4T_2$ state from the spin–orbit interaction.[16] Hence, the $^2E \rightarrow {}^4A_2$ lifetime is not constant, and its values change with the Al^{3+} concentration according to Table S5. Given that the threshold for nonradiative quenching is above 300 K for all samples, the diminishing decay time is ascribed to the thermal occupation of $^4T_2$. Owing to the temperature dependence of decay time for several samples with different Al^{3+} concentrations, the $^4T_2$ location of the Al^{3+} content can be obtained as the activation energy for the temperature-dependent shortening of decay time. The experimental values of $\tau(T)$ were fitted to the following equation describing the effect of thermal activation of $^4T_2$ on decay time

$$\tau(T) = \frac{1 + 3 \exp\left(-\frac{\Delta}{kT}\right)}{\tau_0^{-1} + 3\tau_T^{-1} \exp\left(-\frac{\Delta}{kT}\right)} \tag{3}$$

where τ_0 is the low-temperature decay time equivalent to the $^2E \rightarrow {}^4A_2$ radiative lifetime and τ_T is the radiative lifetime of the $^4T_2 \rightarrow {}^4A_2$ transition. The above formula does not consider the nonradiative quenching of the luminescence nor does it involve any explicit formula for τ_0 ($^2E \rightarrow {}^4A_2$ lifetime is treated as a free parameter). The experimental data using formula 3 are well fitted, and the parameters resulting from the fitting procedure are presented in Table S5.

Pressure-Dependent Photoluminescence. RT pressure-dependent PL spectra were obtained by hydrostatic pressure under excitation at 442 nm of $Ga_{1.98-x}Al_xO_3$:$0.02Cr^{3+}$ for $x = 0.4$ and 1.6 to understand the relationship between the luminescence and structure from the perspective of mechanical

pressure (Figure 4a,b). Under ambient pressure, line and broadband emissions are observed for $x = 0.4$. The strong dependence of the $^4T_2$ state energy on the crystal field strength results in a strong increment in the energy of $^4T_2 \rightarrow {}^4A_2$ transition with pressure. This shift is observed for the broadband emission up to a few kbar, but only line emission is observed above 18 kbar. The same result was previously observed for sample $x = 0$,[17,18] in which the broadband emission disappeared under pressure at approximately 44 kbar.

Owing to the pressure-induced shift of the $^4T_2$ level toward short wavelengths, the thermal energy is too low at RT to induce the emission from the $^4T_2$ level. Therefore, the ^2E state becomes the only emitting state for this system. Simultaneously, the pressure-induced increase of the low-symmetry crystal field component causes an increment in the splitting of R_1 and R_2 lines (see Figure 4c,d) and the change of the relative intensity of R_1 and R_2 lines (Figure 4a). For a pressure higher than 145 kbar, the R_1–R_2 splitting is no longer observed, and the $^2E \rightarrow {}^4A_2$ emission is denoted simply as the R-line. A substantial change of emission spectra between 123 and 140 kbar is also observed. Such a phenomenon is probably caused by a phase transition from β-Ga_2O_3 (monoclinic) to α-Ga_2O_3 (trigonal), which was previously calculated at approximately 95 kbar and experimentally verified for nanostructure materials.[19] This transition begins at 60 kbar, and the nanocrystalline phase is a combination of both phases of gallium oxide for a pressure between 60 and 150 kbar. A similar phenomenon is observed for the sample of $x = 1.6$. In this case, the thermal energy is too low at RT and ambient pressure to induce the emission from the $^4T_2$ level. Hence, the ^2E state is the only emitting state even under atmospheric pressure. Interestingly, after the phase transition in both samples, a new band appears in 750−800 nm. After the phase transition, the energy difference between the R-line emission and a new band emission is larger for samples of $x = 1.6$ than for $x = 0.4$. The pressure shift for R_1 and R_2 lines versus pressure before the phase transition and the
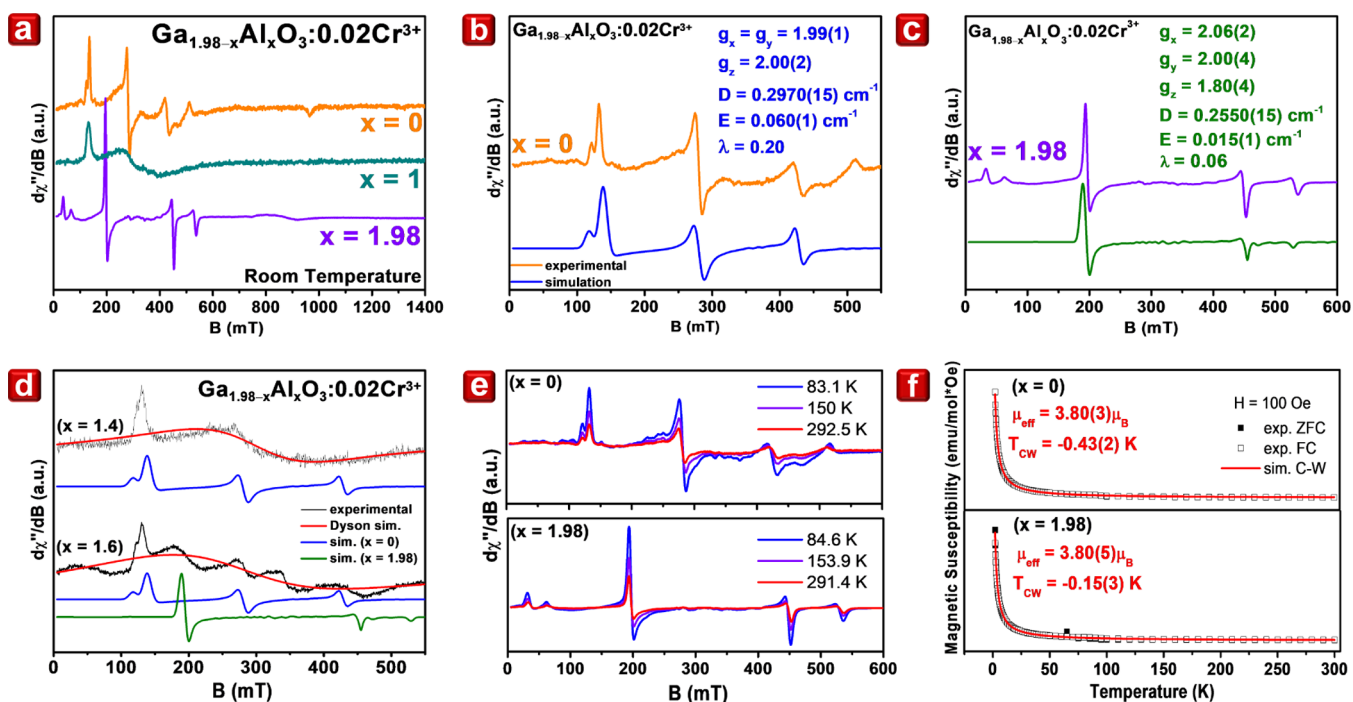
Figure 5. (a) Selected RT EPR spectra for samples of $x = 0$, 1, and 1.98, experimental EPR spectra and its simulation using the EPR-NMR program for (b) $x = 0$ and (c) $x = 1.98$, (d) experimental and simulated EPR spectra for coexistence samples $x = 1.4$ and 1.6, simulated EPR spectra for $x = 0$ and $x = 1.98$ for comparison, (e) EPR spectrum of samples of $x = 0$ and 1.98 at three selected temperatures $T \sim 80$, 150, and 290 K, and (f) magnetic susceptibility in FC and ZFC modes, $H = 100$ Oe, for samples of $x = 0$ and 1.98 (solid red lines mark Curie−Weiss fittings).

R-line and new band after the phase transition are presented in Figure 4c,d for $x = 0.4$ and $x = 1.6$, respectively. In both cases, the R-lines and the new band shift to low energy under increasing pressure. The rate of this shift in both cases is larger for the new band (3.1 cm^{-1}/kbar for $x = 0.4$ and 2.63 cm^{-1}/kbar for $x = 1.6$) than for the R-lines at approximately 1 cm^{-1}/kbar. The direction and magnitude of the pressure-induced shift of R-lines caused by the nephelauxetic effect are in good agreement with the typical pressure shift rate of the ^{2}E → ^{4}A$_2$ transition.[18,20,21] It is impossible to interpret the new broadband as the ^{4}T$_2$ → ^{4}A$_2$ transition because of its pressure to shift to a long wavelength, which is inconsistent with the behavior of the ^{4}T$_2$ state with pressure. The band is tentatively ascribed as a result of the emission of exchange-coupled Cr^{3+} pairs under high pressure. The appearance of the new band was not observed for the sample of $x = 0$ up to 230 kbar.[2,17] The pressure-dependent decay time analysis is discussed in the Supporting Information in detail.

Electron Paramagnetic Resonance. Electron paramagnetic resonance (EPR) was measured to investigate the local environment of Cr^{3+} ions. This method analyzes the closest surroundings of the luminescent center described by the local crystal field, zero-field splitting, and Zeeman splitting parameters to indicate its symmetries and the possible distortion. In Ga$_{1.98-x}$Al$_x$O$_3$:0.02Cr^{3+} ($x = 0-1.98$) phosphor, only Cr^{3+} is a paramagnetic ion with the 3d^3 ground state and electron spin $S = 3/2$. The EPR signal originated from Cr^{3+} ions in an octahedral crystal field within the 0 mT < B < 600 mT range of magnetic induction. The RT EPR spectrum of Ga$_{1.98-x}$Al$_x$O$_3$:0.02Cr^{3+} ($x = 0-1.98$) is depicted in Figure S7. For clarity, the RT EPR spectra for three selected samples of different Al^{3+} contents: $x = 0$, 1, and 1.98 are shown in Figure 5a. For the sample of $x = 1$, one sharp band is assigned to Cr^{3+} ions, and the other wide and Dyson-shaped signal is assigned

to free electrons due to the coexistence of Al^{3+} and Ga^{3+}. This designation is also applicable for samples of $x = 0.2-1.8$. For $x = 0$ and 1.98, their signals come from Cr^{3+} ions under different crystal field strengths at the octahedral site. The energy-level splitting of Cr^{3+} can be described by the following formula

$$H = H_{Zeeman} + H_{ZFS} \qquad (4)$$

$$H = \mu_B B \cdot g \cdot S + D\left(S_z^2 - \frac{1}{3}S(S+1)\right) + E(S_x^2 + S_y^2) \qquad (5)$$

where μ_B represents the Bohr magneton, B represents the induction of magnetic field, g represents the spectroscopic splitting factor, S represents the electron spin, D represents the axial distortion, and E represents the rhombic distortions of octahedral sites ($\lambda = E/D$). The following values were obtained by fitting the spin-Hamiltonian (SH) parameter to the experimental data using the abovementioned formula: $g_x = g_y = 1.99(1)$, $g_z = 2.00(2)$, and $\lambda = 0.20$; and $g_x = 2.06(2)$, $g_y = 2.00(4)$, $g_z = 1.80(4)$, and $\lambda = 0.06$ (including measurement error) for samples of $x = 0$ and $x = 1.98$, respectively. The fitting results of SH parameters by the least square's method are shown in Figure 5b,c.

As shown in Figure 5b,c, the SH parameters indicate C_3 or a lower symmetry of Cr^{3+} with an axial and rhombic octahedral distortion for the sample of $x = 0$, whereas the C_4 symmetry of octahedral sites with only a slight distortion for $x = 1.98$. An EPR signal is found at an extremely low magnetic induction for $x = 1.98$. The shape of this signal indicates its origin from Cr^{3+} ions in octahedral sites with high distortion. However, the intensity is extremely low to determine the SH parameters. Moreover, the samples for the coexistence of Al^{3+} and Ga^{3+} exhibit an EPR signal originating from Cr^{3+} and a Dyson-like
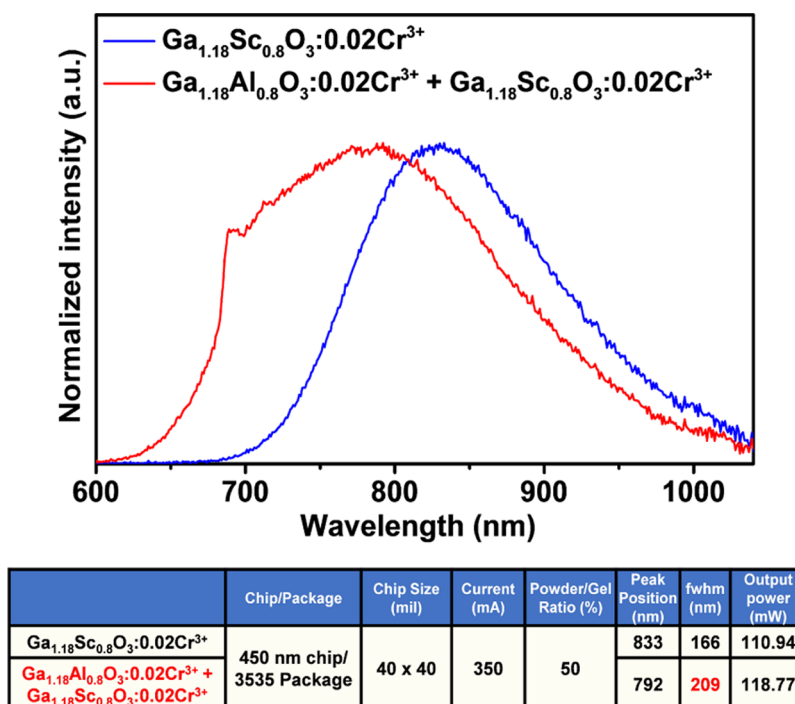
Figure 6. LED package combining one blue LED chip with phosphors composed of $Ga_{1.18}Al_{0.8}O_3$:0.02Cr^{3+} and $Ga_{1.18}Sc_{0.8}O_3$:0.02Cr^{3+} as well as pure $Ga_{1.18}Sc_{0.8}O_3$:0.02Cr^{3+} for comparison.

signal originating from conduction electrons, thereby satisfying the following equation

$$P_{DYSON} = \left[\frac{\Delta B + \alpha(B - B_0)}{4(B - B_0)^2 + \Delta B^2} + \frac{\Delta B + \alpha(B + B_0)}{4(B + B_0)^2 + \Delta B^2} \right]$$

(6)

The fitting results of the Dyson equation to the experimental data of coexistence samples: x = 0.4, 0.8, 1.2, and 1.8 are shown in Figure S8a−d. Relationships between the asymmetry parameter α (Figure S8e) and the integrated intensity of the Dyson signal versus Al^{3+} concentration of samples are also presented (Figure S8f).

The EPR spectra of samples for x = 1.4 and 1.6 with their simulations for Cr^{3+} ions and conduction electrons and the simulated EPR spectra for samples of x = 0 and 1.98 for comparison are presented in Figure 5d. The strong influence of the substitution content of Al^{3+} and its ionic radius is revealed. For samples with $x \leq 1.4$, a signal originating from Cr^{3+} is observed at C_3 symmetry sites (similar to the sample of x = 0). For the sample of x = 1.6, an EPR signal originating from Cr^{3+} is found at C_3 (similar to the sample of x = 0) and at C_4 (similar to the sample of x = 1.98) symmetry sites (Figure 5d). Above x > 1.6, the signal from Cr^{3+} ions in the C_4 symmetry site dominates. This result corresponds to the XRD and luminescent properties. Furthermore, the EPR spectra of the samples with x = 0 and 1.98 at three selected temperatures T = 80, 150, and 290 K are shown in Figure 5e. The EPR temperature studies of magnetic susceptibility indicate antiferromagnetic interactions between Cr^{3+} ions in both samples (x = 0 and 1.98).

Magnetic susceptibility measurement in zero-field-cooled (ZFC) and FC modes with H = 100 Oe was conducted for samples of x = 0 and 1.98 to ensure the existence of only one behavior of isolated Cr^{3+} ions. The fittings to the Curies−Weiss (C−W) law are presented in Figure 5f. The results are

fitted well and show no anomaly to the C−W law. The interactions between Cr^{3+} ions in all the above samples are weak (low values of C−W temperature, T_{cw}) and possess antiferromagnetic properties. The Curie constant, C, which can be used to find the values of the effective magnetic moments, was calculated from the magnetic susceptibility measurement using the following equation

$$\mu_{eff} = 2.827\sqrt{C}\mu_B$$

(7)

The calculated values (μ_{eff} = 3.80μ_B for x = 0 and 1.98) show no difference from the magnetic moment of isolated Cr^{3+} ions ($\sim$3.87μ_B) and therefore indicate the lack of contribution from the pair Cr^{3+} ion system. This finding is in agreement with the results from the EPR method.

LED Package. Ultra-broadband pc-LED was manufactured by utilizing the mixture of $Ga_{1.18}Al_{0.8}O_3$:0.02Cr^{3+} and $Ga_{1.18}Sc_{0.8}O_3$:0.02Cr^{3+} phosphors to evaluate the potential of these phosphors for practical application (Figure 6). The $Ga_{1.18}Sc_{0.8}O_3$:0.02Cr^{3+} phosphor was synthesized using our previous method.[2] The blue LED chip with a 450 nm emission and a chip size of 40 × 40 mil was used as the light source. The obtained LED device can provide an output power of 118.77 mW under 350 mA driven current and a bandwidth of over 200 nm. Moreover, comparing to those phosphors mentioned above, this LED device with a relatively higher radiant flux can prevent the noise from the background of the environment. On the other hand, broad bandwidth over 200 nm makes the devices possible to detect more analytes and obtain more information. Hence, this result indicates that $Ga_{1.98-x}Al_xO_3$:0.02Cr^{3+} can be a potential candidate for NIR light sources in portable devices.

■ CONCLUSIONS

In conclusion, a series of $Ga_{1.98-x}Al_xO_3$:0.02Cr^{3+} solid−solution phosphors were synthesized. XRD refinements

indicate the success of the solid−solution process and the crystal phase change at $x = 1.6$. The luminescent analysis shows the change of broadband to line emission covering from 650 to 950 nm. All samples are provided with high IQE (>90%). A new emission band appearing in 750−850 nm is observed from the high-pressure study and is attributed to the exchange-coupled Cr^{3+} pairs under high pressure. EPR spectra and magnetic susceptibility measurement indicated two kinds of octahedral sites for emission ions and confirmed the lack of contribution of the Cr^{3+} pair system under atmospheric pressure. The ultra-broadband pc-LED prepared by utilizing the mixture of $Ga_{1.18}Al_{0.8}O_3{:}0.02Cr^{3+}$ and $Ga_{1.18}Sc_{0.8}O_3{:}0.02Cr^{3+}$ phosphors can provide the emission spectra with a bandwidth of 209 nm and an output power of 119 mW. This study provides insights into the effect of chemical and mechanical pressure on Cr^{3+}-doped materials and the development of high-quality NIR luminescent materials.

EXPERIMENTAL SECTION

Reagents. Gallium oxide (Ga_2O_3, 99.99%) and aluminum oxide (Al_2O_3, 99.99%) were obtained from Gredmann. Chromium oxide (Cr_2O_3, 99.9%) was purchased from Merck.

Synthesis of $Ga_{1.98-x}Al_xO_3{:}0.02Cr^{3+}$. Starting precursors were weighed according to the stoichiometric ratio, evenly mixed, and ground in an agate mortar for at least 20 min. The mixing precursors were loaded into alumina crucibles and placed in a muffle furnace. All samples were sintered at 1550 °C for 5 h with a heating and cooling rate of 5 °C per minute in the atmosphere. After sintering, the samples were cooled down to RT. Finally, $Ga_{1.98-x}Al_xO_3{:}0.02Cr^{3+}$ phosphors were obtained.

Characterization. The powder XRD patterns of $Ga_{1.98-x}Al_xO_3{:}0.02Cr^{3+}$ were collected by XRD analyzer (D2 PHASER, Bruker) with a Cu Kα source ($\lambda = 1.54178$ Å) to characterize the crystal phase and crystallinity of analytes. Synchrotron powder XRD patterns of $Ga_{1.98-x}Al_xO_3{:}0.02Cr^{3+}$ were acquired from the National Synchrotron Radiation Research Center (NSRRC, Taiwan) BL01C2 beamline ($\lambda = 0.82657$ Å) at RT using a Debye−Scherrer camera. Synchrotron patterns subsequently underwent the Rietveld refinement using Total Pattern Analysis Solutions software (TOPAS 4.2). RT PLE spectra were measured with a FluoroMax-4P spectrofluorometer (Horiba) equipped with a 150 W xenon lamp as an excitation source and an R928 Hamamatsu photomultiplier as a detector to record PL and PLE spectra in the spectral range of 250−850 nm. The temperature and pressure dependence of PL [temperature-dependent PL (TDPL)] spectra were measured through an Andor SR-750-D1spectrometer equipped with a CCD camera (DU420A-OE) and a Kimmon Koha He−Cd laser with 442 nm as the excitation source. In the TDPL measurement, the temperature was controlled using the THMSG600 temperature controller Linkam stage combined with the LNP95 liquid nitrogen cooling pump system to obtain a temperature in the range of 100−600 K. Decay profiles were measured using the apparatus for the time-resolved spectroscopy consisting of a PG 401/SH optical parametric generator pumped by a PL2251A pulsed YAG:Nd laser (EKSPLA). For detection, the equipment consists of a 2501S grating spectrometer (Bruker Optics) combined with a C4334-01 streak camera (Hamamatsu). High-pressure luminescence measurements were performed in a screw-driven Merrill-Bassett type diamond anvil cell with a 0.5 mm diamond culet diameter. The gasket for the pressure chamber was preindented to approximately 0.08 mm. A hole with a diameter of 0.2 mm was drilled in the center of the indentation. $KMgF_3{:}0.5\%Eu^{2+}$ was applied as a pressure sensor, and polydimethylsiloxane oil was used as a pressure-transmitting medium. IQE measurement was conducted using a UV to NIR absolute PL quantum yield spectrometer (C1534-12; Hamamatsu Photonics K.K.) equipped with a NIR PL measurement unit (C13684-01; Hamamatsu Photonics K.K.) consisting of a high-power Xe lamp unit (L13685−01; Hamamatsu Photonics K.K.) and a 475 nm filter for excitation

(A13686−475). X-ray absorption spectroscopy was measured at the 44A1 beamline of the National Taiwan Synchrotron Radiation Research Center (NSRRC), Hsinchu City, Taiwan. Data analysis was conducted using Athena software. EPR spectra were recorded in the temperature range of 80−300 K through the conventional Bruker X-band ELEXSYS E500 CW spectrometer operating at 9.46 GHz and 0.63 mW microwave power. The magnetic induction ranged up to 1.4 T. The first derivative of the absorption spectrum was recorded as a function of the applied magnetic induction. The EPR/NMR program was applied to recognize SH parameters. Magnetic measurements were conducted by a SQUID (Superconducting Quantum Interference Device) magnetometer (Quantum Design MPMS-XL-7). Magnetic susceptibility data were obtained in the ZFC and FC modes and recorded for temperatures up to 300 K and a magnetic field of 100 Oe. Magnetic susceptibility was simulated by applying the C−W law. The susceptibility data were corrected due to the diamagnetism of a sample holder and the constituent atoms by Pascal's constants.

ASSOCIATED CONTENT

Ⓢ Supporting Information

The Supporting Information is available free of charge at https://pubs.acs.org/doi/10.1021/acs.chemmater.1c01041.

Rietveld refinement; sample appearance; crystal field calculation; decay time; and EPR (PDF)

AUTHOR INFORMATION

Corresponding Authors

Sebastian Mahlik − *Institute of Experimental Physics, Faculty of Mathematics, Physics and Informatics, University of Gdańsk, 80-308 Gdańsk, Poland;* Ⓞ orcid.org/0000-0002-9514-049X; Email: sebastian.mahlik@ug.edu.pl

Ru-Shi Liu − *Department of Chemistry, National Taiwan University, 106 Taipei, Taiwan;* Ⓞ orcid.org/0000-0002-1291-9052; Email: rsliu@ntu.edu.tw

Authors

Kuan-Chun Chen − *Department of Chemistry, National Taiwan University, 106 Taipei, Taiwan*

Mu-Huai Fang − *Department of Chemistry, National Taiwan University, 106 Taipei, Taiwan;* Ⓞ orcid.org/0000-0003-1475-0200

Wen-Tse Huang − *Department of Chemistry, National Taiwan University, 106 Taipei, Taiwan*

Mikołaj Kamiński − *Institute of Experimental Physics, Faculty of Mathematics, Physics and Informatics, University of Gdańsk, 80-308 Gdańsk, Poland*

Natalia Majewska − *Institute of Experimental Physics, Faculty of Mathematics, Physics and Informatics, University of Gdańsk, 80-308 Gdańsk, Poland;* Ⓞ orcid.org/0000-0002-1933-0355

Tadeusz Leśniewski − *Institute of Experimental Physics, Faculty of Mathematics, Physics and Informatics, University of Gdańsk, 80-308 Gdańsk, Poland*

Grzegorz Leniec − *Institute of Physics, Department of Mechanical Engineering and Mechatronics, West Pomeranian University of Technology, 70-311 Szczecin, Poland*

Sławomir M. Kaczmarek − *Institute of Physics, Department of Mechanical Engineering and Mechatronics, West Pomeranian University of Technology, 70-311 Szczecin, Poland*

Chia-Wei Yang − *Everlight Electronics Co., Limited, 238 New Taipei City, Taiwan*

Kuang-Mao Lu − *Everlight Electronics Co., Limited, 238 New Taipei City, Taiwan*

Hwo-Shuenn Sheu − *National Synchrotron Radiation Research Center, 300 Hsinchu, Taiwan*

Complete contact information is available at:
https://pubs.acs.org/10.1021/acs.chemmater.1c01041

Notes

The authors declare no competing financial interest.

■ REFERENCES

(1) Fang, M.-H.; Huang, P.-Y.; Bao, Z.; Majewska, N.; Leśniewski, T.; Mahlik, S.; Grinberg, M.; Leniec, G.; Kaczmarek, S. M.; Yang, C.-W.; Lu, K.-M.; Sheu, H.-S.; Liu, R.-S. Penetrating Biological Tissue Using Light-Emitting Diodes with a Highly Efficient Near-Infrared ScBO$_3$:Cr^{3+} Phosphor. *Chem. Mater.* **2020**, *32*, 2166−2171.

(2) Fang, M.-H.; Chen, K.-C.; Majewska, N.; Leśniewski, T.; Mahlik, S.; Leniec, G.; Kaczmarek, S. M.; Yang, C.-W.; Lu, K.-M.; Sheu, H.-S.; Liu, R.-S. Hidden Structural Evolution and Bond Valence Control in Near-Infrared Phosphors for Light-Emitting Diodes. *ACS Energy Lett.* **2020**, *6*, 109−114.

(3) Rajendran, V.; Fang, M.-H.; Guzman, G. N. D.; Lesniewski, T.; Mahlik, S.; Grinberg, M.; Leniec, G.; Kaczmarek, S. M.; Lin, Y.-S.; Lu, K.-M.; Lin, C.-M.; Chang, H.; Hu, S.-F.; Liu, R.-S. Super Broadband Near-Infrared Phosphors with High Radiant Flux as Future Light Sources for Spectroscopy Applications. *ACS Energy Lett.* **2018**, *3*, 2679−2684.

(4) Zeng, H.; Zhou, T.; Wang, L.; Xie, R.-J. Two-Site Occupation for Exploring Ultra-Broadband Near-Infrared Phosphor—Double-Perovskite La$_2$MgZrO$_6$:Cr^{3+}. *Chem. Mater.* **2019**, *31*, 5245−5253.

(5) Fang, Y.; Shang, J.; Liu, D.; Shi, W.; Li, X.; Ma, H. Design, Synthesis, and Application of a Small Molecular NIR-II Fluorophore with Maximal Emission beyond 1200 nm. *J. Am. Chem. Soc.* **2020**, *142*, 15271−15275.

(6) Wang, C.; Wang, X.; Zhou, Y.; Zhang, S.; Li, C.; Hu, D.; Xu, L.; Jiao, H. An Ultra-Broadband Near-Infrared Cr^{3+}-Activated Gallogermanate Mg$_3$Ga$_2$GeO$_8$ Phosphor as Light Sources for Food Analysis. *ACS Appl. Electron. Mater.* **2019**, *1*, 1046−1053.

(7) Hou, C.-C.; Chen, H.-M.; Zhang, J.-C.; Zhuo, N.; Huang, Y.-Q.; Hogg, R. A.; Childs, D. T.; Ning, J.-Q.; Wang, Z.-G.; Liu, F.-Q.; Zhang, Z.-Y. Near-Infrared and Mid-Infrared Semiconductor Broadband Light Emitters. *Light: Sci. Appl.* **2018**, *7*, 17170.

(8) Gaida, C.; Gebhardt, M.; Heuermann, T.; Stutzki, F.; Jauregui, C.; Antonio-Lopez, J.; Schulzgen, A.; Amezcua-Correa, R.; Tunnermann, A.; Pupeza, I.; Limpert, J. Watt-Scale Super-Octave Mid-Infrared Intrapulse Difference Frequency Generation. *Light: Sci. Appl.* **2018**, *7*, 94−101.

(9) Zhang, L.; Zhang, S.; Hao, Z.; Zhang, X.; Pan, G.-h.; Luo, Y.; Wu, H.; Zhang, J. A High-Efficiency Broad-Band Near-Infrared Ca$_2$LuZr$_2$Al$_3$O$_{12}$:Cr^{3+} Garnet Phosphor for Blue LED Chips. *J. Mater. Chem. C* **2018**, *6*, 4967−4976.

(10) Shao, Q.; Ding, H.; Yao, L.; Xu, J.; Liang, C.; Jiang, J. Photoluminescence Properties of a ScBO$_3$:Cr^{3+} Phosphor and Its Applications for Broadband Near-Infrared LEDs. *RSC Adv.* **2018**, *8*, 12035−12042.

(11) Shannon, R. D. Revised Effective Ionic Radii and Systematic Studies of Interatomic Distances in Halides and Chalcogenides. *Acta Crystallogr., Sect. A: Cryst. Phys., Diffr., Theor. Gen. Crystallogr.* **1976**, *32*, 751−767.

(12) Rietveld, H. M. A Profile Refinement Method for Nuclear and Magnetic Structures. *J. Appl. Crystallogr.* **1969**, *2*, 65−71.

(13) Henderson, B.; Imbusch, G. F. *Optical Spectroscopy of Inorganic Solids*; Oxford University Press: Oxford, UK, 2006.

(14) Finley, E.; Gaultois, M. W.; Brgoch, J. Unlocking the Key to Persistent Luminescence with X-Ray Absorption Spectroscopy: a Local Structure Investigation of Cr-Substituted Spinel-Type Phosphors. *Phys. Chem. Chem. Phys.* **2019**, *21*, 19349−19358.

(15) Chang, T. S.; Holzrichter, J. F.; Imbusch, G. F.; Schawlow, A. L. Polarized Fluorescence Study of Cr^{3+} Through a Stress-Induced Phase Transition in SrTiO$_3$. *Solid State Commun.* **1970**, *8*, 1179−1181.

(16) Grinberg, M. $^2E \rightarrow {}^4A_2$ Fluorescence of Cr^{3+} in High and Intermediate Field Garnets. *J. Lumin.* **1993**, *54*, 369−382.

(17) Fang, M.-H.; Li, T.-Y.; Huang, W.-T.; Cheng, C.-L.; Bao, Z.; Majewska, N.; Mahlik, S.; Yang, C.-W.; Lu, K.-M.; Leniec, G.; Kaczmarek, S. M.; Sheu, H.-S.; Liu, R.-S. Surface-Protected High-Efficiency Nanophosphors via Space-Limited Ship-in-a-Bottle Synthesis for Broadband Near-Infrared Mini-Light-Emitting Diodes. *ACS Energy Lett.* **2021**, *6*, 659−664.

(18) Fang, M.-H.; De Guzman, G. N. A.; Bao, Z.; Majewska, N.; Mahlik, S.; Grinberg, M.; Leniec, G.; Kaczmarek, S. M.; Yang, C.-W.; Lu, K.-M.; Sheu, H.-S.; Hu, S.-F.; Liu, R.-S. Ultra-High-Efficiency Near-Infrared Ga$_2$O$_3$:Cr^{3+} Phosphor and Controlling of Phytochrome. *J. Mater. Chem. C* **2020**, *8*, 11013−11017.

(19) He, H.; Orlando, R.; Blanco, M.; Pandey, R. First-Principles Study of The Structural, Electronic, and Optical Properties of Ga$_2$O$_3$ in Its Monoclinic and Hexagonal Phases. *Phys. Rev. B: Condens. Matter Mater. Phys.* **2006**, *74*, 195123.

(20) Grinberg, M.; Barzowska, J.; Shen, Y. R.; Bray, K. L. Inhomogeneous Broadening of Cr^{3+} Luminescence in Doped LiTaO$_3$. *Phys. Rev. B: Condens. Matter Mater. Phys.* **2001**, *63*, 214104.

(21) Grinberg, M.; Barzowska, J.; Shen, Y. R.; Bray, K. L.; Dereń, P.; Hanuza, J. High-Pressure Spectroscopy Characterization of LiSc(WO$_4$)$_2$ Crystals Doped with Trivalent Chromium. *J. Lumin.* **2003**, *102-103*, 699−704.

Chemical and Mechanical Pressure-induced Photoluminescence Tuning via Structural Evolution and Hydrostatic Pressure

Kuan-Chun Chen,[†] Mu-Huai Fang,[†] Wen-Tse Huang,[†] Mikołaj Kamiński,[Φ] Natalia Majewska,[Φ] Tadeusz Leśniewski,[Φ] Sebastian Mahlik,[Φ,*] Grzegorz Leniec,[Ψ] Sławomir M. Kaczmarek,[Ψ] Chia-Wei Yang,[£] Kuang-Mao Lu,[£] Hwo-Shuenn Sheu,[Ω] and Ru-Shi Liu[†,*]

[†]Department of Chemistry, National Taiwan University, Taipei 106, Taiwan

[Φ]Institute of Experimental Physics, Faculty of Mathematics, Physics and Informatics, University of Gdańsk, Wita Stwosza 57, 80-308 Gdańsk, Poland

[Ψ]Institute of Physics, Department of Mechanical Engineering and Mechatronics, West Pomeranian University of Technology, Szczecin, al. Piastow 48, 70-311 Szczecin, Poland

[£]Everlight Electronics Co., Ltd., New Taipei City 238, Taiwan

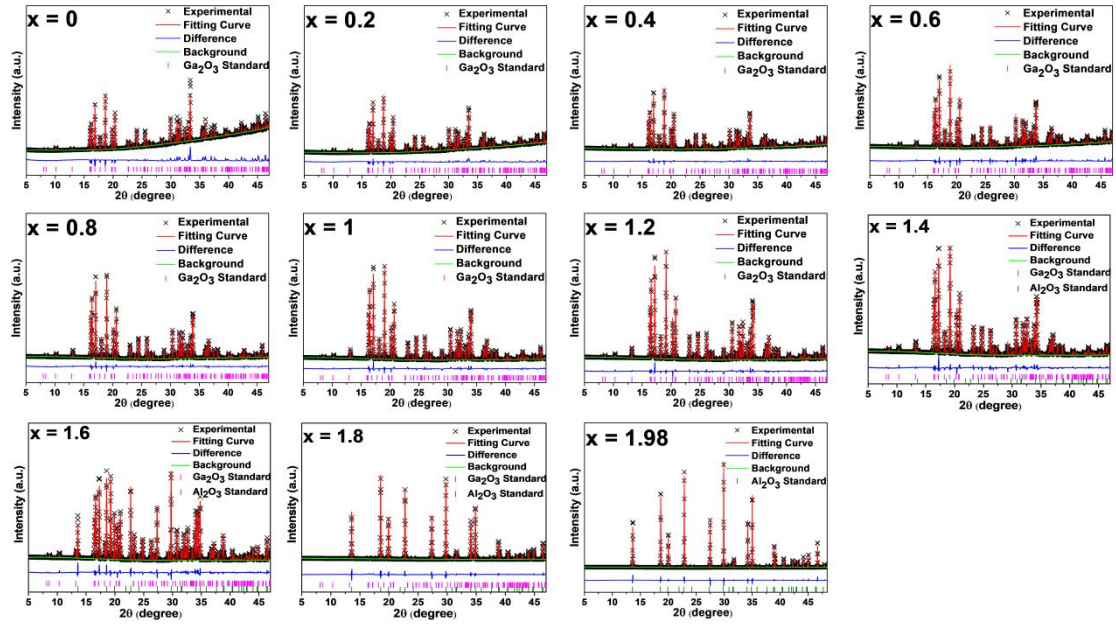[Ω]National Synchrotron Radiation Research Center, Hsinchu 300, Taiwan

Figure S1. Rietveld refinement patterns of $Ga_{1.98-x}Al_xO_3$:0.02Cr^{3+}.

Table S1. Atomic positions derived from Rietveld refinement of $Ga_{1.98-x}Al_xO_3$:0.02Cr^{3+}.

x = 0 (Ga₂O₃ phase)						x = 0.2 (Ga₂O₃ phase)				
Site	x	y	z	Occ	Beq (Å²)	Site	x	y	z	Occ	Beq (Å²)

Site	x	y	z	Occ	Beq (Å²)
Ga1	0.08913(34)	0	0.79008(87)	1	0.001563(16)
Ga2	0.34138(31)	0	0.68790(86)	1	0.001563(16)
O1	0.1637(14)	0	0.1029(53)	1	0.006250(46)
O2	0.4985(14)	0	0.2560(32)	1	0.006250(46)
O3	0.8315(13)	0	0.4389(53)	1	0.006250(46)

Site	x	y	z	Occ	Beq (Å²)
Ga1	0.08915(18)	0	0.79281(45)	0.9435(49)	0.001563(84)
Al1	0.08915(18)	0	0.79281(45)	0.0565(49)	0.001563(84)
Ga2	0.34124(16)	0	0.68785(45)	0.8565(49)	0.001563(78)
Al2	0.34124(16)	0	0.68785(45)	0.1435(49)	0.001563(78)
O1	0.16342(65)	0	0.1064(24)	1	0.06250(20)
O2	0.49938(69)	0	0.2568(15)	1	0.06250(20)
O3	0.82874(64)	0	0.4335(25)	1	0.06250(20)

x = 0.4 (Ga₂O₃ phase) Site	x	y	z	Occ	Beq (Å²)
Ga1	0.08966(13)	0	0.79387(32)	0.8659(26)	0.00625(48)
Al1	0.08966(13)	0	0.79387(32)	0.1341(26)	0.00625(48)
Ga2	0.34100(12)	0	0.68862(32)	0.7341(26)	0.00625(48)
Al2	0.34100(12)	0	0.68862(32)	0.2659(26)	0.00625(48)
O1	0.16306(43)	0	0.1149(13)	1	0.01250(71)
O2	0.49383(43)	0	0.25825(95)	1	0.01250(71)
O3	0.82718(42)	0	0.4215(14)	1	0.01250(71)

x = 0.6 (Ga₂O₃ phase) Site	x	y	z	Occ	Beq (Å²)
Ga1	0.09003(17)	0	0.79345(43)	0.7691(37)	0.003125(64)
Al1	0.09003(17)	0	0.79345(43)	0.2309(37)	0.003125(64)
Ga2	0.34129(16)	0	0.68822(42)	0.6309(37)	0.003125(69)
Al2	0.34129(16)	0	0.68822(42)	0.3691(37)	0.003125(69)
O1	0.16324(56)	0	0.1128(17)	1	0.01250(18)
O2	0.49346(57)	0	0.2594(13)	1	0.01250(18)
O3	0.82623(56)	0	0.4241(18)	1	0.01250(18)

x = 0.8 (Ga₂O₃ phase) Site	x	y	z	Occ	Beq (Å²)
Ga1	0.09087(13)	0	0.79443(32)	0.6804(20)	0.003125(38)
Al1	0.09087(13)	0	0.79443(32)	0.3196(20)	0.003125(38)
Ga2	0.34112(12)	0	0.68751(31)	0.5196(20)	0.003125(42)
Al2	0.34112(12)	0	0.68751(31)	0.4804(20)	0.003125(42)
O1	0.16377(39)	0	0.1114(12)	1	0.01250(53)
O2	0.49076(39)	0	0.25861(84)	1	0.01250(53)
O3	0.82568(39)	0	0.4237(12)	1	0.01250(53)

x = 1 (Ga₂O₃ phase) Site	x	y	z	Occ	Beq (Å²)
Ga1	0.09155(14)	0	0.79474(34)	0.5851(18)	0.01250(37)
Al1	0.09155(14)	0	0.79474(34)	0.4149(18)	0.01250(37)
Ga2	0.34125(13)	0	0.68665(34)	0.4149(18)	0.05341(41)
Al2	0.34125(13)	0	0.68665(34)	0.5851(18)	0.05341(41)
O1	0.16417(38)	0	0.1117(12)	1	0.03392(52)
O2	0.48857(38)	0	0.25745(82)	1	0.03392(52)
O3	0.82473(39)	0	0.4235(12)	1	0.03392(52)

x = 1.2 (Ga₂O₃ phase) Site	x	y	z	Occ	Beq (Å²)
Ga1	0.09184(15)	0	0.79468(35)	0.4747(17)	0.01250(40)
Al1	0.09184(15)	0	0.79468(35)	0.5253(17)	0.01250(40)
Ga2	0.34146(13)	0	0.68628(34)	0.3253(17)	0.03923(44)
Al2	0.34146(13)	0	0.68628(34)	0.6747(17)	0.03923(44)
O1	0.16438(36)	0	0.1091(11)	1	0.07251(48)
O2	0.48937(36)	0	0.25668(76)	1	0.07251(48)
O3	0.82549(36)	0	0.4256(11)	1	0.07251(48)

x = 1.4 (Ga₂O₃ phase) Site	x	y	z	Occ	Beq (Å²)
Ga1	0.09199(16)	0	0.79498(38)	0.3623(16)	0.04548(44)
Al1	0.09199(16)	0	0.79498(38)	0.6377(16)	0.04548(44)
Ga2	0.34147(14)	0	0.68585(36)	0.2377(16)	0.2315(51)
Al2	0.34147(14)	0	0.68585(36)	0.7623(16)	0.2315(51)
O1	0.16435(34)	0	0.1100(11)	1	0.2736(52)
O2	0.48833(34)	0	0.25554(71)	1	0.2736(52)
O3	0.82588(34)	0	0.4253(11)	1	0.2736(52)

x = 1.6 (Ga₂O₃ phase) Site	x	y	z	Occ	Beq (Å²)
Ga1	0.09215(26)	0	0.79670(63)	0.2565(24)	0.02024(71)
Al1	0.09215(26)	0	0.79670(63)	0.7435(24)	0.02024(71)
Ga2	0.34191(23)	0	0.68512(61)	0.1435(24)	0.1718(85)
Al2	0.34191(23)	0	0.68512(61)	0.8565(24)	0.1718(85)
O1	0.16306(48)	0	0.1090(15)	1	0.7226(80)
O2	0.48932(48)	0	0.2560(10)	1	0.7226(80)
O3	0.82621(48)	0	0.4281(15)	1	0.7226(80)

(Al₂O₃ phase) Site	x	y	z	Occ	Beq (Å²)
Al1	0	0	0.35286(12)	0.8842(31)	0.0638(46)
Ga1	0	0	0.35286(12)	0.1158(31)	0.0638(46)
O1	0.30665(69)	0	0.25	1	0.1135(65)

x = 1.8 (Al₂O₃ phase) Site	x	y	z	Occ	Beq (Å²)
Al1	0	0	0.352873(63)	0.9227(36)	0.4227(33)
Ga1	0	0	0.352873(63)	0.0773(36)	0.4227(33)
O1	0.30651(31)	0	0.25	1	0.4889(68)

x = 1.98 (Al₂O₃ phase) Site	x	y	z	Occ	Beq (Å²)
Al1	0	0	0.352111(52)	1	0.3084(20)
O1	0.30650(21)	0	0.25	1	0.2399(26)

Table S2. Refinement results derived from refinement of $Ga_{1.98-x}Al_xO_3:0.02Cr^{3+}$.

	Ga2O3 phase								Mix phase		Al2O3 phase	
x	0	0.2	0.4	0.6	0.8	1.0	1.2	1.4	1.6	1.6	1.8	1.98
a (Å)	12.22591(39)	12.18203(23)	12.13875(17)	12.09367(22)	12.05027(14)	12.00772(16)	11.95882(15)	11.92067(23)	11.89103(22)	4.788693(56)	4.782032(50)	4.761958(32)
b (Å)	3.041178(93)	3.028081(54)	3.012994(40)	3.000698(52)	2.986317(32)	2.973259(35)	2.960104(33)	2.948851(51)	2.941952(49)	-	-	-
c (Å)	5.80938(18)	5.79222(11)	5.771885(81)	5.75511(10)	5.735153(62)	5.716881(69)	5.697569(67)	5.68102(10)	5.67000(10)	13.05508(20)	13.04289(19)	13.00378(12)
β (°)	103.8456(22)	103.8933(12)	103.93099(90)	103.9658(12)	103.99135(71)	104.01532(76)	104.03854(76)	104.0521(11)	104.0664(13)	-	-	-
V	209.723(12)	207.4135(68)	204.8915(50)	202.6763(64)	200.2618(39)	198.0285(42)	195.6664(41)	193.7248(62)	192.4051(60)	259.2652(72)	258.3030(66)	255.3709(41)
Ga2O3 phase (%)	100	100	100	100	100	100	100	96.97(25)	63.39(14)	63.39(14)	0	0
Al2O3 phase (%)	0	0	0	0	0	0	0	3.03(25)	36.61(14)	36.61(14)	100	100
χ^2	1.95	1.29	0.75	1.31	0.76	0.85	0.94	1.25	1.46	1.46	1.47	1.38
R_{wp} (%)	2.61	1.43	0.90	1.62	1.17	1.39	1.59	2.10	2.42	2.42	4.97	7.71
R_p (%)	1.67	0.97	0.62	1.01	0.79	0.91	1.06	1.37	1.57	1.57	3.24	5.70

Table S3. Distortion indexes in $Ga_{1.98-x}Al_xO_3:0.02Cr^{3+}$.

Samples	Ga2O3 phase (IV / VI)	Al2O3 phase (VI)
x = 0	0.00434 / 0.03398	-
x = 0.2	0.00370 / 0.03701	-
x = 0.4	0.01223 / 0.04469	-
x = 0.6	0.00940 / 0.04110	-
x = 0.8	0.00858 / 0.03827	-
x = 1	0.01066 / 0.03811	-
x = 1.2	0.00797 / 0.03299	-
x = 1.4	0.00963 / 0.03295	0.00912
x = 1.6	0.00785 / 0.02897	0.03354
x = 1.8	-	0.03345
x = 1.98	-	0.03069

Table S4. Linear shift parameters for optical transitions in $Ga_{1.98-x}Al_xO_3:0.02Cr^{3+}$.

	x < 1.6		x > 1.6	
	$E(x = 0)$ (cm^{-1})	dE/dx (cm^{-1})	$E(x = 0)$ (cm^{-1})	dE/dx (cm^{-1})
$E\ (^4A_2 \rightarrow {}^4T_1)$	22 612	433	18 595	3 040
$E\ (^4A_2 \rightarrow {}^4T_2)$	16 463	330	13 198	2 326
$E\ (^2E \rightarrow {}^4A_2)\ (R_1)$	14 325	-14.5	14 220*	-8.7*
$E\ (^2E \rightarrow {}^4A_2)\ (R_2)$	14 493	58.0		

*The R_1-R_2 splitting was not observed in the Al_2O_3 crystal phase.

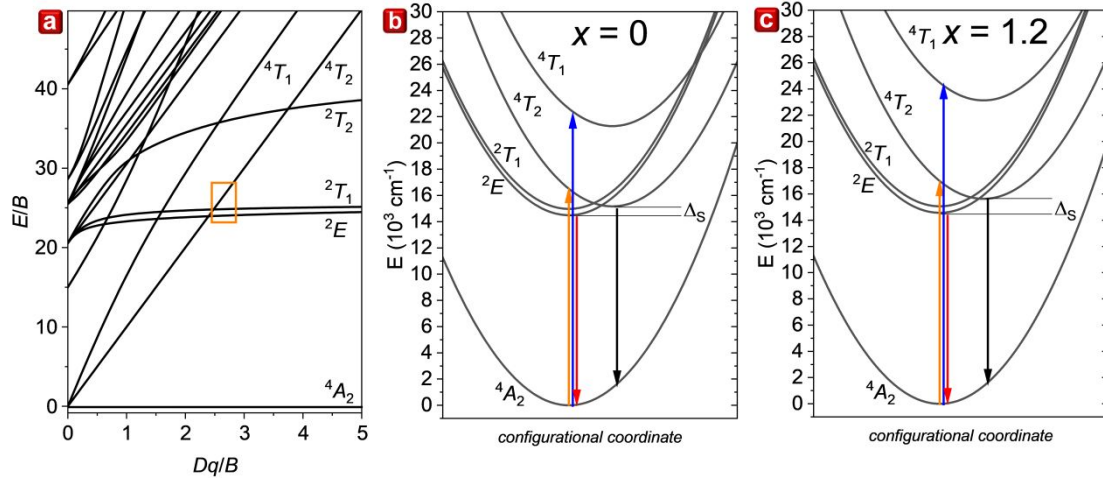Figure S2. (a) Tanabe–Sugano diagram for Cr^{3+} ions. The orange rectangle denotes the approximate region of parameters spanned by $Ga_{1.98-x}Al_xO_3{:}0.02Cr^{3+}$. Configurational coordinate diagrams for samples of x = 0 (b) and x = 1.2 (c), blue and orange arrows denote the $^4A_2 \rightarrow {}^4T_1$ and $^4A_2 \rightarrow {}^4T_2$ transition from PLE spectra, and red and black arrows denote the $^2E \rightarrow {}^4A_2$ and $^4T_2 \rightarrow {}^4A_2$ transition from PL spectra.

Crystal Field Calculation:

The crystal field parameter *Dq* describes the interactions between 3*d* electrons and ligands ions. Racah parameters *B* and *C* describe the interaction between 3*d* electrons in Cr^{3+} ions. The energy of the excitation band maximum of $^4A_2 \rightarrow {}^4T_2$ transition is equal to 10*Dq*. Racah parameters *B* and *C* can be calculated from the following equations:[1]

$$B = Dq\frac{\left[\frac{\Delta E}{Dq}\right]^2 - 10\frac{\Delta E}{Dq}}{15(\frac{\Delta E}{Dq} - 8)}, \tag{S1}$$

$$C = \frac{B}{3.05}\left\{\frac{E(^2E)}{B} - 7.9 + 1.8\frac{B}{Dq}\right\}, \tag{S2}$$

where ΔE is the difference between the energy of the $^4A_2 \rightarrow {}^4T_1$ and $^4A_2 \rightarrow {}^4T_2$ transitions. The energy values of the $^4A_2 \rightarrow {}^4T_1$ and $^4A_2 \rightarrow {}^4T_2$ transitions were obtained from the maximum of the corresponding excitation band, and the value of $^2E \rightarrow {}^4A_2$ transition was measured from the PL spectrum (R1 line emission).
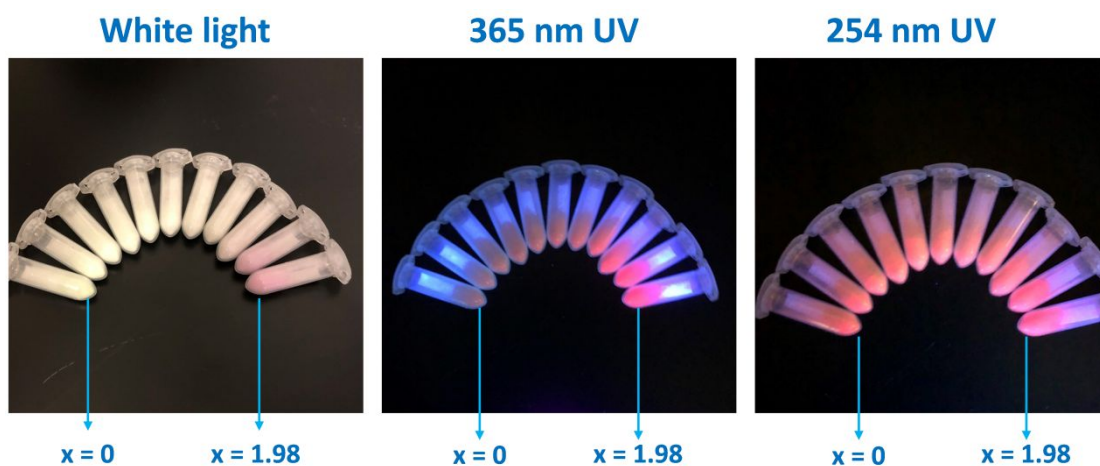
Figure S3. Sample appearance of $Ga_{1.98-x}Al_xO_3$:0.02Cr^{3+}.

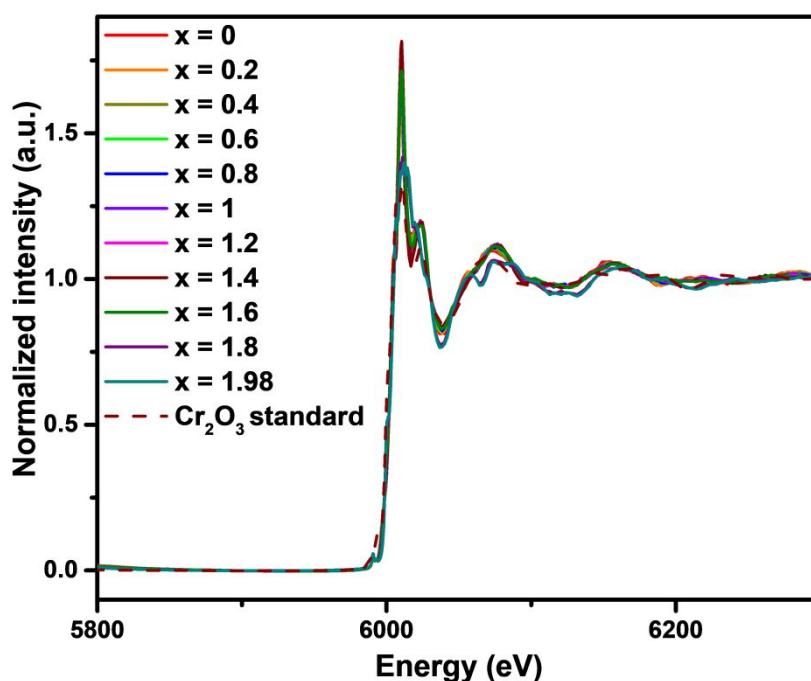Figure S4. Cr *K-edge* X-ray absorption near-edge structure (XANES) spectra of $Ga_{1.98-x}Al_xO_3$:0.02Cr^{3+}.

Pressure-dependent Decay Time Analysis:

Pressure-dependent decay profiles for samples of x = 0.4, 1.6 up to 250 kbar, and upon excitation at 440 nm are shown in Figures S5a and S5b, respectively. The pressure-dependent decay profiles were taken from the emission range 660–700 nm. For x = 1.6, the decay profiles are nearly single exponential in all pressure range. For sample x = 0.4 the decay remains as single exponential under pressure up to 145 kbar and becomes non-exponential for higher pressure. The decay curves for the lower pressure in the case of x = 0.4 and all considered pressure levels for the sample of x =

1.6 were fitted by eq. (2). The obtained decay times as a function of pressure are presented in Figure S5c for x = 0.4 (red dots) and x = 1.6 (black dots). For the sample of x = 0.4 under pressure 145 kbar and higher, the average time decays τ_{av} were calculated using the following formula:

$$\tau_{av} = \frac{\int I(t)t\,dt}{\int I(t)dt} \quad, \tag{S3}$$

where $I(t)$ is the intensity of the signal. These time decay values are presented in Figure.S5c as green dots. The pressure-induced increment of crystal field strength increases the difference between the $^4T_2$ and ^2E excited energy levels and reduces the occupancy of the higher $^4T_2$ state from ^2E. Given that the $^2E \rightarrow {}^4A_2$ transition is spin-forbidden, the line luminescence takes place mainly due to the spin–orbit coupling between ^2E and $^4T_2$ excited states. Depending on the distance between the ^2E and $^4A_2$ states, spin–orbit coupling will decrease with the increasing pressure. Therefore, both effects increase the lifetime of the $^2E \rightarrow {}^4A_2$ line luminescence (probability of transition decrease) under increasing pressure.

This relation works until the pressure p_c = 120 kbar for x = 0.4 and p_c = 103 kbar for x = 1.6 are reached. Above this pressure, the decay time starts to decrease possibly due to the pressure-induced phase transition of Ga_2O_3 as mentioned in the main article. The Cr^{3+} ions in this new trigonal phase decay relatively fast. Under the pressure ranging from 120 kbar to 195 kbar for x = 0.4, a mixed-phase of β-Ga_2O_3 and α-Ga_2O_3 occurs. The shortening of decay times in this region is caused by the increase in the component of the α-Ga_2O_3 crystallographic phase, in which Cr^{3+} ions decay rapidly. Similar behavior is observed for the sample of x = 1.6. By contrast, the dropping of decay times value occurs in low pressure (80–147 kbar) according to the phase transition. For pressure higher than 147 kbar, the increasing decay time is observed again. For this pressure, no mixed-phase occurs, and only a new high-pressure phase and the increase in decay time. These results suggest that the pressure value for x = 0.4 sample to occur in the new phase was not reached. With further increase in pressure, the time decay τ would also increase again.
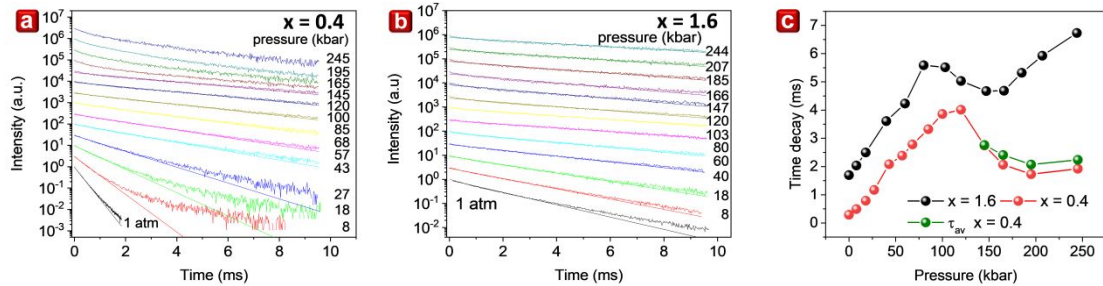

Figure S5. Pressure-dependent decay profiles for samples of (a) x = 0.4 and (b) x = 1.6 under pressure 1 atm–245 kbar, (c) time decay value as a function of pressure for x =

0.4 and x = 1.6.

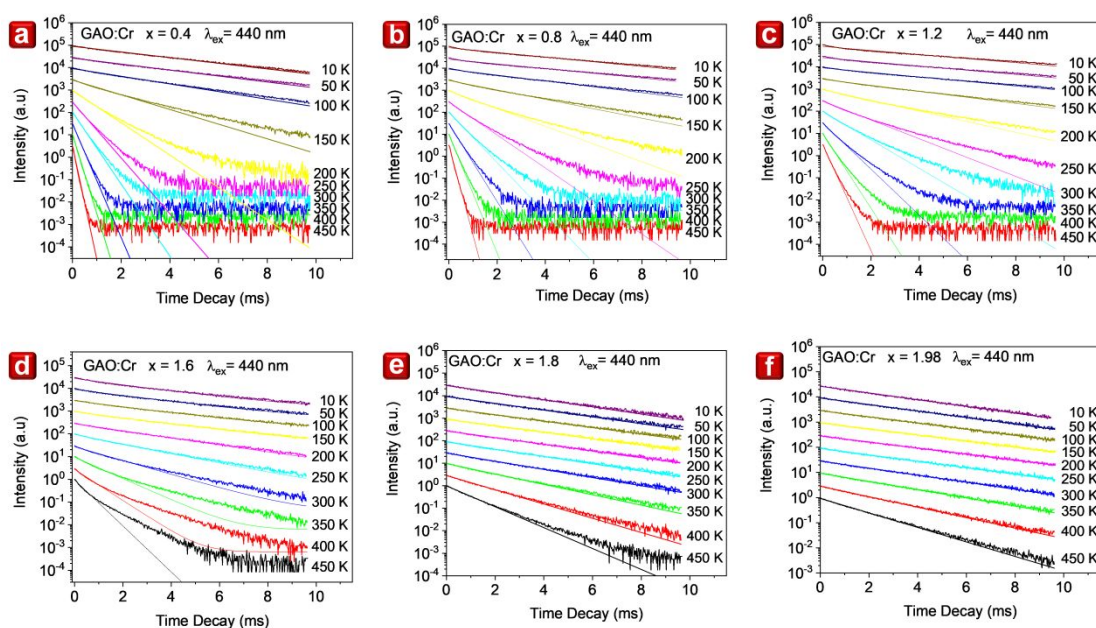Figure S6. Temperature-dependent decay profiles under 440 nm excitation for (a) x = 0.4, (b) x = 0.8, (c) x = 1.2, and (d) x = 1.6, (e) x = 1.8, and (f) x = 1.98.

Table S5. Fitting parameters for temperature-dependent decay time results.

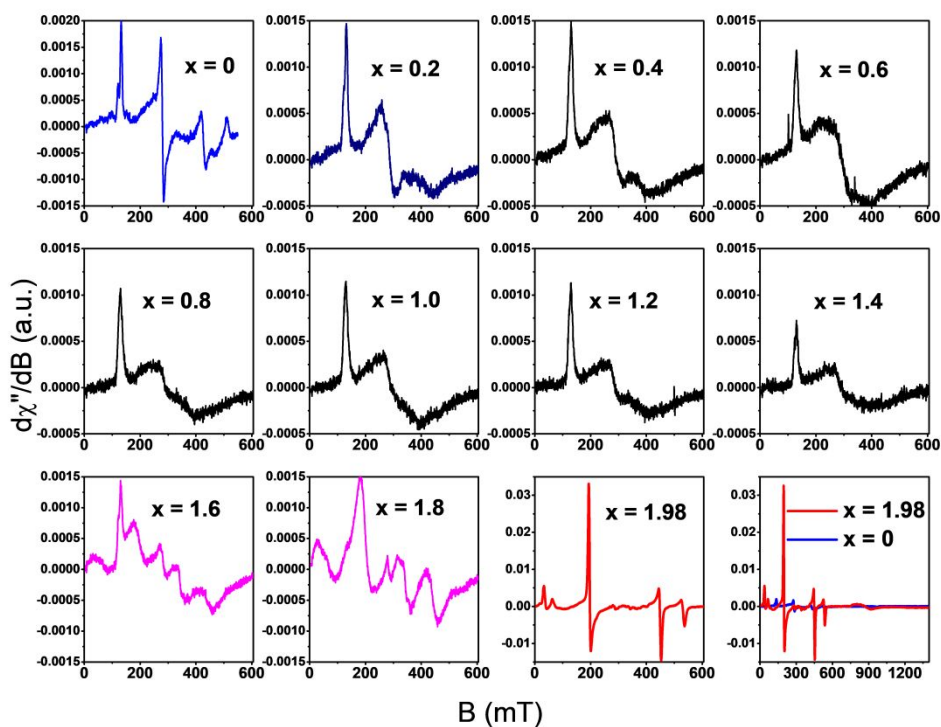| x	0.4	0.8	1.2	1.6	1.8	1.98
τ_T (ms)	0.089	0.108	0.102	0.057	0.046	0.051
τ_0 (ms)	3.45	3.97	4.56	3.08	2.91	3.46
Δ (cm^{-1})	414	475	602	1012	1408	1581

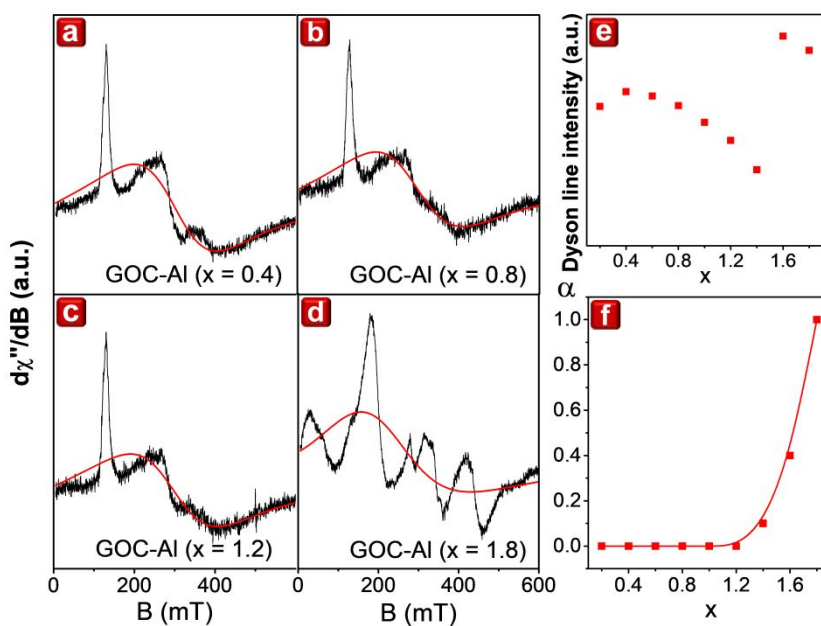Figure S7. Room-temperature electron paramagnetic resonance (EPR) spectra of $Ga_{1.98-x}Al_xO_3{:}0.02Cr^{3+}$.

Figure S8. Fitting results of the Dyson equation to experimental data of coexistence samples: (a) x = 0.4, (b) x = 0.8, (c) x = 1.2, and (d) x = 1.8. Relationships between (e) asymmetry parameter α, and (f) the integrated intensity of the Dyson signal with respect to the Al^{3+} concentration.

Reference:

(1) Merrill, L.; Bassett, W. A. Miniature Diamond Anvil Pressure Cell for Single Crystal X-Ray Diffraction Studies. *Rev. Sci. Instr.* **1974**, *45*, 290–294.

[P3]

Fang, M.-H.; Chen, K.-C.; **Majewska, N.**; Leśniewski, T.; Mahlik, S.; Leniec, G.; Kaczmarek, S. M.; Yang, C.-W.; Lu, K.-M.; Sheu, H.-S.; Liu, R.-S. Hidden Structural Evolution and Bond Valence Control in Near-Infrared Phosphors for Light-Emitting Diodes. *ACS Energy Lett.* **2021**, *6* (1), 109-114.

LETTER

Hidden Structural Evolution and Bond Valence Control in Near-Infrared Phosphors for Light-Emitting Diodes

Mu-Huai Fang, Kuan-Chun Chen, Natalia Majewska, Tadeusz Leśniewski, Sebastian Mahlik, Grzegorz Leniec, Slawomir M. Kaczmarek, Chia-Wei Yang, Kuang-Mao Lu, Hwo-Shuenn Sheu, and Ru-Shi Liu*

Cite This: *ACS Energy Lett.* 2021, 6, 109−114

Read Online

ACCESS | Metrics & More | Article Recommendations | SI Supporting Information

ABSTRACT: We aim to conduct a complete study on the unexpected structure evolution behavior in Cr^{3+}-doped phosphors. A series of $Ga_{2-x}Sc_xO_3:Cr^{3+}$ phosphors are successfully synthesized and confirmed through structural studies, while the lattice parameters change unexpectedly. The unique partial substitution (∼87%) of Sc^{3+} in the octahedral site is demonstrated via Rietveld refinement. Therefore, the bond valence sum calculation explains the reason for this particular Sc^{3+} concentration. The photoluminescent bandwidth and electron−lattice coupling energy initially increase and then decrease, implying an inhomogeneous broadening effect. Time-resolved spectra and electron paramagnetic resonance are utilized to further examine the subtle change in the microstructures and the second coordination sphere effect of Cr^{3+}. $Ga_{1.594}Sc_{0.4}O_3:0.006Cr^{3+}$ exhibits high internal quantum efficiency (99%) and high phosphor-converted light-emitting diode output power (66.09 mW), demonstrating its capability as an outstanding infrared phosphor. This work will motivate further research on unexpected partial substitution during the solid solution process.
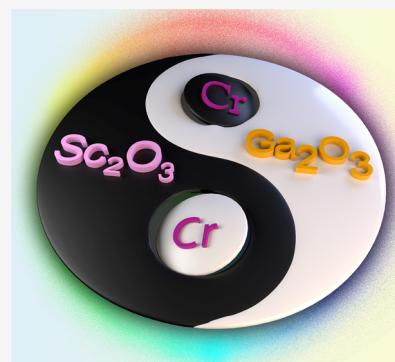
Infrared (IR) luminescent materials have elicited considerable attention and have been utilized in biomolecular imaging, biomodulation, food analysis, and plant cultivation.[1−6] Recently, phosphor-converted IR light-emitting diodes (pc-IR LEDs) have evolved into smart devices with the advantages of high output power, high efficiency, and small size.[7−9] Therefore, IR phosphor materials are crucial components of these devices, affecting the overall performance of the resulting spectrum. Cr^{3+}, as a unique and ideal near-IR (NIR) emitter that can produce either sharp-line or broadband spectra, has become a promising candidate for producing IR light. Although substantial progress has been achieved in this popular topic, most studies have focused on a single compound or on changing activators without systematically tuning the crystal structure and the luminescent wavelength.[10−15] Consequently, understanding the control mechanism is considered an important issue in tuning luminescent properties. A solid solution method is an efficient approach for tuning a material's properties by combining the characteristics of both ends. It is widely utilized in materials science. The evolution of the structural and photoluminescent properties within two ends is generally predictable. Nevertheless, some local structural distortions or phase transitions may result in unexpected photoluminescent properties. Previous studies

have demonstrated some of the mechanisms that explain the unpredictable properties of Eu^{2+}-doped phosphors, such as $Sr(LiAl_3)_{1-x}(SiMg_3)_xN_4:Eu^{2+}$, $(Sr_{1-x}Ba_x)Si_2O_2N_2:Eu^{2+}$, and $Sr_xBa_{2-x}SiO_4:Eu^{2+}$;[16−18] however, research that focuses on Cr^{3+}-doped IR phosphor remains rare. Compared with Eu^{2+}-doped phosphors, Cr^{3+}-doped phosphors exhibit completely different structural behavior and luminescent behavior during the solid solution process. In general, Cr^{3+} strongly prefers occupying octahedral coordination sites. Moreover, a subtle change in the local structure may tune photoluminescence between sharp-line or broadband emissions. This phenomenon has been seldom discussed in previous studies. The overall tuning mechanism remains vague. In the current work, a series of $Ga_{1.994-x}Sc_xO_3:0.006Cr^{3+}$ ($Ga_{2-x}Sc_xO3:Cr^{3+}$) phosphors are synthesized and their unique structural and photoluminescent

properties are characterized, demonstrating their high potential in IR-LED applications.

The synchrotron X-ray diffraction (XRD) patterns of $Ga_{2-x}Sc_xO_3:Cr^{3+}$ phosphors with different Sc^{3+} concentrations are shown in Figure 1a. The pure phase can be obtained at $x =$
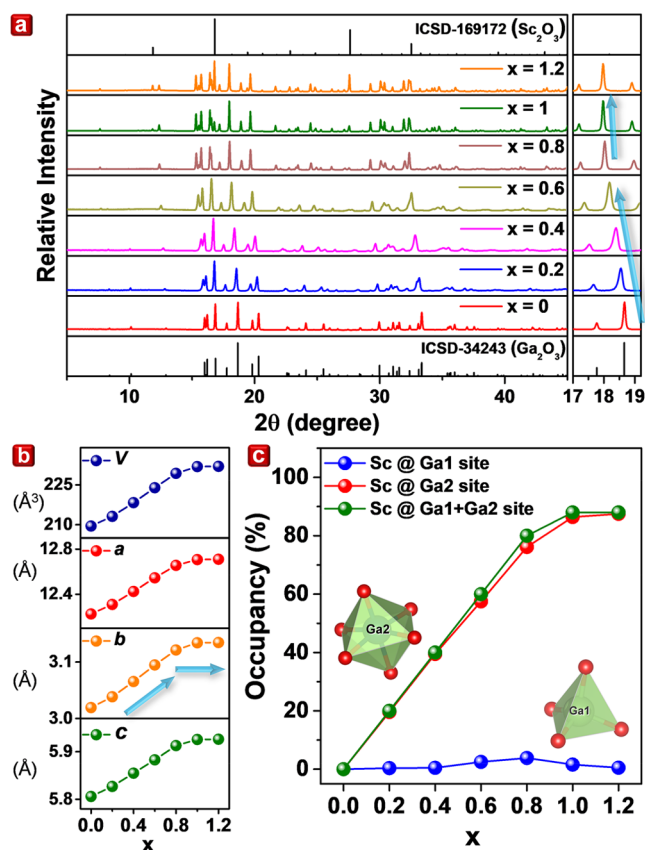

Figure 1. Structural analysis of $Ga_{2-x}Sc_xO_3:Cr^{3+}$ ($x = 0, 0.2, 0.4, 0.6, 0.8, 1.0,$ and 1.2). (a) Synchrotron XRD patterns, (b) refined lattice parameter, and (c) occupancy of Sc^{3+} ions in the Ga1, Ga2, and Ga1+Ga2 sites.

0−0.8, while Sc_2O_3 impurities exist at $x = 1$ and 1.2. Meanwhile, the diffraction peaks shift toward the lower angle with the incorporation of Sc^{3+} ions due to the larger ionic size of Sc^{3+} (0.745 Å; CN = 6) than that of Ga^{3+} (0.47 Å; CN = 6) (CN denotes coordinated number).[19] Unexpectedly, the

diffraction peaks do not shift linearly when $x > 0.8$. This finding may indicate the failure of the Sc^{3+} doping process when $x > 0.8$. To investigate this unique behavior in-depth, Rietveld refinements of $Ga_{2-x}Sc_xO_3:Cr^{3+}$ are conducted and analyzed, as shown in Figure S1 and Tables S1 and S2.[20] The lattice parameters, namely, a, b, c, and V, are linearly increased for $x = 0−0.8$, as shown in Figure 1b. Nevertheless, ascendant speed slows down from $x = 0.8−1.0$ and even stops increasing from $x = 1.0−1.2$. To understand this property, the crystal structure and local coordinated environment of Ga_2O_3 should be carefully examined. Ga_2O_3 possesses a monoclinic structure with a space group of $C2/m$. Two different Ga^{3+} sites, namely, Ga1 and Ga2, are found in the Ga_2O_3 structure. Ga2 is coordinated by six O^{2-} forming octahedron, and Ga1 is coordinated by four O^{2-} forming tetrahedron (Figure S2). Given the similar ionic radii of Ga2 (0.62 Å; CN = 6) and Cr^{3+} (0.615 Å; CN = 6), Cr^{3+} can be incorporated into the Ga2 site. When introducing Sc^{3+} into the Ga1 and Ga2 sites, the actual maximum obtainable amounts of Sc^{3+} in the $Ga_{2-x}Sc_xO_3:Cr^{3+}$ of $x = 1.0$ and 1.2 are 0.880, as calculated from the Rietveld refinement, proving that Sc^{3+} can no longer be incorporated into the host (Table S1). Moreover, when Sc^{3+} ions are doped into the Ga_2O_3 structure, a strongly preferred occupation of Sc^{3+} ions at the Ga2 site is observed due to the larger polyhedral volume at the Ga2 site, as shown in Figure 1c. The maximum doping occupation value at Ga2 is approximately 0.87, indicating that Sc^{3+} cannot completely occupy the Ga2 site. This result will lead to the random distribution of Ga^{3+} and Sc^{3+} ions at the Ga2 site, further affecting the photoluminescent properties.

The preferred occupation of Sc^{3+} ions can also be observed and explain using the bond valence sum (BVS), as shown in Figure 2a.[18,21] For $x = 0$, Sc^{3+} is seriously overbonded with a BVS value higher than +3 (~+4) in the Ga1 and Ga2 sites, denoted as Sc(Ga1) and Sc(Ga2). When the Sc^{3+} concentration starts to increase, the BVS values of Ga(Ga1) and Sc(Ga1) change minimally, and those of Ga(Ga2) and Sc(Ga2) exhibit a continuous decrease. Therefore, Ga(Ga2) becomes gradually underbonded and moves away from its ideal BVS value (+3). By contrast, Sc(Ga2), which originally has an inappropriate BVS value (~+4), gradually decreases and finally approaches ~+3. These results further prove our assumption that Sc^{3+} will exhibit a highly preferred occupation at the Ga2 site. Notably, for $x = 0.4−1.0$, the BVS value of Sc(Ga2) significantly decreases and finally approaches ~+3 ($x = 1.0$),
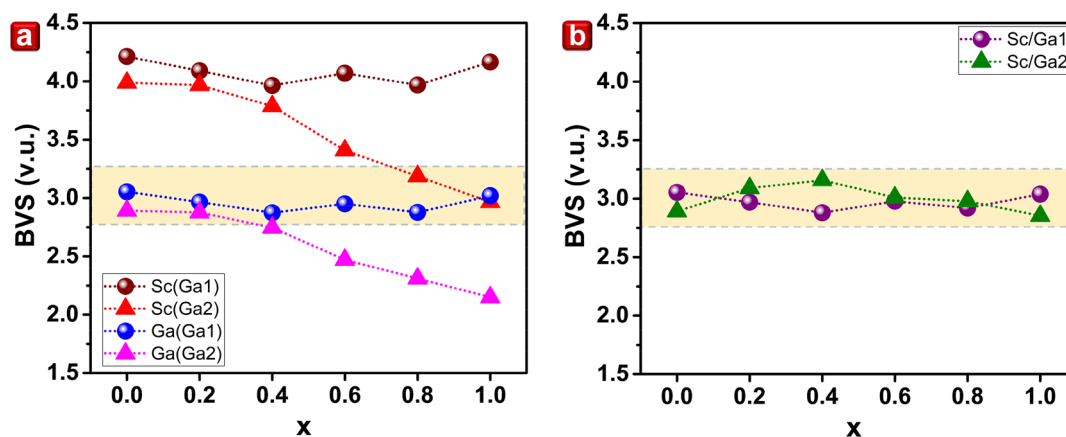

Figure 2. BVS of $Ga_{2-x}Sc_xO_3:Cr^{3+}$ ($x = 0, 0.2, 0.4, 0.6, 0.8,$ and 1.0). (a) BVSs and (b) occupancy-corrected BVSs.

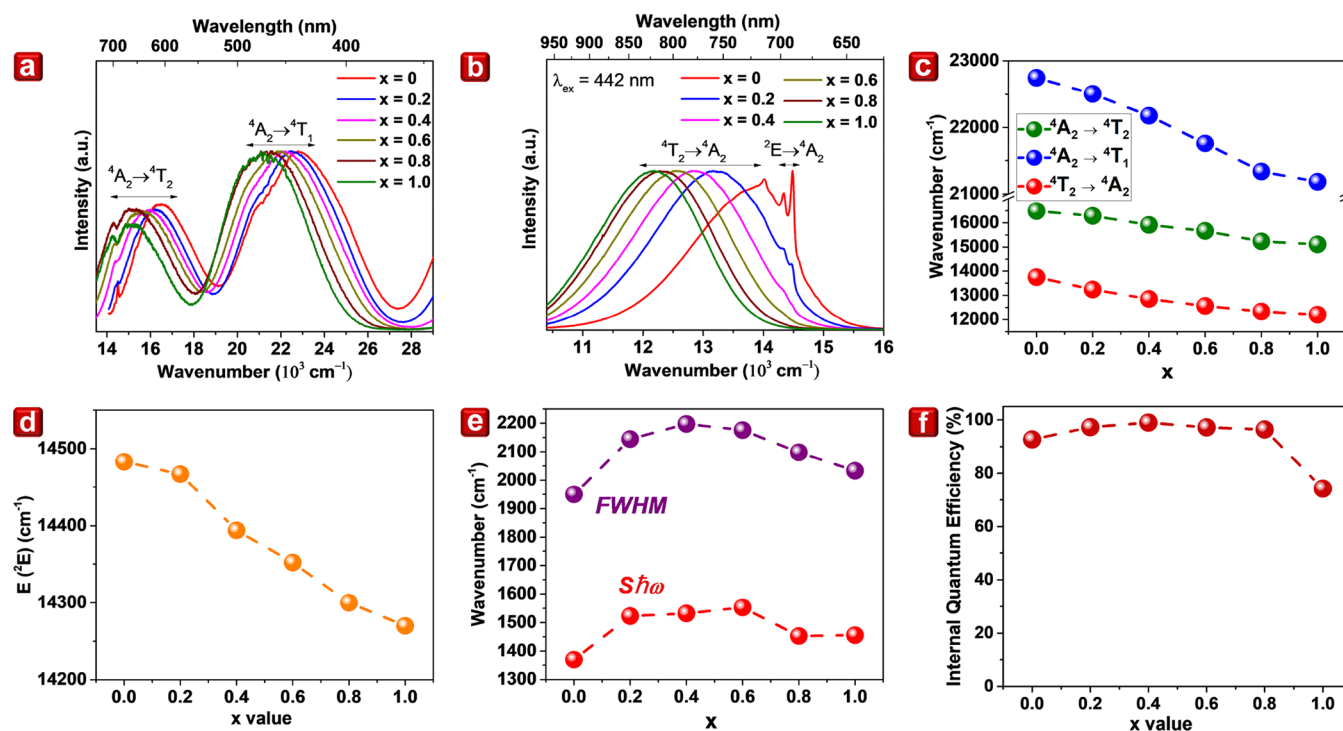**Figure 3.** Photoluminescent properties of $Ga_{2-x}Sc_xO_3:Cr^{3+}$ (x = 0, 0.2, 0.4, 0.6, 0.8, and 1.0). RT (a) PLE spectra upon observation at maximum luminescence, (b) emission spectra upon excitation at 442 nm, (c) position of excitation and emission band, (d) position of ^2E excitation, and (e) fwhm of broadband emission (purple dots) and $S\hbar\omega$ (red dots), and (f) IQE.

which is the ideal value for Sc^{3+} and Ga^{3+}. If Sc^{3+} is further incorporated into the structure, the BVS value may continuously decrease and move away from its ideal value. This phenomenon may explain why we cannot obtain the pure phase of the x = 1.2 sample. Considering the practical occupation values calculated from the Rietveld refinement shown in Figure 1c, the adjusted BVS value with different Sc^{3+} concentrations is then generated, as shown in Figure 2b. For all the samples, changing the Sc^{3+}/Ga^{3+} ratio between the Ga1 and Ga2 sites can balance the deviation in their BVS value. Neither Sc/Ga(Ga1) nor Sc/Ga(Ga2) is highly overbonded or underbonded. The occupancy-corrected BVS values are closed to +3 throughout the entire series. This finding indicates that $Ga_{2-x}Sc_xO_3:Cr^{3+}$ can have a rigid structure, which further affects its thermal stability.[18]

To elucidate the relationship between the local structure and photoluminescent properties, the room temperature (RT) photoluminescence excitation (PLE) spectra of $Ga_{2-x}Sc_xO_3:Cr^{3+}$ for x = 0, 0.2, 0.4, 0.6, 0.8, and 1.0 upon observation at the maximum luminescence and excitation at 442 nm are obtained, as shown in Figure 3a. The PLE spectrum of each compound is composed of two excitation bands that are typical for Cr^{3+} ions in 6-fold octahedral coordination. The higher energy band ($\sim$22000 cm^{-1}, 450 nm) corresponds to the $^4A_2 \rightarrow {}^4T_1$ transition, and the lower energy band ($\sim$16000 cm^{-1}, 650 nm) corresponds to the $^4A_2 \rightarrow {}^4T_2$ transition of Cr^{3+} ions. The red shift of the excitation spectra is observed with increasing Sc^{3+} concentration. Upon the excitation of the $Ga_{2-x}Sc_xO_3:Cr^{3+}$ samples at 442 nm, two distinct emissions with varying proportions are visible in the emission spectrum: a narrow line emission at approximately 700 nm and a broadband emission in the longer wavelengths (Figure 3b). The line emission at 14331 cm^{-1} (697 nm) and 14484 cm^{-1} (690 nm) corresponds to the $^2E \rightarrow {}^4A_2$ spin-

forbidden transition, i.e., R_1 and R_2 lines, respectively. The broadband emission extending from 650 to 950 nm, with a maximum at 720−850 nm, corresponds to the $^4T_2 \rightarrow {}^4A_2$ spin-allowed transition of Cr^{3+} ions. The intensity of the narrow-line emission is prominent for the x = 0 sample, but it diminishes rapidly with increasing Sc^{3+} content and becomes undetectable for $x \geq 0.8$. Simultaneously, the peak wavelength of $^4T_2 \rightarrow {}^4A_2$ emission shifts steadily toward longer wavelengths changing from 720 to 830 nm. The shift of the maxima of the PLE bands with increasing Sc^{3+} concentration for $^4A_2 \rightarrow {}^4T_1$ (blue) and $^4A_2 \rightarrow {}^4T_2$ (green) and the shift of the $^4T_2 \rightarrow {}^4A_2$ emission spectra (red dots) are presented in Figure 3c. Moreover, the position of ^2E excitation versus Sc^{3+} concentration is shown in Figure 3d, and that of the full width at half-maximum (fwhm) and electron−lattice coupling energy ($S\hbar\omega$) versus Sc^{3+} concentration is shown in Figure 3e. The fwhm for x = 0 is approximately 1723.5 cm^{-1}, and a significant increase is observed in the sample codoped with Sc^{3+} up to x = 0.4. Meanwhile, the fwhm decreases slightly when Sc^{3+} concentration is further increased. This effect is related to the inhomogeneous broadening of the PLE band resulting in the distribution of Dq values, which reach the maximum for x = 0.4. The calculation is discussed in detail in the Supporting Information. The internal quantum efficiency (IQE) of $Ga_{2-x}Sc_xO_3:Cr^{3+}$ (x = 0, 0.2, 0.4, 0.6, 0.8, and 1.0) is also measured, as shown in Figure 3f. The IQE values for x = 0−0.8 are higher than 90%, but it decreases significantly for x = 1.0 due to the existence of the Sc_2O_3 impurity phase. The sample of x = 0.4 even accounts for 99% of the IQE value, indicating that this specific formula, $Ga_{1.594}Sc_{0.4}O_3:0.006Cr^{3+}$, can be a promising candidate for practical applications.

To reveal the photoluminescent properties further, time-resolved photoluminescent spectra at 10 K upon excitation at 440 nm are captured using a streak camera, as shown in Figure
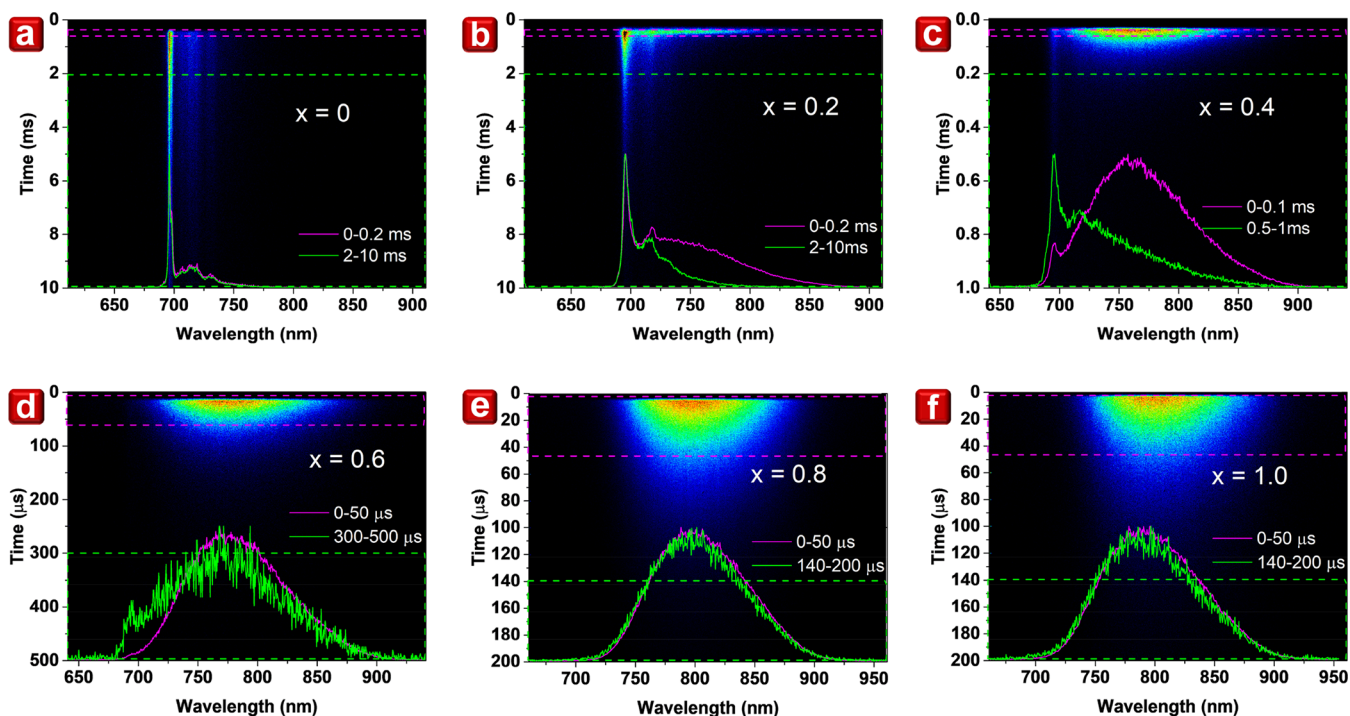
Figure 4. Streak camera image at 10 K with the time-resolved emission spectra of $Ga_{2-x}Sc_xO_3$:Cr^{3+}. (a) $x = 0$, (b) $x = 0.2$, (c) $x = 0.4$, (d) $x = 0.6$, (e) $x = 0.8$, and (f) $x = 1.0$.

4a−f. The time intervals are adjusted in accordance with the luminescence time shortening. The time-resolved photoluminescent spectra are integrated at short (pink curve) and long (green curve) times in Figure 4, with the respective time intervals denoted by dashed rectangles. For the undoped sample ($x = 0$), the emission spectra integrated at shorter and longer times are the same, indicating that only one luminescence center (i.e., the high field case for $Dq/B > 2.4$) is observed in this material. By contrast, for the samples of $x = 0.2−0.6$, the two emission spectra are considerably different. Moreover, the broadening of the R-line emission compared with the $x = 0$ sample and the relatively large fwhm of the broadband emission suggest the distributions of the Cr^{3+} coordinated environment and the crystal field. The reason why the two emission spectra for $x = 0.2−0.6$ are extremely different is that the distribution of crystal field strength spans over the crossing point of the ^2E and $^4T_2$ states (i.e., $Dq/B > 2.4$), and the Cr^{3+} luminescence centers are located in strong and weak crystal fields. Accordingly, we can simultaneously observe broadband and line emissions even at low temperatures.

For the higher concentration ($x = 0.8$ and 1.0) samples, the two emissions appear the same. For $x = 0.8$ and 1, distributions of the Cr^{3+} coordinated environment and the crystal field also occur. However, all the Cr^{3+} centers are in the weak crystal field ($Dq/B < 2.4$), which produces overlapping luminescence bands with substantially identical decay times. In accordance, the shape of the broadband emission that is independent of time corresponds to the observation of solely the $^4T_2 \rightarrow {}^4A_2$ transition.

The photoluminescence decay profiles and calculated decay times at 10 K upon excitation at 442 nm of $Ga_{2-x}Sc_xO_3$:Cr^{3+} ($x = 0, 0.2, 0.4, 0.6, 0.8,$ and 1.0) are measured, as shown in Figure S4. Only a line emission (with phonon structure) is observed for the $x = 0$ sample, while a broadband emission

appears when incorporating Sc^{3+}; the latter starts to dominate as $x \geq 0.4$ (Figure S4a). Notably, the line emission remains visible at 10 K, but it is negligible for $x \geq 0.8$. In Figure S4b, the decay curves are nearly single exponential for $x = 0, 0.6, 0.8,$ and 1, but it becomes clearly nonexponential for $x = 0.2$ and 0.4. For $x = 0$ and $0.6−1.0$, the single exponential formula is used to fit the experimental data, as follows:

$$I(t) = I_1 e^{-t/\tau_1} \tag{1}$$

For $x = 0.2$ and 0.4, the biexponential formula is used to fit the decay profiles, as follows:

$$I(t) = I_1(0)e^{-t/\tau_1} + I_2(0)e^{-t/\tau_2} \tag{2}$$

where $I(t)$ is emission intensity at time t, $I_{1,2}$ is the initial intensity, and $\tau_{1,2}$ is the decay time of luminescence. At 10 K, the longer component τ_2 decreases with increasing Sc^{3+} concentration, while the shorter component τ_1 remains constant. The single exponential decay for the $x = 0$ sample is the result of the fact that the emission at 10 K is pure $^2E \rightarrow {}^4A_2$ emission in the system wherein energy Δ (the difference between the minimum energy of the $^4T_2$ and ^2E electronic manifolds) is positive and relatively large. Following the crystal field approximation, the following formula for a lifetime is developed for this case:[22]

$$\tau_E = \tau_T \frac{(\Delta + S\hbar\omega)^2}{V_{s-o}^2} \tag{3}$$

where $\tau_E = \tau_2$ is the lifetime of the $^2E \rightarrow {}^4A_2$ transition, $\tau_T = \tau_1$ is the lifetime that describes the $^4T_2 \rightarrow {}^4A_2$ transition, and V_{s-o} is the effective spin−orbit coupling constant that combines the ^2E and $^4T_2$ electronic manifolds. Luminescence decay is multiexponential with increasing Sc^{3+} concentration. Given that the emission spectrum becomes a superposition of R lines and the broadband, we assume two exponential decays. The

obtained value of τ_T is relatively constant, and τ_E diminishes in accordance with eq 3 due to the decrease in quantity Δ.

The thermal and electronic properties are also analyzed in detail in the Supporting Information.

To evaluate the potential of $Ga_{2-x}Sc_xO_3:Cr^{3+}$ phosphors in practical applications, a phosphor-converted LED (pc-LED) package is fabricated, as shown in Figure 5.
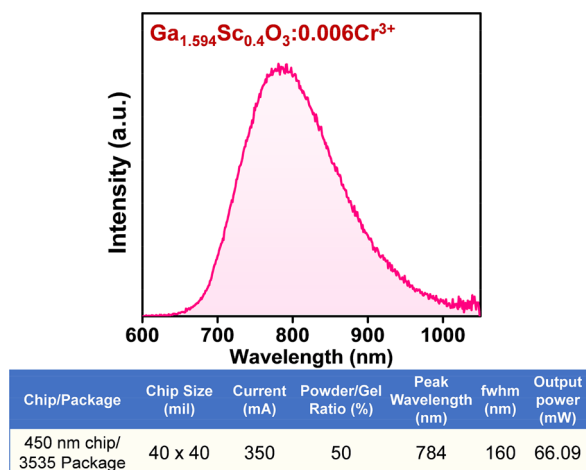

Chip/Package	Chip Size (mil)	Current (mA)	Powder/Gel Ratio (%)	Peak Wavelength (nm)	fwhm (nm)	Output power (mW)
450 nm chip/ 3535 Package	40 × 40	350	50	784	160	66.09

Figure 5. LED package that combines a 450 nm blue LED chip with $Ga_{1.594}Sc_{0.4}O_3:0.006Cr^{3+}$ IR phosphor.

$Ga_{1.594}Sc_{0.4}O_3:0.006Cr^{3+}$, which has one of the highest IQE values in the series, is used as an example. A blue LED chip with emission at 450 nm and a chip size of 40 mil × 40 mil is utilized as the light source. The device can provide 66.09 mW output power in the IR region under a driven current of 350 mA. Moreover, the LED device can provide the emission with a maximum peak at 784 nm and a bandwidth of 160 nm. The results indicate that $Ga_{2-x}Sc_xO_3:Cr^{3+}$ can be a potential candidate for the IR emitter of pc-LED.

In conclusion, a series of $Ga_{2-x}Sc_xO_3:Cr^{3+}$ solid solution phosphors is synthesized. Synchrotron XRD with Rietveld refinement proves that pure phases can be obtained. Meanwhile, lattice parameters have not changed as expected at high Sc^{3+} concentrations. Despite the strongly preferred occupation of Sc^{3+} at the octahedral-coordinated Ga2 site, only partial substitution ($x = 0.87$) can be achieved. This result is unique in the solid solution study. The BVS calculation indicates that the BVS values of Ga(Ga1) and Sc(Ga2) approach their ideal value (+3) exactly at $x = 0.87$, explaining the interesting partial substitution behavior from the Rietveld refinement. The maximum photoluminescence continuously red shifts at 720−850 nm as Sc^{3+} doping increases, while the fwhm and $S\hbar\omega$ initially increase and then decrease, implying inhomogeneous broadening. Time-resolved spectra at 10 K are then utilized to examine further the subtle change in microstructure around Cr^{3+}, supporting the findings of the Rietveld refinement and photoluminescence. To focus on Cr^{3+}, EPR is conducted, showing the distortion and second coordination sphere effect of Cr^{3+}. $Ga_{1.594}Sc_{0.4}O_3:0.006Cr^{3+}$ exhibits a high IQE of 99%, and the pc-LED that uses this compound can provide 66.09 mW of output power, demonstrating its high potential in practical applications.

This work can guide researchers in understanding the unexpected partial substitution during the solid solution process, particularly through the use of experimental and calculated approaches. This research can also provide insights to specialists and general materials to chemistry researchers in analyzing subtle changes in the crystal structure.

■ ASSOCIATED CONTENT

Ⓢ Supporting Information

The Supporting Information is available free of charge at https://pubs.acs.org/doi/10.1021/acsenergylett.0c02373.

Experiment methods, crystal structure, Rietveld refinement and table of refinement results, atomic positions, photoluminescence properties, table of transition energies and other parameters, Tanabe−Sugano diagram and configurational coordinate diagram, thermal property analysis, temperature-dependent photoluminescence and decay curves, decay times, electronic property analysis, EPR spectra (PDF)

■ AUTHOR INFORMATION

Corresponding Author

Ru-Shi Liu − *Department of Chemistry, National Taiwan University, Taipei 106, Taiwan*; ⓞ orcid.org/0000-0002-1291-9052; Email: rsliu@ntu.edu.tw

Authors

Mu-Huai Fang − *Department of Chemistry, National Taiwan University, Taipei 106, Taiwan*; ⓞ orcid.org/0000-0003-1475-0200

Kuan-Chun Chen − *Department of Chemistry, National Taiwan University, Taipei 106, Taiwan*

Natalia Majewska − *Institute of Experimental Physics, Faculty of Mathematic, Physics and Informatics, Gdańsk University, 80-308 Gdańsk, Poland*; ⓞ orcid.org/0000-0002-1933-0355

Tadeusz Leśniewski − *Institute of Experimental Physics, Faculty of Mathematic, Physics and Informatics, Gdańsk University, 80-308 Gdańsk, Poland*

Sebastian Mahlik − *Institute of Experimental Physics, Faculty of Mathematic, Physics and Informatics, Gdańsk University, 80-308 Gdańsk, Poland*; ⓞ orcid.org/0000-0002-9514-049X

Grzegorz Leniec − *Institute of Physics, Department of Mechanical Engineering and Mechatronics, West Pomeranian University of Technology, 70-311 Szczecin, Poland*

Slawomir M. Kaczmarek − *Institute of Physics, Department of Mechanical Engineering and Mechatronics, West Pomeranian University of Technology, 70-311 Szczecin, Poland*

Chia-Wei Yang − *Everlight Electronics Company, Ltd., New Taipei City 238, Taiwan*

Kuang-Mao Lu − *Everlight Electronics Company, Ltd., New Taipei City 238, Taiwan*

Hwo-Shuenn Sheu − *National Synchrotron Radiation Research Center, Hsinchu 300, Taiwan*

Complete contact information is available at:
https://pubs.acs.org/10.1021/acsenergylett.0c02373

Author Contributions

Mu-Huai Fang and Kuan-Chun Chen contributed equally to this paper.

Notes

The authors declare no competing financial interest.

■ REFERENCES

(1) Rajendran, V.; Fang, M.-H.; Guzman, G. N. D.; Lesniewski, T.; Mahlik, S.; Grinberg, M.; Leniec, G.; Kaczmarek, S. M.; Lin, Y.-S.; Lu, K.-M.; Lin, C.-M.; Chang, H.; Hu, S.-F.; Liu, R.-S. Super Broadband Near-Infrared Phosphors with High Radiant Flux as Future Light Sources for Spectroscopy Applications. *ACS Energy Lett.* **2018**, *3*, 2679−2684.

(2) Qiao, J.; Zhou, G.; Zhou, Y.; Zhang, Q.; Xia, Z. Divalent Europium-Doped Near-Infrared-Emitting Phosphor for Light-Emitting Diodes. *Nat. Commun.* **2019**, *10*, 5267.

(3) Fang, Y.; Shang, J.; Liu, D.; Shi, W.; Li, X.; Ma, H. Design, Synthesis, and Application of a Small Molecular NIR-II Fluorophore with Maximal Emission Beyond 1200 nm. *J. Am. Chem. Soc.* **2020**, *142*, 15271−15275.

(4) Huang, L.; Li, Z.; Zhao, Y.; Yang, J.; Yang, Y.; Pendharkar, A. I.; Zhang, Y.; Kelmar, S.; Chen, L.; Wu, W.; Zhao, J.; Han, G. Enhancing Photodynamic Therapy through Resonance Energy Transfer Constructed Near-Infrared Photosensitized Nanoparticles. *Adv. Mater.* **2017**, *29*, 1604789.

(5) Hernández, R.; Kubota, C. Physiological Responses of Cucumber Seedlingunder Different Blue and Red Photon Flux Ratios Using LEDs. *Environ. Exp. Bot.* **2016**, *121*, 66−74.

(6) Xie, R.-J. Light-Emitting Diodes: Brighter NIR-Emitting Phosphor Making Light Sources Smarter. *Light: Sci. Appl.* **2020**, *9*, 155.

(7) De Guzman, G. N. A.; Fang, M. H.; Liang, C.-H.; Bao, Z.; Hu, S. F.; Liu, R. S. Near-Infrared Phosphors and Their Full Potential: A Review on Practical Applications and Future Perspectives. *J. Lumin.* **2020**, *219*, 116944.

(8) Shao, Q.; Ding, H.; Yao, L.; Xu, J.; Liang, C.; Jiang, J. Photoluminescence Properties of a ScBO$_3$:Cr^{3+} Phosphor and Its Applications for Broadband Near-Infrared LEDs. *RSC Adv.* **2018**, *8*, 12035−12042.

(9) Huang, W. T.; Cheng, C. L.; Bao, Z.; Yang, C. W.; Lu, K. M.; Kang, C. Y.; Lin, C. M.; Liu, R. S. Broadband Cr^{3+}, Sn^{4+}-Doped Oxide Nanophosphors for Infrared Mini Light-Emitting Diodes. *Angew. Chem., Int. Ed.* **2019**, *58*, 2069−2072.

(10) Fang, M.-H.; De Guzman, G. N. A.; Bao, Z.; Majewska, N.; Mahlik, S.; Grinberg, M.; Leniec, G.; Kaczmarek, S. M.; Yang, C.-W.; Lu, K.-M.; Sheu, H.-S.; Hu, S.-F.; Liu, R.-S. Ultra-High-Efficiency Near-Infrared Ga$_2$O$_3$:Cr^{3+} Phosphor and Controlling of Phytochrome. *J. Mater. Chem. C* **2020**, *8*, 11013−11017.

(11) Pan, Z.; Lu, Y.-Y.; Liu, F. Sunlight-Activated Long-Persistent Luminescence in the Near-Infrared from Cr^{3+}-Doped Zinc Gallogermanates. *Nat. Mater.* **2012**, *11*, 58−63.

(12) Jia, Z.; Yuan, C.; Liu, Y.; Wang, X.-J.; Sun, P.; Wang, L.; Jiang, H.; Jiang, J. Strategies to Approach High Performance in Cr^{3+}-Doped Phosphors for High-Power NIR-LED Light Sources. *Light: Sci. Appl.* **2020**, *9*, 1−9.

(13) He, S.; Zhang, L.; Wu, H.; Wu, H.; Pan, G.; Hao, Z.; Zhang, X.; Zhang, L.; Zhang, H.; Zhang, J. Efficient Super Broadband NIR Ca$_2$LuZr$_2$Al$_3$O$_{12}$:Cr^{3+},Yb^{3+} Garnet Phosphor for Pc-LED Light Source Toward NIR Spectroscopy Applications. *Adv. Opt. Mater.* **2020**, *8*, 1901684.

(14) Fang, M.-H.; Huang, P.-Y.; Bao, Z.; Majewska, N.; Lesniewski, T.; Mahlik, S.; Grinberg, M.; Leniec, G.; Kaczmarek, S. M.; Yang, C.-W.; Lu, K.-M.; Sheu, H.-S.; Liu, R.-S. Penetrating Biological Tissue Using Light-Emitting Diodes with a Highly Efficient Near-Infrared ScBO$_3$:Cr^{3+} Phosphor. *Chem. Mater.* **2020**, *32*, 2166−2171.

(15) Bai, B.; Dang, P.; Huang, D.; Lian, H.; Lin, J. Broadband Near-Infrared Emitting Ca$_2$LuScGa$_2$Ge$_2$O$_{12}$:Cr^{3+} Phosphors: Luminescence Properties and Application in Light-Emitting Diodes. *Inorg. Chem.* **2020**, *59*, 13481−13488.

(16) Fang, M. H.; Mahlik, S.; Lazarowska, A.; Grinberg, M.; Molokeev, M. S.; Sheu, H. S.; Lee, J. F.; Liu, R. S. Structural Evolution and Effect of the Neighboring Cation on the Photoluminescence of Sr(LiAl$_3$)$_{1-x}$(SiMg$_3$)$_x$N$_4$:Eu^{2+} Phosphors. *Angew. Chem., Int. Ed.* **2019**, *58*, 7767−7772.

(17) Li, G.; Lin, C. C.; Chen, W.-T.; Molokeev, M. S.; Atuchin, V. V.; Chiang, C.-Y.; Zhou, W.; Wang, C.-W.; Li, W.-H.; Sheu, H.-S.; Chan, T.-S.; Ma, C.; Liu, R.-S. Photoluminescence Tuning via Cation Substitution in Oxonitridosilicate Phosphors: DFT Calculations, Different Site Occupations, and Luminescence Mechanisms. *Chem. Mater.* **2014**, *26*, 2991−3001.

(18) Denault, K. A.; Brgoch, J.; Gaultois, M. W.; Mikhailovsky, A.; Petry, R.; Winkler, H.; DenBaars, S. P.; Seshadri, R. Consequences of Optimal Bond Valence on Structural Rigidity and Improved Luminescence Properties in Sr$_x$Ba$_{2-x}$SiO$_4$:Eu^{2+} Orthosilicate Phosphors. *Chem. Mater.* **2014**, *26*, 2275−2282.

(19) Shannon, R. D. Revised Effective Ionic Radii and Systematic Studies of Interatomic Distances in Halides and Chalcogenides. *Acta Crystallogr., Sect. A: Cryst. Phys., Diffr., Theor. Gen. Crystallogr.* **1976**, *32*, 751−767.

(20) Rietveld, H. M. A Profile Refinement Method for Nuclear and Magnetic Structures. *J. Appl. Crystallogr.* **1969**, *2*, 65−71.

(21) Brese, N.; O'keeffe, M. Bond-Valence Parameters for Solids. *Acta Crystallogr., Sect. B: Struct. Sci.* **1991**, *47*, 192−197.

(22) Grinberg, M.; Lesniewski, T.; Mahlik, S.; Liu, R. S. 3d^3 System-Comparison of Mn^{4+} and Cr^{3+} in Different Lattices. *Opt. Mater.* **2017**, *74*, 93−100.

Supporting information

Hidden Structural Evolution and Bond Valence Control in Near-Infrared Phosphors for Light-Emitting Diodes

Mu-Huai Fang,[†] Kuan-Chun Chen,[†] Natalia Majewska,[§] Tadeusz Leśniewski,[§] Sebastian Mahlik,[§] Grzegorz Leniec,[Φ] Slawomir M. Kaczmarek,[Φ] Chia-Wei Yang,[Ψ] Kuang-Mao Lu,[Ψ] Hwo-Shuenn Sheu [Ω], and Ru-Shi Liu[†,*]

[†]Department of Chemistry, National Taiwan University, Taipei 106, Taiwan

[§]Institute of Experimental Physics, Faculty of Mathematic, Physics and Informatics, Gdańsk University, Wita Stwosza 57, 80-308 Gdańsk, Poland

[Φ]Institute of Physics, Department of Mechanical Engineering and Mechatronics, West Pomeranian University of Technology, Szczecin, al. Piastow 48, 70-311 Szczecin, Poland

[Ψ]Everlight Electronics Co., Ltd., New Taipei City 238, Taiwan

[Ω]National Synchrotron Radiation Research Center, Hsinchu 300, Taiwan

Corresponding Author

* rsliu@ntu.edu.tw

EXPERIMENTAL METHODS

Synthesis of $Ga_{1.994-x}Sc_xO_3:0.006Cr^{3+}$ ($Ga_{2-x}Sc_xO_3:Cr^{3+}$). Gallium oxide (Ga_2O_3, Gredmann, 99.99%), scandium oxide (Sc_2O_3, Gredmann, 99.99%), and chromium oxide (Cr_2O_3, Merck, 99.9%) were stoichiometrically weighed, mixed, and carefully ground in an agate mortar for 30 min. Then, the mixing precursors were placed in an alumina crucible and transferred to a muffle furnace. The samples were sintered at 1400 °C for 5 h with a heating and cooling rate of 5 °C. After synthesis, the resulting powder was cooled down to room temperature, and $Ga_{1.994-x}Sc_xO_3:0.006Cr^{3+}$ phosphor was obtained.

LED fabrication. IR–LED was fabricated by mixing ultraviolet (UV) gel with $Ga_{1.594}Sc_{0.4}O_3:0.006Cr^{3+}$ phosphor and transferring the mixture to a 450 nm blue chip with a chip size of 40 mil × 40 mil (3535 package). Then, the gel was solidified by irradiating with 365 nm UV light. The driving current of the device was set to 350 mA.

Characterization. Synchrotron powder X-ray diffraction patterns of $Ga_{1.994-x}Sc_xO_3:0.006Cr^{3+}$ was acquired from the National Synchrotron Radiation Research Center (NSRRC, Taiwan) BL01C2 beamline at room temperature using Debye - Scherrer camera. The pattern then proceeded for Rietveld analysis using Total Pattern Analysis Solutions software (TOPAS 4.2). Room temperature (RT) photoluminescence excitation (PLE) spectra were acquired with a FluoroMax-4P

S2

spectrofluorometer with a 150 W xenon lamp as an excitation source (Horiba) and an R928 Hamamatsu photomultiplier as a detector with a spectral range from 250 to 850 nm. The temperature-dependent emission spectra were measured using an Andor SR-750-D1spectrometer equipped with a CCD camera (DU420A-OE). A Kimmon Koha He–Cd laser with 442 nm was used as an excitation source. The apparatus for time-resolved spectroscopy was used to measure the decay profiles. The apparatus consists of a PG 401/SH optical parametric generator pumped by a PL2251A pulsed YAG:Nd laser (EKSPLA). The detection part consists of a 2501S grating spectrometer (Bruker Optics) combined with a C4334-01 streak camera (Hamamatsu). Data were recorded in the form of the streak images on a 640 by 480 pixel CCD array. The results are transformed into a 2D matrix of photon counts versus wavelength and time (streak image) using the software-based photon-counting algorithm. The first derivative of the absorption spectrum was recorded as a function of the applied magnetic field in the range B = 10–1400 mT on a conventional X-band Bruker ELEXSYS E 500 CW-spectrometer operating at 9.5 GHz with 100 kHz magnetic field modulation. The first derivative of the absorption spectrum was recorded as a function of the applied magnetic induction. EPR/NMR program was used to find spin-Hamiltonian parameters and local symmetry of chromium ions. Optimization and normalization of the parameters were performed using the root-mean-squared deviation method. The

internal quantum efficiency measurement was done using UV to NIR absolute PL

quantum yield spectrometer (C1534–12; Hamamatsu photonics K.K.) equipped with

NIR PL measurement unit (C13684–01; Hamamatsu photonics K.K.) using high power

Xe lamp unit (L13685–01; Hamamatsu photonics K.K.) together with 475 nm filter for

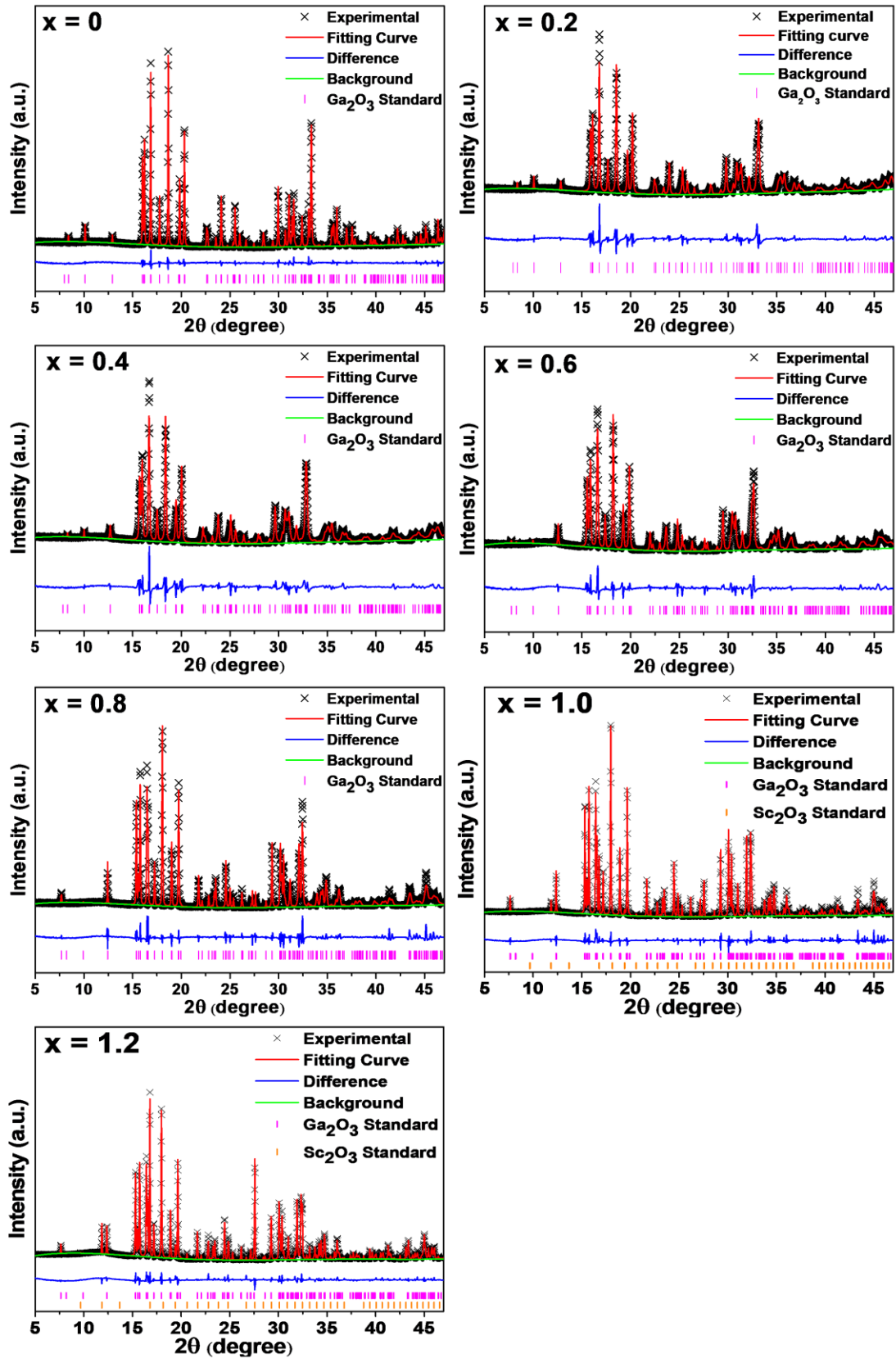excitation (A13686–475).

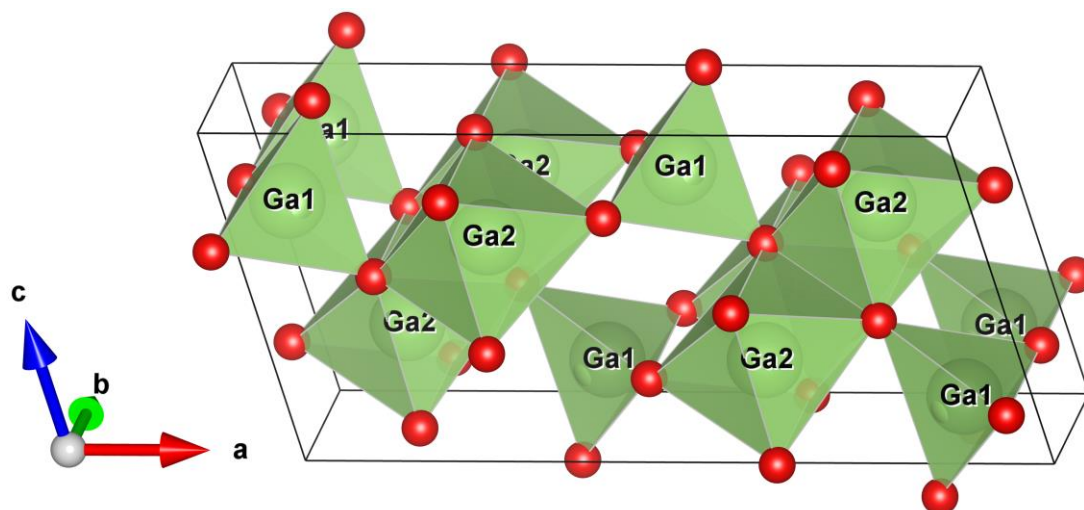Figure S1. Rietveld refinement of $Ga_{2-x}Sc_xO_3$:Cr^{3+} (x = 0, 0.2, 0.4, 0.6, 0.8, 1.0 and

1.2).

Figure S2. Crystal structure of Ga_2O_3. The red and green circles represent the O^{2-} and

Ga^{3+} ions, respectively.

Table S1. Atomic positions derived from Rietveld refinement of $Ga_{2-x}Sc_xO_3:Cr^{3+}$ (x = 0, 0.2, 0.4, 0.6, 0.8, 1.0 and 1.2).

x = 0					
Site	x	y	z	Occ	Beq
Ga1	0.090340(87)	0	0.79516(23)	1	0.00182(26)
Ga2	0.341323(81)	0	0.68650(22)	1	0.00182(26)
O1	0.16433(35)	0	0.1091(13)	1	0.00625(65)
O2	0.49605(36)	0	0.25551(79)	1	0.00625(65)
O3	0.82657(34)	0	0.4267(14)	1	0.00625(65)

x = 0.2					
Site	x	y	z	Occ	Beq
Ga1	0.09078(36)	0	0.79396(93)	0.996(11)	0.00625(79)
Sc1	0.09078(36)	0	0.79396(93)	0.004(11)	0.00625(79)
Ga2	0.34248(25)	0	0.68719(71)	0.804(11)	0.00625(79)
Sc2	0.34248(25)	0	0.68719(71)	0.196(11)	0.00625(79)
O1	0.1650(13)	0	0.1222(32)	1	0.025(20)
O2	0.4942(11)	0	0.2551(22)	1	0.025(20)
O3	0.82409(97)	0	0.4154(35)	1	0.025(20)

x = 0.4					
Site	x	y	z	Occ	Beq
Ga1	0.09080(35)	0	0.79362(99)	0.995(11)	0.01789(84)
Sc1	0.09080(35)	0	0.79362(99)	0.005(11)	0.01789(84)
Ga2	0.34273(28)	0	0.68816(82)	0.605(11)	0.01789(84)
Sc2	0.34273(28)	0	0.68816(82)	0.395(11)	0.01789(84)
O1	0.1638(13)	0	0.1208(33)	1	0.016(21)
O2	0.4917(11)	0	0.2538(25)	1	0.016(21)
O3	0.82309(99)	0	0.4195(36)	1	0.016(21)

x = 0.6					
Site	x	y	z	Occ	Beq
Ga1	0.09101(26)	0	0.79450(75)	0.9751(84)	0.1834(66)
Sc1	0.09101(26)	0	0.79450(75)	0.0249(84)	0.1834(66)
Ga2	0.34388(23)	0	0.68923(67)	0.4249(84)	0.1834(66)
Sc2	0.34388(23)	0	0.68923(67)	0.5751(84)	0.1834(66)
O1	0.16282(96)	0	0.1125(25)	1	0.2147(18)
O2	0.48852(82)	0	0.2497(21)	1	0.2147(18)
O3	0.82300(76)	0	0.4161(24)	1	0.2147(18)

x = 0.8					
Site	x	y	z	Occ	Beq
Ga1	0.09013(20)	0	0.79299(57)	0.9614(69)	0.001562(53)
Sc1	0.09013(20)	0	0.79299(57)	0.0386(69)	0.001562(53)
Ga2	0.34485(20)	0	0.68943(51)	0.2386(69)	0.001562(53)
Sc2	0.34485(20)	0	0.68943(51)	0.7614(69)	0.001562(53)
O1	0.15955(74)	0	0.1004(19)	1	0.2842(18)
O2	0.48870(68)	0	0.2519(17)	1	0.2842(18)
O3	0.82740(61)	0	0.4345(16)	1	0.2842(18)

x = 1.0					
Site	x	y	z	Occ	Beq
Ga1	0.09046(14)	0	0.79193(41)	0.9840(53)	0.001462(39)
Sc1	0.09046(14)	0	0.79193(41)	0.0160(53)	0.001462(39)
Ga2	0.34501(16)	0	0.68905(39)	0.1360(53)	0.001462(39)
Sc2	0.34501(16)	0	0.68905(39)	0.8640(53)	0.001462(39)
O1	0.15803(54)	0	0.0966(14)	1	0.09881(13)
O2	0.48689(51)	0	0.2533(13)	1	0.09881(13)
O3	0.82761(46)	0	0.4247(11)	1	0.09881(13)

x = 1.2					
Site	x	y	z	Occ	Beq
Ga1	0.09050(13)	0	0.79193(40)	0.9949(52)	0.08828(39)
Sc1	0.09050(13)	0	0.79193(40)	0.0051(52)	0.08828(39)
Ga2	0.34514(15)	0	0.68872(37)	0.1251(52)	0.08828(39)
Sc2	0.34514(15)	0	0.68872(37)	0.8749(52)	0.08828(39)
O1	0.15612(51)	0	0.0990(14)	1	0.06522(12)
O2	0.48808(49)	0	0.2534(12)	1	0.06522(12)
O3	0.82677(44)	0	0.4250(11)	1	0.06522(12)

Table S2. Refinement results derived from Rietveld refinement of $Ga_{2-x}Sc_xO_3$:Cr^{3+} (x = 0, 0.2, 0.4, 0.6, 0.8, 1.0 and 1.2).

x	0	0.2	0.4	0.6	0.8	1.0	1.2
a (Å)	12.22651(12)	12.31008(82)	12.4256(10)	12.54651(84)	12.65705(44)	12.70768(23)	12.71088(20)
b (Å)	3.039286(29)	3.05836(20)	3.08544(24)	3.11479(19)	3.14132(10)	3.154200(53)	3.154651(49)
c (Å)	5.805889(60)	5.82697(41)	5.85498(48)	5.88300(37)	5.91300(19)	5.92579(10)	5.92640(10)
β (°)	103.83838(76)	103.7034(48)	103.4523(54)	103.1090(35)	102.7057(19)	102.5187(12)	102.5100(11)
V (Å³)	209.4839(37)	213.133(25)	218.313(31)	223.915(25)	229.343(13)	231.8738(71)	231.9969(66)
Sc_2O_3 (%)	-	-	-	-	-	10.83(24)	30.34(20)
χ^2	0.47	1.01	1.25	1.11	1.29	1.08	0.9
R_{wp} (%)	1.25	2.9	3.61	3.42	3.96	3.41	3.05
R_p (%)	0.85	1.78	2.22	2.26	2.55	2.32	2.21

Photoluminescence Properties:

To explain the spectroscopic properties of Cr^{3+} replacing the Ga^{3+} or Sc^{3+} in $Ga_{2-x}Sc_xO_3$, one should consider the energetic structure of the ion described by Tanabe-Sugano diagram (TSD) and configurational coordinate diagram (CCD) presented in Figure S3a and Figure S3b, respectively. In crystal field approximation, the energetic structure of TSD depends on the values of Racach parameters B and C which describes the Coulomb and exchange interaction between $3d$ electrons in Cr^{3+} and crystal field strength Dq that describes the interaction between $3d$ electrons and ligands ions. The values $B, C,$ and Dq can be determined from the spectroscopic data, but the only value of Dq is related to the point symmetry of Cr^{3+} site. For octahedral symmetry:

$$D = \frac{1}{4\pi\varepsilon_0} \frac{35Ze^2}{4a^5} \tag{s1}$$

$$q = \frac{2}{105} \int \varphi_{3d}^*(r) r^4 \varphi_{3d}(r) dr \tag{s2}$$

Where a is the distance between central ion and ligands, Z is the charge of ligands, ε_0 is dielectric constant, e is the electron charge and $\varphi_{3d}(r)$ is the electronic wavefunction of $3d$ electrons. The diagram presented in Figure S3a allows us to calculate the crystal field strength Dq and Racach parameters B, and C from the spectroscopic data. The energy of the excitation band maximum of the $^4A_2 \rightarrow \ ^4T_2$ transition is equal to $10\ Dq$. Racach parameters (B and C) can be calculated from the following equations:[1]

$$B = Dq \frac{\left[\frac{\Delta E}{Dq}\right]^2 - 10 \cdot \frac{\Delta E}{Dq}}{15(\frac{\Delta E}{Dq} - 8)} \tag{s3}$$

$$C = \frac{B}{3.05} \left\{ \frac{E(\ ^2E)}{B} - 7.9 + 1.8 \frac{B}{Dq} \right\} \tag{s4}$$

where $\triangle E$ is the difference between the energy of the $^4T_1$ and $^4T_2$ states. The obtained values are listed in Table S3.

Table S3. Transition energies and values of 10Dq and Racah parameters B, and C.

x	$^4A_2 \rightarrow {}^4T_2$ (10Dq) (cm^{-1})	$^4A_2 \rightarrow {}^4T_1$ (cm^{-1})	$^4T_2 \rightarrow {}^4A_2$ (cm^{-1})	ΔE (cm^{-1})	$^4A_2$-$^2E(R_1)$ (cm^{-1})	$S\hbar\omega$ (cm^{-1})	B (cm^{-1})	Dq/B	C (cm^{-1})	C/B
0	16488	22745	13750	6257	14483	1370	615	2.68	3290	5.35
0.2	16287	22506	13240	6219	14467	1523	613	2.66	3292	5.37
0.4	15915	22177	12850	6262	14394	1532	623	2.55	3250	5.22
0.6	15667	21760	12560	6093	14352	1553	604	2.59	3279	5.44
0.8	15237	21336	12330	6099	14249	1453	610	2.50	3253	5.33
1.0	15113	21182	12200	6069	14270	1456	608	2.49	3249	5.34

Both 10Dq and energy of the ^2E state (R$_1$ line) decrease with increasing x, while values of B and C parameters do not exhibit clear dependence on x. Considering Table S3, one notices that value Dq/B decreases with increasing x. Specifically, the interesting part is to discuss the behavior of 10Dq (energy of the $^4T_2$ state) and the energy of the ^2E state with increasing x in context to relation (s1). Six-fold coordinated Ga^{3+} and Sc^{3+} ionic radius is equal to 0.67 Å and 0.885 Å, respectively.[2] Thus increase of Sc^{3+} that replaces Ga^{3+} will cause an increase of lattice constant. As a result, decreasing the value of 10Dq with an increasing amount of Sc^{3+} is associated with increasing of the Cr^{3+}– oxygen distance. According to TSD, the ground state $^4A_2$ belongs to the t^3 electronic configuration. The lowest excited state depends on the crystal field strength 10Dq is either $^4T_2$ (in low crystal field) or ^2E state (in high crystal field). The $^4T_2$ as well as the $^4T_1$ belongs to the t^2e electronic configuration, whereas the ^2E belongs to the t^3

electronic configuration.[1] In Figure S3a, energies are presented versus the value of Dq/B.

CCD allows us to understand other details. Specifically, since transitions between spin

doublet and the spin quartet are forbidden, mainly the $^4A_2 \rightarrow {}^4T_1$ and $^4A_2 \rightarrow {}^4T_2$ are

observed in the PLE spectrum, and only a trace of the $^4A_2 \rightarrow {}^2E$ transition is observed.

Additionally, after excitation to the $^4T_2$ state, the changes in electronic configuration

from t^3 to t^2e cause the small expansion of oxygen ligands, which diminish the energy

of the system by a quantity of $S\hbar\omega$:[3]

$$S\hbar\omega = k\frac{(Q_0 - Q_1)^2}{2} \tag{s5}$$

where k is the local elastic constant. This effect is described by CCD presented in Figure

S3b, where electronic energies are presented independence of configurational

coordinate Q. TSD predicts that Cr^{3+} emission changes from the broadband to the sharp

line for the value of Dq/B corresponding to the $^4T_2$ and ^2E states cross over (indicated

in Figure S3a by arrow A). However, due to the lattice relaxation ($S\hbar\omega$) in the $^4T_2$ the

sharp R lines replace the broad band emission for a larger value of Dq/B. Actually,

according to the CCD presented in Figure S3b, it happened when the minimum energy

of the $^4T_2$ electronic manifold becomes higher than the energy of the ^2E electronic

manifold. Thus for analysis of emission spectra, the most important one is quantity Δ,

which can be defined as the difference between the minimum energy of the $^4T_2$ and ^2E
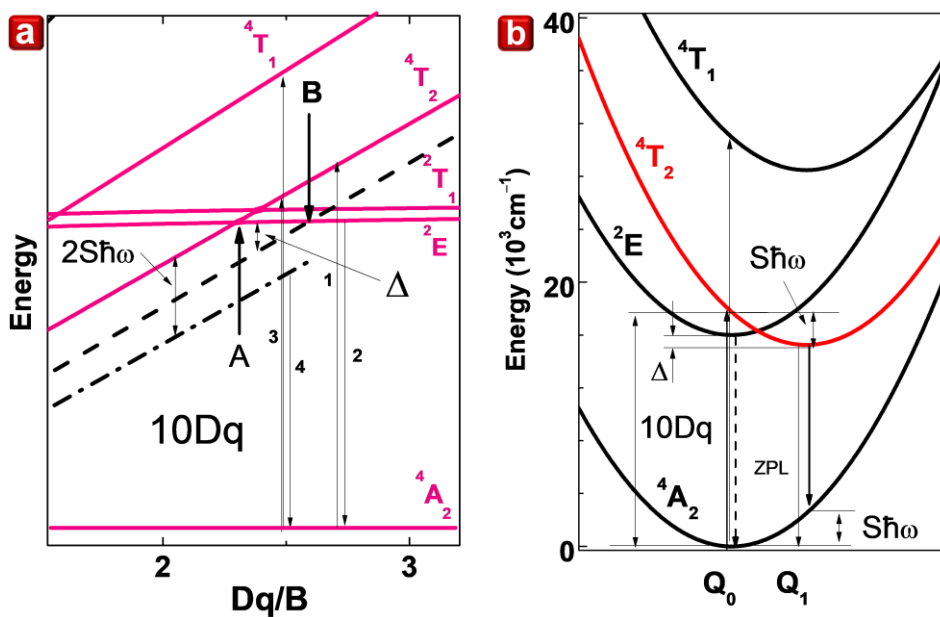
electronic manifold.

Figure S3. Tanabe–Sugano diagram and configurational coordinate diagram. (a) Tanabe–Sugano diagram for Cr^{3+}. The dashed line represents the energy of the zero-phonon line (ZPL) of the $^4T_2 \rightarrow {}^4A_2$ transition and the dashed-dotted line represents the energy of maximum of luminescence related to the $^4T_2 \rightarrow {}^4A_2$ transition. (b) Configurational coordinate diagram representing the low-field Cr^{3+} system.
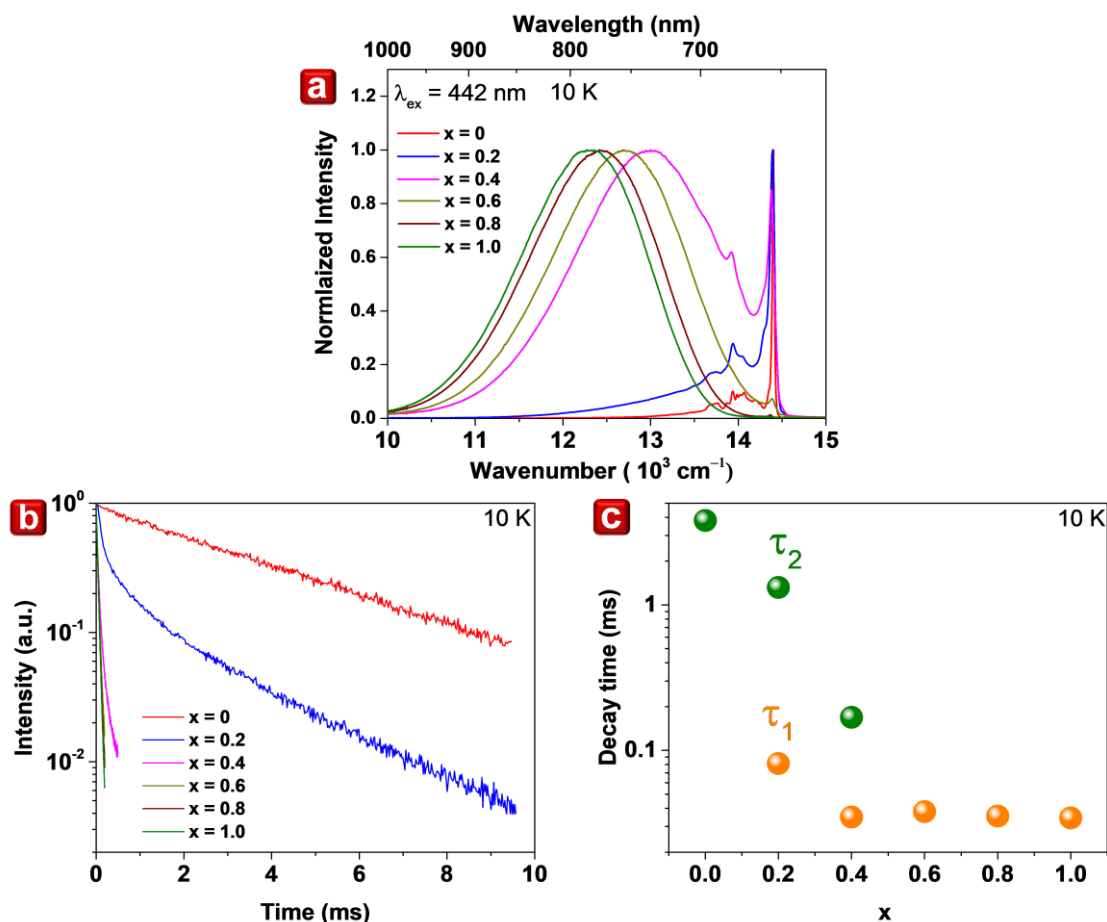
Figure S4. Photoluminescence and decay of $Ga_{2-x}Sc_xO_3:Cr^{3+}$ (x = 0, 0.2, 0.4, 0.6, 0.8, and 1.0). (a) Photoluminescence, (b) decay profiles, and (c) calculated decay times at 10 K upon excitation at 442 nm.

Thermal Property Analysis:

  To understand thermal properties further, the temperature-dependent photoluminescence spectra and decay profiles of $Ga_{2-x}Sc_xO_3:Cr^{3+}$ (x = 0, 0.2, 0.4, 0.6, 0.8, and 1.0) are obtained from the entire emission spectra within a temperature range up to 500 K upon excitation at 440 nm, as shown in Figures S5a–S5f. The temperature-

dependent lifetimes are calculated using the following formula:[4]

$$\tau_E = \tau_T \frac{1+3\,exp\left(-\frac{\Delta}{k_B T}\right)}{\left(\frac{V_{S-O}}{\Delta+S\hbar\omega}\right)^2+3\,exp\left(-\frac{\Delta}{k_B T}\right)},$$
(s6)

and the ratio of the intensity of the broadband to the R lines is equal to

$$\frac{I_{bb}}{I_R} = \frac{\tau_E}{\tau_T} = \frac{1+3\,exp\left(-\frac{\Delta}{k_B T}\right)}{\left(\frac{V_{S-O}}{\Delta+S\hbar\omega}\right)^2+3\,exp\left(-\frac{\Delta}{k_B T}\right)},$$
(s7)

where k_B is the Boltzmann constant. For $x = 0$, only the line emission from the forbidden state is observed up to 100 K with a long decay (Figure S5a). As temperature increases further, the broadband emission (allowed emission) starts to appear and decay begins to shorten significantly. For temperatures higher than 300 K, the broadband emission starts to dominate. In the case of $x = 0.2$, the broadband and line emissions appear at 10 K. The broadband emission starts to dominate with increasing temperature. The presence of broadband and line emission together result in multi-exponential decay profiles. With increasing Sc^{3+} concentration, line emission intensity decreases compared with the intensity of the broadband emission up to a point where only the broadband emission is observed at high Sc^{3+} concentrations, i.e., $x = 0.8$ and 1.0, and decay starts to be single exponential once more. The calculated decay times in the log scale for $Ga_{2-x}Sc_xO_3:Cr^{3+}$ ($x = 0, 0.2, 0.4, 0.6, 0.8,$ and 1.0) are shown in Figure S6a. For $x = 0$ and 0.6–1.0, the single exponential formula, Equation (1), is fitted. For $x =$

0.2 and 0.4, the two exponential formula, Equation (2), is used. The long decay time component τ_2 starts to decrease from 100 K. Meanwhile, the short decay time component τ_1 remains constant up to 350 K and then starts to decrease. The temperature-dependent FWHM $Ga_{2-x}Sc_xO_3:Cr^{3+}$ ($x = 0$, 0.2, 0.4, 0.6, 0.8, and 1.0) is also calculated, as shown in Figure S6b. For samples with a positive value of Δ ($x = 0$–0.4), the luminescence lifetime diminishes with temperature following Equation (s6). This effect is accompanied by the increasing intensity of the broadband emission to the R line. For $x = 0.6$–1.0, where the value of Δ is negative, the emission consists only of the broadband-related to $^4T_2 \rightarrow {}^4A_2$ transition and lifetime is stable and equal to τ_T.

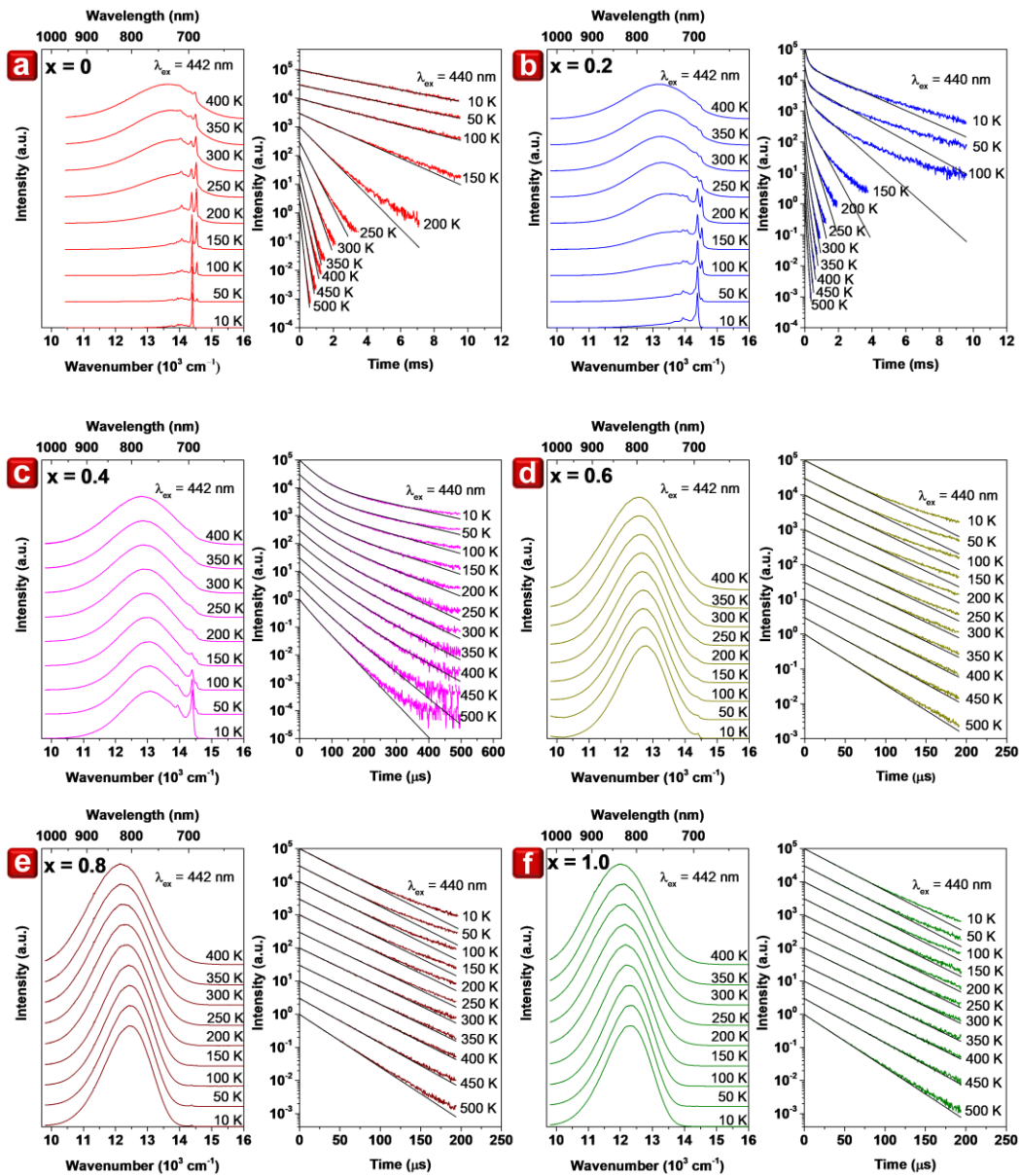Figure S5. Temperature-dependent photoluminescence and decay curve of Ga$_{2-x}$Sc$_x$O$_3$:Cr^{3+}. (a) $x = 0$, (b) $x = 0.2$, (c) $x = 0.4$, (d) $x = 0.6$, (e) $x = 0.8$, and (f) $x = 1.0$.
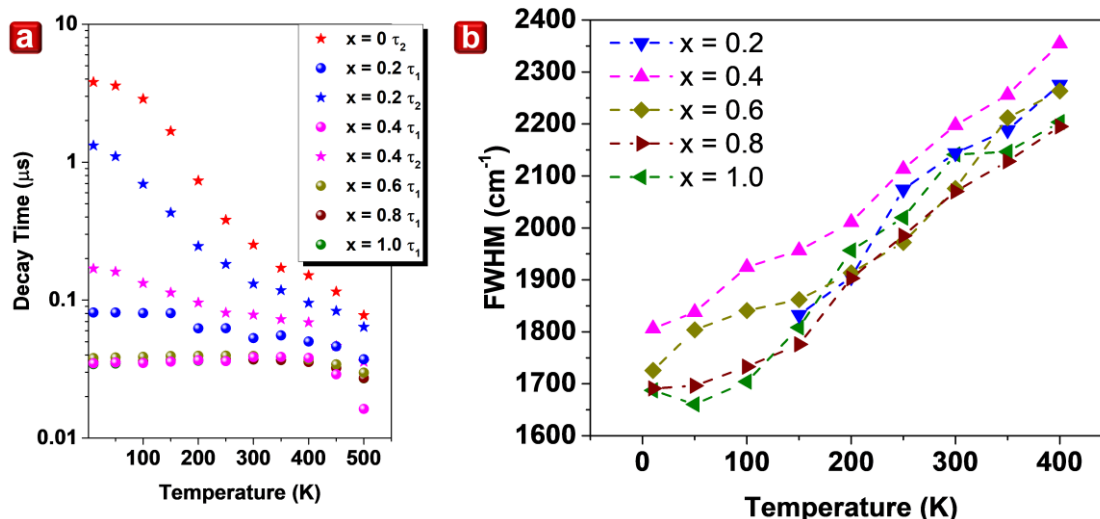
Figure S6. Temperature-dependent decay times and FWHM of $Ga_{2-x}Sc_xO_3:Cr^{3+}$ ($x = 0$, 0.2, 0.4, 0.6, 0.8, and 1.0). (a) Calculated temperature-dependent decay times and (b) temperature-dependent FWHM.

Electronic Property Analysis:

To directly analyze the properties of the Cr^{3+} ions, element-selective equipment should be utilized. Consequently, the electron paramagnetic resonance (EPR) spectra of $Ga_{2-x}Sc_xO_3:Cr^{3+}$ ($x = 0$, 0.2, 0.4, 0.6, 0.8, and 1.0) are obtained, as shown in Figure S7. In $Ga_{2-x}Sc_xO_3:Cr^{3+}$, the Cr^{3+} ions are paramagnetic dopants and their EPR spectra can be observed using an X-band spectrometer. The Cr^{3+} ions belong to d^3 electronic configurations with a ground state of $^4A_{2g}$, which is degenerated fourfold. Degeneracy is removed by the symmetric crystal field, and the ground state is split into two Kramers doublets with a spin of S = 3/2. The EPR spectra of $Ga_{2-x}Sc_xO_3:Cr^{3+}$ in powder form with different particle orientations can be observed within the magnetic induction range

of B = 10–1200 mT, depending on the nearest environment of these ions. The EPR

spectra from the isolated Cr^{3+} ions in the tetrahedral site are located at $g_{eff} \sim 2$.

Meanwhile, in the octahedral site, the g_{eff} will be 4–5 depending on the distortions of

the Cr^{3+} site. The EPR signals observed for the $Ga_{2-x}Sc_xO_3$:Cr^{3+} compound with

different concentrations of diamagnetic Sc^{3+} ions originate from the isolated Cr^{3+} ions

in the octahedral site, which is a typical EPR spectrum for Cr^{3+} in this site. The EPR

spectra vary significantly depending on the concentration of diamagnetic Sc^{3+} ions. For

$x = 0$, we observe EPR lines within the entire range of magnetic induction, $g_{eff} = 5.56$,

5.09, 2.46, 1.59, and 0.71. For $x = 1.0$, we observe only two EPR lines at $g_{eff} = 3.77$ and

1.98. The EPR lines indicate that the signal originates from the isolated Cr^{3+} ions in the

octahedral site in different crystal fields. The following spin-Hamiltonian (SH) formula

is used to determine the symmetry of Cr^{3+} ions with S = 3/2:

$$H = \mu_B B \cdot g \cdot S + D\left(S_z^2 - \frac{1}{3}S(S+1)\right) + E\left(S_x^2 + S_y^2\right), \qquad (s8)$$

where μ_B is the Bohr magneton, B is the induction of the magnetic field, g is the

effective spectroscopic splitting factor, S is the electron spin, and D is the axial and E

is the rhombic distortions of an octahedral. For the $x = 0$ compound, the spectroscopic

splitting parameters $g_x = 1.94(2)$, $g_y = 1.97(2)$, and $g_z = 2.01(2)$. For the $x = 1.0$

compound, the parameters $g_x = 1.92(2)$, $g_y = 1.96(2)$, and $g_z = 2.05(2)$ are obtained

(measurement errors are denoted in parentheses). The zero-field splitting parameters, λ

= E/D = 0.189 and 0.023, indicate a significant and slight distortion of the Cr^{3+} site for

$x = 0$ and 1.0, respectively. The results of the fitting of the SH parameters via the least-

squares method are also presented. From the SH parameters, we can determine that Cr^{3+}

ions are substituted into the Ga^{3+} sites for $x = 0$. For the $x = 1.0$ compound, Cr^{3+} ions

are substituted into the same site, but the symmetry of Cr^{3+} ions is affected by the Sc^{3+}

ions from the second coordination sphere. However, this EPR transition is not

proportional to the concentration of Sc^{3+} ions due to the considerable difference

between the ionic radii of Cr^{3+}/Ga^{3+} and Sc^{3+}. Cr^{3+} ions are substituted into sites wherein

ion radii are similar. In $x = 1.0$, the ion radii between Cr^{3+} and Ga^{3+} are similar. From

the EPR spectra $x = 0.2$–0.8, we observe the signal from the Cr^{3+} ions at the Ga^{3+} site.

Ga–Cr–Ga/Ga–Cr–Sc/Sc–Cr–Sc (second coordination sphere) type systems are

elongated in different directions of the crystallographic axes, leading to the extension

of the EPR linewidth because the powder signal is an envelope of all type of signals.

The crystal lattice will only become orderly when most Ga^{3+} ions are replaced with Sc^{3+}

ions. The Cr^{3+} ion environment is under the influence of the Sc^{3+} ions from the second

coordination sphere. An ordered crystal lattice and a single phase of the $x = 1$ material

indicate that diamagnetic Sc^{3+} ions are substituted only into the octahedral sites of Ga^{3+}
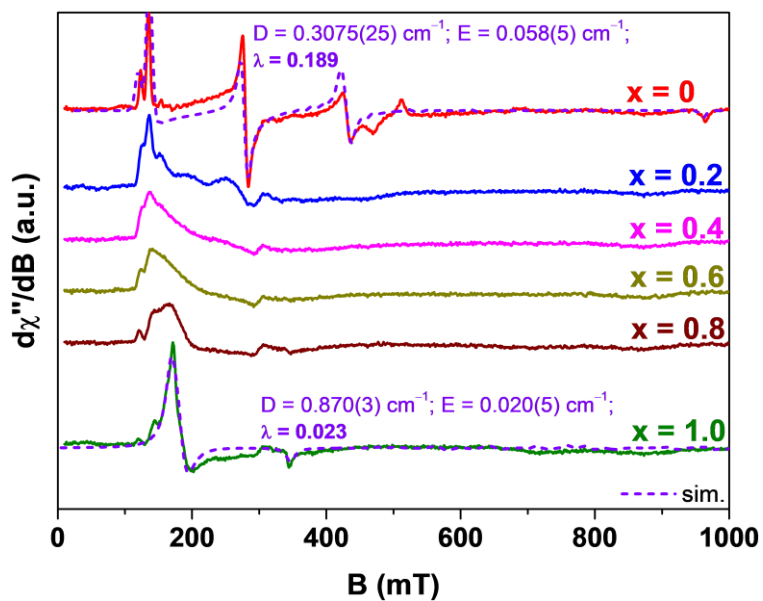
ions.

Figure S7. Experimental and simulation EPR spectra of $Ga_{2-x}Sc_xO_3:Cr^{3+}$ (x = 0, 0.2, 0.4, 0.6, 0.8, and 1.0).

References:

(1)   Henderson, B.; Imbusch, G. F., *Optical Spectroscopy of Inorganic Solids*. Oxford University Press: 2006; Vol. 44.

(2)   Shannon, R. D. Revised Effective Ionic Radii and Systematic Studies of Interatomic Distances in Halides and Chalcogenides. *Acta Crystallogr. Sect. A* **1976**, *32*, 751.

(3)   Grinberg, M.; Lesniewski, T. Non-Radiative Processes and Luminescence Quenching in Mn^{4+} Doped Phosphors. *J. Lumin.* **2019**, *214*, 116574.

(4)   Grinberg, M.; Lesniewski, T.; Mahlik, S. and Liu, R. S. $3d^3$ System–Comparison of Mn^{4+} and Cr^{3+} in Different Lattices. *Opt. Mater.* **2017**, *74*, 93.

[P4]

Majewska, N.; Muñoz, A.; Liu, R.-S.; Mahlik, S. Influence of Chemical and Mechanical Pressure on the Luminescence Properties of Near-Infrared Phosphors, Chem. Mater. 2023.

https://doi.org/10.1021/acs.chemmater.3c00203

Article

Influence of Chemical and Mechanical Pressure on the Luminescence Properties of Near-Infrared Phosphors

Natalia Majewska,* Alfonso Muñoz, Ru-Shi Liu, and Sebastian Mahlik

Cite This: https://doi.org/10.1021/acs.chemmater.3c00203

Read Online

ACCESS | Metrics & More | Article Recommendations | Supporting Information

ABSTRACT: In this study, we aim to compare the changes in the luminescence properties of Ga_2O_3:Cr^{3+} modified by Al or Sc ion substitution (chemical pressure) and hydrostatic pressure. We find the same behavior for $Ga_{2-x}Al_xO_3$:Cr^{3+} and different behavior for $Ga_{2-x}Sc_xO_3$:Cr^{3+} in terms of the optical properties under chemical and mechanical pressure. We consider Al substitution, which does not affect the chemical bond angles in the Cr^{3+} local environment and changes the crystal volume, like mechanical pressure does. As confirmed by Raman spectroscopy, the Sc ions cause lattice distortion and influence the chemical bond lengths and angles in the Cr^{3+} local environment. The energy structure diagrams of all levels of the d^3 configuration of the Cr^{3+} ion as a function of pressure are calculated by considering the pressure dependence of the Racah parameters. The energy structure diagrams presented in the paper show a decrease in the energy of the ^2E, $^2T_1$, and $^2T_2$ excited levels with an increase in Dq. This does not align with the behavior predicted for these excited levels by the standard Tanabe–Sugano diagram. It seems correct that a high-pressure experiment involving Cr^{3+} and other transition metals should be interpreted using the method and diagrams presented herein.
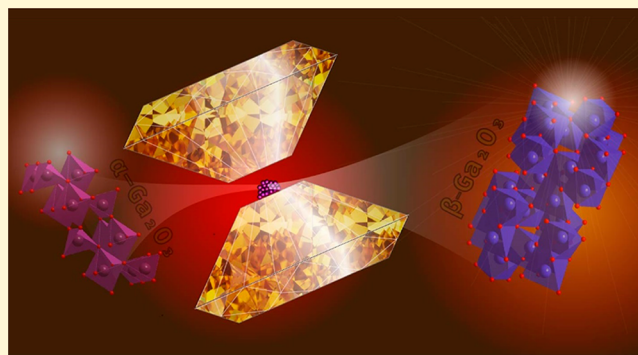
1. INTRODUCTION

The luminescence of the Cr^{3+} ion has been widely investigated. The most common Cr^{3+}-doped material is ruby crystal (Al_2O_3:Cr^{3+}), which formed the first solid-state-based laser in 1960. Today, the Cr^{3+} ion as a luminescent center attracts interest due to its potential new application. One of the crucial applications of Cr^{3+}-doped materials is biological imaging utilizing near-infrared (NIR) persistent luminescence.[1,2] Moreover, Cr^{3+} ions can be unique NIR emitters for phosphor-converted NIR light-emitting diodes with potential applications in food freshness analysis, agriculture, and human health monitoring.[3−9] Cr^{3+} ions are also tested in luminescence thermometry using the dependence of the shape of the emission spectrum on temperature.[10−14] Another interesting application of Cr^{3+} ions is luminescence manometry, in which the effects of pressure on the luminescence properties are studied.[15,16]

One promising NIR phosphor for practical applications is Ga_2O_3 activated by Cr^{3+} ions. Its luminescence is characterized by a broad efficient emission in the wavelength range of 700−950 nm, with maximum emission at 740 nm.[17−19] Additionally, codoping with Sc ions causes a red-shift in emission.[20] This shift is due to the decrease in the crystal field strength Dq around Cr^{3+} ions generated by lattice extension due to substituting larger Sc for Ga ions. Interestingly, a similar effect was observed in the yttrium gallium garnet with an increase in only the amount of Cr^{3+}.[21]

Since the development of the diamond anvil cell (DAC) in the late 1950s,[22] the DAC has become the most popular device in high-pressure studies. The DAC comprises two opposed diamond anvils that create a pressure chamber with a metal gasket. The pressure chamber contains the tested sample, pressure sensor, and medium to transmit pressure and ensure hydrostaticity. The DAC can be used for in situ Raman and luminescence spectroscopy, allowing for atomic-level understanding. By exposing the phosphor material to high pressure, we directly influence the interaction of the crystal environment with luminescent centers and cause significant changes in the energy structures of the studied systems. This has been directly observed through changes in the emission and absorption or the position of excitation bands or indirectly through the quenching or enhancement of luminescence intensity.

Investigating the optical properties of inorganic compounds doped with transition metals is an essential issue in a high-pressure study.[23] The research on Cr^{3+}-doped compounds, especially ruby, is the most significant.[24] The first widely
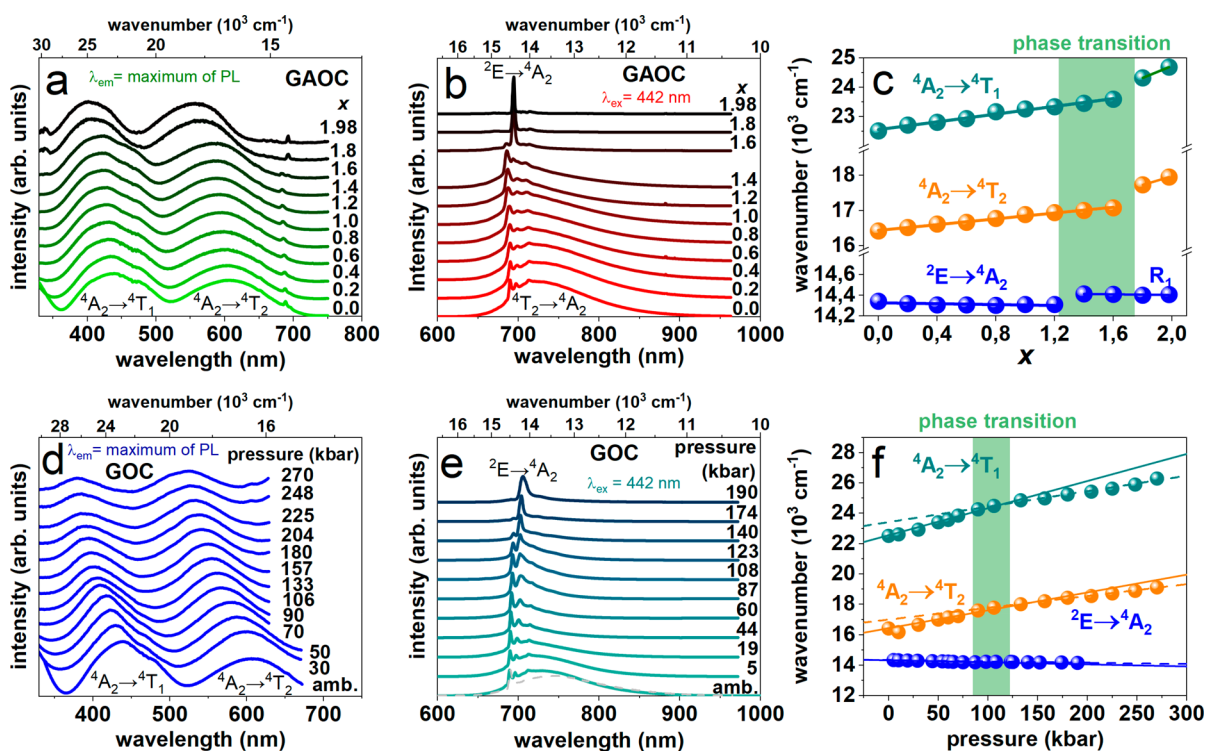
Figure 1. (a) RT PLE spectra, (b) PL spectra, and (c) positions of excitation bands and narrow line emission vs x content of $Ga_{2-x}Al_xO_3:Cr^{3+}$ (GAOC; $x = 0-1.98$). Pressure-dependent (d) PLE and (e) PL of $Ga_2O_3:Cr^{3+}$ (GOC; $x = 0$). (f) Positions of excitation bands and narrow line emission vs pressure. PL spectra were obtained upon excitation at 442 nm, and PLE spectra were observed at maximum luminescence.

observed and studied effect was the influence of high pressure on the $^2E \rightarrow {}^4A_2$ transition (so-called R lines). For d^3, the applied pressure forces a decrease in interatomic distances and a shift of the emission of the $^2E \rightarrow {}^4A_2$ transition toward lower energy values on the order of a single inverse centimeter per kilobar (e.g., $Al_2O_3:Cr^{3+}$).[24] This effect can be explained by the nephelauxetic effect, namely the expansion of the d^3 electron cloud when a high pressure is applied.[25−27] The situation is entirely different for the spin-allowed $^4T_2 \rightarrow {}^4A_2$ transition, which strongly depends on the crystal field and the influence of high pressure. For this transition, a pressure-induced blue-shift is observed on the order of tens of inverse centimeters per kilobar. The pressure-induced blue-shift should also be observed in the absorption and excitation spectra of Cr^{3+} containing the most prominent $^4A_2 \rightarrow {}^4T_2$ and $^4A_2 \rightarrow {}^4T_1$ transitions. However, due to the difficulties associated with measuring this type of spectrum as a function of pressure, only a few studies have produced such results.[28−31]

The most frequently used model describing the energy levels of transition metal ions is the Tanabe−Sugano (T−S) diagram. According to the T−S diagram, a pressure-induced increase in crystal field interaction Dq should increase the energy distance of the $^4T_2$ and $^4T_1$ states to the $^4A_2$ state, which is usually observed. However, for the $^2E \rightarrow {}^4A_2$ transition, the T−S diagram predicts a relationship (slight blue-shift) that is the opposite of the observed ones (red-shift).[32]

The overall conclusion from the structural point of view is that the same effect as mechanical pressure is also observed when chemical pressure (CP) is applied (incorporating larger or smaller ions to expand or contract the crystal lattice while maintaining the structure). Using chemical pressure, we can tune the luminescence properties of the Cr^{3+}-activated Ga_2O_3 material and obtain a similar effect by applying external

mechanical pressure (MP). Incorporating an ion with a larger ionic radius in the crystal lattice causes an increase in the atomic distance in the crystal, decreasing the crystal field strength around the ion. In contrast, incorporating an ion with a smaller ionic radius causes a decrease in the atomic distance in the crystal lattice, increasing the crystal field strength.

However, Fernandes et al.[33] showed from a superconducting point of view that the trends can be opposite. They found qualitatively different behavior in the chemical and hydrostatic pressure dependences of the critical temperature in the $Gd_{1-x}Y_xBa_2Cu_3O_7$ solid solutions. The substitution of a smaller ion results in a depression of T_c, whereas the application of hydrostatic pressure increases T_c. They also showed that the qualitatively different behavior under CP or MP is due to the highly inhomogeneous character of the chemical pressure, which induces an expansion of the Cu(2)−O(4) distance despite the overall compression of the unit cell.

The studies of the electronic properties of $(Al_xGa_{1-x})_2O_3$ alloys were performed by Wang et al.,[34] showing a band gap increase with Al codoping for β and α phases, while the basic luminescence of $Al_{2x}Ga_{2(1-x)}O_3:Cr^{3+}$ was previously reported by Morgan et al.[35]

Schneider and Waring first determined the phase equilibrium diagram of the quasi-binary system $Sc_2O_3–Ga_2O_3$.[36] The results of $Ga_{2-x}Sc_xO_3$ ($0.42 \leq x \leq 0.52$) were published by Kuz'micheva et al.,[37] showing the lattice structure of the crystal. Jasenovec et al.[38] showed an increase in the optical band gap of ∼0.7 eV for β-$(Sc_xGa_{1-x})_2O_3$ ($x = 0.1$), while Yahia et al.[39] showed the single-crystal structure and solid-state NMR data of $Ga_{2-x}Sc_xO_3$ ($x = 0.83$).

In previous studies, we performed fundamental research on luminescence and structural properties, showing the behavior of the lattice parameters for materials based on Cr^{3+}-doped

gallium oxide modified by partial matrix substitution.[20,40] This paper focuses on the competitive impact of CP and MP on the luminescence properties of Cr^{3+}-activated Ga_2O_3 codoped with Al^{3+} and Sc^{3+} ions. We investigate two different polymorphs of Ga_2O_3: β-Ga_2O_3 and α-Ga_2O_3. β-Ga_2O_3 crystallizes in the monoclinic crystal structure with space group $C2/m$, while α-Ga_2O_3 crystallizes in the trigonal corundum-like structure with space group $R\bar{3}c$.[17] The α phase was obtained by applying high hydrostatic pressure in the gigapascal range. This work shows the unique high-pressure excitation photoluminescence spectra of the studied materials, allowing us to construct the exact energy structures as a function of pressure. The presented analysis and calculations remain relevant to other Cr^{3+}-activated materials and can be applied to other transition metal ion systems.

2. RESULTS AND DISCUSSION

The incorporation of the smaller Al^{3+} (ionic radius of 0.39 Å, CN of 4; ionic radius of 0.54 Å, CN of 6) in place of the Ga^{3+} ion (0.47 Å, CN of 4; 0.62 Å, CN of 6) (CN denotes coordination number)[41] causes the reduction of the Cr−O atomic distance in the crystal lattice, thus increasing the crystal field strength around the Cr^{3+} ion, the so-called chemical pressure (CP).[40] On the contrary, introducing the Sc^{3+} ion (0.745 Å, CN of 6)[41] into the Ga_2O_3 lattice, which has an ionic radius larger than that of Ga^{3+}, causes the opposite behavior versus that seen for the incorporation of Al^{3+} ions. In the case of Sc^{3+} doping, the Cr−O atomic distance in the crystal lattice increases, decreasing the crystal field strength around the Cr^{3+} ion.[20] The first one is comparable to applying external mechanical pressure, while the former has the opposite effect.

2.1. $Ga_{2−x}Al_xO_3$:Cr^{3+}. Figure 1a shows the room-temperature (RT) photoluminescence excitation (PLE) spectra of $Ga_{2−x}Al_xO_3$:Cr^{3+} (GAOC; x = 0−1.98; step 0.2) observed at maximum luminescence. The PLE spectra comprise two excitation bands typical for Cr^{3+} ions in 6-fold octahedral coordination. The high-energy band in the range of 350−500 nm corresponds to the $^4A_2 \rightarrow {}^4T_1$ transition, and the low-energy band in the range of 500−700 nm corresponds to the $^4A_2 \rightarrow {}^4T_2$ spin-allowed transitions of Cr^{3+} ions. With an increase in x content, both bands shift toward higher energies (shorter wavelengths), as expected due to the increased crystal field strength Dq in the vicinity of Cr^{3+} ions caused by the incorporation of smaller Al ions in place of Ga ions. Figure 1b shows the RT photoluminescence (PL) spectra of GAOC upon excitation at 442 nm. For samples with low x content, both narrow line and broadband emissions of Cr^{3+} are observed. Narrow line emission around 690 nm corresponds to the $^2E \rightarrow {}^4A_2$ transition (R_1 and R_2 lines, accompanied by a weak phonon structure). The broadband emission from 650 to 950 nm corresponds to the transition from the $^4T_2$ excited state to the $^4A_2$ ground state. With an increase in x, the $^2E \rightarrow {}^4A_2$ emission shifts linearly toward higher energies at a rate much lower than those of the $^4T_1 \rightarrow {}^4A_2$ and $^4T_2 \rightarrow {}^4A_2$ transitions. Additionally, as x increases, the location of the $^4T_2 \rightarrow {}^4A_2$ band shifts linearly toward higher energy. When x = 1.6, there is a rapid change in the emission spectra due to the phase transition from the β (monoclinic) to α (trigonal) phase of Ga_2O_3, which is proven by the XRD spectra shown in ref 40.

The energies of the $^4A_2 \rightarrow {}^4T_1$ and $^4A_2 \rightarrow {}^4T_2$ transitions determined from excitation spectra and the $^2E \rightarrow {}^4A_2$ transition from emission spectra are shown in Figure 1c. The errors are

smaller than the size of the points. The parameters of the linear shift were acquired by fitting a linear function and are listed in Table S1.

High-pressure experiments were performed to compare the impact of CP and MP on the luminescence properties of the samples under study. Panels d and e of Figure 1 show RT pressure-dependent PLE spectra upon observation at maximum luminescence and PL spectra upon excitation at 442 nm, respectively, for Ga_2O_3:Cr^{3+} (GOC), which in Figure 1a is marked as the x = 0 sample. The PL spectra simultaneously show narrow line ($^2E \rightarrow {}^4A_2$) and broadband ($^4T_2 \rightarrow {}^4A_2$) emission at ambient pressure. With an increase in pressure due to the decreasing distance between ions and thus increasing strength of crystal field Dq on Cr^{3+} ions, the two excitation bands presented in Figure 1d shift toward higher energy, as expected. A substantial shift is also observed for the $^4T_2 \rightarrow {}^4A_2$ broadband emission up to a few kilobars; however, above 44 kbar, only narrow line emission is observed. Broadband quenching is associated with the pressure-induced shift of the $^4T_2$ state toward higher energies. This causes the thermal energy (thermal population of electrons from the lowest ^2E to $^4T_2$ state) to be too low at room temperature to induce emission from the $^4T_2$ state, and the lowest excited ^2E state becomes the only emitting state.[18,42]

The change in the relative intensity of the R_1 and R_2 lines (Figure 1e) is observed, and the R_2 line is no longer monitored for pressures of >145 kbar. Furthermore, a significant change in emission spectra between 123 and 140 kbar is observed. Such a phenomenon is caused by a mechanical pressure-induced phase transition from β-Ga_2O_3 to α-Ga_2O_3.[43−45] The phase transition is irreversible, and the sample stays in the new pressure-induced α phase when the pressure is released. The emission change is shown under ambient conditions before and after pressure was applied (gray line in Figure 1e). The shape of the emission spectra after the phase transition agrees with that reported for α-Ga_2O_3:Cr^{3+} reported by Back et al.[17]

Additionally, inversion of the intensities two excitation bands is observed for the α phase above 133 kbar. The same phenomena were observed for the Ga_2O_3:Cr^{3+} sample by Back et al.[17] The intensity inversion can be due to changing the $^4A_2 \rightarrow {}^4T_1$ and $^4A_2 \rightarrow {}^4T_2$ radiative transition probabilities for the GOC in the α phase compared to the β phase. This effect can be explained by the influence of the admixture of the ^2E and $^2T_1$ states in the overlapping (resonant) $^4T_2$ states. Another interpretation is that breaking the parity selection rules by deviations from inversion symmetry can affect the $^4A_2 \rightarrow {}^4T_1$ transition more strongly than the $^4A_2 \rightarrow {}^4T_2$ transition.[46]

A similar phenomenon in these materials is found for the radiative transition probabilities of the R_1 and R_2 lines.

Energies of the broadband excitation spectra (the $^4A_2 \rightarrow {}^4T_1$ and $^4A_2 \rightarrow {}^4T_2$ transitions) and R line emission spectra versus pressure are presented in Figure 1f. The errors are within the scatter size. With an increase in MP, the $^4A_2 \rightarrow {}^4T_1$ and $^4A_2 \rightarrow {}^4T_2$ bands shift toward higher energies, while the R lines shift toward lower energies (longer wavelength). The pressure dependence of the excitation band and R line emission is linear; however, a change in the shift rate is observed at ∼125 kbar, where a phase transition occurs. The liner fitting was performed separately for the β (solid line) and α phases (dashed line) up to 125 and 125−300 kbar, respectively, and then interpolated over the range of occurrence.
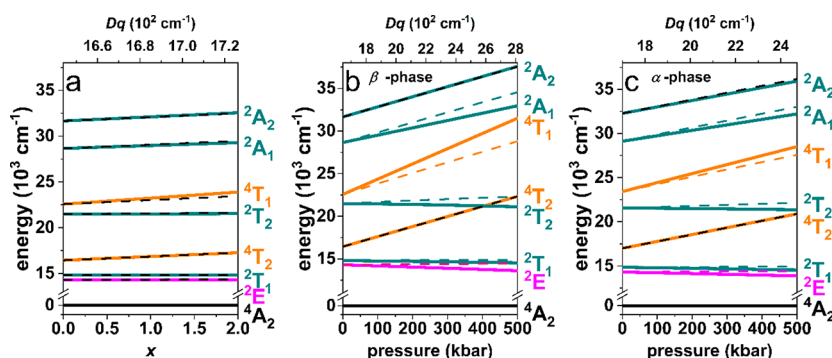
Figure 2. Energy structure diagram of the selected subterms of the d^3 configuration of the Cr^{3+} ion as a function of (a) x and pressure for GOC (x = 0) in the (b) β and (c) α phases. For comparison, the calculations were carried out assuming that B and C are not dependent on pressure (dashed lines), which is equivalent to the T−S diagram with constant values of B and C.

The linear fit parameters of the shifts caused by MP before and after phase transition are listed in Table S1.

It is seen that the pressure shift rate dE/dp of both the excitation band and R line emission is lower for the α phase than for the β phase. The direction and magnitude of the pressure shift of the excitation bands and emission R lines agree with the typical pressure shift rates of the $^4A_2 \rightarrow {}^4T_1$, $^4A_2 \rightarrow {}^4T_2$,[28−31] and $^2E \rightarrow {}^4A_2$ transitions of the Cr^{3+}-doped inorganic lattice.[18,47−50]

One can consider the effect of impacts of CP and MP that cause increased energy in the transition between $^4T_1/{}^4T_2$ and $^4A_2$ due to the decreasing Cr−O distance. Figure 1c, Figure 1f, and Table S1 show that when the $^2E \rightarrow {}^4A_2$ transition is considered, the energy decreases with an increase in x and pressure.

Knowing the location of the $^4T_2$, $^4T_1$, and ^2E states allows us to calculate crystal field parameter Dq, which describes the interactions between 3d electrons and ligand ions, and Racah parameters B and C, which represent the interaction between 3d electrons in Cr^{3+} versus CP and MP, respectively. The energy of the excitation band maximum of the $^4A_2 \rightarrow {}^4T_2$ transition equals 10Dq. Racah parameters B and C can be calculated from eqs S1 and S2 of the Supporting Information.

Panels a and b of Figure S1 show the values of the calculated parameters for the applied CP and MP, respectively. As x increases, Dq and B increase while C decreases (Figure S1a). Qualitatively, decreases in both B and C are expected to occur with pressure due to enhancements in the covalency from increased metal−ligand orbital overlap as the nearest neighbor bond length decreases.[51] The calculation of Racah parameters shows the different behavior of B and C parameters. The former decreases with x, and the latter increases with x. In principle, the variation with x of B and C determines the energy shift of the ^2E state (nephelauxetic red-shift). However, an increase in pressure will also affect the electrostatic repulsion of the electron densities of Cr^{3+} and the surrounding ligands. This, in turn, should lead to increased Racah parameters, which can explain the opposite behavior of the C parameter under pressure.

Knowing these three parameters (Dq, B, and C) makes it possible to generate the entire energy structure of the Cr^{3+} ion, i.e., to calculate the energy of all crystal field levels of the d^3 configuration. Furthermore, knowing the spectral shift with respect to pressure or x allows determinatioon of the CP and MP dependence of the entire energy structure of Cr^{3+}. The x- and pressure-dependent Dq, B, and C parameters were

determined on the basis of the data listed in Table S1. The experimentally obtained linear dependencies of Dq, B, and C were extrapolated to the pressure range of 0−500 kbar to calculate the energy structure (see Figure S2a,b).

Figure 2 shows the results of calculations of the energy structure of selected subterms as a function of x (for GAOC) and pressure (GOC) for the β and α phases together with the analysis carried out assuming that parameters B and C do not change with pressure (dashed lines). This is equivalent to the T−S diagram for B and C for α- and β-Ga_2O_3 at ambient pressure. The main difference between these energy structure diagrams compared to the standard T−S diagram is that the energy of the excited levels belonging to the t_2^3 crystal field configuration, i.e., the lowest doublet subterms (^2E, $^2T_1$, and $^2T_2$), decreases instead of increasing. Figure 2 shows that in the analyzed pressure range for GOC, the energies of the crystal field levels have a linear dependence, which should be considered as the effect of linear extrapolation of the pressure change of Dq, B, and C.

For the x dependence of the energy structure of the Cr^{3+} ion for GAOC, only a slight change for all energy levels is observed because the crystal field change is small in the considered x region.

It is worth noting that the presented energy structure diagrams show a decrease in the energy of the excited levels belonging to the t_2^3 crystal field configuration (^2E, $^2T_1$, and $^2T_2$) with an increase in Dq (in the case of the pressure- and x-dependent results). This behavior is consistent with the observed change in the direction of the $^2E \rightarrow {}^4A_2$ transition. This is not in line with the behavior inferred from the superficial analysis of the T−S diagram (i.e., under the assumption that B remains constant during the pressure-induced compression of the material). In this case, the T−S diagram predicts a slight increase in the ^2E energy level with pressure. Only the $^4T_2$ state agrees perfectly with the typical T−S diagram because this state depends on only the Dq value [$10Dq = E(^4A_2 \rightarrow {}^4T_2)$]. The fact mentioned above confirms the need to consider the changes in Racah parameters when describing the results of spectroscopic studies of transition metal-doped materials as a function of pressure.

One can argue that the pressure behavior of the ^2E state can still be determined from the T−S diagram because it represents CF subterm energies scaled by factor B. Then, if one knows the dependence of B with respect to pressure, one can reconstruct the correct pressure behavior of ^2E. However, this reasoning is not entirely correct because the T−S diagram
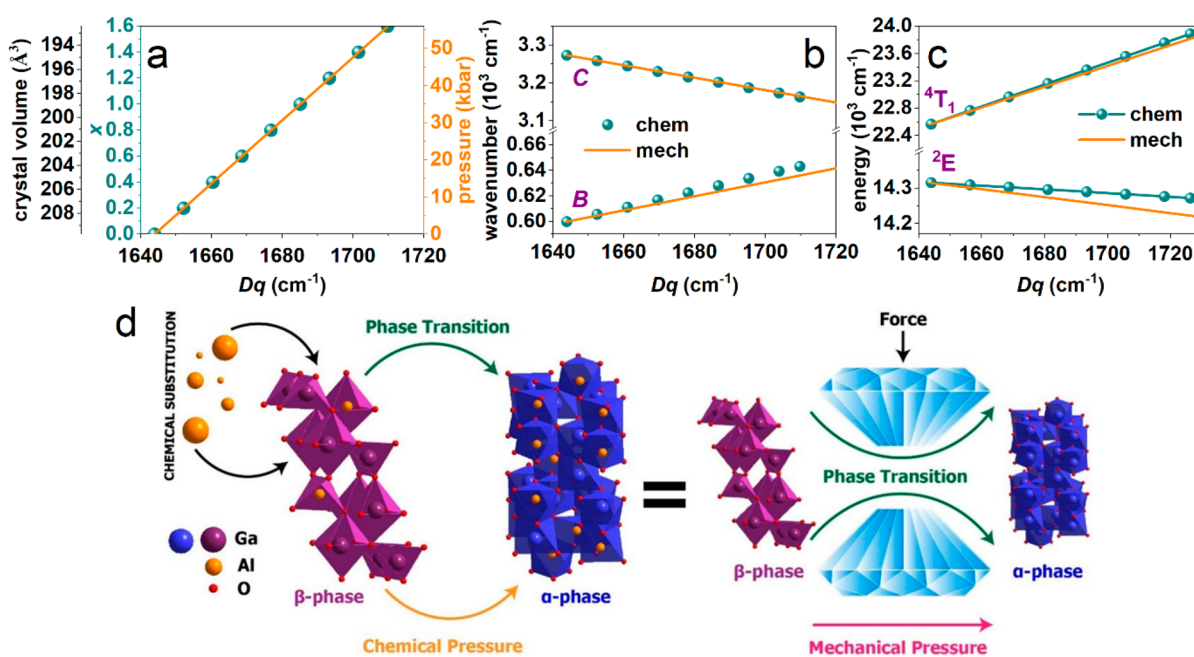
Figure 3. Comparison of the (a) Dq value, (b) C and B parameters, and (c) ^{2}E and ^{4}T$_1$ states for mechanical and chemical pressure. (d) Schematic view of the influence of chemical and mechanical pressure on GAOC samples.

assumes a constant C/B ratio (i.e., $C \propto B$), whereas C and B can (and, in our case, do) change independently with pressure. Moreover, in our results, B actually increases, which would indicate that the ^{2}E energy should increase with pressure, which contradicts the experimental results (in our case, the nephelauxetic shift is manifested by a decrease in C rather than B).

Panels c and d of Figure S2 present an energetic structure for all calculated subterms of the Cr^{3+} ion as a function of x and pressure for the β and α phases. The Dq/B ratio is also shown in Figure S2. The Dq/B ratio decreases with an increase in x (Figure S2a) and decreases with an increase in pressure for the β phase (Figure S2b). In the α phase, the dependence is the opposite of that in the β phase.

In conclusion, we observed a more significant change in the location of the ^{4}T$_2$, ^{4}T$_1$, and ^{2}E states of the Cr^{3+} ion with pressure for the β phase; hence, there was a more substantial pressure change in Dq, B, and C compared to those for the α phase. This is probably due to the smaller compressibility of α-Ga$_2$O$_3$ compared to that of β-Ga$_2$O$_3$, for which the theoretically calculated bulk moduli (B_0) are 217 and 171.1 GPa, respectively. The B_0 value found in the literature equals 145,[52] 160,[53] 174,[54] 142,[55] 134,[55] 184,[56] and 166 GPa[57] for β-Ga$_2$O$_3$ and 190,[52] 210,[44] 220,[45] and 354 GPa[58] for α-Ga$_2$O$_3$.

From the point charge model, the pressure-induced decrease in the distance between the ions in the crystal lattice increases crystal field strength Dq as follows:[59,60]

$$\frac{dDq}{dp} = -nDq\frac{1}{R}\frac{dR}{dp} = Dq\frac{nK}{3B_0} \quad (1)$$

$$B_0 = -V\frac{dP}{dV} \quad (2)$$

where dimensionless coefficient K characterizes how pressure's macroscopic impact alters the central ion's local environment. K values of 1, <1, and >1 indicate that the ion−ligand system's compression is equivalent to, smaller than, and larger than that

of the bulk lattice, respectively. B_0 is the bulk modulus. n is an exponential factor in the radial dependence of the Dq crystal field strength parameter R and should be equal to 5. R is the average distance between ligands and the Cr^{3+} ion. V is the cell volume. To calculate B_0, we assumed that the local compressibility in the vicinity of the Cr^{3+} ion is the same as the lattice compressibility ($K = 1$). Taking the experimental values from the data in panels b and c of Figure 2, Dq at ambient is 1643.9 and 1699.6 cm^{-1} and dDq/dp is 1.77 and 0.78 cm^{-1}/kbar for the β and α phases, respectively. We can calculate B_0 to be 154.5 GPa (1545 kbar) and 364.4 GPa (3644 kbar) for the β and α phases, respectively. It should be noted that, in the literature, for transition metal ions in different materials, the quantity nK is ≪5, indicating that the local compressibility is smaller than the bulk compressibility in almost all cases.[59,60] Therefore, the B_0 value we obtained can be regarded as an upper limit.

In this part, we want to compare the influence of CP and MP on the emitting states of Cr^{3+} in a modified Ga$_2$O$_3$ matrix. Figure 3 compares the Dq value, C and B parameters, and ^{2}E and ^{4}T$_1$ state changes obtained by CP and MP. The codoping of Ga$_2$O$_3$ with Al causes an increase in the crystal field strength, which is similar to the case in which mechanical pressure is applied. Figure 3a compares the Dq values obtained using CP (cyan color) and MP (orange color). This figure shows that by changing the x value from 0.0 to 1.6 (CP), which is equivalent to the change in the crystal volume from 209.7 to 192.4 Å^3,[40] we changed the Dq value from 1640 to 1720 cm^{-1} (cyan dots). It is equivalent to the change in MP from atmospheric pressure to 55 kbar. As shown in Figure S3, by applying a mechanical pressure of ≤300 kbar, we can obtain a Dq value of ≤2000 cm^{-1}.

In summary, in the studied material, changing x to approximately 0.1 is equivalent to applying a mechanical pressure of ~3.4 kbar. In the Al-doped Ga$_2$O$_3$ material, the maximum x value at which material can be doped without causing a phase transition is 1.6, which gives an equal pressure
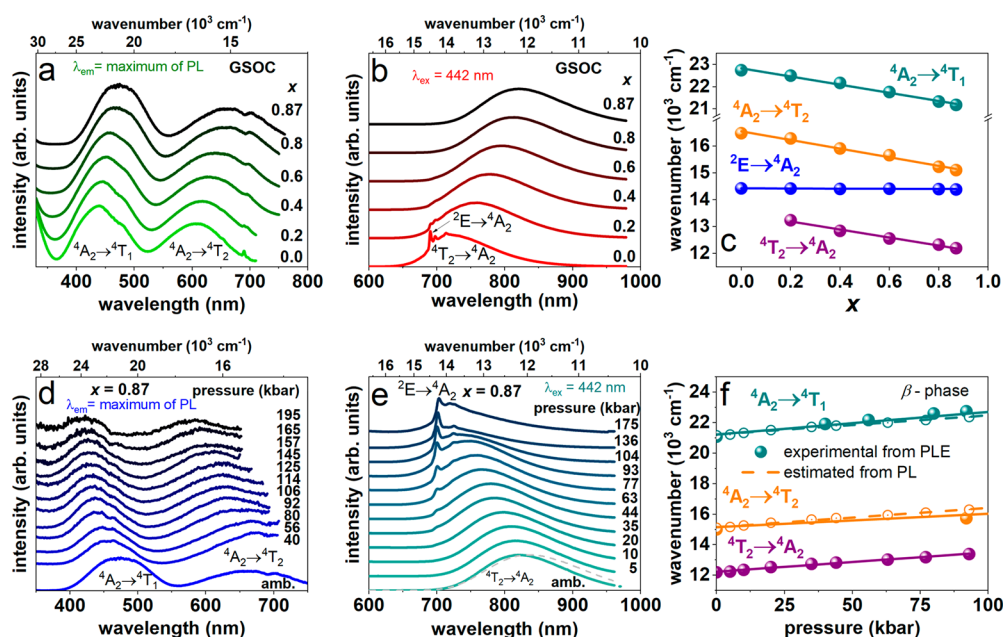
Figure 4. (a) RT PLE spectra, (b) PL spectra, and (c) positions of excitation bands and narrow line emission vs x content of $Ga_{2-x}Sc_xO_3:Cr^{3+}$ for x = 0−0.87. Pressure-dependent (d) PLE and (e) PL spectra and (f) positions of excitation bands and narrow line emission vs pressure for GSOC (x = 0.87). PL spectra were recorded upon excitation at 442 nm, and PLE spectra were observed at maximum luminescence.

of ∼55 kbar, a quite broad range in the case of chemical pressure. Figure 3b compares the C and B parameters for CP (cyan color) and MP (orange color). Surprisingly, the C values match ideally for CP and MP. In the case of B values, there is little difference in slope for CP and MP, but they still fit satisfactorily. These results show that, in this case, CP has the same tendency as MP. In this case, matrix modification does not significantly influence the chemical bond character as it would take place by substituting ions in the first coordination zone. In our case, we consider it an ion substitution in the neighboring unit cell, which changes the crystal volume and chemical bond characteristics, like mechanical pressure does.

Figure 3c compares the ^2E and $^4T_1$ state changes obtained by CP and MP. The behavior of the $^4T_1$ state is quite similar, while the slope for the ^2E state is slightly different. The MP, in this case, is equivalent to the CP, which is schematically shown in Figure 3d.

2.2. $Ga_{2-x}Sc_xO_3:Cr^{3+}$. Figure 4a shows the room-temperature PLE spectra of $Ga_{2-x}Sc_xO_3:Cr^{3+}$ (GSOC; x = 0, 0.2, 0.4, 0.6, 0.8, and 0.87) observed at maximum luminescence, where the x = 0 sample is the previously described $Ga_2O_3:Cr^{3+}$ sample. With an increase in x, excitation bands related to the $^4A_2 \rightarrow {^4T_2}$ and $^4A_2 \rightarrow {^4T_1}$ transitions shift toward lower energies, which is the opposite to the GAOC samples. Such an effect is expected due to the reduction in crystal field strength Dq in the vicinity of Cr^{3+} ions caused by the incorporation of larger Sc ions in place of Ga ions.

Figure 4b shows the PL spectra of GSOC upon excitation at 442 nm. Codoping with Sc causes a red-shift of the emission spectra related to the $^4T_2 \rightarrow {^4A_2}$ transition. The $^2E \rightarrow {^4A_2}$ line transition is visible only for samples with low scandium content (x = 0 and 0.2).

The energies of the $^4A_2 \rightarrow {^4T_1}$ and $^4A_2 \rightarrow {^4T_2}$ transition maxima were determined from excitation, and those of the $^4T_2 \rightarrow {^4A_2}$ transition from the PL spectra. It is possible to determine the maxima of the $^2E \rightarrow {^4A_2}$ transition at room temperature only for x = 0 and 0.2 samples. For other samples,

we took the position of the ^2E state from the luminescence at 10 K shown in previous studies.[20] Because of the temperature shift of the ^2E state, we checked the energy difference of this state in 10 K and RT for x = 0 and 0.2. Assuming that the temperature shift is the same for all samples (3.5 nm), we estimated the position of the ^2E state at RT. The results are shown in Figure 4c. The errors are contained in the size of the points. As x increases, the locations of the $^4A_2 \rightarrow {^4T_1}$ and $^4A_2 \rightarrow {^4T_2}$ excitation bands and the $^4T_2 \rightarrow {^4A_2}$ emission bands shift linearly toward lower energies. The parameters acquired from the linear fit are listed in Table S2.

Panels d and e of Figure 4 show pressure-dependent PLE upon observation at a maximum luminescence and PL spectra upon excitation at 442 nm for the sample with the highest Sc content (GSOC; x = 0.87). The $^4A_2 \rightarrow {^4T_1}$ and $^4A_2 \rightarrow {^4T_2}$ excitation bands shift toward higher energy (Figure 4d). A similar pressure-induced blue-shift has also been observed for the PL spectra related to the $^4T_2 \rightarrow {^4A_2}$ broadband emission for pressures of ≤104 kbar. For higher pressures, only narrow line emission is observed, and this is due to the increase in energy separation between the $^4T_2$ and ^2E states and phase transition. After pressure is released, the emission spectra are slightly different and shift toward lower energies. Similar to the case in GAOC, in GSOC, the pressure-induced phase transition occurs at ∼100 kbar and is irreversible.

Due to the experimental setup limitation, we could not correctly record the $^4A_2 \rightarrow {^4T_2}$ transition band up to 92 kbar. For pressures of ≤100 kbar (β phase), we estimated the energy of the $^4A_2 \rightarrow {^4T_1}$ and $^4A_2 \rightarrow {^4T_2}$ bands from the $^4T_2 \rightarrow {^4A_2}$ transition from PL spectra in Figure 4e and summarized in Table S2. The energy difference between the $^4A_2 \rightarrow {^4T_1}$ and $^4A_2 \rightarrow {^4T_2}$ transitions does not change, and $S\hbar\omega$ increases very slightly with pressure. However, we assumed that the pressure changes in $S\hbar\omega$ are small enough to be neglected in further analysis (the assumption is compatible with the stable full width at half-maximum under high pressure). A comparison of the $^4A_2 \rightarrow {^4T_1}$ and $^4A_2 \rightarrow {^4T_2}$ energies for the β phase
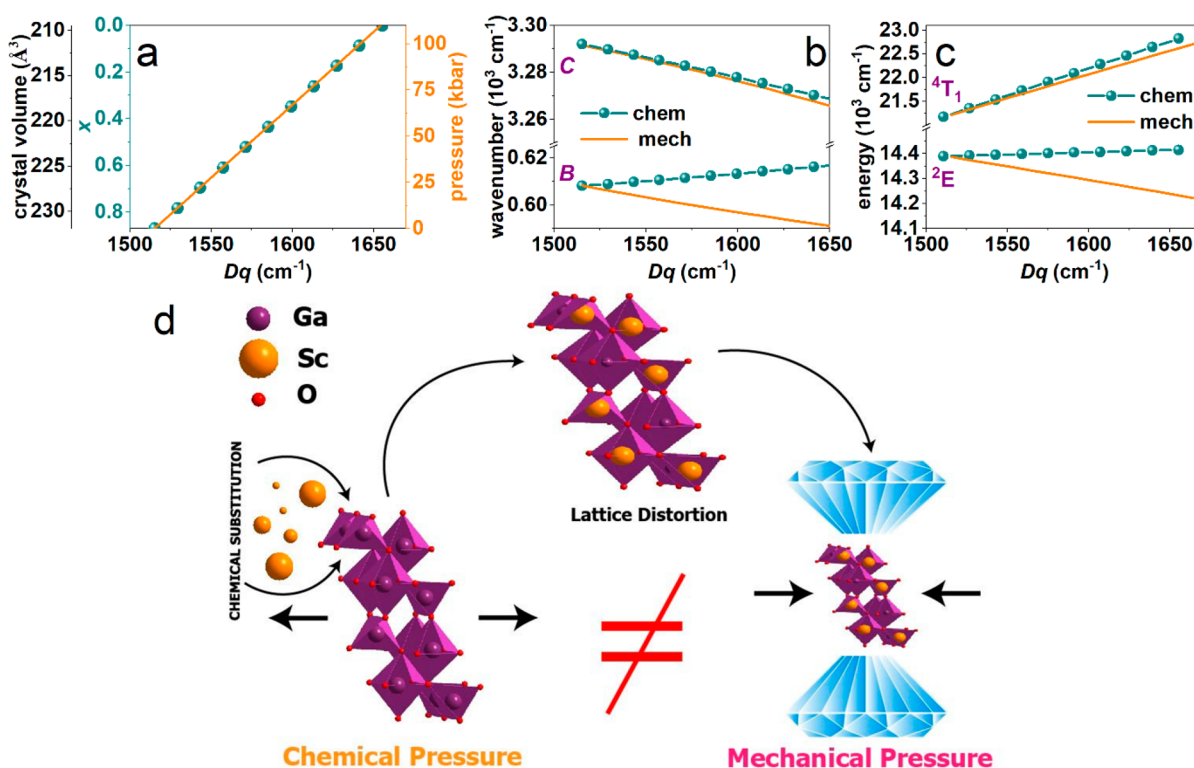
Figure 5. Comparison of the (a) Dq value, (b) C and B parameters, and (c) ^2E and $^4T_1$ states for mechanical and chemical pressure. (d) Schematic view of the influence of chemical and mechanical pressure on GSOC samples.

estimated from PL spectra and taken from PLE spectra is shown in Figure 4f, indicating good agreement. To compare the CP and MP, only the β phase is considered, and the pressure shift of the α phase is shown in the Supporting Information. The pressure dependence of the $^4A_2 \rightarrow {}^4T_1$, $^4A_2 \rightarrow {}^4T_2$, and $^4A_2 \rightarrow {}^4T_2$ transitions is presented in Figure S4a, and the energy of the R line is shown in Figure S4b. The errors are within the point size. Linear fitting was performed to estimate the $^4A_2 \rightarrow {}^4T_1$ and $^4A_2 \rightarrow {}^4T_2$ energies, and the parameters of the linear shift caused by MP before and after the phase transition are listed in Table S2, together with the parameters of the linear shift caused by CP.

Figure S4c shows the Dq, B, and C values for the applied CP, while Figure S4d those for MP, calculated using eqs S1 and S2. As x increases, as expected, Dq decreases (increasing the Cr–O distance) as does the B parameter, while C increases, which is the opposite of the case for GAOC. As the pressure increases, the Dq parameter increases as expected while the values of B and C decrease. In the case of chemical pressure, we also observe the opposite behavior for B and C parameters, the same as for the GAOC sample.

Figure 5a compares the Dq values obtained using CP (cyan color) and MP (orange color). Codoping of Ga_2O_3 with Sc causes a decrease in the crystal field strength, opposite, when mechanical pressure is applied. On the contrary, reducing the x content of Sc in $Ga_{2-x}Sc_xO_3$:Cr^{3+} from 0.87 to 0.0 causes a decrease in the unit cell volume from 231.9 to 209.5 Å^3, and the Dq value increases from 1510 to 1670 cm^{-1} (cyan dots). It is equivalent to the change in MP from atmospheric pressure to ~110 kbar (changing x to 0.1 is equivalent to applying an MP of 12.6 kbar).

Figure 5b compares the B and C parameters, while Figure 5c compares the ^2E and $^4T_1$ state changes for CP (cyan color) and

MP (orange color). The behavior of C and the $^4T_1$ state are similar for both CP and MP, while the B parameters and ^2E state have the opposite tendency. In the case of chemical pressure, the behavior of the ^2E state with Sc codoping is the opposite of what is expected. As Dq increases (the x content decreases), the ^2E state shifts toward higher energies (blue-shift) and not toward the expected lower energies (red-shift). Along with the decrease in x content, the Cr–O distances decrease. Nevertheless, the local environment changes, as well, and this change in the local environment has a more substantial influence on the behavior of the ^2E state, weakening the nephelauxetic effect even though decreasing the distance should increase it. This shows that CP and MP are not equivalent to Sc-doped Ga_2O_3.

In conclusion, it is seen that for the sample codoped with Al, the effect of CP and MP is equivalent, which means, as described previously, that matrix modification by Al does not significantly influence the chemical bond angles. In the case of Sc-doped samples, CP and MP do not follow the same tendency. The Sc ion may strongly influence the chemical bond lengths and angles, causing changes in lattice distortion. The codoping by scandium changes the structure, as confirmed by Raman spectra, which will be discussed below. By applying pressure for GSOC, we reduce the volume of the cell, but we cannot reverse the distortion caused by the codoping. The MP, in this case, is not equivalent to the CP, which is schematically shown in Figure 5d.

2.3. Raman Spectra. Figure 6a shows the x-dependent RT Raman frequency values for $x = 0.0$ (GOC), 0.2, 0.4, 0.6, 0.8, and 0.87 at room temperature and ambient pressure. The GOC ($x = 0$) sample shows 11 Raman lines from 100 to 900 cm^{-1}, with the most intense line at 201 cm^{-1}, which agrees with the literature.[43,61,62] The values of the Raman peaks are
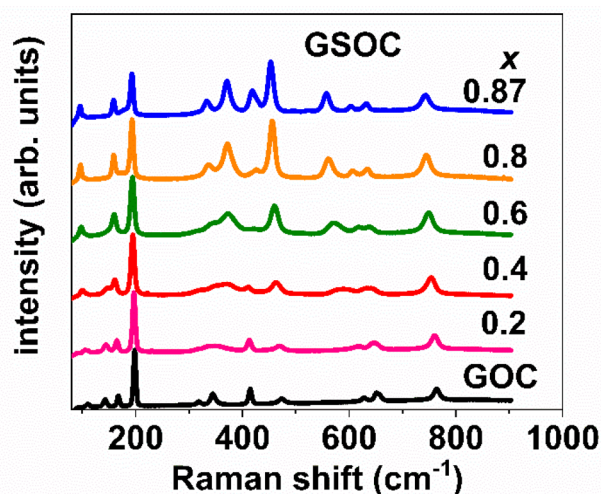
Figure 6. Raman spectra of $Ga_{2-x}Sc_xO_3$:Cr^{3+} for different values of x (0−0.87) under room conditions.

listed in Table S3. The observed Raman peaks can be classified into three groups: (i) libration and translation of the Ga_IO_4 chains for the $A_g^{(1)}$−$A_g^{(3)}$, $B_g^{(1)}$, and $B_g^{(2)}$ modes, (ii) deformation of the Ga_IO_4 and $Ga_{II}O_6$ chains for the $A_g^{(4)}$−$A_g^{(6)}$, $B_g^{(3)}$, and $B_g^{(4)}$ modes, and (iii) stretching and bending of the Ga_IO_4 chains for the $A_g^{(7)}$−$A_g^{(10)}$ and $B_g^{(5)}$ modes.[61] With an increase in x, the Raman peaks broaden up to $x = 0.6$, and for higher values of x, they begin to be well resolved again. The broadening of the Raman peaks in the spectra with an increase in x suggests an increase in the degree of environmental disorder and an increase in the distribution of lattice vibration energies in the crystal up to $x = 0.6$. With a further increase in x, ordering in the crystal structure appears, which is proven by spectroscopic studies by Fang et al.[20] Additionally, the Raman peaks shift with an increase in x (see Figure S5) and the linear shift parameter is summarized in Table S3. All Raman peaks shift toward lower energies, except the $B_g^{(2)}$ mode, which shifts toward higher energies. Incorporation of Sc^{3+} with an atomic weight (44.96 u) lower than that of Ga^{3+} (69.72 u) is expected to cause a shift of the Raman peaks toward a higher wavenumber. However, increasing the interatomic distance by incorporating larger Sc^{3+} ions in place of Ga^{3+} ions leads to a decrease in the Raman peak frequencies. The observed shift in the Raman spectra of GSOC is a combination of both effects. For the $x \geq 0.8$ samples, there is a significant difference in the intensities of the Raman peaks, where the most intense line for GSOC is located at 457 cm^{-1}. Furthermore, the line at 142 cm^{-1} disappears, and an additional line appears in the Raman spectra at 561 cm^{-1}, which is not observed in the GOC Raman spectra. This line is related to the scandium codopant (Sc−O Raman mode). The change in the Raman spectra for $x \geq 0.8$ samples confirms the previously discussed change in crystal structure with Sc codoping.

Theoretical calculations were performed to support the experimental data. From the calculation studies of Ga_2O_3, there are 30 vibration modes, where 15 are Raman-active and 15 are IR-active modes. The lattice parameters of the studied materials used for calculation are listed in ref 20.

Figure S6 shows the experimental Raman spectra with the theoretically calculated Raman spectra of GOC and GSOC for $x = 0.87$ at room temperature and ambient pressure. In many cases, the relative intensities of Raman modes can be correlated

with the type of atomic displacement involved. The substitution of Ga by Sc is expected to decrease the overall mass and is likely to lead to a decrease in Raman intensity. Vertical ticks in panels a and b of Figure S6 indicate the *ab initio*-computed frequencies of first-order Raman-active modes. The frequency values of the calculated and experimental Raman modes are listed in Tables S4 and S5 for GOC and GSOC ($x = 0.87$), respectively. Panels c and d of Figure S6 show the theoretically calculated intensities of the Raman modes. We can see that the experimental Raman spectra agree satisfactorily with the theoretical prediction for GOC and GSOC.

Theoretical and experimental high-pressure investigations of Raman spectra were also performed. The analysis and discussion can be found in the Supporting Information.

3. CONCLUSIONS

This study focuses on the comparison between chemical and mechanical pressure for two reference series of samples: $Ga_{2-x}Al_xO_3$:Cr^{3+} (GAOC; $x = 0−2$; step 0.2) and $Ga_{2-x}Sc_xO_3$:Cr^{3+} (GSOC; $x = 0−087$; step 0.2). We found that GAOC exhibits qualitatively the same behavior, while GSOC exhibits different behavior of chemical and mechanical pressure dependences of the luminescence properties. In the case of Al, we can consider it as ion substitution in the neighbor unit cell, which changes the crystal properties like mechanical pressure does. Codoping of Ga_2O_3 with Sc ions causes lattice distortion in the Cr^{3+} local environment, and by applying pressure for GSOC, we reduce the volume of the cell; however, we cannot reverse the distortion caused by the codoping.

Additionally, for GAOC, the x- and pressure-dependent energy diagrams were calculated, considering the change in Racah parameters with pressure. The energy structure diagrams presented in the paper show a decrease in the energy of the excited levels belonging to the t_2^3 crystal field configuration (^2E, $^2T_1$, and $^2T_2$) with an increase in Dq (in the case of both pressure- and x-dependent results). This behavior is consistent with the observed change in the direction of the $^2E \rightarrow {}^4A_2$ transition. It seems correct that a high-pressure experiment involving Cr^{3+} and other transition metals should be performed using the method and diagrams presented in this paper.

4. EXPERIMENTAL METHODS

4.1. Spectroscopic Characterization. RT photoluminescence excitation (PLE) spectra were recorded with a FluoroMax-4P spectrofluorometer (Horiba) equipped with a 150 W xenon lamp as an excitation source and a model R928 Hamamatsu photomultiplier as a detector.

The pressure-dependent emission spectra were recorded using an Andor SR-750-D1 spectrometer equipped with a CCD camera (DU420A-OE) and a Kimmon Koha He−Cd laser at 442 nm.

The decay profiles were measured using a time-resolved spectroscopy apparatus consisting of a PG 401/SH optical parametric generator pumped by a PL2251A pulsed YAG:Nd laser (EKSPLA). The detection comprises a 2501S grating spectrometer (Bruker Optics) combined with a C4334-01 streak camera (Hamamatsu). Data were recorded as streak images on a 640 pixel × 480 pixel CCD array. Software based on the photon counting algorithm transforms the result into a two-dimensional matrix of photon counts versus wavelength and time (streak image).[63]

Raman spectra were recorded using a confocal micro-Raman system equipped with a microscope and a Horiba Jobin Yvon Lab

Ram Aramis spectrometer with a laser providing excitation light at 532 nm with a 1800 l/mm grating.

High-pressure luminescence measurements were performed in a screw-driven Merrill-Bassett-type diamond anvil cell with a 0.5 mm diamond culet diameter.[64] The gasket for the pressure chamber was preindented to 0.07 mm. A hole with a diameter of 0.2 mm was drilled in the center of the indentation. $KMgF_3$:0.5%Eu^{2+} was used as a pressure sensor,[65] and polydimethylsiloxane oil was used as a pressure-transmitting medium.

4.2. Energy Diagram Calculation. The energy levels were calculated by diagonalizing the $\mathcal{H}_{CF} + \mathcal{H}_{ee}$ Hamiltonian matrices for the respective subterms (matrices 1−8 in the Supporting Information).[66,67] The matrix row describes a given subterm of the crystal field and can have dimensions from 1 to 5. The row of the above matrix is associated with mixing crystal field subterms with the same symbol, derived from different atomic terms and, in particular, from different crystal field configurations. For such subterms, the lines in the energy diagram are curved (a similar phenomenon occurs in T−S diagrams). Details of the calculation methods are described in ref 68.

4.3. Theoretical *Ab Initio* Simulation Details. *Ab initio* calculations for β- and α-Ga_2O_3 were performed within the framework of density functional theory.[69] This work used the generalized gradient approximation (GGA) with the Perdew−Burke−Ernzerhof parametrization for solids (PBEsol) for the exchange and correlation energy.[70] A dense Monkhorst−Pack grid of special k-points[71] ($6 \times 6 \times 6$ for the C phase and $4 \times 4 \times 4$ for the A and B phases) and a plane-wave basis set with energy cutoffs of 530 eV were used. This ensures convergence of 1 meV per formula unit for the total energy. For each phase, the lattice parameters and atomic positions at selected volumes were fully optimized by calculating the forces on the atoms and the stress tensor. The optimization criterion was to relax the configuration until the deviations of the stress tensor from the diagonal form were <0.1 GPa. The forces on the atoms were <0.004 eV/Å. The stress for each volume and theoretical pressure $P(V)$ were obtained through this process. The set of accurate values of energy (E), volume (V), and pressure (P), provided by calculations, allows us to derive the enthalpy (H) as a pressure function $H(P)$ and to determine the relative stability of the phase under study and the transition pressure. Lattice-dynamical properties were obtained for the Γ point using the direct force constants approach at several pressures.[72] The diagonalization of the dynamical matrix, which requires separate calculations of highly converged forces, provides the frequency of the Raman and infrared modes. These calculations also allow the identification of the symmetry and eigenvectors of the vibrational modes for the considered structure. The Raman spectra were simulated using Phonon[73] under nonpolarized light and polycrystalline sample conditions.

ASSOCIATED CONTENT

SI Supporting Information

The Supporting Information is available free of charge at https://pubs.acs.org/doi/10.1021/acs.chemmater.3c00203.

Linear shift parameters for optical transitions in GAOC for chemical and mechanical pressure for the β and α phases (Table S1); dependence of Dq, B, and C on x content and pressure (MP) for the β and α phases (Figure S1); extrapolated pressure-dependent Dq, B, and C parameters in the range of 0−500 kbar for the β and α phases for GAOC; energy structure diagram of all subterms of the d^3 configuration of the Cr^{3+} ion as a function of x and pressure for GOC ($x = 0$) in the α and β phases together with the Dq/B behavior (Figure S2); comparison of the Dq values for chemical and mechanical pressure (Figure S3); experimental and calculated positions of two excited states from emission spectra and the position of the R line versus pressure;

dependence of Dq, B, and C on x content (CP) and pressure (MP) for the β phases (Figure S4); linear shift parameters for optical transitions in GSOC for chemical pressure and mechanical pressure for the β and α phases (Table S2); x-dependent spectral positions of the Raman peaks of the phonon modes of β-Ga_2O_3 (Figure S5); experimental and theoretical Raman spectra of GOC and GSOC ($x = 0.87$) (Figure S6); spectral positions of the Raman peaks of the phonon modes of β-Ga_2O_3 (in inverse centimeters) and spectral shift rate β of selected Raman peaks (Table S3); theoretical and experimental zero-pressure frequencies ω_0 and linear pressure coefficients a of the Raman-active modes in the β phase of GOC and GSOC (Tables S4 and S5); and pressure-dependent experimental Raman spectra of GOC and GSOC and pressure-dependent experimental and theoretical frequencies of the Raman-active modes observed in GOC and GSOC ($x = 0.87$) (Figure S7) (PDF)

AUTHOR INFORMATION

Corresponding Author

Natalia Majewska − *Institute of Experimental Physics, Faculty of Mathematics, Physics and Informatics, University of Gdansk, 80-308 Gdansk, Poland;* ⓞ orcid.org/0000-0002-1933-0355; Email: natalia.majewska@phdstud.ug.edu.pl

Authors

Alfonso Muñoz − *Departamento Física, Malta Consolider Team, and Instituto de Materiales y Nanotecnología, Universidad de La Laguna, La Laguna 38206 Tenerife, Spain;* ⓞ orcid.org/0000-0003-3347-6518

Ru-Shi Liu − *Department of Chemistry, National Taiwan University, Taipei 106, Taiwan;* ⓞ orcid.org/0000-0002-1291-9052

Sebastian Mahlik − *Institute of Experimental Physics, Faculty of Mathematics, Physics and Informatics, University of Gdansk, 80-308 Gdansk, Poland;* ⓞ orcid.org/0000-0002-9514-049X

Complete contact information is available at:
https://pubs.acs.org/10.1021/acs.chemmater.3c00203

Notes

The authors declare no competing financial interest.

ACKNOWLEDGMENTS

REFERENCES

(1) Zhuang, Y.; Ueda, J.; Tanabe, S. Enhancement of Red Persistent Luminescence in Cr^{3+}-Doped $ZnGa_2O_4$ Phosphors by Bi_2O_3 Codoping. *Appl. Phys. Express* **2013**, *6*, No. 052602.

(2) Katayama, Y.; Kobayashi, H.; Tanabe, S. Deep-Red Persistent Luminescence in Cr^{3+}-Doped LaAlO3 Perovskite Phosphor for in Vivo Imaging. *Appl. Phys. Express* **2015**, *8*, No. 012102.

(3) Viana, B.; Sharma, S. K.; Gourier, D.; Maldiney, T.; Teston, E.; Scherman, D.; Richard, C. Long Term In vivo Imaging with Cr^{3+} Doped Spinel Nanoparticles Exhibiting Persistent Luminescence. *J. Lumin.* **2016**, *170*, 879−887.

(4) Basavaraju, N.; Sharma, S.; Bessière, A.; Viana, B.; Gourier, D.; Priolkar, K. R. Red Persistent Luminescence in $MgGa_2O_4$:Cr^{3+}; a New Phosphor for in Vivo Imaging. *J. Phys. D: Appl. Phys.* **2013**, *46*, 375401.

(5) Sharma, S. K.; Gourier, D.; Viana, B.; Maldiney, T.; Teston, E.; Scherman, D.; Richard, C. Persistent Luminescence of AB_2O_4:Cr^{3+} (A = Zn, Mg, B = Ga, Al) Spinels: New Biomarkers for in Vivo Imaging. *Opt. Mater.* **2014**, *36*, 1901−1906.

(6) Wang, C.; Wang, X.; Zhou, Y.; Zhang, S.; Li, C.; Hu, D.; Xu, L.; Jiao, H. An Ultra-Broadband Near-Infrared Cr^{3+}-Activated Gallogermanate $Mg_3Ga_2GeO_8$ Phosphor as Light Sources for Food Analysis. *ACS Appl. Electron. Mater.* **2019**, *1*, 1046−1053.

(7) Rajendran, V.; Fang, M.-H.; Guzman, G. N. D.; Lesniewski, T.; Mahlik, S.; Grinberg, M.; Leniec, G.; Kaczmarek, S. M.; Lin, Y.-S.; Lu, K.-M.; Lin, C.-M.; Chang, H.; Hu, S.-F.; Liu, R.-S. Super Broadband Near-Infrared Phosphors with High Radiant Flux as Future Light Sources for Spectroscopy Applications. *ACS Energy Lett.* **2018**, *3*, 2679−2684.

(8) Huang, L.; Li, Z.; Zhao, Y.; Yang, J.; Yang, Y.; Pendharkar, A. I.; Zhang, Y.; Kelmar, S.; Chen, L.; Wu, W.; Zhao, J.; Han, G. Enhancing Photodynamic Therapy through Resonance Energy Transfer Constructed Near-Infrared Photosensitized Nanoparticles. *Adv. Mater.* **2017**, *29*, 1604789.

(9) Fang, Y.; Shang, J.; Liu, D.; Shi, W.; Li, X.; Ma, H. Design, Synthesis, and Application of a Small Molecular NIR-II Fluorophore with Maximal Emission beyond 1200 Nm. *J. Am. Chem. Soc.* **2020**, *142*, 15271−15275.

(10) Chen, D.; Wan, Z.; Zhou, Y.; Ji, Z. Cr^{3+}-Doped Gallium-Based Transparent Bulk Glass Ceramics for Optical Temperature Sensing. *J. Eur. Ceram. Soc.* **2015**, *35*, 4211−4216.

(11) Ueda, J.; Back, M.; Brik, M. G.; Zhuang, Y.; Grinberg, M.; Tanabe, S. Ratiometric Optical Thermometry Using Deep Red Luminescence from $^4T_2$ and ^2E States of Cr^{3+} in $ZnGa_2O_4$ Host. *Opt. Mater.* **2018**, *85*, 510−516.

(12) Back, M.; Ueda, J.; Brik, M. G.; Tanabe, S. Pushing the Limit of Boltzmann Distribution in Cr^{3+}-Doped $CaHfO_3$ for Cryogenic Thermometry. *ACS Appl. Mater. Interfaces* **2020**, *12*, 38325−38332.

(13) Back, M.; Ueda, J.; Brik, M. G.; Lesniewski, T.; Grinberg, M.; Tanabe, S. Revisiting Cr^{3+}-Doped $Bi_2Ga_4O_9$ Spectroscopy: Crystal Field Effect and Optical Thermometric Behavior of Near-Infrared-Emitting Singly-Activated Phosphors. *ACS Appl. Mater. Interfaces* **2018**, *10*, 41512−41524.

(14) Brites, C. D. S.; Lima, P. P.; Silva, N. J. O.; Millán, A.; Amaral, V. S.; Palacio, F.; Carlos, L. D. Thermometry at the Nanoscale. *Nanoscale* **2012**, *4*, 4799−4829.

(15) Szymczak, M.; Woźny, P.; Runowski, M.; Pieprz, M.; Lavín, V.; Marciniak, L. Temperature Invariant Ratiometric Luminescence Manometer Based on Cr^{3+} Ions Emission. *Chem. Eng. J.* **2023**, *453*, 139632.

(16) Szymczak, M.; Runowski, M.; Lavín, V.; Marciniak, L. Highly Pressure-Sensitive, Temperature Independent Luminescence Ratiometric Manometer Based on MgO:Cr^{3+} Nanoparticles. *Laser Photonics Rev.* **2023**, *17*, 2200801.

(17) Back, M.; Ueda, J.; Nambu, H.; Fujita, M.; Yamamoto, A.; Yoshida, H.; Tanaka, H.; Brik, M. G.; Tanabe, S. Boltzmann Thermometry in Cr^{3+}-Doped Ga_2O_3 Polymorphs: The Structure Matters! *Adv. Opt. Mater.* **2021**, *9*, 2100033.

(18) Fang, M.-H.; De Guzman, G. N.; Bao, Z.; Majewska, N.; Mahlik, S.; Grinberg, M.; Leniec, G.; Kaczmarek, S.; Yang, C.-W.; Lu, K.-M.; Sheu, H.-S.; Hu, S.-F.; Liu, R.-S. Ultra-High-Efficiency Near-Infrared Ga_2O_3:Cr^{3+} Phosphor and Controlling of Phytochrome. *J. Mater. Chem. C* **2020**, *8*, 11013−11017.

(19) Luchechko, A.; Vasyltsiv, V.; Zhydachevskyy, Y.; Kushlyk, M.; Ubizskii, S.; Suchocki, A. Luminescence Spectroscopy of Cr^{3+} Ions in Bulk Single Crystalline β-Ga_2O_3. *J. Phys. D: Appl. Phys.* **2020**, *53*, 354001.

(20) Fang, M.-H.; Chen, K.-C.; Majewska, N.; Leśniewski, T.; Mahlik, S.; Leniec, G.; Kaczmarek, S. M.; Yang, C.-W.; Lu, K.-M.; Sheu, H.-S.; Liu, R.-S. Hidden Structural Evolution and Bond Valence Control in Near-Infrared Phosphors for Light-Emitting Diodes. *ACS Energy Lett.* **2021**, *6*, 109−114.

(21) Dereń, P. J.; Watras, A.; Gągor, A.; Pązik, R. Weak Crystal Field in Yttrium Gallium Garnet (YGG) Submicrocrystals Doped with Cr^{3+}. *Cryst. Growth Des.* **2012**, *12*, 4752−4757.

(22) Bassett, W. A. Diamond Anvil Cell, 50th Birthday. *High Press. Res.* **2009**, *29*, 163−186.

(23) Grinberg, M. Principles of Energetic Structure and Excitation-Energy Transfer Based on High-Pressure Measurements. In *Phosphors, Up Conversion Nano Particles, Quantum Dots and Their Applications: Vol. 1*; Liu, R.-S., Ed.; Springer: Berlin, 2017; pp 67−151.

(24) Syassen, K. Ruby under Pressure. *High Press. Res.* **2008**, *28*, 75−126.

(25) Suchocki, A.; Biernacki, S. W.; Kamińska, A.; Arizmendi, L. Nephelauxetic Effect in Luminescence of Cr^{3+}-Doped Lithium Niobate and Garnets. *J. Lumin.* **2003**, *102−103*, 571−574.

(26) Suchocki, A.; Biernacki, S. W.; Grinberg, M. Nephelauxetic Effect in High-Pressure Luminescence of Transition-Metal Ion Dopants. *J. Lumin.* **2007**, *125*, 266−270.

(27) Biernacki, S. W.; Kamińska, A.; Suchocki, A.; Arizmendi, L. Nephelauxetic Effect in LiNbO$_3$:Cr^{3+} Crystals. *Appl. Phys. Lett.* **2002**, *81*, 442−444.

(28) Gluchowski, P.; Strek, W. Luminescence and Excitation Spectra of Cr^{3+}:$MgAl_2O_4$ Nanoceramics. *Mater. Chem. Phys.* **2013**, *140*, 222−227.

(29) Goto, T.; Ahrens, T. J.; Rossman, G. R. Absorption Spectra of Cr^{3+} in Al_2O_3 under Shock Compression. *Phys. Chem. Minerals* **1979**, *4*, 253−263.

(30) Taran, M. N.; Ohashi, H.; Langer, K.; Vishnevskyy, A. A. High-Pressure Electronic Absorption Spectroscopy of Natural and Synthetic Cr^{3+}-Bearing Clinopyroxenes. *Phys. Chem. Minerals* **2011**, *38*, 345−356.

(31) Duclos, S. J.; Vohra, Y. K.; Ruoff, A. L. Pressure Dependence of the $^4T_2$ and $^4T_1$ Absorption Bands of Ruby to 35 GPa. *Phys. Rev. B* **1990**, *41*, 5372−5381.

(32) Sugano, S. *Multiplets of Transition-Metal Ions in Crystals*; Elsevier, 2012.

(33) Fernandes, A. A. R.; Santamaria, J.; Bud'ko, S. L.; Nakamura, O.; Guimpel, J.; Schuller, I. K. Effect of Physical and Chemical Pressure on the Superconductivity of High-Temperature Oxide Superconductors. *Phys. Rev. B* **1991**, *44*, 7601−7606.

(34) Wang, T.; LI, W.; Ni, C.; Janotti, A. Band Gap and Band Offset of Ga_2O_3 and $(Al_xGa_{1-x})_2O_3$ Alloys. *Phys. Rev. Applied* **2018**, *10*, No. 011003.

(35) Morgan, G. P.; Treacy, J. F.; Glynn, T. J.; Imbusch, G. F.; Remeika, J. P. Luminescence from $Al_{2x}Ga_{2(1-x)}O_3$:Cr^{3+}. *J. Lumin.* **1979**, *18−19*, 175−178.

(36) Schneider, S. J.; Waring, J. L. Phase Equilibrium Relations in the Sc_2O_3-Ga_2O_3 System. *J. Res. Natl. Bur. Stand A Phys. Chem.* **1963**, *67A*, 19−25.

(37) Kuz'micheva, G. M.; Rybakov, V. B.; Kutovoi, S. A. Preparation and Structure of $Ga_{2-x}Sc_xO_3$ ($0.42 \leq x \leq 0.52$). *Inorg. Mater.* **2004**, *40*, 1066−1069.

(38) Jesenovec, J.; Dutton, B. L.; Remple, C.; Smith-Gray, N.; Murugesan, M.; Peterson, C.; Downing, B. K.; Krishnamoorthy, S.; McCluskey, M. D.; McCloy, J. S. Alternative Alloy to Increase Bandgap in Gallium Oxide, β-$(Sc_xGa_{1-x})_2O_3$, and Rare Earth Stark Luminescence. *J. Cryst. Growth* **2022**, *596*, 126823.

(39) Yahia, H. B.; van Wüllen, L.; Balamurugan, S.; Rodewald, U. C.; Eckert, H.; Pöttgen, R. Single-Crystal Structure and Solid-State NMR of $Ga_{2-x}Sc_xO_3$ (x = 0.83). *Z. Naturforsch. B* **2011**, *66*, 14−20.

(40) Chen, K.-C.; Fang, M.-H.; Huang, W.-T.; Kamiński, M.; Majewska, N.; Leśniewski, T.; Mahlik, S.; Leniec, G.; Kaczmarek, S. M.; Yang, C.-W.; Lu, K.-M.; Sheu, H.-S.; Liu, R.-S. Chemical and Mechanical Pressure-Induced Photoluminescence Tuning via Structural Evolution and Hydrostatic Pressure. *Chem. Mater.* **2021**, *33*, 3832−3840.

(41) Shannon, R. D. Revised Effective Ionic Radii and Systematic Studies of Interatomic Distances in Halides and Chalcogenides. *Acta Cryst. A* **1976**, *32*, 751−767.

(42) Fang, M.-H.; Li, T.-Y.; Huang, W.-T.; Cheng, C.-L.; Bao, Z.; Majewska, N.; Mahlik, S.; Yang, C.-W.; Lu, K.-M.; Leniec, G.; Kaczmarek, S. M.; Sheu, H.-S.; Liu, R.-S. Surface-Protected High-Efficiency Nanophosphors via Space-Limited Ship-in-a-Bottle Synthesis for Broadband Near-Infrared Mini-Light-Emitting Diodes. *ACS Energy Lett.* **2021**, *6*, 659−664.

(43) Machon, D.; McMillan, P. F.; Xu, B.; Dong, J. High-Pressure Study of the β-to-α Transition in Ga_2O_3. *Phys. Rev. B* **2006**, *73*, No. 094125.

(44) He, H.; Orlando, R.; Blanco, M. A.; Pandey, R.; Amzallag, E.; Baraille, I.; Rérat, M. First-Principles Study of the Structural, Electronic, and Optical Properties of Ga_2O_3 in Its Monoclinic and Hexagonal Phases. *Phys. Rev. B* **2006**, *74*, 195123.

(45) Lipinska-Kalita, K. E.; Kalita, P. E.; Hemmers, O. A.; Hartmann, T. Equation of State of Gallium Oxide to 70 GPa: Comparison of Quasihydrostatic and Nonhydrostatic Compression. *Phys. Rev. B* **2008**, *77*, No. 094123.

(46) van Bunningen, A. J.; Sontakke, A. D.; Wakui, S.; Meijerink, A. Temperature Quenching of Cr^{3+} in $ASc(Si_{1-x}Ge_x)_2O_6$ (A = Li/Na) Solid Solutions. *Opt. Mater.* **2022**, *128*, 112433.

(47) Grinberg, M.; Barzowska, J.; Shen, Y.; Bray, K. L. Inhomogeneous Broadening of Cr^{3+} Luminescence in Doped $LiTaO_3$. *Phys. Rev. B* **2001**, *63*, 214104.

(48) Grinberg, M.; Barzowska, J.; Shen, Y. R.; Bray, K. L.; Dereń, P.; Hanuza, J. High-Pressure Spectroscopy Characterisation of $LiSc(WO_4)_2$ Crystals Doped with Trivalent Chromium. *J. Lumin.* **2003**, *102−103*, 699−704.

(49) Merkle, L. D.; Spain, I. L.; Powell, R. C. Effects of Pressure on the Spectra and Lifetimes of $Nd_xY_{1-x}P_5O_{14}$ and Ruby. *J. Phys. C: Solid State Phys.* **1981**, *14*, 2027−2038.

(50) Quérel, G.; Reynard, B. High-Pressure Luminescence Spectroscopy of Transition Elements: Experimental Setup and Preliminary Results on Cr^{3+} in Silicate Glasses. *Chem. Geol.* **1996**, *128*, 65−75.

(51) Bray, K. L. High Pressure Probes of Electronic Structure and Luminescence Properties of Transition Metal and Lanthanide Systems. In *Transition Metal and Rare Earth Compounds: Excited States, Transitions, Interactions I*; Yersin, H., Ed.; Topics in Current Chemistry; Springer: Berlin, 2001; pp 1−94.

(52) Yoshioka, S.; Hayashi, H.; Kuwabara, A.; Oba, F.; Matsunaga, K.; Tanaka, I. Structures and Energetics of Ga_2O_3 Polymorphs. *J. Phys.: Condens. Matter* **2007**, *19*, 346211.

(53) Luan, S.; Dong, L.; Jia, R. Analysis of the Structural, Anisotropic Elastic and Electronic Properties of β-Ga_2O_3 with Various Pressures. *J. Cryst. Growth* **2019**, *505*, 74−81.

(54) Varley, J. B.; Weber, J. R.; Janotti, A.; Van de Walle, C. G. Oxygen Vacancies and Donor Impurities in β-Ga_2O_3. *Appl. Phys. Lett.* **2010**, *97*, 142106.

(55) Caracas, R.; Cohen, R. E. Post-Perovskite Phase in Selected Sesquioxides from Density-Functional Calculations. *Phys. Rev. B* **2007**, *76*, 184101.

(56) Clark, S. J.; Segall, M. D.; Pickard, C. J.; Hasnip, P. J.; Probert, M. I. J.; Refson, K.; Payne, M. C. First Principles Methods Using CASTEP. *Z. Kristallogr. Cryst. Mater.* **2005**, *220*, 567−570.

(57) Furthmüller, J.; Bechstedt, F. Quasiparticle Bands and Spectra of Ga_2O_3 Polymorphs. *Phys. Rev. B* **2016**, *93*, 115204.

(58) Wang, H.; He, Y.; Chen, W.; Zeng, Y. W.; Stahl, K.; Kikegawa, T.; Jiang, J. Z. High-Pressure Behavior of β-Ga_2O_3 Nanocrystals. *J. Appl. Phys.* **2010**, *107*, No. 033520.

(59) Grinberg, M. High Pressure Spectroscopy of Rare Earth Ions Doped Crystals—New Results. *Opt. Mater.* **2006**, *28*, 26−34.

(60) Grinberg, M.; Suchocki, A. Pressure-Induced Changes in the Energetic Structure of the $3d^3$ Ions in Solid Matrices. *J. Lumin.* **2007**, *125*, 97−103.

(61) Onuma, T.; Fujioka, S.; Yamaguchi, T.; Itoh, Y.; Higashiwaki, M.; Sasaki, K.; Masui, T.; Honda, T. Polarized Raman Spectra in β-Ga_2O_3 Single Crystals. *J. Cryst. Growth* **2014**, *401*, 330−333.

(62) Kranert, C.; Sturm, C.; Schmidt-Grund, R.; Grundmann, M. Raman Tensor Elements of β-Ga_2O_3. *Sci. Rep.* **2016**, *6*, 35964.

(63) Kubicki, A. A.; Bojarski, P.; Grinberg, M.; Sadownik, M.; Kukliński, B. Time-Resolved Streak Camera System with Solid State Laser and Optical Parametric Generator in Different Spectroscopic Applications. *Opt. Commun.* **2006**, *263*, 275−280.

(64) Merrill, L.; Bassett, W. A. Miniature Diamond Anvil Pressure Cell for Single Crystal X-ray Diffraction Studies. *Rev. Sci. Instrum.* **1974**, *45*, 290−294.

(65) Barzowska, J.; Lesniewski, T.; Mahlik, S.; Seo, H. J.; Grinberg, M. $KMgF_3:Eu^{2+}$ as a New Fluorescence-Based Pressure Sensor for Diamond Anvil Cell Experiments. *Opt. Mater.* **2018**, *84*, 99−102.

(66) Henderson, B.; Imbusch, G. F. *Optical Spectroscopy of Inorganic Solids; Monographs on the Physics and Chemistry of Materials*; Oxford University Press: Oxford, U.K., 2006.

(67) Sugano, S. *Multiplets of Transition-Metal Ions in Crystals*; Elsevier, 2012.

(68) Leśniewski, T. Evolution of the full energy structure of Mn^{4+} in fluoride phosphors under high pressure conditions. *Phys. Chem. Chem. Phys.* **2023**, *25*, 14449.

(69) Hohenberg, P.; Kohn, W. Inhomogeneous electron gas. *Phys. Rev. B* **1964**, *136*, B864.

(70) Perdew, J. P.; Ruzsinszky, A.; Csonka, G. I.; Vydrov, O. A.; Scuseria, G. E.; Constantin, L. A.; Zhou, X.; Burke, K. Restoring the Density-Gradient Expansion for Exchange in Solids and Surfaces. *Phys. Rev. Lett.* **2008**, *100*, 136406.

(71) Monkhorst, H. J.; Pack, J. D. Special points for Brillouin-zone integrations. *Phys. Rev. B* **1976**, *13*, 5188.

(72) Parlinski, K.; Li, Z. Q.; Kawazoe, Y. First-Principles Determination of the Soft Mode in Cubic ZrO_2. *Phys. Rev. Lett.* **1997**, *78*, 4063.

(73) Parlinski, K.; Piekarz, P. Ab Initio Determination of Raman Spectra of Mg_2SiO_4 and $Ca_2MgSi_2O_7$ Showing Mixed Modes Related to LO/TO Splitting. *J. Raman Spectrosc.* **2021**, *52*, 1346−1359.

Supporting information

Chemical and Mechanical Pressure Influence on Luminescence Properties of Near-Infrared Phosphors

Natalia Majewska[1,], Alfonso Muñoz[2], Ru-Shi Liu[3], and Sebastian Mahlik[1]*

[1]Institute of Experimental Physics, Faculty of Mathematics, Physics and Informatics, University of Gdansk, Wita Stwosza 57, 80-308 Gdansk, Poland

[2]Departamento Física, Malta Consolider Team, and Instituto de Materiales y Nanotecnología, Universidad de La Laguna, La Laguna 38206, Tenerife, Spain

[3]Department of Chemistry, National Taiwan University, Taipei 106, Taiwan

Corresponding Author

Natalia Majewska - *e-mail address: natalia.majewska@phdstud.ug.edu.pl

Energy diagram calculation

4A2 (t23):

$$[-15B] \tag{1}$$

4T2 (t22(3T1)e):

$$[10Dq - 15B] \tag{2}$$

2A1 (t22(1E)e):

$$[10Dq - 11B + 3C] \tag{3}$$

2A2 (t22(1E)e):

$$[10Dq + 9B + 3C] \tag{4}$$

4T1 (t22(3T1)e, t2e2(3A2)):

$$\begin{bmatrix} 10Dq - 3B & 6B \\ & 20Dq - 12B \end{bmatrix} \tag{5}$$

2E (t23, t2e2(1A1), t22(1E)e, e3):

$$\begin{bmatrix} -6B + 3C & -6\sqrt{2}B & -3\sqrt{2} & 0 \\ & 10Dq + 8B + 6C & 10B & \sqrt{2}(2B + C) \\ & & 10Dq - B + 3C & 2\sqrt{3}B \\ & & & 30Dq - 4B + 4C \end{bmatrix} \tag{6}$$

2T2 (t23, t22(3T1)e, t22(1T2)e, t2e2(1A1) , t2e2(1E)):

$$\begin{bmatrix} 5C & -3\sqrt{3B} & -5\sqrt{3B} & 4B + 2C & 2B \\ & 10Dq - 6B + 3C & 3B & 3\sqrt{3B} & -3\sqrt{3B} \\ & & 10Dq + 4B + 3C & -\sqrt{3B} & \sqrt{3B} \\ & & & 20Dq + 6B + 5C & 10B \\ & & & & 20Dq - 2B + 3C \end{bmatrix} \tag{7}$$

2T1(t23, t22(3T1)e, t22(1T2)e, t2e2(3A2) , t2e2(1E)):

$$\begin{bmatrix} -6B+3C & -3B & 3B & 0 & -2\sqrt{3}B \\ & 10Dq+3C & -3B & 3B & 3\sqrt{3B} \\ & & 10Dq-6B+3C & -3B & -\sqrt{3B} \\ & & & 20Dq-6B+3C & 2\sqrt{3}B \\ & & & & 20Dq-2B+3C \end{bmatrix} \quad (8)$$

Crystal field Dq, Racah B and C, and β₁ parameters

The energy of the excitation band maximum of the $^4A_2\rightarrow{}^4T_2$ transition equals $10Dq$. Racah parameters B and C can be calculated from the equations:[1]

$$B = Dq\,\frac{\left[\frac{\Delta E}{Dq}\right]^2 - 10\cdot\frac{\Delta E}{Dq}}{15\left(\frac{\Delta E}{Dq} - 8\right)}\,, \qquad (S1)$$

$$C = \frac{B}{3.05}\left\{\frac{E(^2E - {}^4A_2)}{B} - 7.9 + 1.8\frac{B}{Dq}\right\}, \qquad (S2)$$

where ΔE is the difference between the energy of the $^4A_2\rightarrow{}^4T_1$ and $^4A_2\rightarrow{}^4T_2$ transitions.

RESULTS

$Ga_{2-x}Al_xO_3:Cr^{3+}$

Table S1 Linear shift parameters for optical transitions in GAOC for chemical and mechanical pressure for the β- and α-phases.

	chemical pressure		mechanical pressure			
	β-phase		β-phase		α-phase	
	$E(x=0)$	dE/dx	$E(p=0)$	dE/dp	$E(p=0)$	dE/dp
	(cm^{-1})	(cm^{-1})	(cm^{-1})	$(cm^{-1}/kbar)$	(cm^{-1})	$(cm^{-1}/kbar)$
$E\,(^4A_2 \rightarrow {}^4T_1)$	22 568	660	22 568	17.9	23 425	10.2
$E\,(^4A_2 \rightarrow {}^4T_2)$	16 439	412	16 439	12	16 996	7.8
$E\,(^2E \rightarrow {}^4A_2)$	14 328	-22	14 328	-1.34	14 330	-0.9
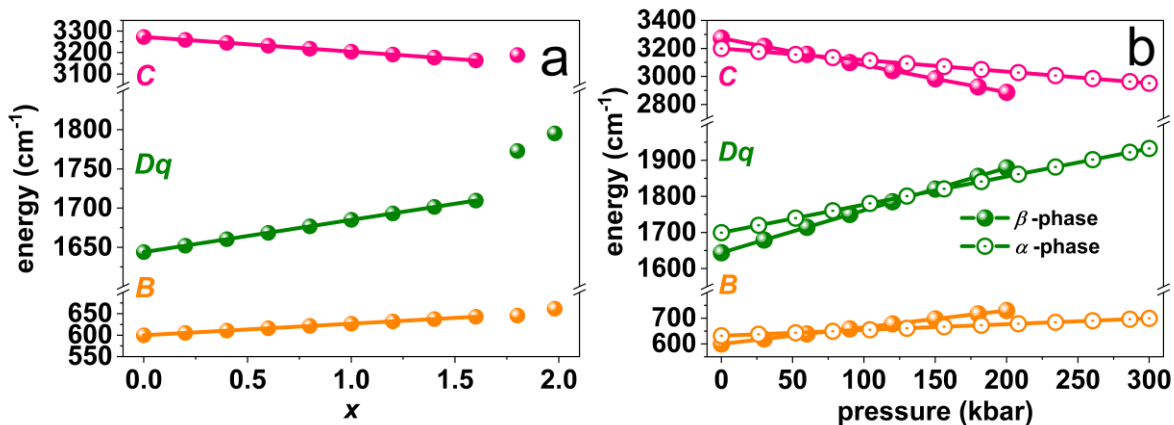
Figure S1 *Dq, B,* and *C* depend on (a) *x* content (CP) and (b) pressure (MP) for β- and α-phases.
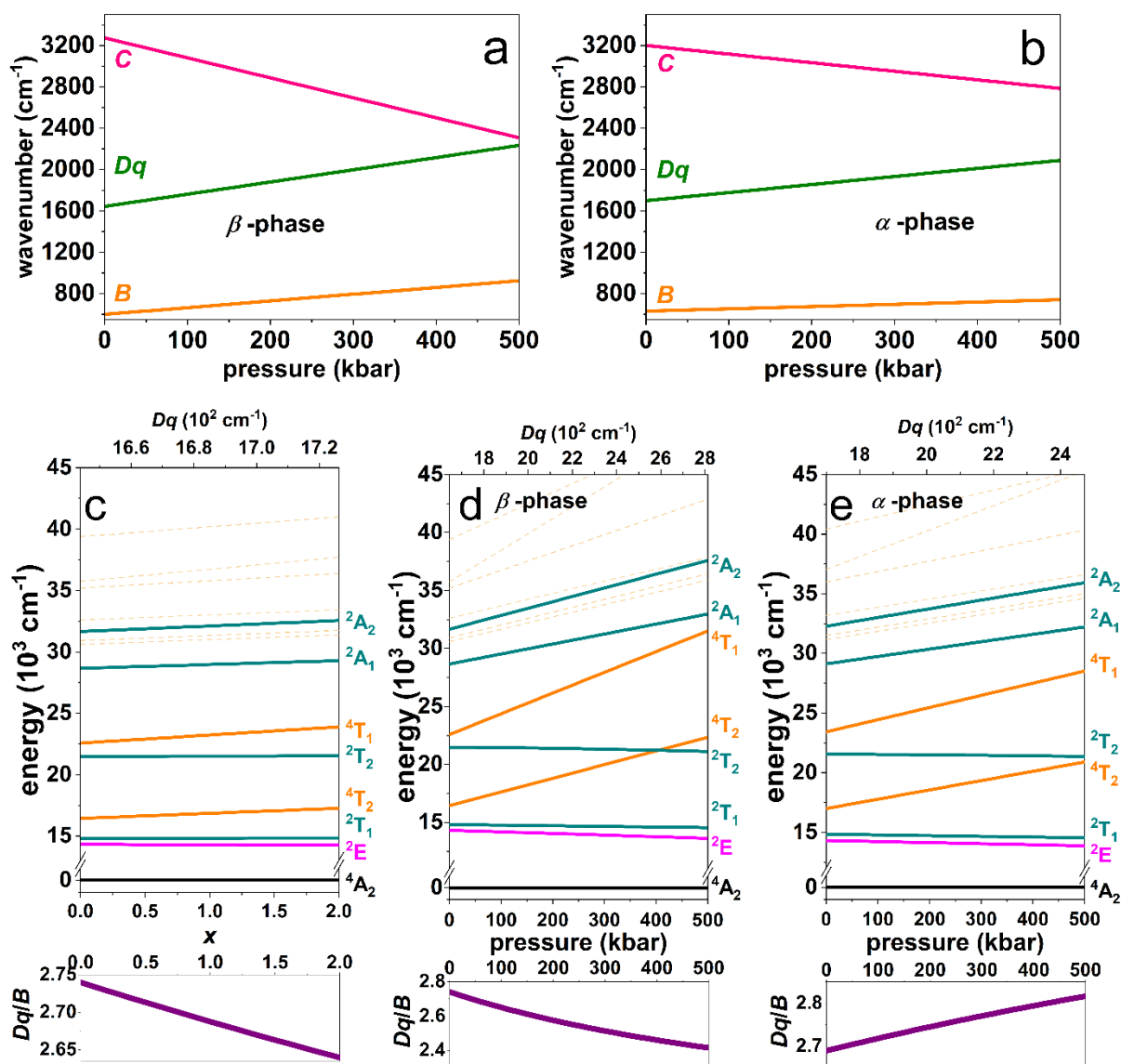
Figure S2 Extrapolated pressure-dependent *Dq, B, C,* and *β* parameters in the 0-500 kbar range for the (a) *β*-phase and (b) *α*-phase for GAOC. The energy structure diagram of all subterms of the d^3 configuration of the Cr^{3+} ion as a function of (c) *x* and *p* for GOC (*x* = 0) in the (d) *α*- and (e) *β*-phase together with the *Dq/B* behavior.
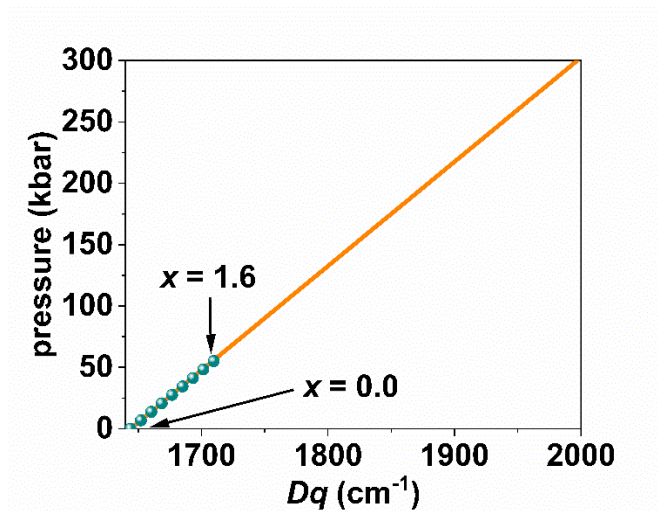
Figure S3 Comparison of the *Dq* value for chemical (changing *x* content in the range 0-1.6, cyan dots) and mechanical pressure (changing pressure from 0-300 kbar, orange line).

$Ga_{2-x}Sc_xO_3:Cr^{3+}$
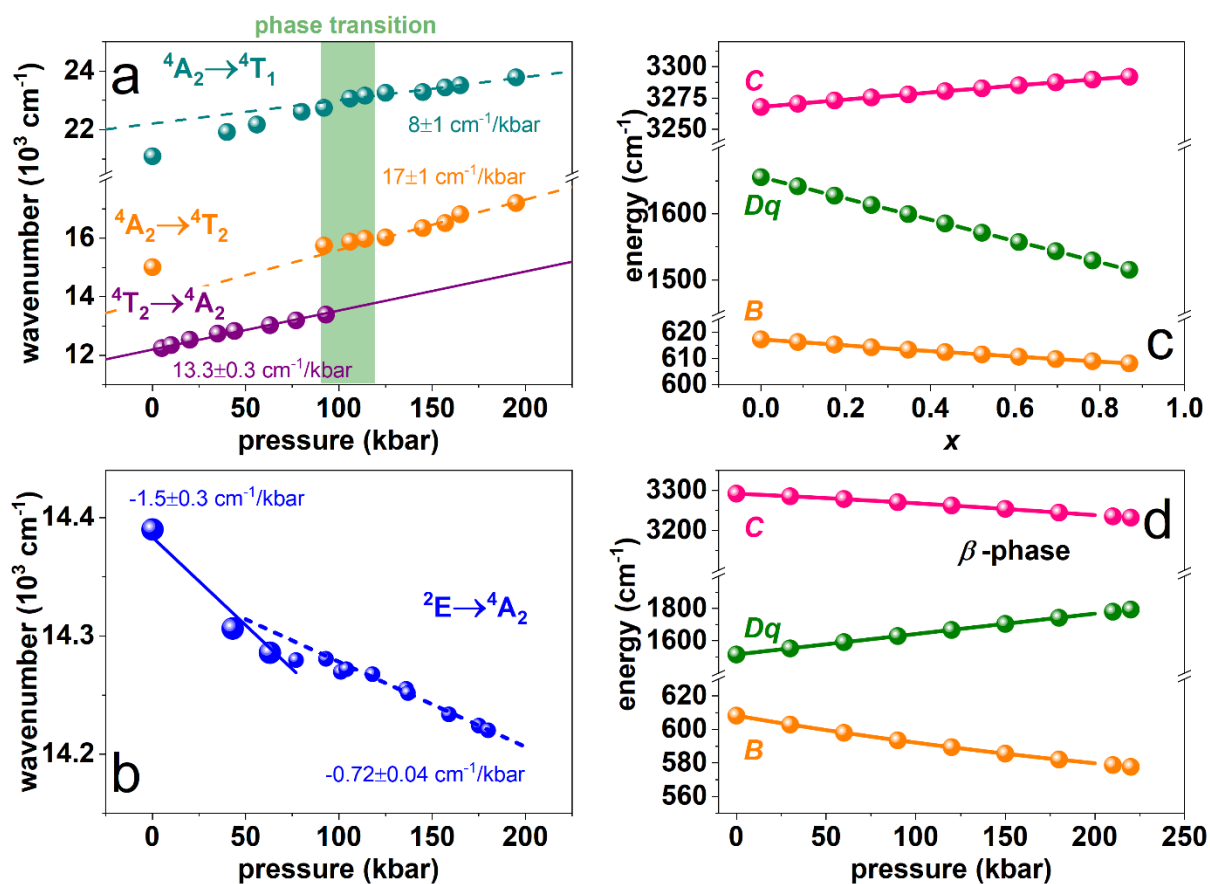
Figure S4 The experimental and calculated position of two excited states from emission spectra and (b) the position of the R-line vs. pressure. *Dq, B,* and *C,* parameters dependence on (c) *x* content (CP) and (d) pressure (MP) for *β*-phases. The size of the dots corresponds to the position determination error.

Table S2 Linear shift parameters for optical transitions in GSOC for chemical pressure and mechanical pressure for the β- and α-phases.

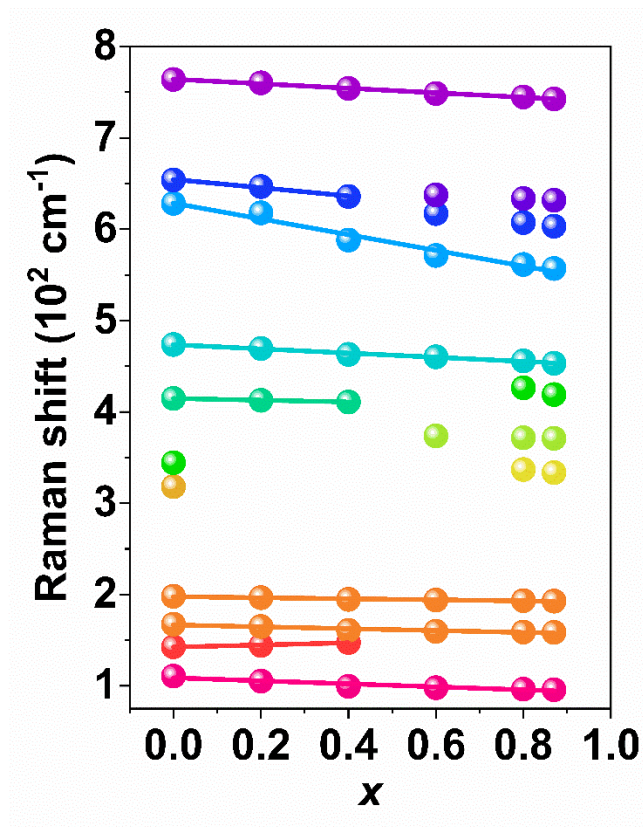|	chemical pressure		mechanical pressure			
	β-phase		β-phase		α-phase	
	$E(x=0)$ (cm^{-1})	dE/dx (cm^{-1})	$E(p=1\text{bar})$ (cm^{-1})	dE/dp (cm^{-1}/kbar)	$E(p=1\text{bar})$ (cm^{-1})	dE/dp (cm^{-1}/kbar)
$E\,({}^4A_2 \rightarrow {}^4T_1)$	22 831	-1 839	21 230	12.5	22 207	8
$E\,({}^4A_2 \rightarrow {}^4T_2)$	16 554	-1 609	15 153	12.6	13 871	17
$E\,({}^2E \rightarrow {}^4A_2)$	14 429	-26.41	14 405	-1.5	14 350	-0.72
$E\,({}^4T_2 \rightarrow {}^4A_2)$	13 495	-1 497	12 196	13.3	-	-

Raman spectra

Figure S5 Shift of the Raman peaks in β-Ga$_{2-x}$Sc$_x$O$_3$:Cr^{3+} at room temperature as a function of the Sc concentration (x).
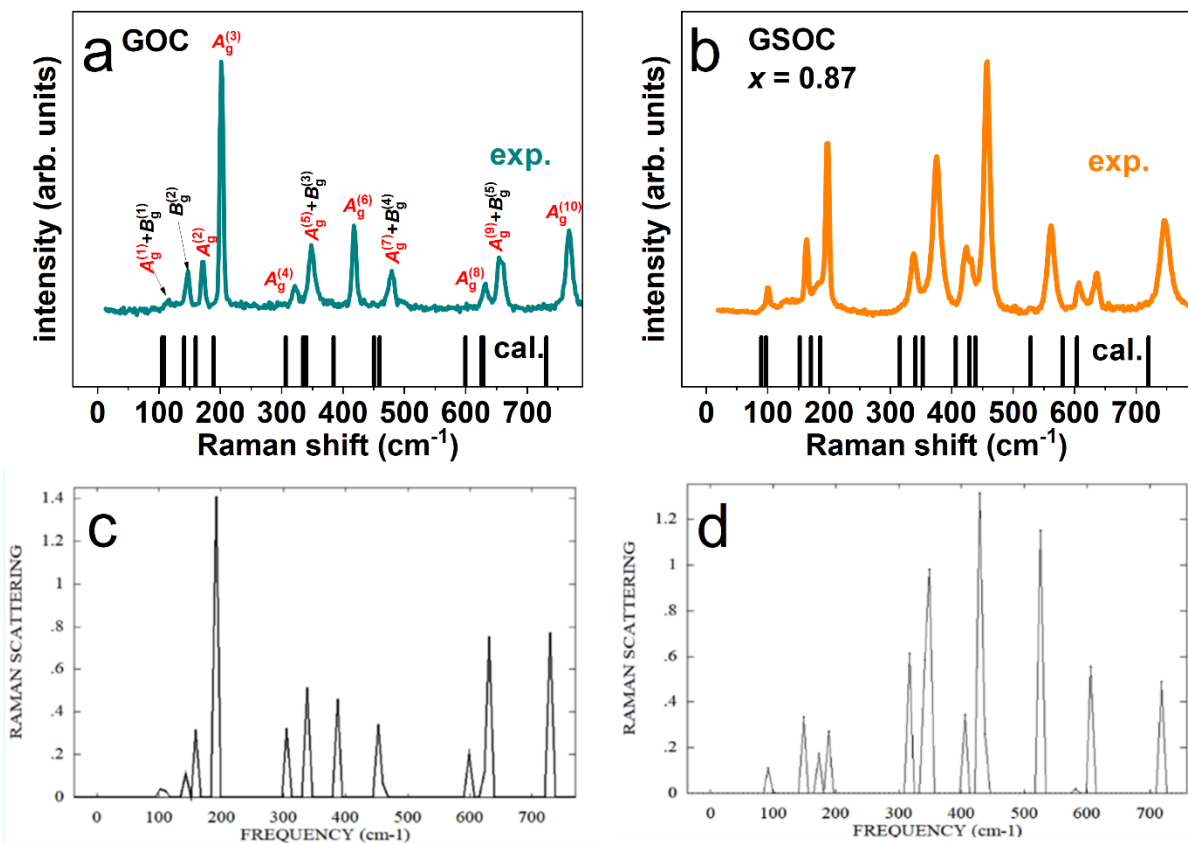
Figure S6 (a, b) The experimental Raman spectra of GOC and GSOC $x = 0.87$, and (c, d) simulated Raman spectra of GOC and GSOC $x = 1.0$. Vertical ticks in a and b indicate the *ab initio* computed frequencies of first-order Raman-active modes.

Table S3 Experimental RT frequencies of the Raman peaks of pure β-Ga_2O_3, given in cm^{-1}, and its spectral shift rate, $\delta = d\omega/dx$, upon increasing Sc concentration (x) as obtained by linear fitting $\omega = \omega_0 + \delta \cdot x$.

Raman mode	$A_g^{(1)}$, $B_g^{(1)}$	$B_g^{(2)}$	$A_g^{(2)}$	$A_g^{(3)}$	$A_g^{(4)}$	$A_g^{(5)}$, $B_g^{(3)}$	$A_g^{(6)}$	$A_g^{(7)}$, $B_g^{(4)}$	$A_g^{(8)}$	$A_g^{(9)}$, $B_g^{(5)}$	$A_g^{(10)}$
ω_0 (cm^{-1})	108±1	142±1	167±1	198±1	318±1	344±2	415±1	473±1	629±5	655±1	764±1
δ (cm^{-1})	-16±2	12±2	-10±2	-5.8±0.5	-	-	-9.6±0.1	-22±2	-86±7	-45±5	-24±1

Table S4 Theoretical (The.) and experimental (Exp.) zero-pressure frequencies, ω_0, and linear pressure coefficients, $\gamma = d\omega/dp$, for the Raman-active modes in the β-phase of GOC.

Raman mode	The. ω_0 (cm^{-1})	Exp. ω_0 (cm^{-1})	The. γ cm^{-1}/kbar	Exp. γ cm^{-1}/kbar
Ag$^{(1)}$	105	108		
Bg$^{(1)}$	108	108		
Bg$^{(2)}$	140	142		
Ag$^{(2)}$	160	167	0.045±0.003	0.04±0.01
Ag$^{(3)}$	189	198	0.084±0.001	0.088±0.004
Ag$^{(4)}$	306	318		
Ag$^{(5)}$	335	344		
Bg$^{(3)}$	340	344	0.345±0.003	0.32±0.02
Ag$^{(6)}$	384	414	0.164±0.005	0.155±0.005
Ag$^{(7)}$	450	473		
Bg$^{(4)}$	459	473		
Ag$^{(8)}$	599	629		
Bg$^{(5)}$	625	655		
Ag$^{(9)}$	628	655		
Ag$^{(10)}$	731	766	0.448±0.008	0.44±0.1

Table S5 Theoretical (The.) and experimental (Exp.) zero-pressure frequencies, ω_0, with the error and linear pressure coefficients, $\gamma = d\omega/dp$, for the Raman-active modes in the β-phase of GSOC, $x = 1.0$ and $x = 0.87$, respectively.

Raman mode	The. ω_0 (cm^{-1})	Exp. ω_0 (cm^{-1})	The. γ (cm^{-1}/kbar)	Exp. γ (cm^{-1}/kbar)
Ag$^{(1)}$	89	-		
Bg$^{(1)}$	97	100		
Bg$^{(2)}$	152	163	0.042±0.002	0.019±0.003
Ag$^{(2)}$	170	-		
Ag$^{(3)}$	185	195	0.087±0.003	0.085±0.005
Ag$^{(4)}$	315	337	0.16±0.01	0.20±0.02
Ag$^{(5)}$	341	375		
Bg$^{(3)}$	352	375	0.375±0.001	0.35±0.01
Ag$^{(6)}$	406	424	0.407±0.002	0.33±0.02
Ag$^{(7)}$	428	457		
Bg$^{(4)}$	438	457	0.298±0.001	0.349±0.007
Ag$^{(8)}$	528	561	0.494±0.004	0.43±0.01
Bg$^{(5)}$	580	607		
Ag$^{(9)}$	603	636		
Ag$^{(10)}$	720	747	0.438±0.006	0.36±0.01

Pressure dependence of Raman spectra
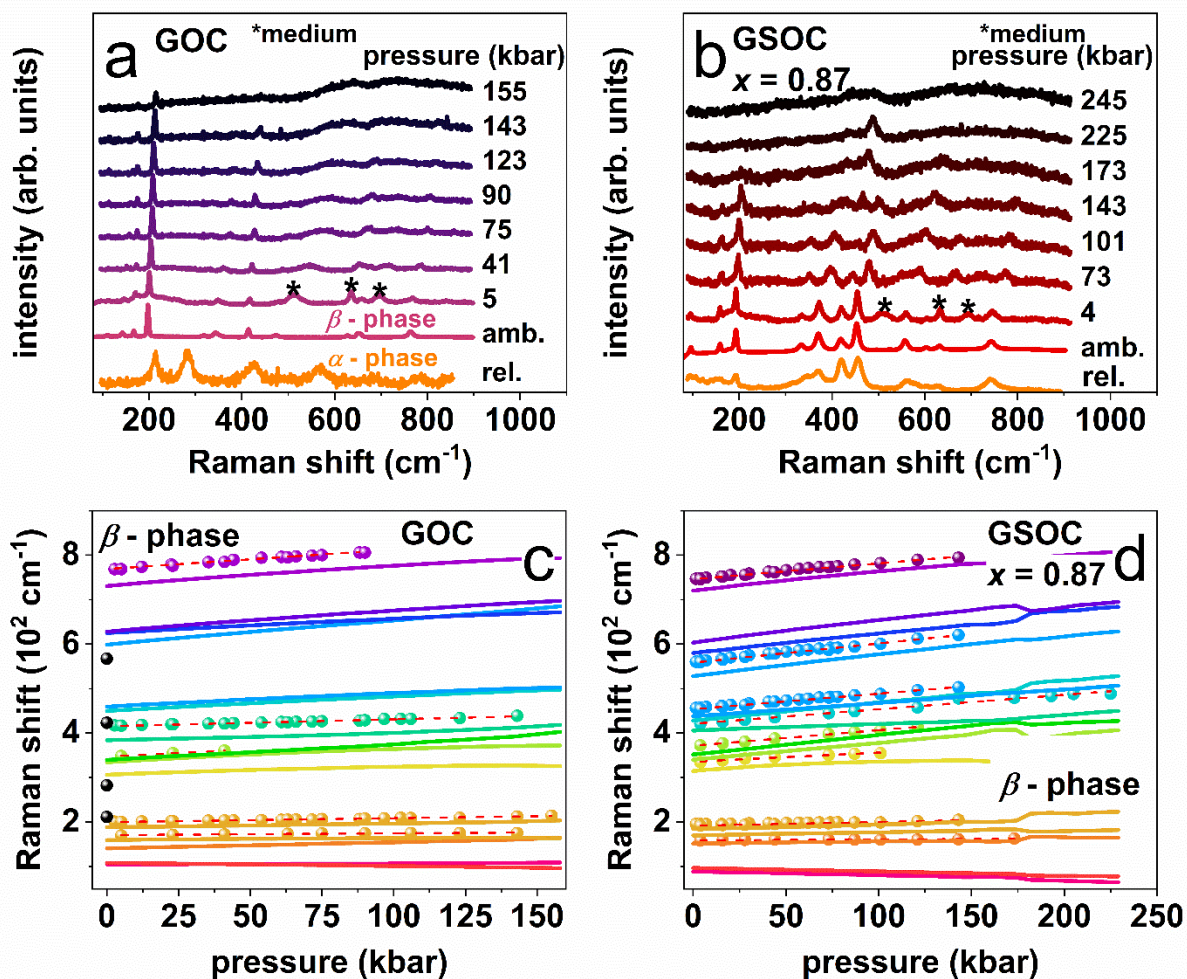
Figure S7 Pressure-dependent experimental Raman spectra of (a) GOC and (b) GSOC. Pressure-dependent experimentally and theoretically calculated frequencies of the Raman-active modes represented by symbols and lines, respectively, observed in (c) GOC and (d) GSOC, $x = 0.87$. Black dots in (c) correspond to the Raman frequencies of the α-phase in the ambient environment after decompression. In the case of the GSOC sample, the calculation vere performed for $x = 1.0$.

Figures S7 a and b show the pressure dependence of Raman spectra for GOC and GSOC. The Raman lines marked by the asterisk (*) come from the medium used. It is seen that the Raman

modes are visible up to 155 and 225 kbar for GOC and GSOC, respectively. **Figures S7** c and d show the pressure dependence of the Raman-active modes for GOC and GSOC, respectively. The experimentally (dots) and theoretically obtained (solid line) frequencies of the Raman peaks are represented as a function of pressure to confirm the mode identification. All Raman frequencies increase linearly with pressure. As observed, the frequencies and pressure coefficients of the most intense Raman modes agree with those theoretically expected, so we obtain a good correlation with a match between the experimental and theoretical frequencies and pressure coefficients. **Tables S4 and S5** summarize the theoretical and empirical frequencies and pressure coefficients from a linear fitting $\omega=\omega_0+\alpha \cdot p$, $\gamma = d\omega/dp$ (red dashed line) for the GOC and GOCS, $x = 0.87$, respectively. Their determined pressure coefficients vary greatly from 0.044 cm^{-1}/kbar Ag$^{(2)}$ to 0.44 cm^{-1}/kbar Ag$^{(10)}$ for GOC and 0.019 cm^{-1}/kbar Ag$^{(2)}$ to 0.43 cm^{-1}/kbar Ag$^{(8)}$. The data gathered in **Tables S4** and **S5** show the order of magnitude smaller linear pressure coefficients γ for the group (i) libration and translation of the Ga$_I$O$_4$ chains than for group (ii) deformation of the Ga$_I$O$_4$ and Ga$_{II}$O$_6$ and (iii) stretching and bending of Ga$_I$O$_4$.

After compressing the sample up to 300 kbar and decompressing, the spectra are shown in **Figure S7** a and c for GOC and GSOC, respectively (orange color). We can see that for the GOC sample, the Raman spectra changed significantly. This Raman spectrum is typical for Ga$_2$O$_3$ in the α-phase.[2] This indicates the phase transition (previously shown by luminescence spectroscopy). Additionally, in the GOC sample, PT occurs for all crystal volumes, and there is no mixing phase. We could not observe the exact pressure of the phase transition because of the weak intensities of the Raman spectra at high pressure. The luminescence studies show that the phase transition occurs at approximately 100-120 kbar (see **Figure 1** d and f). However, we did not detect any Raman peaks of the α-phase at 100-120 kbar. The local structure around the Cr^{3+} ion (local phase

transition) changes faster than the PT of the whole structure. The Cr^{3+} ion luminescence is sensitive to local changes, so we can observe the change in the local phase transition faster than the Raman spectroscopy, which is sensitive to global vibration changes. For the GSOC sample, the spectra after decompression still resemble the Raman spectra of Ga_2O_3 in the β-phase (but the signal is broadened and much weaker). Because luminescence spectroscopy showed that the phase transition occurs (change in emission spectra before compression and after decompression, see **Figure 4** d), the Raman spectra after decompression (orange line) are the mix of α- and β-phase.

REFERENCES

(1)   Henderson, B.; Imbusch, G. F. Optical Spectroscopy of Inorganic Solids; Monographs on the Physics and Chemistry of Materials. *Oxford University Press: Oxford, New York*, **2006**.

(2)   Machon, D.; McMillan, P. F.; Xu, B.; Dong, J. High-Pressure Study of the β -to- α Transition in Ga_2O_3. *Phys. Rev. B* **2006**, *73*, 094125.

[P5]

Chang, C.-Y.; **Majewska, N.**; Chen, K.-C.; Huang, W.-T.; Leśniewski, T.; Leniec, G.; Kaczmarek, S. M.; Pang, W. K.; Peterson, V. K.; Cherng, D.-H.; Lu, K.-M.; Mahlik, S.; Liu, R.-S. Broadening Phosphor-Converted Light-Emitting Diode Emission: Controlling Disorder. *Chem. Mater.* **2022**, *34* (22), 10190-10199.

https://doi.org/10.1021/acs.chemmater.2c03045

Broadening Phosphor-Converted Light-Emitting Diode Emission: Controlling Disorder

Chih-Yu Chang,[∇] Natalia Majewska,[∇] Kuan-Chun Chen, Wen-Tse Huang, Tadeusz Leśniewski, Grzegorz Leniec, Sławomir M. Kaczmarek, Wei Kong Pang, Vanessa K. Peterson, Ding-Hua Cherng, Kuang-Mao Lu, Sebastian Mahlik,* and Ru-Shi Liu*

ACCESS | 📊 Metrics & More | 📖 Article Recommendations | 🔵 Supporting Information

ABSTRACT: Near-infrared (NIR) phosphor-converted light-emitting diodes (pc-LEDs) are a highly efficient perspective NIR light source, with application hindered by a narrow emission band. In this work, we broaden the emission of a new series of NIR phosphors by controlling crystal structure disorder through cation cosubstitution. By substituting Ga^{3+} with $(Al_{0.68}In_{0.32})^{3+}$, we create a $Ga_{2-x}(Al_{0.68}In_{0.32})_xO_3:Cr^{3+}$ phosphor series in which the average crystal size is maintained, while cation disorder varies. The increased deviation of the cation radii in the substitution leads to increased electron−phonon coupling, with a resulting emission spectrum covering the 650−1000 nm range with a 30% increase in the emission full width at half-maximum (FWHM) and a relatively high internal quantum efficiency of ∼80%. A transition from the β phase to the α phase, which differs in structure from the undoped parent, is created by the application of high pressure and possesses ultra-broad-band emission and an FWHM of ∼190 nm. This work shows that the emission bandwidth can be controlled through disorder and its influence on the Stokes shift, as captured by the effective Huang−Rhys factor.
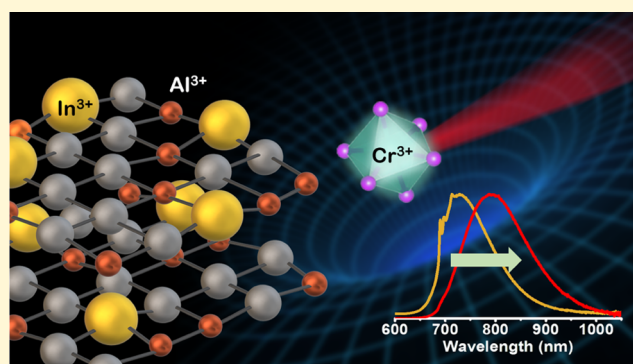
INTRODUCTION

Near-infrared (NIR) light sources are becoming increasingly popular due to their varied applications in areas including food analysis, bioimaging, and plant cultivation, as a result of their high sensitivity, relatively deep penetration, and low light scattering.[1−7] With the growing demand for NIR light sources, traditional incandescent bulbs and halogen lamps are decreasing in popularity because of their low efficiency, high cost, and high operating temperature.[8] Phosphor-converted light-emitting diodes (pc-LEDs) are composed of phosphor materials coated onto blue LEDs and are both highly efficient and of small size, enabling application in portable devices.[9] To fulfill the full potential of these devices, NIR phosphors with highly efficient broad-band emissions are required.

An ideal NIR phosphor emits light in the emission window of 650−1350 nm with a high full width at half-maximum (FWHM) and internal quantum efficiency (IQE). Unfortunately, no materials developed thus far achieve these metrics.[10] Typical NIR phosphors can be categorized into types I and II.[11] Type I NIR phosphors have high efficiency but low FWHM, whereas type II have relatively low IQE, but excellent broad-band emission.[12,13] For practical application, phosphors with characteristics between these two must be developed, either by broadening the emission spectrum of type I phosphors or enhancing the efficiency of type II materials.

The current work targets broadening of the emission of the $Ga_{1.98-x}(Al_{0.68}In_{0.32})_xO_3:0.02Cr^{3+}$ series of type I phosphor materials.

Attempts to broaden the FWHM of type I phosphors have focused mostly on tuning the crystal field strength of the activator by lattice expansion, thus broadening the emission spectrum with a red shift.[14] However, lattice distortion and structural disorder can enhance the electron−phonon coupling and the degree of crystal field energy splitting, thereby also leading to a broader emission spectrum.[15]

Previous studies report Ga_2O_3 to have highly efficient (IQE > 90%) NIR emission with a maximum emission peak at 715 nm using a Cr^{3+} activator.[16] Broadened emission is found for the $Ga_{2-x}Sc_xO_3:Cr^{3+}$ and $Ga_{2-x}In_xO_3:Cr^{3+}$ material series,[17,18] while lattice shrinkage in $Ga_{2-x}Al_xO_3:Cr^{3+}$ narrowed the emission spectrum.[19] Accordingly, we explore the influence of structural disorder on the emission by introducing cation substitution into the Ga_2O_3 system.
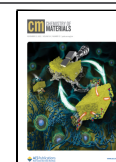
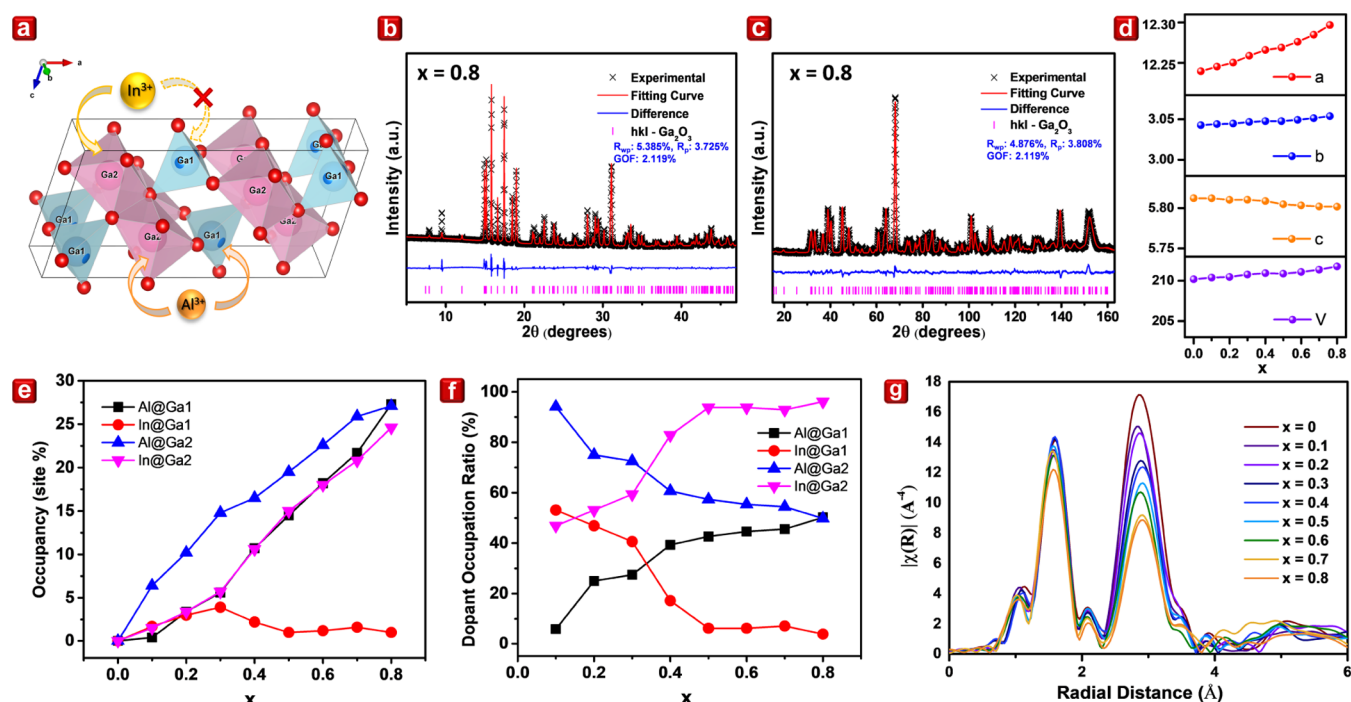**Figure 1.** Structural characterization of $Ga_{1.98-x}(Al_{0.68}In_{0.32})_xO_3:0.02Cr^{3+}$. (a) Schematic of doping in the crystal structure of Ga_2O_3 (ICSD entry #34243) with space group symmetry $C2/m$. Oxygen is shown in red. (b) XRD and (c) NPD data of $Ga_{1.98-x}(Al_{0.68}In_{0.32})_xO_3:0.02Cr^{3+}$ at $x = 0.8$ with the corresponding refinement profile. The figures of merit are the profile R-factor R_p, the weighted profile R-factor R_{wp}, and the goodness of fit (GOF). (d) Lattice parameter and cell volume of the $Ga_{1.98-x}(Al_{0.68}In_{0.32})_xO_3:0.02Cr^{3+}$ series. Lines through points are a guide to the eye and errors are smaller than the points. (e) Site occupancy (%) of Al and In, and (f) % of total Al and In at Ga1 and Ga2 sites in $Ga_{1.98-x}(Al_{0.68}In_{0.32})_xO_3:0.02Cr^{3+}$. Lines through points are a guide to the eye. (g) Cr K-edge EXAFS data of $Ga_{1.98-x}(Al_{0.68}In_{0.32})_xO_3:0.02Cr^{3+}$.

We explore the $Ga_{2-x}(Al_{0.68}In_{0.32})_xO_3:Cr^{3+}$ series in which the average radius of $Al_{0.68}In_{0.32}$ matches that of Ga^{3+} and crystal structure disorder may change while maintaining crystal volume.[20,21] We synthesize and study the structure and luminescence properties of the series, provide the theoretical link between the two, and demonstrate the potential application of the $Ga_{1.18}(Al_{0.544}In_{0.256})O_3:0.02Cr^{3+}$ ($x = 0.8$) material in a NIR pc-LED.

RESULTS AND DISCUSSION

Structural Analysis. β-Ga_2O_3 is monoclinic with the $C2/m$ space group, with Ga at four-coordinate tetrahedral Ga1 ($4i$) and six-coordinate octahedral Ga2 ($4i$) sites (Figure 1a). X-ray powder diffraction (XRD) of $Ga_{1.98-x}(Al_{0.68}In_{0.32})_xO_3:0.02Cr^{3+}$ ($x = 0-0.9$; Figure S1) shows that replacing Ga with $Al_{0.68}In_{0.32}$ yields a phase pure material isostructural to β-Ga_2O_3 until $x = 0.9$.

We investigate the $Ga_{1.98-x}(Al_{0.68}In_{0.32})_xO_3:0.02Cr^{3+}$ ($x = 0-0.8$) structure using synchrotron XRD (S-XRD) and neutron powder diffraction (NPD), with joint Rietveld[22] refinement results shown in Figures S2 and 1b–d and Tables S1 and S2. The lattice is expectedly influenced by In and Al substitution, with a and b increasing and c slightly decreasing with increasing x. A maximum increase of 0.468(5)% occurs for a, with an increase in volume V of <1%, much smaller than those for $Ga_{2-x}Sc_xO_3:Cr^{3+}$ and $Ga_{2-x}In_xO_3:Cr^{3+}$ systems.[18,19]

The occupancies of substituents at Ga1 and Ga2 sites are determined using Rietveld refinement shown in Figure 1e,f, and Table S1. Preference for the six-coordinate octahedral Ga2 site occurs for In at $x > 0.3$, with only some In occupying the Ga1 site. Note that at a coordination number (CN) of 4, the radius of In^{3+} is 0.62 Å and is 0.8 Å at a CN of 6, these being

larger than those for Ga^{3+} (0.47 Å at CN = 4 and 0.62 Å at CN = 6).[23] Conversely, Al^{3+} is smaller than Ga^{3+}, being 0.39 Å at CN = 4 and 0.535 Å at CN = 6, and we find a slight preference for Al at Ga2 sites.[23] Notably, we find Al saturates at the same occupancy at Ga1 and Ga2 sites, at an amount similar to In at Ga2 sites (Figure 1e). The convergence of the preference of Al at both sites is ascribed to the strong preference of In for Ga2 sites (Figure 1f), where larger In is compensated by smaller Al, expanding a, as the pair $(Al^{3+}-In^{3+})$ is slightly larger than $(Ga^{3+}-Ga^{3+})$.

Cr valence was probed using X-ray absorption near-edge structure (XANES) analysis (Figure S3) with extended X-ray absorption fine structure (EXAFS) analysis used to determine Cr bonding (Figure 1g). Given that six-coordinate Cr^{3+} has a similar radius (0.615 Å) to Ga^{3+}, it emits light in the NIR region only at octahedral sites, and we, therefore, assume that Cr^{3+} occupies the Ga2 site.[23–25] The EXAFS feature at the smallest distance can be attributed to the O^{2-} environment, with a second feature at approximately 3 Å attributable to metal environments, arising from Ga in the sample of $x = 0$. Each Ga2 site comprised seven tetrahedra and four octahedra (Figure S4). Considering elemental site occupancy, we calculate the weight difference surrounding Cr^{3+} (Table S3) and note a drop in the intensity of the backscattering signal commensurate with this, further evidencing the Al/In substitution. Also, the decrease in intensity for both features can be attributed to the enhanced destructive interferences ascribed from the disordered environment for Cr^{3+}.

Raman spectra of the series at room temperature (RT) and ambient pressure are shown in Figure S5a. Of the 30 vibrational modes, 15 are Raman active and 11 within 100–900 cm^{-1} with most at 200 cm^{-1} (the $A_g^{(3)}$ mode).[26,27] Peaks
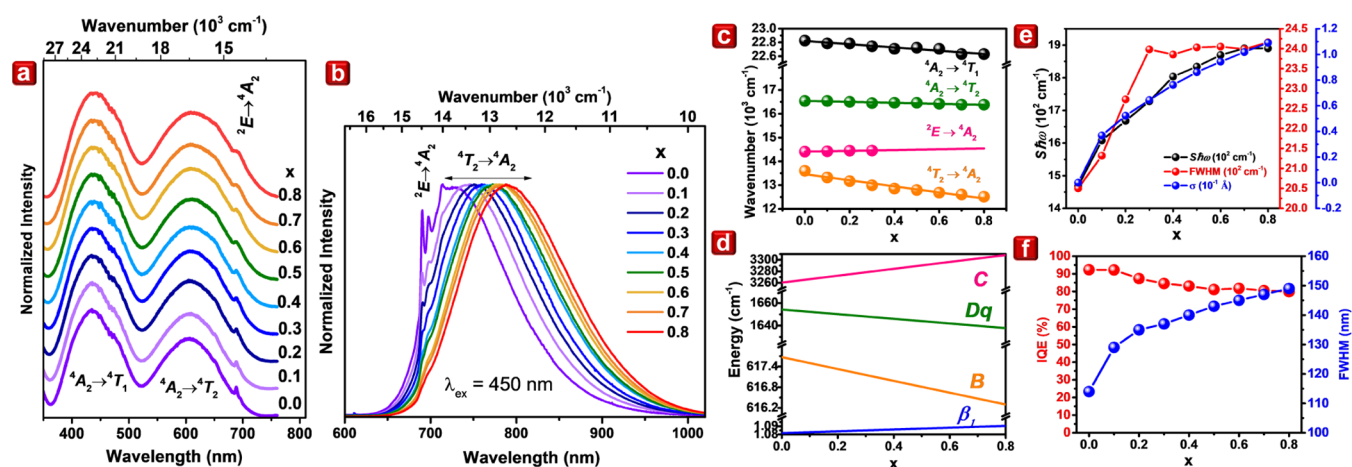
Figure 2. Photoluminescence properties of $Ga_{1.98-x}(Al_{0.68}In_{0.32})_xO_3$:$0.02Cr^{3+}$ ($x = 0-0.8$) at room temperature. (a) PLE spectra with transitions identified and shown offset in y for clarity, (b) emission spectra upon excitation at 450 nm with transitions identified, and (c) energies of peaks of emissions from transitions shown in (a) and (b). Lines are linear fits through the points. (d) Calculated crystal field parameter Dq, Racah parameters B and C, and nephelauxetic parameter β_1. (e) Comparison between $S\hbar\omega$ and the degree of disorder (σ) over x and full width at half-maximum (FWHM) of emission, and (f) internal quantum efficiency (IQE) and FWHM with x. Lines through points are a guide to the eye.

broaden with increasing x, with only two lines resolved for sample $x = 0.8$, suggesting a change in the local environment and a more asymmetrical structure that increases the distribution of vibrational energies in the crystal, indicating increased disorder.[28] Peak positions and their rate of shifts are given in Figure S5b and Table S4.

Photoluminescence (PL). PL excitation (PLE) and PL spectra of $Ga_{1.98-x}(Al_{0.68}In_{0.32})_xO_3$:$0.02Cr^{3+}$ ($x = 0-0.8$) at RT are shown in Figure 2a,b, respectively. PLE spectra comprise two excitation bands typical for six-coordinate octahedral Cr^{3+}, a higher energy band with a peak at 440 nm corresponding to the $^4A_2 \rightarrow {}^4T_1$ transition, and a lower energy band with a peak at 620 nm corresponding to the $^4A_2 \rightarrow {}^4T_2$ transition. Upon excitation at 442 nm, narrow lines and broad-band emission are observed simultaneously. A line emission at approximately 700 nm arises from the $^2E \rightarrow {}^4A_2$ spin-forbidden transition, also known as the R-line of Cr^{3+}. The broad-band emission extending from 650 to 1000 nm arises from the $^4T_2 \rightarrow {}^4A_2$ spin-allowed transition.

A red shift of the broad band and a blue shift of R-line emission are observed with increasing x. A 62 nm red shift of the broad-band $^4T_2 \rightarrow {}^4A_2$ emission occurs from 722 to 784 nm. The red shift of excitation bands arising from $^4A_2 \rightarrow {}^4T_1$ and $^4A_2 \rightarrow {}^4T_2$ is also observed but is significantly smaller than the emission band, suggesting an increase in the electron–lattice interaction parameter $S\hbar\omega$ with increasing x.

The intensity of the R-line emission decreases with increasing x and is unobserved for $x > 0.3$. The energies for maximum excitations arising from the $^4A_2 \rightarrow {}^4T_1$ (black dots) and $^4A_2 \rightarrow {}^4T_2$ (green dots) transitions and $^4T_2 \rightarrow {}^4A_2$ (orange dots) and $^2E \rightarrow {}^4A_2$ (pink dots) transitions versus x are plotted in Figure 2c. The rate of the shift in peak energies with x obtained from linear fit to data in Figure 2c is presented in Table S5.

Substitution of larger In^{3+} for Ga^{3+} is expected to decrease crystal field strength, and we calculate the crystal field parameter Dq and Racah parameters B and C that quantify Cr^{3+} 3d electron interactions,[25,29] with calculation details given in the Supporting Information and calculated parameters in Figure 2d. These parameters are calculated for the mixed Cr^{3+} environment arising from Al and In substitution, with the

environment for Cr^{3+} obtained for the $Ga_{2-x}In_xO_3$:Cr^{3+} and $Ga_{2-x}Al_xO_3$:Cr^{3+} materials.[18,19]

We introduce the disorder parameter (σ) as the deviation of the radii of the elements doped, which quantifies the radii differences from the parent material Ga_2O_3 in the structure. Though Lin et al. suggested σ^2 as the parameter to quantify the disorder effect, the square-rooted parameter σ has more statistical meaning that serves as a better parameter to compare with the disorder of the system.[21] The calculation of σ can be found in Table S6 and the comparison with the electron–lattice interaction parameter $S\hbar\omega$ and FWHM is shown in Figure 2e. The increase of σ is highly correlated with increased $S\hbar\omega$ with x, from 1470 to 1940 cm^{-1}, evidencing enhanced electron–phonon coupling controlled through disorder. This phenomenon broadens the emission peak, and the FWHM of the emission peak is compared with IQE in Figure 2f. Increasing inhomogeneity of the Cr^{3+} surroundings with increasing Al and In substitution increases both the emission FWHM and $S\hbar\omega$, noting that values may be overestimated as a result of reabsorption between inhomogeneous Cr^{3+} centers. The FWHM of emissions from the series broadens from 114 to 148 nm, and IQE is maintained between 93 and 80%, indicating promise for practical application. It is worth noting that in comparison with the single-doped phosphor $Ga_{2-x}In_xO_3$:Cr^{3+}, the addition of Al^{3+} has almost doubled the broadening effect under the same concentrations of In^{3+}.[18] Therefore, this has proved that the electron–phonon coupling effect is essential in broadening emission spectra.

The decay of emission upon excitation at 440 nm at RT for $Ga_{1.98-x}(Al_{0.68}In_{0.32})_xO_3$:$0.02Cr^{3+}$ is shown in Figure S6a. Single exponential decay occurs for the sample without indium and aluminum ($x = 0$) and is multiexponential for other samples, likely arising from the inhomogeneous surroundings of Cr^{3+}. The average decay time is calculated using the following equation

$$\tau_{av} = \frac{\int t \cdot I(t) \mathrm{d}t}{\int I(t) \mathrm{d}t} \tag{1}$$

where $I(t)$ is the intensity at time t and is shown in Figure S6b. Replacing Ga^{3+} for In^{3+} expands the crystal lattice and reduces
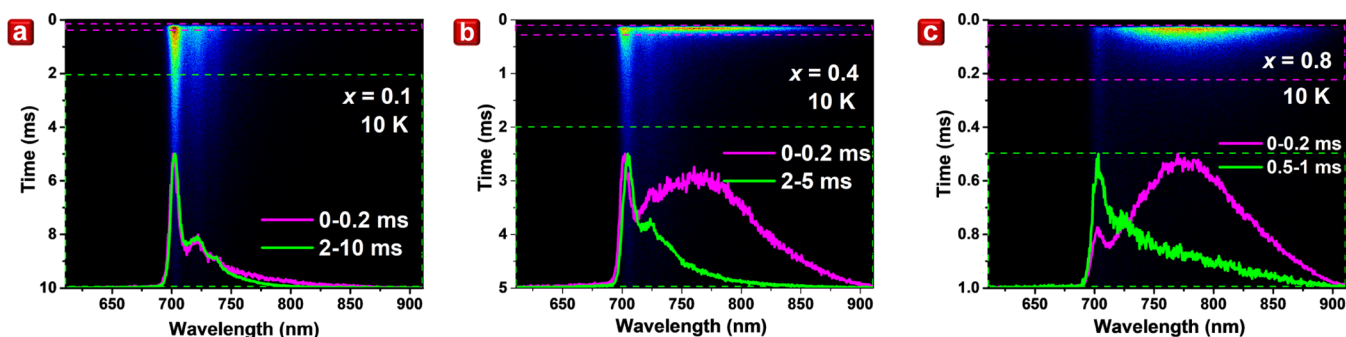
Figure 3. Streak camera images at, and emission spectra within, two time windows for emissions upon excitation at 440 nm from $Ga_{1.98-x}(Al_{0.68}In_{0.32})_xO_3$:0.02$Cr^{3+}$ at 10 K for compositions (a) $x = 0.1$, (b) $x = 0.4$, and (c) $x = 0.8$. Images are recorded at 10 ms for $x = 0.1$, 5 ms for $x = 0.4$, and 1 ms for $x = 0.8$. Intensity is shown from highest in red through yellow and blue to lowest in black.
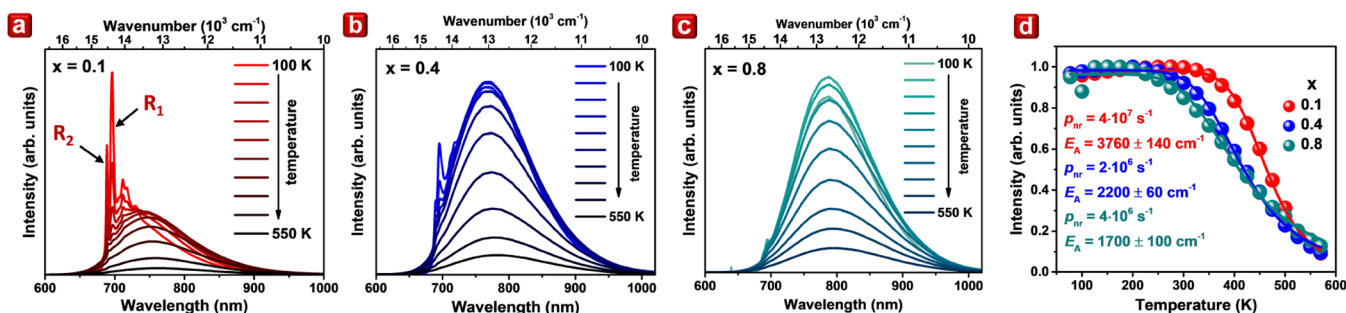

Figure 4. PL spectra between 100 and 550 K for $Ga_{1.98-x}(Al_{0.68}In_{0.32})_xO_3$:0.02$Cr^{3+}$ for (a) $x = 0.1$, (b) $x = 0.4$, and (c) $x = 0.8$. (d) The integrated intensity of spectra in (a)−(c) is described (solid lines), yielding the probabilities of nonradiative and radiative transitions, p_{nr} and p_r, respectively, and E_A as the activation energy for the nonradiative process.

the crystal field around Cr^{3+}, in turn decreasing the energy of the $^4T_2$ state relative to the lowest excited state ^2E. Thermal occupation of the $^4T_2$ state leads to increased broad-band emission from the $^4T_2 \rightarrow \, ^4A_2$ transition and shortening of the emission decay time as confirmed by the decay of RT luminescence with x.

Temperature-Dependent Luminescence. The luminescence properties of Cr^{3+} in Ga_2O_3 are well known, therefore, we focus on mixed-ion samples $x = 0.1$, 0.4, and 0.8.[16,17,30−32] Streak camera images at 10 K upon excitation at 440 nm and time-resolved emission spectra are shown in Figure 3, recorded at time ranges of 10 ms for $x = 0.1$, 5 ms for $x = 0.4$, and 1 ms for $x = 0.8$, along with emission spectra for two time ranges. Previous studies of Ga_2O_3:Cr^{3+} show that its emission spectrum does not change with time, indicating a single luminescence center, unlike the time-dependent evolution of luminescence spectra for Al- and In-substituted materials.[17] Moreover, the broadening of the R-line and Raman lines compared with the sample at $x = 0$ and the relatively large FWHM of the broad-band emission for the $x = 0.1$, 0.4, and 0.8 materials suggest a distribution of Cr^{3+} short-range environments. Rationally, at least two distinct luminescent centers may exist, $GaInO_3$:Cr^{3+}-like environments that produce a shorter timescale emission (pink), and a $GaAlO_3$:Cr^{3+}-like environment that produces a longer timescale emission (green). As the mean crystal field strength decreases with x, the relative intensity of the $^4T_2$ emission increases, and its average decay time decreases; however, $^4T_2$ and ^2E emissions occur simultaneously at 10 K.

Temperature-dependent PL spectra within 100−550 K for $x = 0.1$, 0.4, and 0.8 are shown in Figure 4a−c. For the sample of $x = 0.1$ at 100 K, a dominant R_1 line, a thermally occupied R_2

line, and phonon sidebands are observed.[30,31,33] Broad-band emission intensity increases with temperature as electrons activate from the ^2E to $^4T_2$ state. At 250 K, the broad-band emission dominates, and for samples of $x = 0.4$ and 0.8, it extends from 650 to 1000 nm even at 100 K. With increased temperature for sample $x = 0.1$, the intensity of the R_2 emission increases relative to R_1, until it dominates at a higher temperature (200 K), as a result of the higher radiative transition probability of R_2 than that of R_1 for strongly distorted tetrahedral Cr^{3+}.[34] Notably, the R_2/R_1 intensity ratio does not exceed 1, indicating a lack of population inversion between the R_2 and R_1 states. As expected for high x, the energy between the $^4T_2$ and ^2E states is smaller than that for low x, with thermal occupancy of the $^4T_2$ state at lower temperatures.

The temperature-dependent emission intensity of samples $x = 0.1$, 0.4, and 0.8 within 77−570 K is shown in Figure 4d. For $x = 0.1$, luminescence intensity is stable up to 300 K and starts decreasing at a higher temperature. Emission intensity decreases earlier with temperature for samples with higher x, beginning at ~200 K. Data in Figure 4d are described by

$$I(T) = \frac{I(0)}{1 + A \exp\left(-\frac{E_A}{kT}\right)} \tag{2}$$

where $I(T)$ is the luminescence intensity at temperature T, k is Boltzmann's constant, $I(0)$ is the luminescence intensity at $T = 0$ K, and E_A is the activation energy for the nonradiative process. A is a dimensionless constant equal to p_{nr}/p_r, probabilities of nonradiative and radiative transitions, respectively. $1/p_r = \tau_0$, the radiative lifetime of emission obtained from the intensity decay at a low temperature. E_A
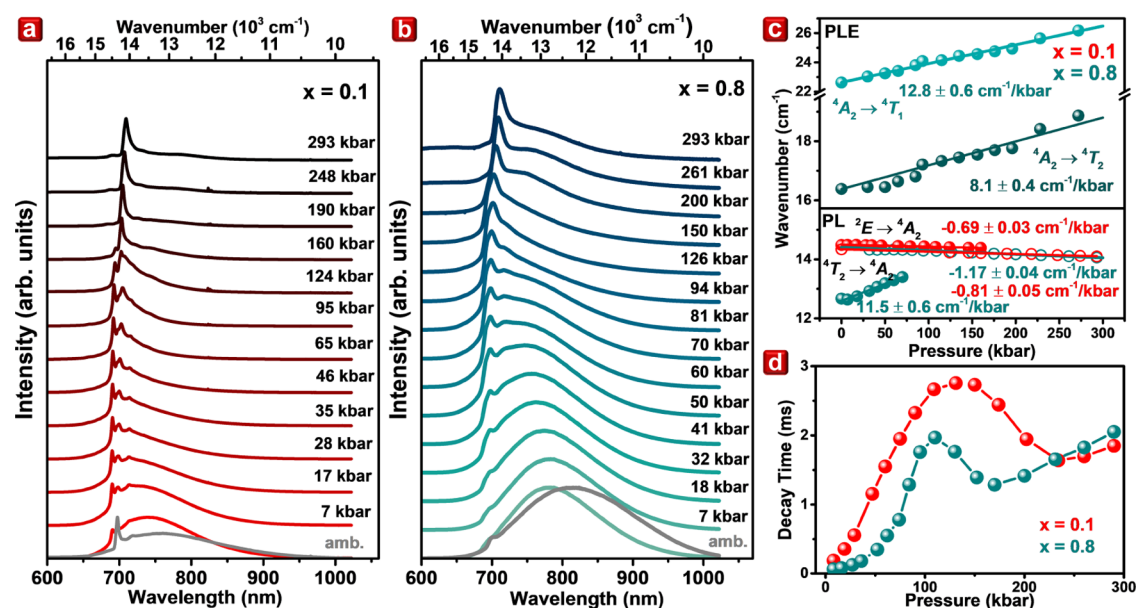
Figure 5. Pressure-dependent PL spectra for $Ga_{1.98-x}(Al_{0.68}In_{0.32})_xO_3$:$0.02Cr^{3+}$ excited upon 442 nm at ambient pressure to 293 kbar for samples (a) $x = 0.1$ and (b) $x = 0.8$. Data are offset in y for clarity. The gray line is the emission spectrum following the release of applied pressure. (c) Pressure dependence of line and broad-band emissions. Open dots in the PL $^2E \rightarrow {}^4A_2$ transition are shifts of the R_1 line, while the closed dots are the shifts of the R_2 line. Errors are smaller than the points, and lines through the points are linear fits with slopes as indicated. (d) Pressure dependence of the calculated average decay time.

relates to nonradiative de-excitation processes and is independent of the $^4T_2-{}^2E$ energy difference. E_A is 3760 ± 140, 2200 ± 60, and 1700 ± 100 cm^{-1} for $x = 0.1$, 0.4, and 0.8, respectively, thereby increasing the thermally stimulated nonradiative process and causing nonradiative relaxation. The nature of the nonradiative de-excitation process is speculative. Decreases in E_A correlate with the decreased band gap with x, where the nonradiative process may be related to the ionization transition from excited-state Cr^{3+} to the conduction band, consistent with the increased nephelauxetic effect as calculated.[18,35,36] On the other hand, increased electron–phonon coupling and the Huang–Rhys factor (S) induce phonon-assisted cross-relaxation between excited and ground states.[37] The temperature-dependent decay of luminescence intensity for selected samples is shown in Figure S7a–c. For sample $x = 0.1$, emission from the forbidden state dominates to 100 K with a long decay time. At higher temperatures, the broad-band emission (allowed transition) increases, and decay time significantly shortens. For temperatures higher than 250 K, broad-band emission with a short decay time dominates. In the case of samples $x = 0.4$ and 0.8, the broad-band emission is significant at a lower temperature, causing a shorter decay time compared with sample $x = 0.1$. The decay of luminescence intensity at low temperatures is multiexponential owing to the different Cr^{3+} environments.

The average decay times calculated using eq 1 as a function of temperature for samples $x = 0.1$, 0.4, and 0.8 are shown in Figure S7d. We find that the radiative lifetime is unaffected by the thermal occupation of the $^4T_2$ state for Cr^{3+} at 10 K and is, therefore, attributable to the $^2E \rightarrow {}^4A_2$ transition, the probability of which is influenced by the $^4T_2$ state, owing to spin–orbit interactions.[38] Notably, the 10 K radiative lifetime does not purely arise from the $^2E \rightarrow {}^4A_2$ transition but is affected by the faster $^4T_2 \rightarrow {}^4A_2$ transition, where distributions of the Cr^{3+} environment and crystal field lead to broad-band emission with faster decay. With increasing x, the contribution

of the $^4T_2 \rightarrow {}^4A_2$ transition to luminescence intensity increases, and the lifetime at 10 K decreases from 2.37 ms at $x = 0.1$ to 0.09 ms at $x = 0.8$.

Pressure-Dependent Luminescence. Pressure-dependent PL spectra at RT upon excitation at 442 nm of samples $x = 0.1$ and 0.8 are shown in Figure 5a,b, respectively. Line and broad-band emissions are observed simultaneously for the two samples at ambient pressure. The strong influence of the $^4T_2$ state on crystal field strength leads to a substantial increase in the energy of the $^4T_2 \rightarrow {}^4A_2$ transition with pressure. For sample $x = 0.1$, the maximum broad-band $(^4T_2 \rightarrow {}^4A_2)$ emission intensity shifts to shorter wavelengths (higher energy) with increased pressure. Above 35 kbar, the broad-band emission disappears and only the line emission is observed, due to the low thermal population of the $^4T_2$ state at RT, with the emission arising from the ^2E state. Similar effects have been described for $x = 0$ in previous studies.[16,32] The relative intensity of the R_1 and R_2 lines changes with applied pressure, with the R_1 line intensifying. The emission spectrum changes significantly between 124 and 160 kbar, with only one line visible above 160 kbar, likely as a result of the β-Ga_2O_3 (monoclinic) to α-Ga_2O_3 (trigonal) phase transition, theoretically calculated to occur at 95 kbar and observed experimentally for a nanostructured material.[39] According to Lipinska-Kalita et al.,[40] the transition commences at 60 kbar, and between 60 and 150 kbar, a combination of both phases occurs. Other studies report the phase transition in the bulk material to occur at approximately 200 kbar.[41] Furthermore, since only one R-line is observable after the release to ambient pressure rather than two broad R-lines, we eliminate the possibility of only a change in disorder.

The energies of R_1 and R_2 lines as a function of pressure for sample $x = 0.1$ is presented in Figure 5c (red points, opened as R_1 and closed as R_2), where shifts to longer wavelengths (lower energy) occur with pressure. Linear fits data in Figure 5c yield
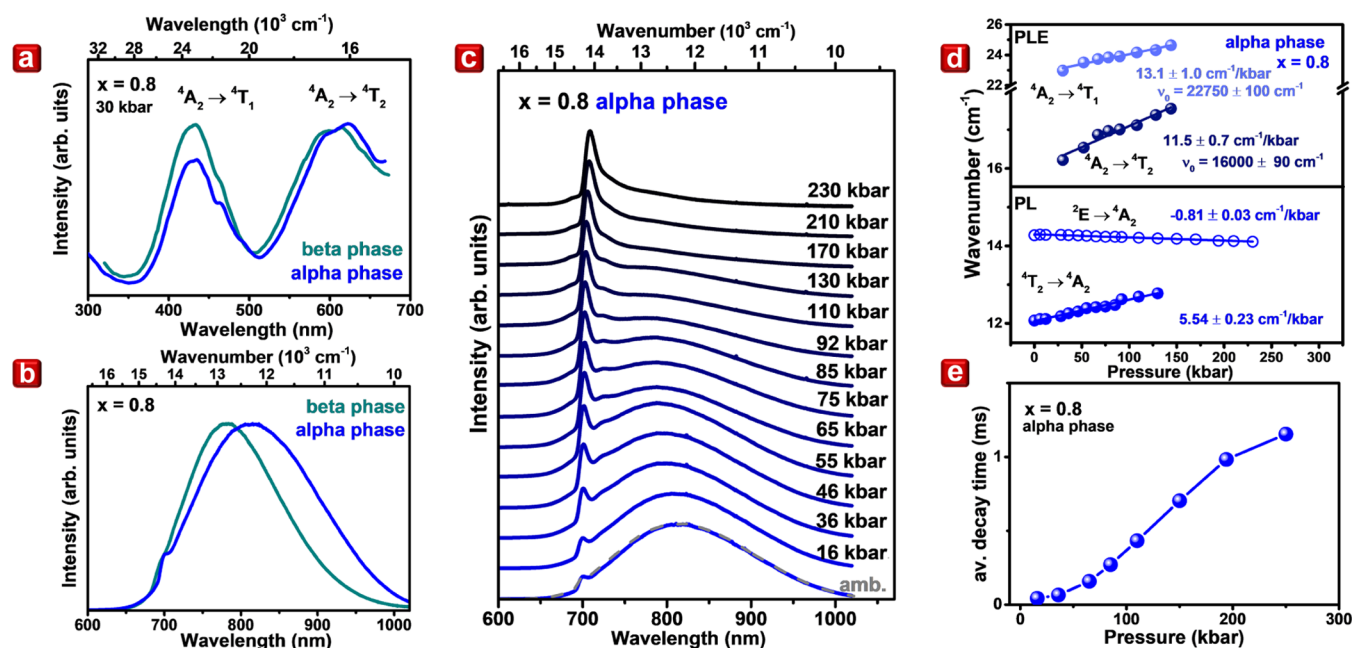
Figure 6. Luminescence properties of α- and β-Ga$_{1.98-x}$(Al$_{0.68}$In$_{0.32}$)$_x$O$_3$:0.02Cr^{3+} with $x = 0.8$. (a) PLE spectra upon maximum emission at 30 kbar, (b) PL spectra upon excitation at 440 nm, (c) pressure-dependent emission spectra excited upon 442 nm at ambient pressure to 230 kbar, (d) line and broad-band emission and broad-band excitation shift with pressure along with linear fits, and (e) decay time at different pressures for sample x = 0.8 (line through points is a guide to the eye).

slopes of -0.69 ± 0.03 cm^{-1}/kbar for R$_2$ and -0.81 ± 0.05 cm^{-1}/kbar for R$_1$, and details are presented in Table S7.

Pressure-dependent PLE spectra of sample $x = 0.8$ are shown in Figure S8a. The maxima of the two excitation bands and broad-band (^{4}T$_2 \rightarrow$ ^{4}A$_2$) emissions from sample $x = 0.8$ shift to a shorter wavelength (higher energy) with pressure at 12.8 ± 0.6 cm^{-1}/kbar (^{4}A$_2 \rightarrow$ ^{4}T$_1$), 8.1 ± 0.4 cm^{-1}/kbar (^{4}A$_2 \rightarrow$ ^{4}T$_2$), and 11.5 ± 0.6 cm^{-1}/kbar (^{4}T$_2 \rightarrow$ ^{4}A$_2$), and the R-line emission shifts to a longer wavelength (lower energy) at -1.17 ± 0.04 cm^{-1}/kbar, as shown in Figure 5c. The direction and magnitude of the pressure shift of the ^{2}E $\rightarrow$ ^{4}A$_2$ and ^{4}T$_2 \rightarrow$ ^{4}A$_2$ transitions are in agreement with previous work.[16,34,42] The larger effect of pressure for sample $x = 0.8$ indicates a less rigid structure that is more sensitive to compression, as consistent with the lower pressure at which phase transformation occurs.

The pressure-dependent decay of luminescence intensity on excitation at 440 nm for samples $x = 0.1$ and 0.8 up to 300 kbar is shown in Figure S8b,c, respectively. The average decay time (τ_{av}) calculated using eq 1 is presented in Figure 5d. The pressure-induced increase in crystal field strength causes an increase in the energetic separation of the ^{4}T$_2$ and ^{2}E excited states, reducing the occupancy of the higher ^{4}T$_2$ and leading to elongation of the decay time in the low-pressure range up to 100 kbar. Between 100−200 kbar, the decay time decreases as a result of the phase transition and the faster decay of emission from Cr^{3+} in the trigonal phase. Between 130 and 240 kbar for $x = 0.1$, a mixture of β and α phases is found, where the reduced decay time in this region arises from increases in the quantity of the α-Ga$_2$O$_3$ phase. Similar behavior is observed for the $x = 0.8$ sample, with the decrease in decay time occurring at a lower pressure range (100−170 kbar).

Above 200 kbar at $x = 0.1$ and 150 kbar at $x = 0.8$, the decay time for emissions arising from the ^{2}E $\rightarrow$ ^{4}A$_2$ transition increases. This effect can be explained by the degree of admixing of the ^{4}T$_2$ spin-quartet state into the ^{2}E spin-doublet

state. The admixture of spin-quartet ^{4}T$_2$ occurs as a result of spin−orbit interactions and is responsible for lifting the spin selection rule for the ^{2}E $\rightarrow$ ^{4}A$_2$ transition. The increase in the separation of the ^{4}T$_2$ and ^{2}E states diminishes the amount of the admixture, lowering the probability of the ^{4}T$_2 \rightarrow$ ^{4}A$_2$ radiative transition with pressure, as observed for Ga$_{1.98-x}$Al$_x$O$_3$:0.02Cr^{3+}.[19]

High-Pressure Phase. The phase transition from β- to α-Ga$_2$O$_3$ occurs in these materials at elevated pressure. The β- to α-Ga$_2$O$_3$ phase transition is irreversible, and we note a significant change in the emission spectrum after the release of pressure compared to that before pressure application (gray line in Figure 5a,b), suggesting that an α-Ga$_{1.98-x}$(Al$_{0.68}$In$_{0.32}$)$_x$O$_3$:0.02Cr^{3+} structure for $x = 0.1$ and 0.8 is obtained under high pressure in a diamond anvil cell. The luminescence properties of such a system have not been studied previously, although α-Ga$_2$O$_3$:Cr^{3+} was studied by Back et al.[43] α-Ga$_2$O$_3$ is trigonal with the $R\bar{3}c$ space group symmetry, as shown in Figure S9. The PLE spectrum for α- and β-Ga$_{1.98-x}$(Al$_{0.68}$In$_{0.32}$)$_x$O$_3$:0.02Cr^{3+} at $x = 0.8$ at 30 kbar is shown in Figure 6a. The wavelength of the maximum intensity of the ^{4}A$_2 \rightarrow$ ^{4}T$_1$ band emission is roughly in the same place for both samples, whereas the ^{4}A$_2 \rightarrow$ ^{4}T$_2$ band of the α phase occurs at longer wavelengths than those for the β phase, and an inversion of the excitation-band intensities is observed between the two phases as observed for Ga$_2$O$_3$:Cr^{3+}.[43] This intensity inversion arises from changes in radiative transition probabilities, where the β phase has a higher radiative probability of the ^{4}A$_2 \rightarrow$ ^{4}T$_1$ transition and the α phase has a higher ^{4}A$_2 \rightarrow$ ^{4}T$_2$ radiative transition probability. A similar phenomenon is found for the radiative transition probabilities of the R$_1$ and R$_2$ lines.

The PL spectrum for α- and β-Ga$_{1.98-x}$(Al$_{0.68}$In$_{0.32}$)$_x$O$_3$:0.02Cr^{3+} at $x = 0.8$ (Figure 6b) shows an approximately 30 nm red shift and an increase of the FWHM to 193 nm of the
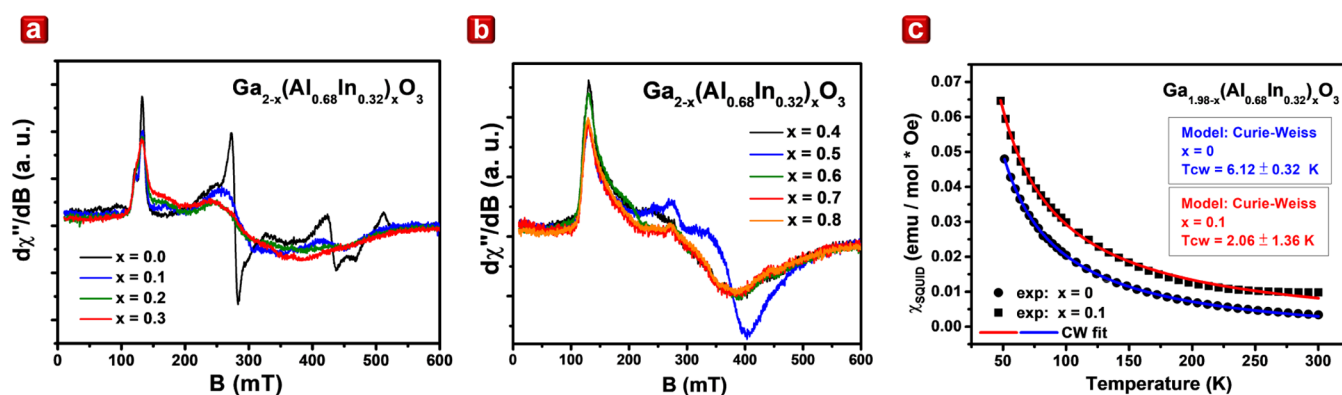
Figure 7. EPR measurements of $Ga_{1.98-x}(Al_{0.68}In_{0.32})_xO_3$:$0.02Cr^{3+}$ at room temperature for (a) samples $0.0 \leq x \leq 0.3$ and a magnetic field range of $10-600$ mT and (b) samples $0.4 \leq x \leq 0.8$ and a magnetic field range of $100-600$ mT. (c) Magnetic susceptibility with temperature for $x = 0$ and 0.1 with Curie–Weiss behavior fits.

broad-band emission from the α phase compared with the β phase. Moreover, the R-line emission of the α phase occurs at lower energies than those for the β phase, and its average decay time is significantly shorter (0.02 ms) than that for the β phase (0.05 ms), as shown in Figure S10a. Crystal field parameters for α- and β-$Ga_{1.98-x}(Al_{0.68}In_{0.32})_xO_3$:$0.02Cr^{3+}$ at $x = 0.8$ are shown in Table S8. Decreases in crystal field strength and increased electron–phonon coupling contribute to the broadening of the emission spectrum. Pressure-dependent PLE and PL spectra for α-$Ga_{1.98-x}(Al_{0.68}In_{0.32})_xO_3$:$0.02Cr^{3+}$ at $x = 0.8$ are shown in Figures S10b and 6c. The positions of $^4A_2 \rightarrow \, ^4T_1$ and $^4A_2 \rightarrow \, ^4T_2$ transition emissions are estimated to have shifted by 13.1 ± 1.0 and 11.5 ± 0.7 cm^{-1}/kbar, respectively, whereas the R-line and broad-band emissions shift by -0.81 ± 0.03 and 5.54 ± 0.23 cm^{-1}/kbar, respectively, as shown in Figure 6d. The shift in the broad-band emission of α-$Ga_{1.98-x}(Al_{0.68}In_{0.32})_xO_3$:$0.02Cr^{3+}$ is 2 times smaller than that for the β phase (11.5 ± 0.6 cm^{-1}/kbar), whereas the R-line shift for both materials is roughly the same. The significantly different pressure dependence of features for the $^4A_2 \rightarrow \, ^4T_2$ transition (excitation band) and the $^4T_2 \rightarrow \, ^4A_2$ transition (emission band) between the α and β phases suggests a change in $S\hbar\omega$ with pressure.

The pressure-dependent decay of intensity upon excitation at 440 nm of the α sample at $x = 0.8$ up to 250 kbar is shown in Figure S10c, with the average decay time τ_{av} calculated using eq 1. The decay time increases with pressure (Figure 6e) as a result of the reduction in the occupancy of the higher $^4T_2$ state. Notably, the α-phase is stable even when the pressure is released, and the considered relation between chemical and mechanical pressures in detail is described in the Supporting Information. The crystal field and energy level diagram as a function of x and pressure are calculated, with details given in the Supporting Information. However, since the α-phased samples were acquired in the diamond anvil cell, the amount of samples is too little for further structural characterization.

Electron Paramagnetic Resonance (EPR) Studies. EPR spectra are sensitive to the short-range environment of luminescent paramagnetic chromium ions. EPR spectra of $Ga_{1.98-x}(Al_{0.68}In_{0.32})_xO_3$:$0.02Cr^{3+}$ with x between 0 and 0.8 (Figures 7a,b) are similar to those for Ga_2O_3[16] and Ga_2O_3@ MSN (nanophosphor)[32] materials doped with Cr.

Differences in the position of the EPR line are defined as the effective value of the spectroscopic splitting ratio $g_{eff} = 41.488$ f/B_{rez}, where f is the microwave frequency and B_{rez} is the

position of the resonance EPR line. Notably, no significant changes are observed in the nearest neighbor Cr^{3+} environment for $x \leq 0.3$ ($g_{eff} = 5.10(2)$) and $x \geq 0.4$ ($g_{eff} = 5.22(2)$), although a substantial increase in the EPR line width and shifts in the maximum intensity of the low-field magnetic induction line are found with the magnetic field. These results are consistent with increasing inhomogeneity of the Cr^{3+} environment with increased $Al_{0.68}In_{0.32}$ concentrations, corroborating further the presence of at least two Cr^{3+} centers ($GaInO_3$:Cr^{3+} and $GaAlO_3$:Cr^{3+}) as shown by optical studies. Detailed calculations of the SH parameters and the temperature dependence of the magnetic susceptibility (SQUID) are shown in the Supporting Information, and magnetic susceptibility with temperature is shown in Figure 7c.

Weak ferromagnetic interactions between Cr^{3+} in axial symmetry (C_4) sites, with high distortion in an octahedral environment, are noted, consistent with the significant elongation of the a-axis and explaining the persistence of the trigonal α-phase following pressure release.

LED Performance. Since the amount of the α-phased samples was too little for demonstration, a NIR pc-LED was fabricated by coating $Ga_{1.18}(Al_{0.544}In_{0.256})O_3$:$0.02Cr^{3+}$ ($x = 0.8$) onto a blue LED chip with an emission wavelength of 452 nm. Figure 8 shows the emission spectrum centered at 784 nm and extending over $650-1000$ nm with an FWHM of 156 nm and an output power of 68.8 mW under 350 mA current. The appearance of the device is shown in the upper inset of Figure 8, and the demonstration of practical use is shown in the lower inset of Figure 8, showing its possible applications as a NIR light source.

CONCLUSIONS

A series of $Ga_{1.98-x}(Al_{0.68}In_{0.32})_xO_3$:$0.02Cr^{3+}$ with $x = 0-0.8$ broad-band NIR phosphors were synthesized. X-ray and neutron powder diffraction reveals the series to be phase pure. Luminescent studies of the series show a broadened emission spectrum with increased electron–phonon coupling with x caused by the introduction of short-range structural disorder. The series produces NIR emissions over $650-1000$ nm with > 80% IQE. Time-resolved spectroscopy reveals the simultaneous presence of high and low crystal field Cr^{3+} centers. A pressure-induced transformation from the β phase to the α phase that differs in emission properties from those for α-Ga_2O_3:Cr^{3+} is found, emitting an even broader spectrum with an FWHM of 193 nm. EPR and SQUID studies support
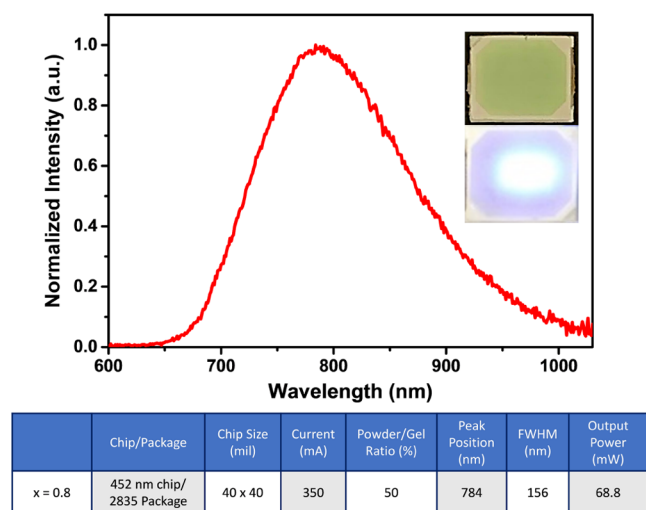
	Chip/Package	Chip Size (mil)	Current (mA)	Powder/Gel Ratio (%)	Peak Position (nm)	FWHM (nm)	Output Power (mW)
x = 0.8	452 nm chip/ 2835 Package	40 x 40	350	50	784	156	68.8

Figure 8. Emission spectrum of a NIR pc-LED containing $Ga_{1.98-x}(Al_{0.68}In_{0.32})_xO_3$: $0.02Cr^{3+}$ at $x = 0.8$. The LED device is shown in the inset.

increased disorder in Cr^{3+} environments across the series with increasing x. We demonstrate the practical application of the $Ga_{1.18}Al_{0.544}In_{0.256}O_3$:$0.02Cr^{3+}$ (sample $x = 0.8$) phosphor by fabricating a NIR pc-LED. This work shows that the emission width is controllable through emission center disorder introduced by codoping.

■ EXPERIMENTAL SECTION

Reagents. Gallium oxide (Ga_2O_3, 99.9%) and aluminum oxide (Al_2O_3, 99.9%) were purchased from Gredmann. Indium oxide (In_2O_3, 99.9%) was purchased from Alfa Aesar. Chromium oxide (Cr_2O_3, 99.9%) was purchased from Merck.

Synthesis of $Ga_{1.98-x}(Al_{0.68}In_{0.32})_xO_3$:$0.02Cr^{3+}$ ($x = 0-0.9$). The material was synthesized using a solid solution method. The precursors were weighed stoichiometrically and ground in an agate mortar for 20 min. The mixed powders were transferred into alumina crucibles and sintered at 1550 °C for 5 h in air and then ground in an agate mortar.

Further characterization and experimental measurements are provided in the Supporting Information.

■ ASSOCIATED CONTENT

Ⓢ Supporting Information

The Supporting Information is available free of charge at https://pubs.acs.org/doi/10.1021/acs.chemmater.2c03045.

Detailed experimental characterization results; XRD and NPD refinements; X-ray absorption near-edge spectroscopy (XANES); Raman spectroscopy; luminescence measurements; crystal field calculations including pressure-dependent energy diagrams; decay profiles; chemical pressure studies; EPR; and SQUID measurements (PDF)

■ AUTHOR INFORMATION

Corresponding Authors

Sebastian Mahlik − *Institute of Experimental Physics, Faculty of Mathematics, Physics and Informatics, University of Gdansk, 80-308 Gdansk, Poland*; Email: sebastian.mahlik@ug.edu.pl

Ru-Shi Liu − *Department of Chemistry, National Taiwan University, Taipei 106, Taiwan*; ◉ orcid.org/0000-0002-1291-9052; Email: rsliu@ntu.edu.tw

Authors

Chih-Yu Chang − *Department of Chemistry, National Taiwan University, Taipei 106, Taiwan*

Natalia Majewska − *Institute of Experimental Physics, Faculty of Mathematics, Physics and Informatics, University of Gdansk, 80-308 Gdansk, Poland*; ◉ orcid.org/0000-0002-1933-0355

Kuan-Chun Chen − *Department of Chemistry, National Taiwan University, Taipei 106, Taiwan*

Wen-Tse Huang − *Department of Chemistry, National Taiwan University, Taipei 106, Taiwan*

Tadeusz Leśniewski − *Institute of Experimental Physics, Faculty of Mathematics, Physics and Informatics, University of Gdansk, 80-308 Gdansk, Poland*; ◉ orcid.org/0000-0003-2451-7760

Grzegorz Leniec − *Department of Technical Physics, Faculty of Mechanical Engineering and Mechatronics, West Pomeranian University of Technology Szczecin, 70-311 Szczecin, Poland*

Sławomir M. Kaczmarek − *Department of Technical Physics, Faculty of Mechanical Engineering and Mechatronics, West Pomeranian University of Technology Szczecin, 70-311 Szczecin, Poland*

Wei Kong Pang − *Institute for Superconducting and Electronic Materials, University of Wollongong, North Wollongong, New South Wales 2522, Australia*; ◉ orcid.org/0000-0002-5118-3885

Vanessa K. Peterson − *Institute for Superconducting and Electronic Materials, University of Wollongong, North Wollongong, New South Wales 2522, Australia; Australian Centre for Neutron Scattering, Australian Nuclear Science and Technology Organisation, Sydney, New South Wales 2232, Australia*; ◉ orcid.org/0000-0002-5442-0591

Ding-Hua Cherng − *Everlight Electronics Co., Ltd., New Taipei City 238, Taiwan*

Kuang-Mao Lu − *Everlight Electronics Co., Ltd., New Taipei City 238, Taiwan*

Complete contact information is available at:
https://pubs.acs.org/10.1021/acs.chemmater.2c03045

Author Contributions

∇C.-Y.C. and N.M. contributed equally to this work. The manuscript was written through the contributions of all authors. All authors have given approval for the final version of the manuscript.

Notes

The authors declare no competing financial interest.

■ ACKNOWLEDGMENTS

■ REFERENCES

(1) Osborne, B. G. *Near-Infrared Spectroscopy in Food Analysis; Encyclopedia of Analytical Chemistry: Applications, Theory and Instrumentation*; John Wiley & Sons, Ltd., 2006.

(2) Kotcherlakota, R.; Nimushakavi, S.; Roy, A.; Yadavalli, H. C.; Mukherjee, S.; Haque, S.; Patra, C. R. Biosynthesized Gold Nanoparticles: In Vivo Study of Near-Infrared Fluorescence (NIR)-Based Bio-Imaging and Cell Labeling Applications. *ACS Biomater. Sci. Eng.* **2019**, *5*, 5439−5452.

(3) Xiang, J.; Chen, J.; Zhang, N.; Yao, H.; Guo, C. Far Red and Near Infrared Double-Wavelength Emitting Phosphor Gd_2ZnTiO_6: Mn^{4+}, Yb^{3+} for Plant Cultivation LEDs. *Dyes Pigm.* **2018**, *154*, 257−262.

(4) Pei, P.; Chen, Y.; Sun, C.; Fan, Y.; Yang, Y.; Liu, X.; Lu, L.; Zhao, M.; Zhang, H.; Zhao, D.; Liu, X.; Zhang, F. X-ray-Activated Persistent Luminescence Nanomaterials for NIR-II Imaging. *Nat. Nanotechnol.* **2021**, *16*, 1011−1018.

(5) Wang, C.; Wang, X.; Zhou, Y.; Zhang, S.; Li, C.; Hu, D.; Xu, L.; Jiao, H. An Ultra-Broadband Near-Infrared Cr^{3+}-Activated Gallogermanate $Mg_3Ga_2GeO_8$ Phosphor as Light Sources for Food Analysis. *ACS Appl. Electron. Mater.* **2019**, *1*, 1046−1053.

(6) Xie, R.-J. Light-Emitting Diodes: Brighter NIR-Emitting Phosphor Making Light Sources Smarter. *Light: Sci. Appl.* **2020**, *9*, No. 155.

(7) Fang, M. H.; Huang, P. Y.; Bao, Z.; Majewska, N.; Lesniewski, T.; Mahlik, S.; Grinberg, M.; Leniec, G.; Kaczmarek, S. M.; Yang, C.-W.; Lu, K. M.; Sheu, H.-S.; Liu, R. S. Penetrating Biological Tissue Using Light-Emitting Diodes with a Highly Efficient Near-Infrared $ScBO_3$: Cr^{3+} Phosphor. *Chem. Mater.* **2020**, *32*, 2166−2171.

(8) Hayashi, D.; van Dongen, A. M.; Boerekamp, J.; Spoor, S.; Lucassen, G.; Schleipen, J. A Broadband LED Source in Visible to Short-Wave-Infrared Wavelengths for Spectral Tumor Diagnostics. *Appl. Phys. Lett.* **2017**, *110*, No. 233701.

(9) Xu, X.; Shao, Q.; Yao, L.; Dong, Y.; Jiang, J. Highly Efficient and Thermally Stable Cr^{3+}-Activated Silicate Phosphors for Broadband Near-Infrared LED Applications. *Chem. Eng. J.* **2020**, *383*, No. 123108.

(10) Smith, A. M.; Mancini, M. C.; Nie, S. Second Window for In Vivo Imaging. *Nat. Nanotechnol.* **2009**, *4*, 710−711.

(11) De Guzman, G. N. A.; Fang, M. H.; Liang, C. H.; Bao, Z.; Hu, S. F.; Liu, R. S. Near-Infrared Phosphors and Their Full Potential: A Review on Practical Applications and Future Perspectives. *J. Lumin.* **2020**, *219*, No. 116944.

(12) Shao, Q.; Ding, H.; Yao, L.; Xu, J.; Liang, C.; Jiang, J. Photoluminescence Properties of a $ScBO_3$: Cr^{3+} Phosphor and Its Applications for Broadband Near-Infrared LEDs. *RSC Adv.* **2018**, *8*, 12035−12042.

(13) Rajendran, V.; Fang, M. H.; Guzman, G. N. D.; Lesniewski, T.; Mahlik, S.; Grinberg, M.; Leniec, G.; Kaczmarek, S. M.; Lin, Y. S.; Lu, K. M.; Lin, C. M.; Chang, H.; Hu, S. F.; Liu, R. S. Super Broadband Near-Infrared Phosphors with High Radiant Flux as Future Light Sources for Spectroscopy Applications. *ACS Energy Lett.* **2018**, *3*, 2679−2684.

(14) Rajendran, V.; Chang, H.; Liu, R. S. Recent Progress on Broadband Near-Infrared Phosphors-Converted Light Emitting Diodes for Future Miniature Spectrometers. *Opt. Mater.: X* **2019**, *1*, No. 100011.

(15) Wen, D.; Liu, H.; Guo, Y.; Zeng, Q.; Wu, M.; Liu, R. S. Disorder-Order Conversion-Induced Enhancement of Thermal Stability of Pyroxene NIR Phosphors. *Angew. Chem.* **2022**, *134*, No. e202204411.

(16) Fang, M. H.; De Guzman, G. N. A.; Bao, Z.; Majewska, N.; Mahlik, S.; Grinberg, M.; Leniec, G.; Kaczmarek, S. M.; Yang, C. W.; Lu, K. M.; Sheu, H.-S.; Hu, S. F.; Liu, R. S. Ultra-High-Efficiency Near-Infrared Ga_2O_3: Cr^{3+} Phosphor and Controlling of Phytochrome. *J. Mater. Chem. C* **2020**, *8*, 11013−11017.

(17) Fang, M. H.; Chen, K. C.; Majewska, N.; Lesniewski, T.; Mahlik, S.; Leniec, G.; Kaczmarek, S. M.; Yang, C. W.; Lu, K. M.; Sheu, H.-S.; S, F.; Liu, R. S. Hidden Structural Evolution and Bond Valence Control in Near-Infrared Phosphors for Light-Emitting Diodes. *ACS Energy Lett.* **2021**, *6*, 109−114.

(18) Zhong, J.; Zhuo, Y.; Du, F.; Zhang, H.; Zhao, W.; Brgoch, J. Efficient and Tunable Luminescence in $Ga_{2−x}In_xO_3$: Cr^{3+} for Near-Infrared Imaging. *ACS Appl. Mater. Interfaces* **2021**, *13*, 31835−31842.

(19) Chen, K. C.; Fang, M. H.; Huang, W. T.; Kamiński, M.; Majewska, N.; Leśniewski, T.; Mahlik, S.; Leniec, G.; Kaczmarek, S. M.; Yang, C.-W.; Lu, K. M.; Sheu, H.-S.; Liu, R. S. Chemical and Mechanical Pressure-Induced Photoluminescence Tuning via Structural Evolution and Hydrostatic Pressure. *Chem. Mater.* **2021**, *33*, 3832−3840.

(20) Xia, Z.; Liu, Q. Progress in Discovery and Structural Design of Color Conversion Phosphors for LEDs. *Prog. Mater. Sci.* **2016**, *84*, 59−117.

(21) Lin, C. C.; Tsai, Y. T.; Johnston, H. E.; Fang, M. H.; Yu, F.; Zhou, W.; Whitfield, P.; Li, Y.; Wang, J.; Liu, R. S.; Attfield, J. P. Enhanced Photoluminescence Emission and Thermal Stability from Introduced Cation Disorder in Phosphors. *J. Am. Chem. Soc.* **2017**, *139*, 11766−11770.

(22) Rietveld, H. M. A Profile Refinement Method for Nuclear and Magnetic Structures. *J. Appl. Crystallogr.* **1969**, *2*, 65−71.

(23) Shannon, R. D. Revised Effective Ionic Radii and Systematic Studies of Interatomic Distances in Halides and Chalcogenides. *Acta Crystallogr., A* **1976**, *32*, 751−767.

(24) Rajendran, V.; Fang, M. H.; Huang, W. T.; Majewska, N.; Lesniewski, T.; Mahlik, S.; Leniec, G.; Kaczmarek, S. M.; Pang, W. K.; Peterson, V. K.; Lu, K. M.; Chang, H.; Liu, R. S. Chromium Ion Pair Luminescence: A Strategy in Broadband Near-Infrared Light-Emitting Diode Design. *J. Am. Chem. Soc.* **2021**, *143*, 19058−19066.

(25) Henderson, B.; Imbusch, G. F. *Optical Spectroscopy of Inorganic Solids*; Oxford University Press, 2006; pp 413−433.

(26) Onuma, T.; Fujioka, S.; Yamaguchi, T.; Itoh, Y.; Higashiwaki, M.; Sasaki, K.; Masui, T.; Honda, T. Polarized Raman Spectra in β-Ga_2O_3 Single Crystals. *J. Cryst. Growth* **2014**, *401*, 330−333.

(27) Kranert, C.; Sturm, C.; Schmidt-Grund, R.; Grundmann, M. Raman Tensor Elements of β-Ga_2O_3. *Sci. Rep.* **2016**, *6*, No. 35964.

(28) Zhang, L.; Wang, D.; Hao, Z.; Zhang, X.; Pan, G. H.; Wu, H.; Zhang, J. Cr^{3+}-Doped Broadband NIR Garnet Phosphor with Enhanced Luminescence and Its Application in NIR Spectroscopy. *Adv. Opt. Mater.* **2019**, *7*, No. 1900185.

(29) Brik, M. G.; Camardello, S.; Srivastava, A.; Avram, N.; Suchocki, A. Spin-Forbidden Transitions in the Spectra of Transition Metal Ions and Nephelauxetic Effect. *ECS J. Solid State Sci. Technol.* **2016**, *5*, R3067.

(30) Walsh, C.; Donegan, J.; Glynn, T.; Morgan, G.; Imbusch, G.; Remeika, J. Luminescence from β-Ga_2O_3: Cr^{3+}. *J. Lumin.* **1988**, *40−41*, 103−104.

(31) Vasyltsiv, V.; Luchechko, A.; Zhydachevskyy, Y.; Kostyk, L.; Lys, R.; Slobodzyan, D.; Jakieła, R.; Pavlyk, B.; Suchocki, A. Correlation Between Electrical Conductivity and Luminescence Properties in β-Ga_2O_3: Cr^{3+} and β-Ga_2O_3: Cr, Mg Single Crystals. *J. Vac. Sci. Technol., A* **2021**, *39*, No. 033201.

(32) Fang, M. H.; Li, T. Y.; Huang, W. T.; Cheng, C. L.; Bao, Z.; Majewska, N.; Mahlik, S.; Yang, C. W.; Lu, K. M.; Leniec, G.; Kaczmarek, S. M.; Sheu, H.-S.; Liu, R. S. Surface-Protected High-Efficiency Nanophosphors via Space-Limited Ship-in-a-Bottle Synthesis for Broadband Near-Infrared Mini-Light-Emitting Diodes. *ACS Energy Lett.* **2021**, *6*, 659−664.

(33) Lu, Y.-Y.; Liu, F.; Gu, Z.; Pan, Z. Long-Lasting Near-Infrared Persistent Luminescence from β-Ga_2O_3: Cr^{3+} Nanowire Assemblies. *J. Lumin.* **2011**, *131*, 2784−2787.

(34) Chang, T.; Holzrichter, J.; Imbusch, G.; Schawlow, A. Polarized Fluorescence Study of Cr^{3+} Through a Stress-Induced Phase Transition in $SrTiO_3$. *Solid State Commun.* **1970**, *8*, 1179−1181.

(35) Zhong, J.; Zhuang, W.; Xing, X.; Liu, R.; Li, Y.; Liu, Y.; Hu, Y. Synthesis, Crystal Structures, and Photoluminescence Properties of Ce^{3+}-doped $Ca_2LaZr_2Ga_3O_{12}$: New Garnet Green-Emitting Phosphors for White LEDs. *J. Phys. Chem. C* **2015**, *119*, 5562−5569.

(36) Zhong, J.; Zhao, W.; Du, F.; Wen, J.; Zhuang, W.; Liu, R.; Duan, C.-K.; Wang, L.; Lin, K. Identifying the Emission Centers and Probing the Mechanism for Highly Efficient and Thermally Stable Luminescence in the La$_3$Si$_6$N$_{11}$: Ce^{3+} Phosphor. *J. Phys. Chem. C* **2018**, *122*, 7849−7858.

(37) Song, E.; Ming, H.; Zhou, Y.; He, F.; Wu, J.; Xia, Z.; Zhang, Q. Cr^{3+}-Doped Sc-Based Fluoride Enabling Highly Efficient Near Infrared Luminescence: A Case Study of K$_2$NaScF$_6$: Cr^{3+}. *Laser Photonics Rev.* **2021**, *15*, No. 2000410.

(38) Grinberg, M. ^{2}E → ^{4}A$_2$ Fluorescence of Cr^{3+} in High and Intermediate Field Garnets. *J. Lumin.* **1993**, *54*, 369−382.

(39) He, H.; Orlando, R.; Blanco, M. A.; Pandey, R.; Amzallag, E.; Baraille, I.; Rérat, M. First-Principles Study of the Structural, Electronic, and Optical Properties of Ga$_2$O$_3$ in Its Monoclinic and Hexagonal Phases. *Phys. Rev. B* **2006**, *74*, No. 195123.

(40) Lipinska-Kalita, K. E.; Chen, B.; Kruger, M.; Ohki, Y.; Murowchick, J.; Gogol, E. High-Pressure X-ray Diffraction Studies of the Nanostructured Transparent Vitroceramic Medium K$_2$O−SiO$_2$−Ga$_2$O$_3$. *Phys. Rev. B* **2003**, *68*, No. 035209.

(41) Machon, D.; McMillan, P. F.; Xu, B.; Dong, J. High-Pressure Study of the β-to-α Transition in Ga$_2$O$_3$. *Phys. Rev. B* **2006**, *73*, No. 094125.

(42) Grinberg, M.; Barzowska, J.; Shen, Y.; Bray, K.; Dereń, P.; Hanuza, J. High-Pressure Spectroscopy Characterisation of LiSc (WO$_4$)$_2$ Crystals Doped with Trivalent Chromium. *J. Lumin.* **2003**, *102−103*, 699−704.

(43) Back, M.; Ueda, J.; Nambu, H.; Fujita, M.; Yamamoto, A.; Yoshida, H.; Tanaka, H.; Brik, M. G.; Tanabe, S. Boltzmann Thermometry in Cr^{3+}-Doped Ga$_2$O$_3$ Polymorphs: The Structure Matters! *Adv. Opt. Mater.* **2021**, *9*, No. 2100033.

Broadening Phosphor-Converted Light-Emitting Diode Emission: Controlling Disorder

Chih-Yu Chang[†,‡], Natalia Majewska[§,‡], Kuan-Chun Chen[†], Wen-Tse Huang[†], Tadeusz Leśniewski[§], Grzegorz Leniec[&], Sławomir M. Kaczmarek[&], Wei Kong Pang[#], Vanessa K. Peterson[#,ϕ], Ding-Hua Cherng[⊥], Kuang-Mao Lu[⊥], Sebastian Mahlik[,§], Ru-Shi Liu[*,†]*

‡ These authors contributed equally

† Department of Chemistry, National Taiwan University, Taipei 106, Taiwan

§ Institute of Experimental Physics, Faculty of Mathematics, Physics and Informatics, University of Gdansk, Wita Stwosza 57, 80-308 Gdansk, Poland

& Department of Technical Physics, Faculty of Mechanical Engineering and Mechatronics, West Pomeranian University of Technology Szczecin, al. Piastow 48, 70-311 Szczecin, Poland

Institute for Superconducting and Electronic Materials, University of Wollongong, Squires Way, North Wollongong, New South Wales 2522, Australia

ϕ Australian Centre for Neutron Scattering, Australian Nuclear Science and Technology Organisation, Sydney, New South Wales 2232, Australia

⊥ Everlight Electronics Co., Ltd., New Taipei City 238, Taiwan

Experimental and Characterization

XRD and NPD

X-ray powder diffraction (XRD) data were obtained at room temperature (RT) using a Bruker D2 phaser desktop diffractometer with Cu$K\alpha_1$ radiation within the 2θ range of 10−80°. RT synchrotron XRD (S-XRD) data were obtained at 0.77491(1) Å using a Debye–Scherrer camera at the National Synchrotron Radiation Research Center (Taiwan) BL01C2 beamline. The S-XRD wavelength was determined accurately using the LaB_6 660a National Institute of Standards and Technology (NIST) standard reference material (SRM). High-resolution neutron powder diffraction (NPD) data were obtained using the Echidna instrument at the Open Pool Australian light-water research reactor of the Australian Nuclear Science and Technology Organisation within the 2θ range of 4–164° with 1.623628(5) Å neutrons as determined using the NIST $La^{11}B_6$ 660b SRM.[1]

The Inorganic Crystal Structure Database structure model #ICSD34243 was used as the starting structure from which the structures of the $Ga_{1.98–x}(Al_{0.68}In_{0.32})_xO_3:0.02Cr^{3+}$ series were determined. Refinements were performed simultaneously against S-XRD and NPD data using Rietveld analysis with the academic Total Pattern Analysis Solutions software (version 5.0).[2] Refined parameters included background, peak-shape parameters, lattice parameters, atomic positions, site-occupancy factors, and isotropic atomic-displacement parameters. Crystal structures were visualized with VESTA software.[3]

X-ray Spectroscopy Characterization

X-ray absorption near-edge structure measurements (XANES) and extended X-ray absorption fine structure (EXAFS) at the Cr *K*-edge were acquired at the National Synchrotron Radiation Research Center (Taiwan) BL44A1 in total fluorescence yield mode. Data analysis and conversion are obtained with ATHENA and ARTEMIS software.

Raman Spectroscopy Characterization

Raman spectra were recorded on a micro-Raman system comprising a confocal microscope and a Horiba Jobin Yvon Lab Ram Aramis spectrometer with 1800 l/mm grating and a single-mode laser source at 532 nm. Data analysis and conversion were performed with LabSpec 5 software provided by Horiba.

Room-Temperature Luminescence Spectra

RT photoluminescence excitation (PLE) spectra were measured using a FluoroMax-4P spectrofluorometer (Horiba) equipped with a 150 W xenon lamp as an excitation source and an R928 Hamamatsu photomultiplier as a detector.

Internal Quantum Efficiency (IQE)

IQE measurement was conducted using an ultra-violet (UV) to NIR absolute photoluminescence (PL) quantum yield spectrometer (C1534−12; Hamamatsu Photonics K.K.) equipped with a NIR PL measurement unit (C13684−01; Hamamatsu Photonics K.K.) comprising a high-power Xe lamp unit (L13685−01; Hamamatsu Photonics K.K.) and a 475 nm filter for excitation (A13686–475).

Temperature and Pressure-Dependent Spectrum

Temperature and pressure-dependent emission spectra were measured using an Andor SR-750-D1 spectrometer equipped with a charge-coupled device (CCD) camera (DU420A-OE) and a Kimmon Koha He-Cd 442 nm laser. The temperature was controlled using a THMS600 Linkam stage temperature controller with an LNP95 liquid nitrogen cooling-pump system, allowing measurements at 77–600 K.

Luminescence

Luminescence was measured with an apparatus for time-resolved spectroscopy comprising a PG 401/SH optical parametric generator pumped by a PL2251A pulsed neodymium-doped yttrium aluminum garnet (YAG:Nd) laser (EKSPLA). The detector consisted of a 2501S grating spectrometer (Bruker Optics) combined with a C4334-01 streak camera (Hamamatsu). Data were recorded as streak images on a 640 x 480 pixel CCD array. The photon counting algorithm transformed data into a 2D matrix of photon counts versus wavelength and time (streak image).[4] Samples were cooled with an APD Cryogenics closed-cycle DE-202 optical cryostat, which enabled the temperature to be varied between 10 and 450 K.

High-Pressure Studies

High-pressure luminescence measurements were performed in a screw-driven Merrill-Bassett type diamond anvil cell with a 0.5 mm diamond culet diameter.[5] The gasket for the pressure chamber was pre-indented to around 0.07 mm. A hole with a diameter of 0.2 mm was drilled into the center of the indentation. $KMgF_3$:0.5%Eu^{2+} was used as a pressure sensor, and polydimethylsiloxane oil was used as a pressure-transmitting medium.[6]

Electron Paramagnetic Resonance (EPR) Studies

EPR spectra were recorded at 82–300 K by using a conventional X-band spectrometer ELEXSYS E500 operating at 9.46 GHz and 0.62 mW microwave power. The first derivative of the absorption spectrum was recorded as a function of the applied magnetic induction, which ranged from 0 to 1.4 T. The EPR/NMR program was used to determine spin-Hamiltonian (SH) parameters and the local symmetry of paramagnetic ions.[7] Optimization and normalization of the parameters were conducted using the root-mean-squared deviation method.

Static Magnetic-Susceptibility Measurements

Static magnetic-susceptibility measurements were performed using a superconducting quantum interference device (SQUID) MPMS-XL7 magnetometer. Measurements were recorded from ~ 50 K to room temperature at a magnetic field of 1 kOe. Susceptibility data were corrected for the diamagnetism of the sample holder and constituent atoms using Pascal's constants.[8]

Supporting Figures and Tables

XRD data
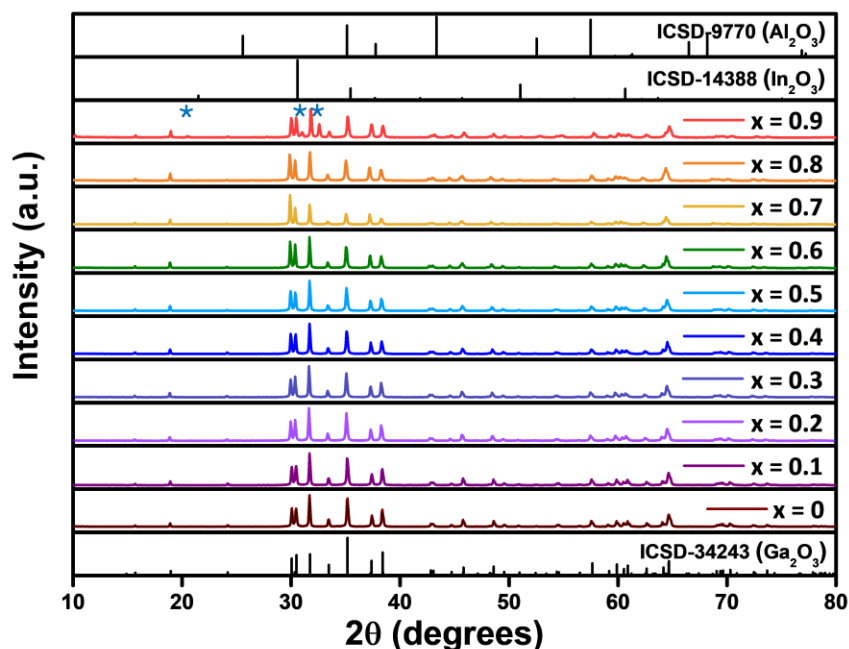
Figure S1. XRD data of the $Ga_{1.98-x}(Al_{0.68}In_{0.32})_xO_3{:}0.02Cr^{3+}$ (x = 0−0.9) series, along with calculations for the structural end-members Ga_2O_3 (ICSD database entry #34243), Al_2O_3 (ICSD database entry #9770), and In_2O_3 (ICSD database entry #14388). Asterix in the x = 0.9 sample are impurities.

S-XRD and NPD Refinement Results
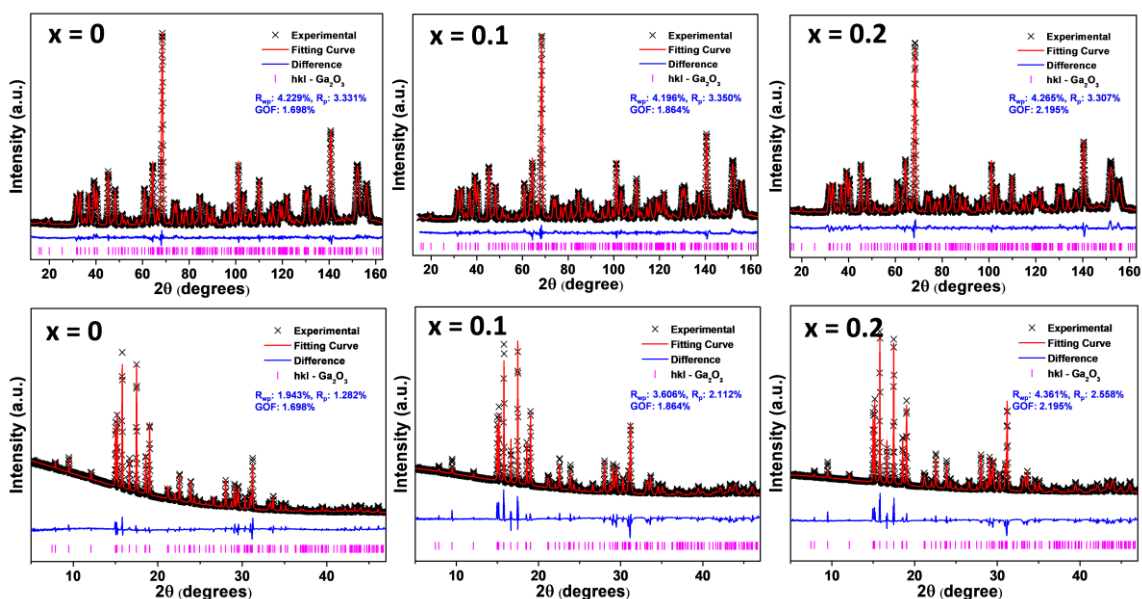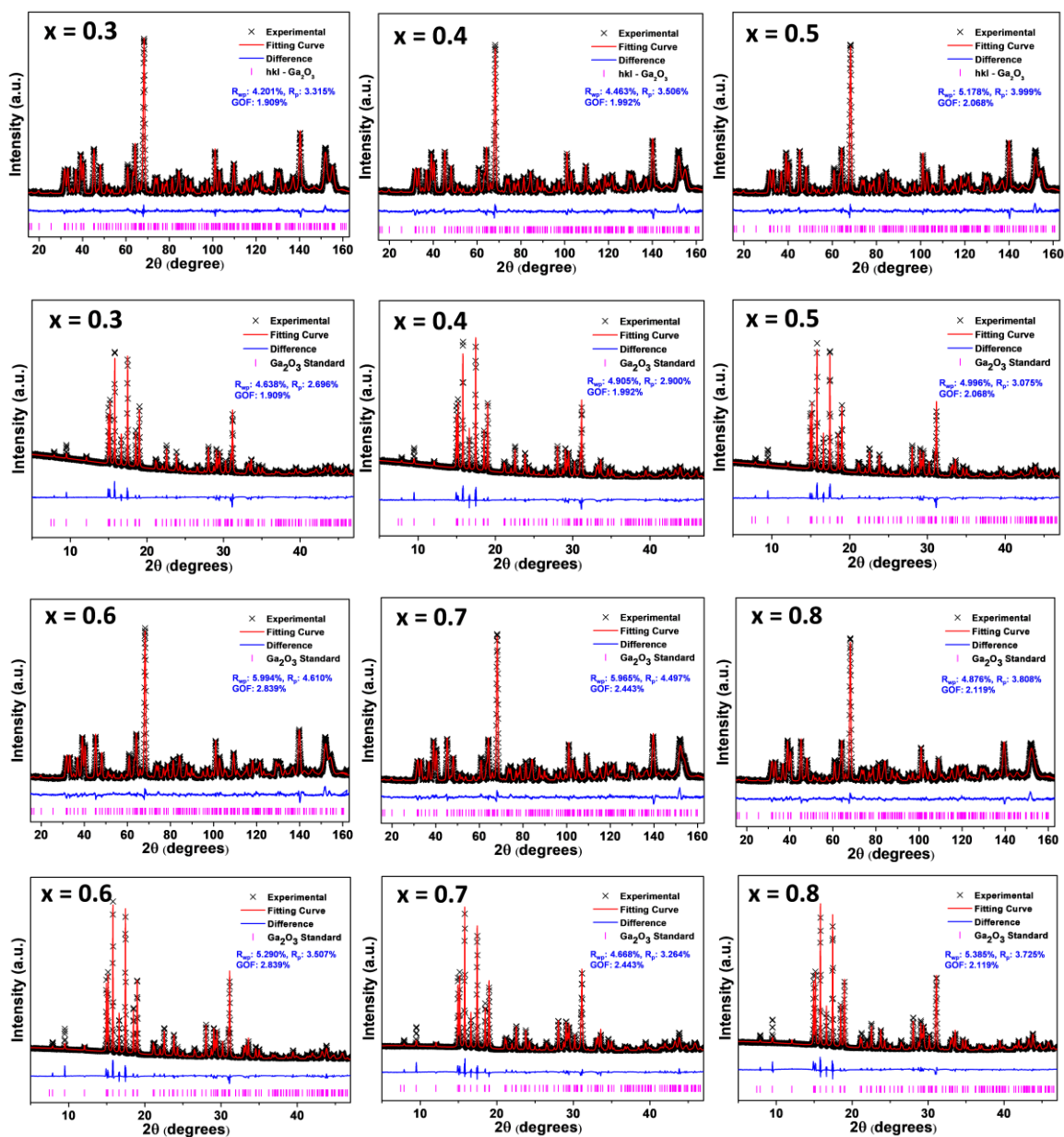
Figure S2. Rietveld refinement of $Ga_{1.98-x}(Al_{0.68}In_{0.32})_xO_3:0.02Cr^{3+}$ (x = 0, 0.1, 0.2, 0.3, 0.4, 0.5, 0.6, 0.7, and 0.8) structures using NPD (upper) and S-XRD (lower) data. Figures of merit are the profile R-factor R_p, the weighted profile R-factor R_{wp}, and the goodness of fit (GOF).

Table S1. Atomic positions and occupancies derived from the Rietveld refinement of $Ga_{1.98-x}(Al_{0.68}In_{0.32})_xO_3{:}0.02Cr^{3+}$ (x = 0, 0.1, 0.2, 0.3, 0.4, 0.5, 0.6, 0.7, and 0.8).

x = 0							Ga_2O_3
Site	x	y	z	Occ.	Multiplicity & Wyckoff	Beq (Å²)	Atoms
Ga1	0.0915(5)	0	0.7951(12)	1	4i	3.5(2)	1
Ga2	0.3424(3)	0	0.6823(9)	1	4i	4.6(2)	1
O1	0. 1600(20)	0	0.075(6)	1	4i	6.4(7)	4
O2	0. 4913(12)	0	0.259(3)	1	4i	2.3(5)	4
O3	0. 8235(11)	0	0.471(4)	1	4i	0.9(5)	4

x = 0.1							$Ga_{1.90(4)}Al_{0.07(4)}In_{0.03(4)}O_3$
Site	x	y	z	Occ.	Multiplicity & Wyckoff	Beq (Å²)	Atoms
Ga1	0.09064(9)	0	0.7937(3)	0.979(10)	4i	0.36(2)	3.92(4)
Al1	0.09064(9)	0	0.7937(3)	0.004(7)	4i	0.36(2)	0.02(3)
In1	0.09064(9)	0	0.7937(3)	0.017(7)	4i	0.36(2)	0.07(3)
Ga2	0.34140(10)	0	0.6852(3)	0.921(10)	4i	0.31(3)	3.68(4)
Al2	0.34140(10)	0	0.6852(3)	0.064(7)	4i	0.31(3)	0.26(3)
In2	0.34140(10)	0	0.6852(3)	0.015(7)	4i	0.31(3)	0.06(3)
O1	0.16431(14)	0	0.1087(3)	1	4i	0.451(14)	4
O2	0.49585(13)	0	0.2542(3)	1	4i	0.451(14)	4
O3	0.82685(13)	0	0.4346(3)	1	4i	0.451(14)	4

x = 0.2							$Ga_{1.80(3)}Al_{0.14(3)}In_{0.07(3)}O_3$
Site	x	y	z	Occ.	Multiplicity & Wyckoff	Beq (Å²)	Atoms
Ga1	0.09060(11)	0	0.7939(3)	0.936(6)	4i	0.48(2)	3.74(2)
Al1	0.09060(11))	0	0.7939(3)	0.034(4)	4i	0.48(2)	0.14(2)
In1	0.09060(11)	0	0.7939(3)	0.030(4)	4i	0.48(2)	0.12(2)
Ga2	0.34139(12)	0	0.6858(3)	0.864(6)	4i	0.60(3)	3.46(2)
Al2	0.34139(12)	0	0.6858(3)	0.102(4)	4i	0.60(3)	0.41(2)
In2	0.34139(12)	0	0.6858(3)	0.034(4)	4i	0.60(3)	0.14(2)
O1	0.16401(18)	0	0.1085(4)	1	4i	0.654(18)	4
O2	0.49534(16)	0	0.2542(4)	1	4i	0.654(18)	4
O3	0.82678(17)	0	0.4335(4)	1	4i	0.654(18)	4

x = 0.3							$Ga_{1.70(4)}Al_{0.20(3)}In_{0.10(3)}O_3$
Site	x	y	z	Occ.	Multiplicity & Wyckoff	Beq (Å²)	Atoms
Ga1	0.09089(11)	0	0.7941(3)	0.904(7)	4i	0.47(2)	3.62(3)
Al1	0.09089(11)	0	0.7941(3)	0.056(5)	4i	0.47(2)	0.22(2)
In1	0.09089(11)	0	0.7941(3)	0.039(5)	4i	0.47(2)	0.16(2)
Ga2	0.34140(12)	0	0.6857(3)	0.796(7)	4i	0.51(3)	3.18(3)
Al2	0.34140(10)	0	0.6857(3)	0.148(5)	4i	0.51(3)	0.59(2)
In2	0.34140(10)	0	0.6857(3)	0.057(5)	4i	0.51(3)	0.23(2)
O1	0.16408(16)	0	0.1081(4)	1	4i	0.655(17)	4
O2	0.49470(15)	0	0.2540(3)	1	4i	0.655(17)	4
O3	0.82671(15)	0	0.4337(4)	1	4i	0.655(17)	4

x = 0.4							$Ga_{1.60(4)}Al_{0.27(3)}In_{0.13(3)}O_3$
Site	x	y	z	Occ.	Multiplicity & Wyckoff	Beq (Å²)	Atoms
Ga1	0.09097(12)	0	0.7939(3)	0.872(7)	4i	0.47(3)	3.48(3)
Al1	0.09097(12)	0	0.7939(3)	0.107(5)	4i	0.47(3)	0.43(2)
In1	0.09097(12)	0	0.7939(3)	0.022(5)	4i	0.47(3)	0.09(2)
Ga2	0.34156(13)	0	0.6851(4)	0.728(7)	4i	0.68(3)	2.92(3)
Al2	0.34156(13)	0	0.6851(4)	0.165(5)	4i	0.68(3)	0.66(2)
In2	0.34156(13)	0	0.6851(4)	0.106(5)	4i	0.68(3)	0.42(2)
O1	0.16428(18)	0	0.1079(4)	1	4i	0.774(19)	4
O2	0.49403(16)	0	0.2534(4)	1	4i	0.774(19)	4
O3	0.82700(17)	0	0.4325(4)	1	4i	0.774(19)	4

x = 0.5							$Ga_{1.50(6)}Al_{0.34(4)}In_{0.16(4)}O_3$
Site	x	y	z	Occ.	Multiplicity & Wyckoff	Beq (Å²)	Atoms
Ga1	0.09083(12)	0	0.7933(4)	0.845(6)	4i	0.56(2)	3.38(4)
Al1	0.09083(12)	0	0.7933(4)	0.145(4)	4i	0.56(2)	0.58(3)
In1	0.09083(12)	0	0.7933(4)	0.010(4)	4i	0.56(2)	0.04(3)
Ga2	0.34241(13)	0	0.6855(4)	0.655(6)	4i	0.64(3)	2.62(4)
Al2	0.34241(13)	0	0.6855(4)	0.195(4)	4i	0.64(3)	0.78(3)
In2	0.34241(13)	0	0.6855(4)	0.150(4)	4i	0.64(3)	0.60(3)
O1	0.16312(19)	0	0.1065(5)	1	4i	0.79(2)	4
O2	0.49397(17)	0	0.2535(4)	1	4i	0.79(2)	4
O3	0.82756(18)	0	0.4333(5)	1	4i	0.79(2)	4

x = 0.6							$Ga_{1.40(4)}Al_{0.41(3)}In_{0.19(3)}O_3$
Site	x	y	z	Occ.	Multiplicity & Wyckoff	Beq (Å²)	Atoms
Ga1	0.09078(14)	0	0.7939(4)	0.807(8)	4i	0.97(4)	3.22(3)
Al1	0.09078(14)	0	0.7939(4)	0.182(6)	4i	0.97(4)	0.73(2)
In1	0.09078(14)	0	0.7939(4)	0.012(5)	4i	0.97(4)	0.05(2)
Ga2	0.34285(14)	0	0.6865(4)	0.593(8)	4i	1.33(5)	2.38(3)
Al2	0.34285(14)	0	0.6865(4)	0.226(6)	4i	1.33(5)	0.90(2)
In2	0.34285(14)	0	0.6865(4)	0.180(5)	4i	1.33(5)	0.72(2)
O1	0.1628(3)	0	0.1074(6)	1	4i	1.21(3)	4
O2	0.4934(2)	0	0.2534(5)	1	4i	1.21(3)	4
O3	0.8271(2)	0	0.4326(6)	1	4i	1.21(3)	4

x = 0.7							$Ga_{1.30(3)}Al_{0.48(1)}In_{0.22(1)}O_3$
Site	x	y	z	Occ.	Multiplicity & Wyckoff	Beq (Å²)	Atoms
Ga1	0.09058(13)	0	0.7937(4)	0.767(4)	4i	0.51(3)	3.07(2)
Al1	0.09058(13)	0	0.7937(4)	0.217(3)	4i	0.51(3)	0.87(1)
In1	0.09058(13)	0	0.7937(4)	0.016(3)	4i	0.51(3)	0.06(1)
Ga2	0.34334(13)	0	0.6880(4)	0.533(4)	4i	0.66(4)	2.13(2)
Al2	0.34334(13)	0	0.6880(4)	0.259(3)	4i	0.66(4)	1.04(1)
In2	0.34334(13)	0	0.6880(4)	0.208(3)	4i	0.66(4)	0.83(1)
O1	0.1629(2)	0	0.1056(5)	1	4i	0.79(3)	4
O2	0.4923(2)	0	0.2523(4)	1	4i	0.79(3)	4
O3	0.8274(2)	0	0.4322(6)	1	4i	0.79(3)	4

x = 0.8							$Ga_{1.20(3)}Al_{0.54(1)}In_{0.26(1)}O_3$
Site	x	y	z	Occ.	Multiplicity & Wyckoff	Beq (Å²)	Atoms
Ga1	0.09065(13)	0	0.7920(4)	0.716(4)	4i	0.71(3)	2.87(2)
Al1	0.09065(13)	0	0.7920(4)	0.273(3)	4i	0.71(3)	1.09(1)
In1	0.09065(13)	0	0.7920(4)	0.010(3)	4i	0.71(3)	0.04(1)
Ga2	0.34328(13)	0	0.6877(4)	0.484(4)	4i	1.06(4)	1.93(2)
Al2	0.34328(13)	0	0.6877(4)	0.271(3)	4i	1.06(4)	1.08(1)
In2	0.34328(13)	0	0.6877(4)	0.246(3)	4i	1.06(4)	0.98(1)
O1	0.16210(20)	0	0.1056(5)	1	4i	1.17(3)	4
O2	0.49162(19)	0	0.2524(4)	1	4i	1.17(3)	4
O3	0.82750(20)	0	0.4315(5)	1	4i	1.17(3)	4

Table S2. Refinement-weighted profile R-factor (R_{wp}), profile R-factor (R_p), and goodness of fit (GOF), as well as refined lattice parameters and volume of $Ga_{1.98-x}(Al_{0.68}In_{0.32})_xO_3:0.02Cr^{3+}$.

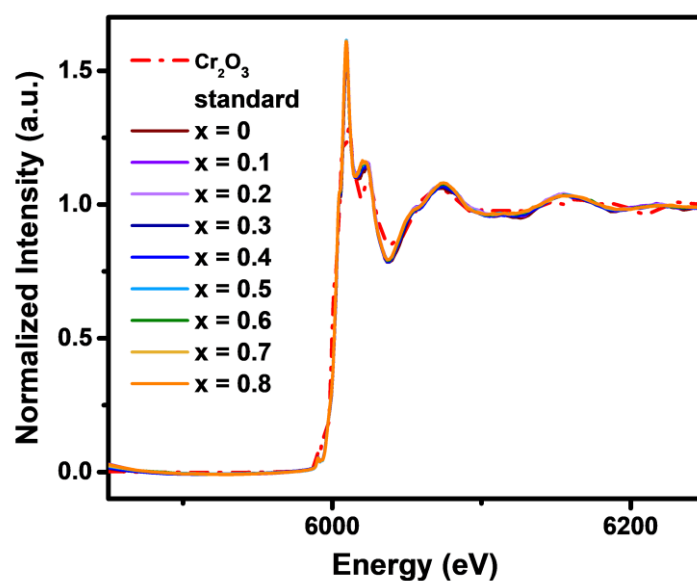| x	0	0.1	0.2	0.3	0.4	0.5	0.6	0.7	0.8
a (Å)	12.2395(2)	12.2453(2)	12.2503(3)	12.2587(3)	12.2660(3)	12.2689(4)	12.2760(4)	12.2848(4)	12.2968(4)
b (Å)	3.04280(4)	3.04415(5)	3.04482(7)	3.04668(6)	3.04779(7)	3.04783(8)	3.04935(8)	3.05145(8)	3.05388(8)
c (Å)	5.81229(8)	5.81215(9)	5.81018(14)	5.81029(13)	5.80877(14)	5.80468(16)	5.80328(17)	5.80204(18)	5.80181(17)
β (°)	103.8345(12)	103.8130(16)	103.796(2)	103.772(2)	103.746(2)	103.707(3)	103.677(2)	103.634(3)	103.586(2)
V	210.184(5)	210.392(6)	210.468(9)	210.765(8)	210.936(9)	210.875(11)	211.079(10)	211.369(11)	211.779(11)
R_{wp} (%) NPD	4.229	4.196	4.265	4.201	4.463	5.178	5.994	5.965	4.876
R_p (%) NPD	3.331	3.350	3.307	3.315	3.506	3.999	4.610	4.497	3.808
R_{wp} (%) XRD	1.943	3.606	4.361	4.638	4.905	4.996	5.290	4.668	5.385
R_p (%) XRD	1.282	2.112	2.558	2.696	2.900	3.075	3.507	3.264	3.725
GOF	1.698	1.864	2.195	1.909	1.992	2.068	2.839	2.443	2.119

Figure S3. Cr *K*-edge XANES spectra of $Ga_{1.98-x}(Al_{0.68}In_{0.32})_xO_3:0.02Cr^{3+}$ (x = 0, 0.1, 0.2, 0.3, 0.4, 0.5, 0.6, 0.7, and 0.8).
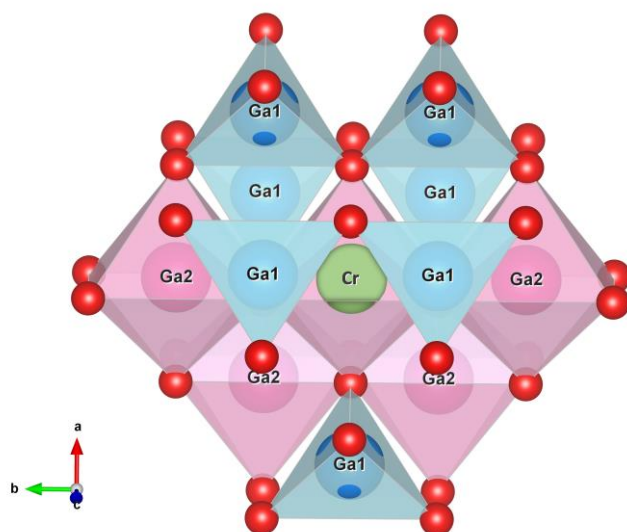
Figure S4. Schematic of the crystal structure of Cr^{3+} in $Ga_2O_3{:}Cr^{3+}$ obtained from Rietveld refinement (sample x = 0). Oxygen is shown in red, tetrahedra in blue, and octahedra in pink.

Table S3. Calculated formula weight of $Ga_{1.98-x}(Al_{0.68}In_{0.32})_xO_3{:}0.02Cr^{3+}$ (x = 0, 0.1, 0.2, 0.3, 0.4, 0.5, 0.6, 0.7, and 0.8) using site occupancies derived from Rietveld refinements.

x	Ga1	Al1	In1	Ga2	Al2	In2	Weight
0	1.000	0	0	1.000	0	0	69.72
0.1	0.979 (10)	0.004 (7)	0.017 (7)	0.921 (10)	0.064 (7)	0.015 (7)	69.35 (79)
0.2	0.936 (6)	0.034 (4)	0.030 (4)	0.864 (6)	0.102 (4)	0.034 (4)	68.63 (46)
0.3	0.905 (7)	0.056 (5)	0.039 (5)	0.795 (7)	0.148 (5)	0.057 (5)	67.95 (56)
0.4	0.871 (7)	0.107 (5)	0.022 (5)	0.729 (7)	0.165 (5)	0.106 (5)	66.62 (56)
0.5	0.845 (6)	0.145 (4)	0.010 (4)	0.655 (6)	0.195 (4)	0.150 (4)	65.50 (46)
0.6	0.806 (8)	0.182 (6)	0.012 (5)	0.594 (8)	0.226 (6)	0.180 (5)	64.56 (60)
0.7	0.767 (4)	0.217 (3)	0.016 (3)	0.533 (4)	0.259 (3)	0.208 (3)	63.67 (33)
0.8	0.717 (4)	0.273 (3)	0.010 (3)	0.483 (4)	0.271 (3)	0.246 (3)	62.41 (33)

Raman Shift

Ga_2O_3 has 30 vibration modes, among which 15 are Raman-active. Sample x = 0 exhibits 11 Raman features ranging from 100–900 cm^{-1}, with the most intense at 200 cm^{-1} ($A_g^{(3)}$), in agreement with the literature.[9-10] The observed Raman peaks can be classified into three groups: (i) libration and translation of $Ga1O_4$ chains including $A_g^{(1)}$–$A_g^{(3)}$, $B_g^{(1)}$, and $B_g^{(2)}$ modes, (ii) deformation of $Ga1O_4$ and $Ga2O_6$ including $A_g^{(4)}$–$A_g^{(6)}$, $B_g^{(3)}$, and $B_g^{(4)}$ modes, and (iii) stretching and bending of $Ga1O_4$ including $A_g^{(7)}$–$A_g^{(10)}$ and $B_g^{(5)}$ modes.

Raman peaks shift with increased x, as shown in Figure S5, where peak position is taken from the maximum intensity directly from the Raman spectra and errors ($\pm$ 4 cm^{-1}) are smaller than the points ($\pm$ 16 cm^{-1}). The rate of shift is calculated from a linear fit to data in S5b and shown in Table S4. Most peaks shift to higher energies and only $A_g^{(6)}$ and $A_g^{(9)}$ + $B_g^{(5)}$ modes shift to lower energies.
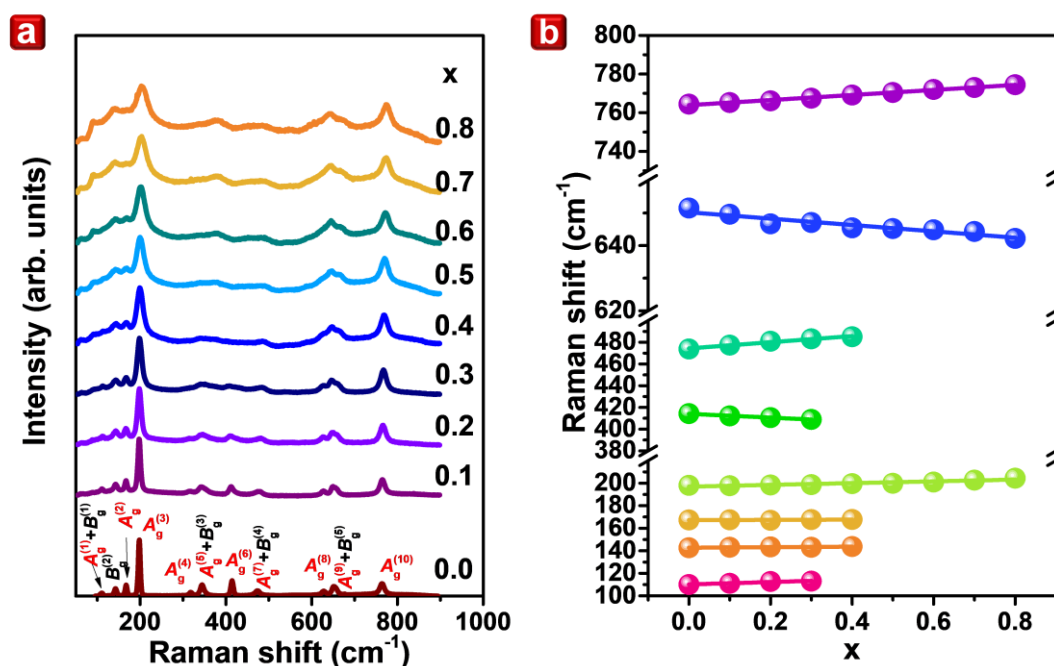

Figure S5. (a) Raman spectra and (b) shift of selected peaks of the series $Ga_{1.98-x}(Al_{0.68}In_{0.32})_xO_3:0.02Cr^{3+}$ (x= 0−0.8). Data in (a) are offset for clarity with modes identified in the x = 0 spectra and in (b) errors are smaller than the points and lines are a linear fit.

Table S4. Positions of Raman peaks of $Ga_{1.98-x}(Al_{0.68}In_{0.32})_xO_3:0.02Cr^{3+}$ (x= 0−0.8) at x = 0 and dE/dx of selected peaks, where peak position E is the maximum intensity and dE/dx is obtained from linear fit to data in Fig. S5b.

Raman mode	$A_g^{(1)}, B_g^{(1)}$	$B_g^{(2)}$	$A_g^{(2)}$	$A_g^{(3)}$	$A_g^{(4)}$	$A_g^{(5)}, B_g^{(3)}$	$A_g^{(6)}$	$A_g^{(7)}, B_g^{(4)}$	$A_g^{(8)}$	$A_g^{(9)}, B_g^{(5)}$	$A_g^{(10)}$
Energy (cm^{-1})	110	145	170	204	320	349	420	477	632	655	770
dE/dx (cm^{-1})	11 ± 2	2.2 ± 0.8	1.2 ± 0.8				−17.5 ± 0.8	28 ± 2		−9 ± 1	13 ± 1
Regression (r^2)	0.947	0.723	0.444				0.996	0.978		0.900	0.994

Energy-Level Shift with x

Table S5. Rate of shifts of peak energies for optical transitions in $Ga_{1.98-x}(Al_{0.68}In_{0.32})_xO_3:0.02Cr^{3+}$ with x obtained from linear fits to data in Figure 2c, where E is the intercept and dE/dx is the slope.

	E (x = 0) (cm^{-1})	dE/dx (cm^{-1})	Regression (r^2)
$E\,(^4A_2 \rightarrow {}^4T_1)$	22,821 ± 15	−236 ± 32	0.930
$E\,(^4A_2 \rightarrow {}^4T_2)$	16,542 ± 13	−205 ± 28	0.927
$E\,(^4T_2 \rightarrow {}^4A_2)$	13,460 ± 81	−1280 ± 175	0.956
$E\,(^2E \rightarrow {}^4A_2)$	14,409 ± 10	166 ± 23	0.948

Crystal Field Calculation

The crystal field parameter Dq and the Racah parameters B and C are calculated from the following equations:[11]

$$10Dq = E(^4A_2 \rightarrow {}^4T_2) \tag{s1}$$

$$B = Dq\frac{\left[\frac{\Delta E}{Dq}\right]^2 - 10\cdot\frac{\Delta E}{Dq}}{15(\frac{\Delta E}{Dq}-8)} \tag{s2}$$

$$C = \frac{B}{3.05}\left\{\frac{E(^2E)}{B} - 7.9 + 1.8\frac{B}{Dq}\right\} \tag{s3}$$

where $E(^4A_2 \rightarrow {}^4T_2)$ is the energy of the peak of the excitation arising from the $^4A_2 \rightarrow {}^4T_2$ transition and ΔE is the difference between the energy of the $^4A_2 \rightarrow {}^4T_1$ and $^4A_2 \rightarrow {}^4T_2$

transitions.

With increased x, Dq and B decrease, whereas C increases. The calculation of Racah parameters shows different behaviors of B and C, i.e., the former decreases and the latter increases with x. In principle, the variation with x of B and C determines the energy shift of the ^2E state (nephelauxetic redshift). However, the opposite sign of the B and C shift makes it hard to interpret. According to Brik et al.[12], the nephelauxetic parameter β_1 is the best indicator of the combined influence of B and C on the location of the ^2E emitting state, indicating the change in covalency of Cr^{3+}-ligand bonds.

The nephelauxetic parameter β_1 was calculated according to the following relation[12]:

$$\beta_1 = \sqrt{\left(\frac{B}{B_0}\right)^2 + \left(\frac{C}{C_0}\right)^2} \tag{s4}$$

where $B_0 = 918$ cm^{-1} and $C_0 = 3850$ cm^{-1} are the Racah parameter values for free Cr^{3+}.

Disorder induced by substitution (standard deviation = σ)

The standard deviation of substituted ionic radii in the system is calculated from the radii and occupancies of In and Al at Ga sites. Since Ga1 is tetrahedral and Ga2 octahedral, we consider the radii of the substituted elements with coordination number (CN) = 4 for Ga1 and CN = 6 for Ga2 sites. Therefore, for Ga1, $Ga^{3+} = 0.47$ Å, $Al^{3+} = 0.39$ Å, $In^{3+} = 0.62$ Å; while for Ga2, $Ga^{3+} = 0.62$ Å, $Al^{3+} = 0.535$Å, $In^{3+} = 0.8$ Å are used. The standard deviation is then calculated using the following equation:

$$\sigma = \sqrt{\frac{1}{N}\sum_{i=1}^{N}(x_i - \bar{\mu})^2} \tag{s5}$$

Where N is the total number of elements, x_i is the radius of certain elements i, and $\bar{\mu}$ is the average radii of the system. The results of the calculation are shown in Table S6 and the comparison with the concentration of dopants is shown in Figure 2e.

Table S6. Calculated standard deviation of radii (σ) considering the occupancies of different elements derived from the Rietveld refinement of $Ga_{1.98-x}(Al_{0.68}In_{0.32})_xO_3$: $0.02Cr^{3+}$ (x = 0, 0.1, 0.2, 0.3, 0.4, 0.5, 0.6, 0.7, and 0.8).

x	σ^2(Al)	σ^2(In)	σ^2(total)	σ	σ^2(Al,%)	σ^2(In,%)	σ^2(IV)	σ^2(VI)	σ^2(total)	σ	σ^2(IV,%)	σ^2(VI,%)
0	-	-	0	0	-	-	-	-	0	0	-	-
0.1	0.000488	0.000869	0.001357	0.036831	35.97%	64.03%	0.000408	0.000948	0.001357	0.036831	30.08%	69.92%
0.2	0.000955	0.001777	0.002731	0.05226	34.95%	65.05%	0.000893	0.001839	0.002731	0.05226	32.68%	67.32%
0.3	0.001428	0.002724	0.004152	0.064436	34.39%	65.61%	0.001236	0.002916	0.004152	0.064436	29.77%	70.23%
0.4	0.001877	0.003929	0.005806	0.076199	32.33%	67.67%	0.00118	0.004627	0.005806	0.076199	20.32%	79.68%
0.5	0.002337	0.005085	0.007422	0.08615	31.49%	68.51%	0.001153	0.006269	0.007422	0.08615	15.54%	84.46%
0.6	0.002798	0.006102	0.008900	0.094338	31.44%	68.56%	0.001435	0.007465	0.0089	0.094338	16.12%	83.88%
0.7	0.003260	0.007099	0.010359	0.101781	31.47%	68.53%	0.001749	0.00861	0.010359	0.101781	16.88%	83.12%
0.8	0.003705	0.008195	0.011901	0.10909	31.13%	68.87%	0.001972	0.009928	0.011901	0.10909	16.57%	83.43%

In contributes more to disorder in the system and increases with x. Since In prefers octahedral Ga2 sites, the 6-coordinate site contributes more to disorder in the system.

Room-Temperature Luminescence

The average decay time (τ_{av}) of Cr^{3+} emission was calculated using Equation (1):

$$\tau_{av} = \frac{\int t \cdot I(t)\, dt}{\int I(t)\, dt} \tag{1}$$

where $I(t)$ is the maximum intensity of the luminescence. The average luminescence decay time of Cr^{3+} in the $Ga_{1.98-x}(Al_{0.68}In_{0.32})_xO_3$:$0.02Cr^3$ series is shown below.
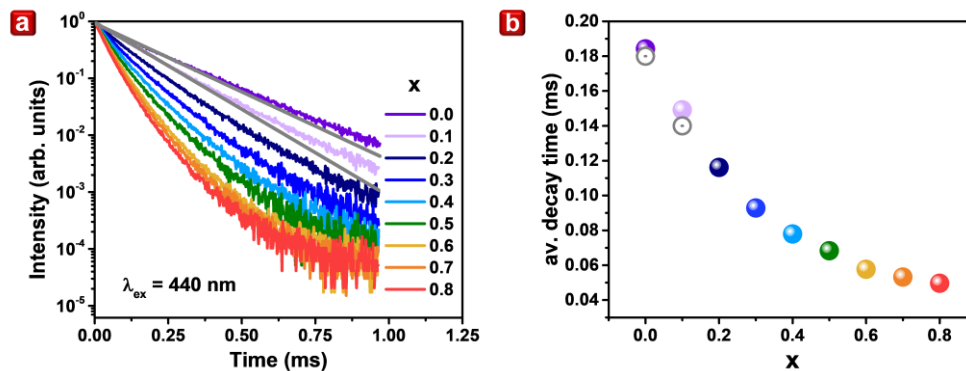

Figure S6. (a) Intensity decay of emissions at 440 nm and (b) calculated average decay times of the series $Ga_{1.98-x}(Al_{0.68}In_{0.32})_xO_3$:$0.02Cr^3$ for x = 0−0.8. The data for x = 0 and 0.1 were

fitted using an exponential decay function in terms of the mean lifetime for luminescence, τ, (shown in gray):

$$I(t) = I_0 e^{-\frac{t}{\tau}} \tag{s6}$$

where $I(t)$ is the emission intensity at time t and I_0 is the initial intensity.
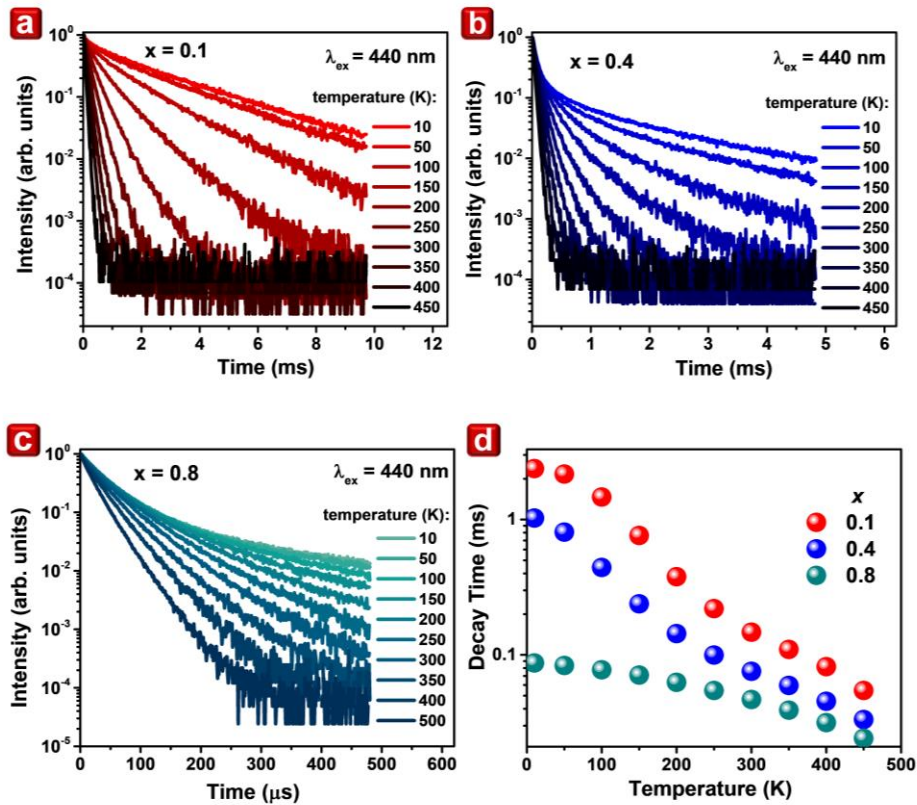
Temperature-Dependent Decay of Luminescence

Figure S7. (a–c) Decay of luminescent intensity and (d) decay time with an excitation wavelength (λ_{ex}) of 440 nm of samples x = 0.1, 0.4, and 0.8. Errors in (d) are smaller than the points.

Energy Level Shift with Pressure

Table S7. Rate of shifts of peak energies for optical transitions in $Ga_{1.98-x}(Al_{0.68}In_{0.32})_xO_3$: $0.02Cr^{3+}$ with x obtained from linear fits to data in Figure 5c, where E is the intercept and dE/d kbar is the slope.

x = 0.8	E (p = 1 bar) (cm⁻¹)	dE/dp (cm⁻¹/kbar)	Regression (r²)
$E\ (^4A_2 \rightarrow {}^4T_1)$	22,636.8	12.8 ± 0.6	0.999
$E\ (^4A_2 \rightarrow {}^4T_2)$	16,378.7	8.1 ± 0.4	0.999
$E\ (^2E \rightarrow {}^4A_2)$	14,406.10	-1.17 ± 0.04	0.995
$E\ (^4T_2 \rightarrow {}^4A_2)$	12,593.2	11.5 ± 0.6	0.980

x = 0.1	E (p = 1 bar) (cm⁻¹)	dE/dp (cm⁻¹/kbar)	Regression (r²)
$E\ (^2E \rightarrow {}^4A_2)$, R_1	14,497.69	-0.69 ± 0.03	0.977
$E\ (^2E \rightarrow {}^4A_2)$, R_2	14,299.25	-0.81 ± 0.05	0.981

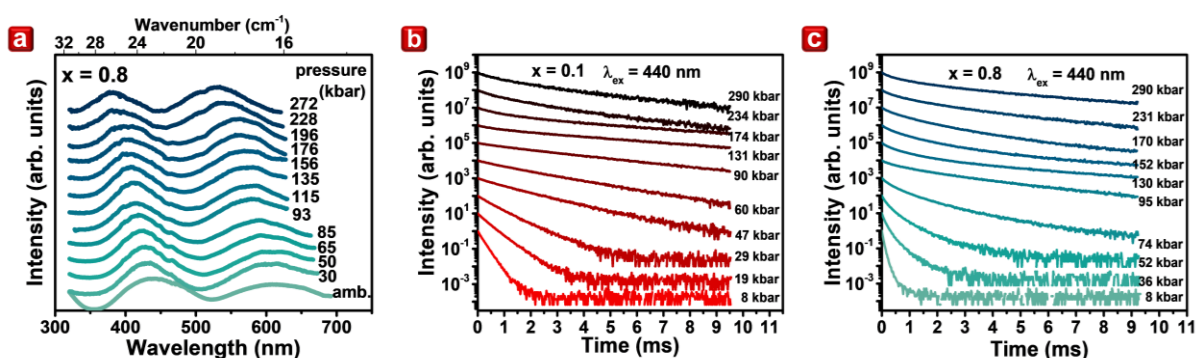**Pressure-Dependent Decay of Luminescence**

Figure S8. (a) Pressure dependence of the room temperature excitation spectrum upon observation at a maximum of emission of sample x = 0.8. Spectra are offset in y for clarity. Pressure dependence of luminescent intensity with an excitation wavelength (λ_{ex}) of 440 nm of (b) x = 0.1 and (c) x = 0.8 samples, respectively.
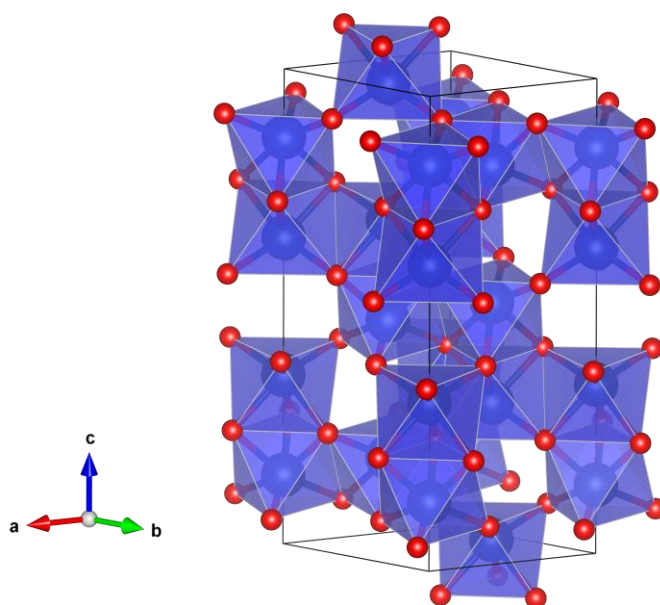
Crystal Structure of Alpha Ga₂O₃

Figure S9. Crystal structure of α-Ga₂O₃ for the ICSD database entry #27431. Oxygen atoms are red and Ga-containing octahedra are blue.

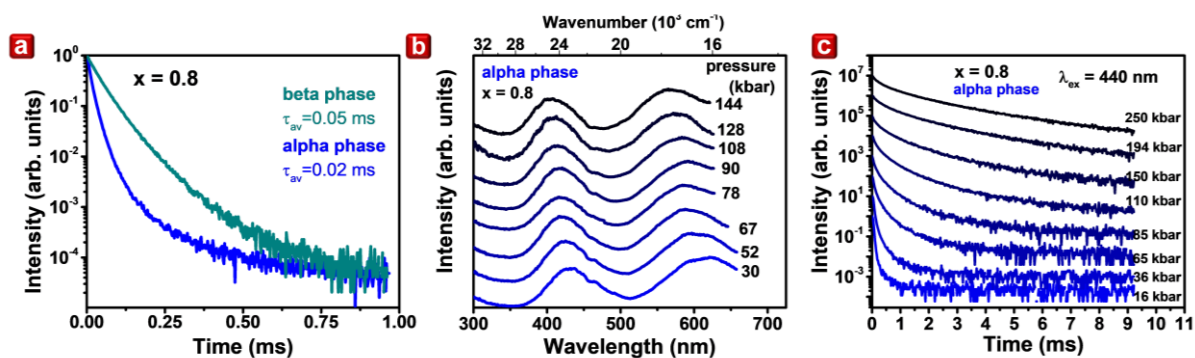**Luminescence Decay and Emission Spectrum of the Alpha Phase**

Figure S10. (a) Decay of luminescent intensity at RT and ambient pressure of α- and β-Ga$_{1.98-}$$_x$(Al$_{0.68}In_{0.32}$)$_x$O₃:0.02Cr^{3+} at x = 0.8 upon excitation at 440 nm with average decay time. (b) Excitation spectra and (c) decay of intensity of emissions from α-Ga$_{1.98-}$$_x$(Al$_{0.68}In_{0.32}$)$_x$O₃:0.02Cr^{3+} at x = 0.8 at RT with increased pressure with an excitation wavelength (λ_{ex}) of 440 nm.

Crystal-Field Calculations for α-Ga$_{1.98-x}$(Al$_{0.68}$In$_{0.32}$)$_x$O$_3$:0.02Cr^{3+} at x = 0.8

Table S8. The electron-lattice interaction parameter $S\hbar\omega$, FWHM, and crystal field parameters Dq, B, and C for β- and α-Ga$_{1.98-x}$(Al$_{0.68}$In$_{0.32}$)$_x$O$_3$:0.02Cr^{3+} at x = 0.8.

	β-Ga$_2$O$_3$	α-Ga$_2$O$_3$
$S\hbar\omega$ (cm^{-1})	1,890	1,980
FWHM (cm^{-1})	2,416	2,741
Dq (cm^{-1})	1,638	1,612
B (cm^{-1})	622	686
C (cm^{-1})	3,243	3,075
Dq/B	2.66	2.35
C/B	5.4	4.48

Crystal-Field Calculation and Pressure-Dependent Energy-Structure Diagram

The determination of $^4T_2$, $^4T_1$, and ^2E states with pressure enable the calculation of parameters Dq, B and C, and β_1. Dq was calculated using Equation (s1), B and C were calculated using Equations (s2) and (s3), and β_1 was calculated using Equation (s4). The energy of the $^4A_2 \rightarrow$ $^4T_1$, $^4A_2 \rightarrow {}^4T_2$, and $^2E \rightarrow {}^4A_2$ transitions are obtained from the corresponding excitation band maxima and are shown in Table S9.

These parameters for the α and β phases at x = 0.8 are shown in Figure S11. With increased pressure (p), Dq and B increase, whereas C decreases. β_1 increases with pressure for the β phase and decreases with pressure for the α phase.

These three parameters (Dq, B, and C) enable the generation of the entire energy structure of Cr^{3+}, i.e., the energy of all crystal-field levels of the d^3 configuration, and its variation with pressure and x using data in Tables S5 and S9, respectively.

Table S9. Position and linear pressure shift of emissions for optical transitions in β- and α-Ga$_{1.98-x}$(Al$_{0.68}$In$_{0.32}$)$_x$O$_3$:0.02Cr^{3+} at x = 0.8.

	beta phase		alpha phase	
	E (p = 1 bar) (cm^{-1})	dE/dp (cm^{-1}/ kbar)	E (p = 1 bar) (cm^{-1})	dE/dp (cm^{-1}/ kbar)
E ($^4A_2 \rightarrow {}^4T_1$)	22,672 ± 50	12.8 ± 0.6	22,750 ± 100	13 ± 1
E ($^4A_2 \rightarrow {}^4T_2$)	16,379 ± 30	8.1 ± 0.4	16,000 ± 90	11 ± 1
E ($^4T_2 \rightarrow {}^4A_2$)	12,593 ± 13	11.5 ± 0.6	12,058 ± 15	5.5 ± 0.2
E ($^2E \rightarrow {}^4A_2$)	14,388 ± 6	−1.17 ± 0.04	14,299 ± 10	−0.81 ± 0.03
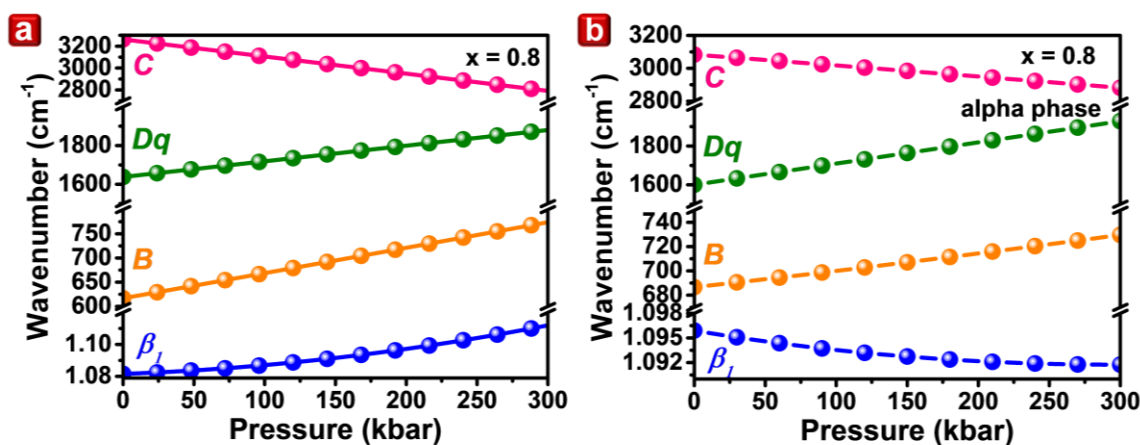
Figure S11. Pressure dependent Dq, B, C, and β_1 for Ga$_{1.98-x}$(Al$_{0.68}$In$_{0.32}$)$_x$O$_3$:0.02Cr^{3+} at x = 0.8 in the (a) beta and (b) alpha phase. Lines through points are a guide to the eye and errors are smaller than the points.

The calculated energy level diagram of β- and α-Ga$_{1.98-x}$(Al$_{0.68}$In$_{0.32}$)$_x$O$_3$:0.02Cr^{3+} as a function of x and pressure is shown in Figure S12. The experimentally obtained linear dependences of Dq, B, and C were extrapolated to the pressure range 0–1000 kbar in the energy structure calculation and shown in Figure S13. Within the analyzed pressure range, the energies of the crystal field levels have a linear dependence, considered as the effect of linear extrapolation of the pressure change of Dq, B, and C. Furthermore, the x-dependent energy structure of Cr^{3+} shows all energy levels are relatively invariant with x.
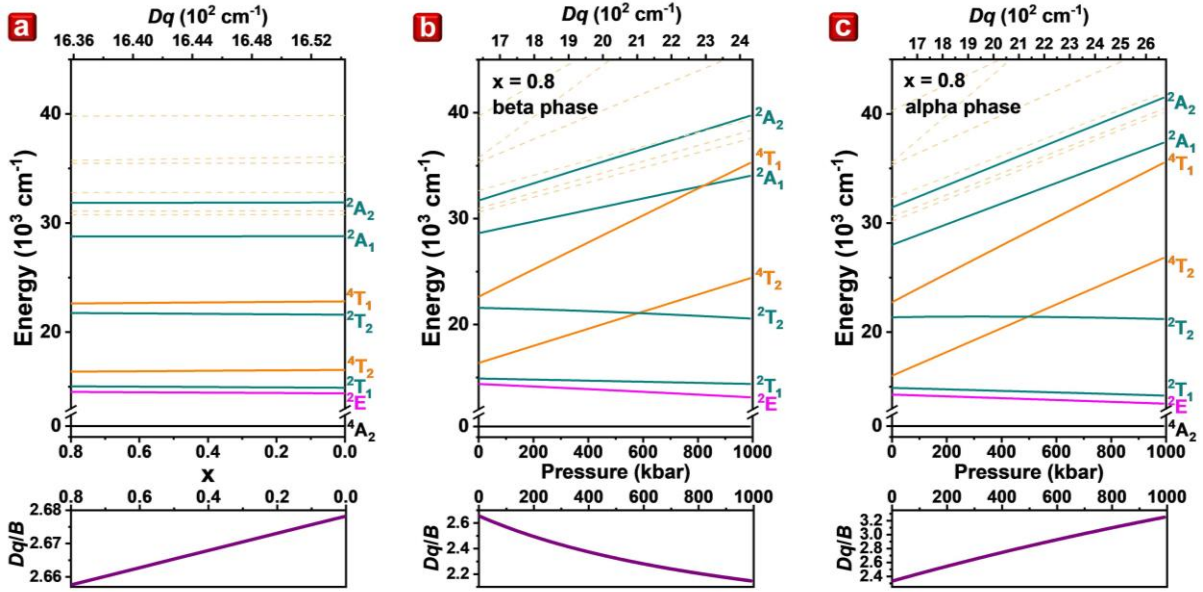
Figure S12. Energy-level diagram of d^3 Cr^{3+} in Ga$_{1.98-x}$(Al$_{0.68}$In$_{0.32}$)$_x$O$_3$:0.02Cr^{3+} as a function of (a) x for the β phase, and pressure for x = 0.8 in the (b) β and (c) α phase.
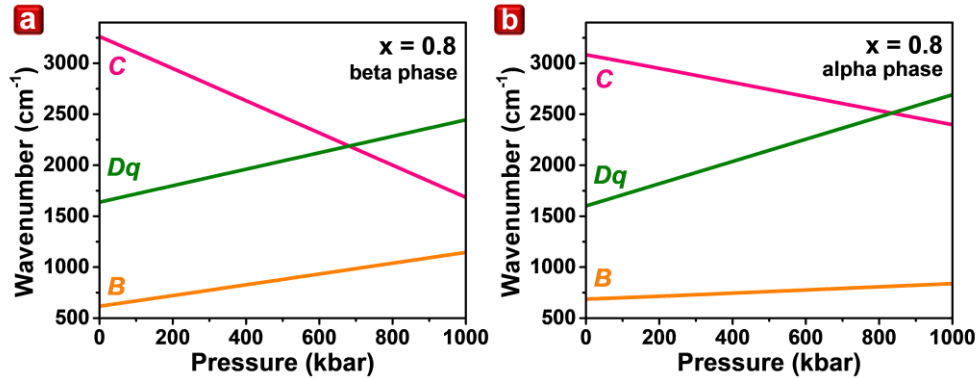
Figure S13. Experimentally obtained linear dependence of Dq, B, and C for Ga$_{1.98-x}$(Al$_{0.68}$In$_{0.32}$)$_x$O$_3$:0.02Cr^{3+} at x = 0.8 extrapolated to the pressure range 0–1000 kbar for the (b) β and (c) α phase.

The main difference between these energy structure diagrams compared with the standard constructed Tanabe–Sugano diagrams (where B and C are constant, and only Dq changes) is that the energy of the excited levels belonging to the t_2^3 crystal field configuration, i.e., the lowest doublet subterms (^2E, $^2T_1$, and $^2T_2$) decreases instead of increasing. Notably, the presented energy structure diagrams show a decrease in energy of the excited levels belonging to the t_2^3 crystal field configuration (^2E, $^2T_1$, and $^2T_2$) with increased Dq, for both pressure and x-dependence. This behavior is consistent with the observed change in the direction of the $^2E \rightarrow {}^4A_2$ transition shift and is not in line with the behavior predicted for the exciting levels of

the $t_2{}^3$ configuration by the standard Tanabe–Sugano diagram (calculated assuming that B and C are constant and only Dq changes). The aforementioned fact confirms the need to consider the changes in Racah parameters when describing the results of spectroscopic studies of transition-metal-doped materials as a function of pressure.

As also shown in Figure S13, Dq/B increases with decreased x (Figure S13a) and decreases with increased pressure (Figure S13b). In the α phase, the dependence is opposite to that in the β phase in that the change in Dq/B is opposite to that of β_1.

Chemical Pressure

Variation in ionic radius can be used to mimic external pressure, providing a valuable tuning parameter, and is known as chemical pressure. We compare the influence of chemical and mechanical pressure on the emitting states of Cr^{3+} in $Ga_{1.98-x}(Al_{0.68}In_{0.32})_xO_3:0.02Cr^{3+}$. Figure S14 compares the changes in Dq, C, and B, and ^2E and $^4T_1$ states induced by chemical and mechanical pressure with x. Co-doping Ga_2O_3 with In decreases the crystal field, and the opposite occurs when mechanical pressure is applied. Dq values obtained using chemical (cyan) and mechanical (red) pressure are compared, and the inset in Figure S14 shows that varying x from 0.8 to 0.0 (chemical pressure) can change Dq from 1638 to 1654 cm^{-1} (cyan dots), an equivalent change in mechanical pressure from atmospheric to 20 kbar. By applying mechanical pressure to 300 kbar, we can obtain Dq to 1880 cm^{-1}. In summary, a change in x of 0.1 is equivalent to mechanical pressure of about 2.5 kbar, with the maximum x = 0.8 in the series being equivalent to approximately 20 kbar.
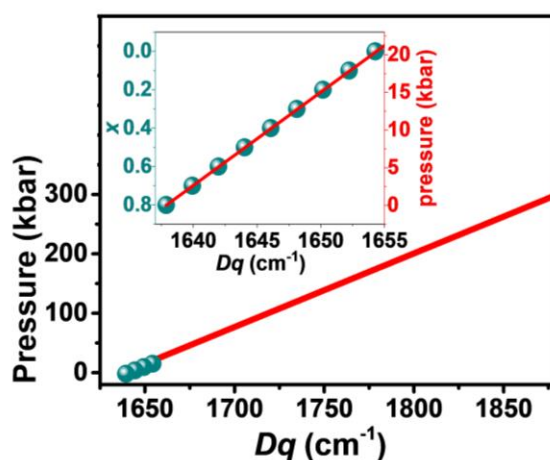

Figure S14. Dq in $Ga_{1.98-x}(Al_{0.68}In_{0.32})_xO_3:0.02Cr^{3+}$ with chemical (x) and mechanical pressure.

EPR and SQUID Measurements

EPR spectra were described by assuming Spin Hamiltonian (SH):

$$H = \mu_B B \cdot g \cdot S + D\left(S_z^2 - \frac{1}{3}S(S+1)\right) + E\left(S_x^2 + S_y^2\right) \tag{s7}$$

where μ_B is the Bohr magneton; B is the induction of magnetic field; g is the spectroscopic splitting matrix; S is the electron spin including diagonal elements S_x, S_y, and S_z; and D and E are axial and rhombic distortions of octahedra, respectively. The Bohr magneton is the physical unit used to describe the magnetic moment of the electron. In SH calculations, the Bohr magneton is expressed as $\mu_B B = e \cdot h/2m_e$, where m_e, h, and e are the electron mass, Planck's constant, and electron charge, respectively. The calculated g including diagonal elements g_x, g_y, and g_z, as well as D and E, and SH parameters indicate the axial symmetry of Cr^{3+} ions ($g_x = g_y$ = 1.96, g_z = 2.01) with significant increasing distortion from ideal octahedral coordination with x (from $E = 0.065$ cm^{-1} and $D = 0.32$ cm^{-1} to $D = 0.35$ cm^{-1} for x = 0 and x = 0.8, respectively).

The fits of the SH model to experimental spectra are shown in Figure S15. Although EPR spectra are similar, the series can be divided into two groups, low (x ≤ 0.3) and high (x ≥ 0.4) $Al_{0.68}In_{0.32}$ concentrations. SH parameters above and below these concentrations do not change, indicating that the Cr^{3+} environment does not change. However, increased x (especially between x = 0.3 and x = 0.4) induces significant broadening of the EPR line (low-field magnetic induction component) and a shift of the maximum of this signal toward higher magnetic induction, indicating increasing inhomogeneity of the Cr^{3+} environment. The increase in D indicates an increase in the axial distortion of the nearest environment of Cr^{3+}. A significant increase in EPR linewidth and the change in shape, specifically from Lorentzian to Gaussian used to fit SH parameters, may indicate the occurrence of at least two different Cr^{3+} ($GaInO_3$:Cr^{3+} and $GaAlO_3$:Cr^{3+}) centers since several Lorentzian lines form a Gaussian line. Furthermore, with the increased contribution of Gaussian lines when fitting, we speculate the presence of magnetic centers with slightly different nearest environments.

The temperature dependence of magnetic susceptibility $\chi(T)$ (SQUID) behaves according to the Curie–Weiss law:

$$\chi(T) = \chi_{dia} + \frac{C}{T - T_{CW}} \qquad (s8)$$

where T_{CW} is the Curie–Weiss temperature and C is the Curie constant. A significant difference in the strength of the interaction between Cr^{3+} ions occurs for compounds without diamagnetic ions ($T_{CW}(x = 0) \approx 6$ K), and for samples with $Al_{0.68}In_{0.32}$ additions ($T_{CW}(x = 0.1) \approx 2$ K). This finding is related to the expansion of the crystal lattice due to the inclusion of the larger ionic radius dopant In. With increased x, T_{CW} decreases, indicating a change in the strength of ferromagnetic interaction strongly correlated with the distance between Cr^{3+} ions, leading to a change in the crystal field. This conclusion is confirmed by structural and optical studies, and we emphasize that an additional EPR line (blue line, Figures S15a and S15b) with $g_{eff} = 2.0023$ (free electrons) was added to all SH parameters fittings as the effect from conduction electrons is commonly observed in chromium compounds. The fitted results confirm the electrons in the conduction band were thermally excited for all studied materials.
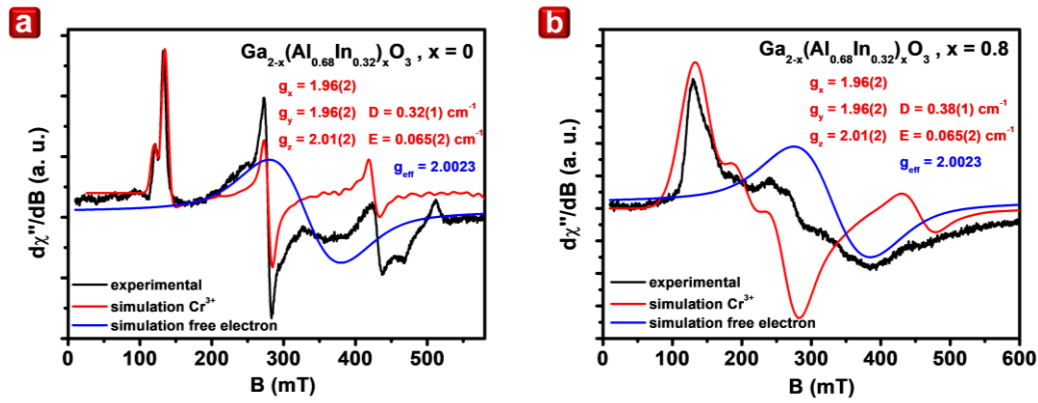

Figure S15. EPR spectrum of $Ga_{1.98-x}(Al_{0.68}In_{0.32})_xO_3$:$0.02Cr^{3+}$ samples (a) x = 0 and (b) x = 0.8 with the fitted EPR (simulation, red) and obtained SH parameters.

References

1. Liss, K.-D.; Hunter, B.; Hagen, M.; Noakes, T.; Kennedy, S. Echidna—The New High-Resolution Powder Diffractometer being Built at OPAL. *Physica B Condens. Matter* **2006**, *385*, 1010–1012.

2. Coelho, A. A. TOPAS and TOPAS-Academic: An Optimization Program Integrating Computer Algebra and Crystallographic Objects Written in C++. *J. Appl. Crystallogr.* **2018**, *51*, 210–218.

3. Momma, K.; Izumi, F. VESTA 3 for Three-Dimensional Visualization of Crystal, Volumetric and Morphology Data. *J. Appl. Crystallogr.* **2011**, *44*, 1272–1276.

4. Kubicki, A. A.; Bojarski, P.; Grinberg, M.; Sadownik, M.; Kukliński, B. Time-Resolved Streak Camera System with Solid State Laser and Optical Parametric Generator in Different Spectroscopic Applications. *Opt. Commun.* **2006**, *263*, 275–280.

5. Merrill, L.; Bassett, W. A. Miniature Diamond Anvil Pressure Cell for Single Crystal X-ray Diffraction Studies. *Rev. Sci. Instrum* **1974**, *45*, 290–294.

6. Barzowska, J.; Lesniewski, T.; Mahlik, S.; Seo, H. J.; Grinberg, M. $KMgF_3$: Eu^{2+} as a New Fluorescence-Based pressure Sensor for Diamond Anvil Cell Experiments. *Opt. Mater.* **2018**, *84*, 99–102.

7. Mombourquette, M.; Weil, J.; McGavin, D. EPR-NMR User's Manual. *Department of Chemistry, University of Saskatchewan, Saskatoon, SK, Canada* **1996**.

8. Bain, G. A.; Berry, J. F. Diamagnetic Corrections and Pascal's Constants. *J. Chem. Educ.* **2008**, *85*, 532.

9. Onuma, T.; Fujioka, S.; Yamaguchi, T.; Itoh, Y.; Higashiwaki, M.; Sasaki, K.; Masui, T.; Honda, T. Polarized Raman Spectra in β-Ga2O3 Single Crystals. *J. Cryst. Growth* **2014**, *401*, 330–333.

10. Kranert, C.; Sturm, C.; Schmidt-Grund, R.; Grundmann, M. Raman Tensor Elements of β-Ga_2O_3. *Sci. Rep.* **2016**, *6*, 1–9.

11. Henderson, B.; Imbusch, G. F. *Optical Spectroscopy of Inorganic Solids*. Oxford University Press: 2006; Vol. 44.

12. Brik, M.; Camardello, S.; Srivastava, A.; Avram, N.; Suchocki, A. Spin-Forbidden Transitions in the Spectra of Transition Metal Ions and Nephelauxetic Effect. *ECS J. Solid State Sci. Technol.* **2015**, *5*, R3067.

[P6]

Rajendran, V.; Fang, M.-H.; Huang, W.-T.; **Majewska, N.**; Lesniewski, T.; Mahlik, S.; Leniec, G.; Kaczmarek, S. M.; Pang, W. K.; Peterson, V. K.; Lu, K.-M.; Chang, H.; Liu, R.-S. Chromium Ion Pair Luminescence: A Strategy in Broadband Near-Infrared Light-Emitting Diode Design. *J. Am. Chem. Soc.* **2021**, 143 (45), 19058-19066.

https://doi.org/10.1021/jacs.1c08334.

Chromium Ion Pair Luminescence: A Strategy in Broadband Near-Infrared Light-Emitting Diode Design

Veeramani Rajendran, Mu-Huai Fang, Wen-Tse Huang, Natalia Majewska, Tadeusz Lesniewski, Sebastian Mahlik, Grzegorz Leniec, Slawomir M. Kaczmarek, Wei Kong Pang, Vanessa K. Peterson, Kuang-Mao Lu, Ho Chang,* and Ru-Shi Liu*

ACCESS | Metrics & More | Article Recommendations | SI Supporting Information

ABSTRACT: Portable near-infrared (NIR) light sources are in high demand for applications in spectroscopy, night vision, bioimaging, and many others. Typical phosphor designs feature isolated Cr^{3+} ion centers, and it is challenging to design broadband NIR phosphors based on Cr^{3+}−Cr^{3+} pairs. Here, we explore the solid-solution series $SrAl_{11.88-x}Ga_xO_{19}$:0.12Cr^{3+} (x = 0, 2, 4, 6, 8, 10, and 12) as phosphors featuring Cr^{3+}−Cr^{3+} pairs and evaluate structure−property relations within the series. We establish the incorporation of Ga within the magentoplumbite-type structure at five distinct crystallographic sites and evaluate the effect of this incorporation on the Cr^{3+}−Cr^{3+} ion pair proximity. Electron paramagnetic measurements reveal the presence of both isolated Cr^{3+} and Cr^{3+}−Cr^{3+} pairs, resulting in NIR luminescence at approximately 650−1050 nm. Unexpectedly, the origin of broadband NIR luminescence with a peak within the range 740−820 nm is related to the Cr^{3+}−Cr^{3+} ion pair. We demonstrate the application of the $SrAl_{5.88}Ga_6O_{19}$:0.12Cr^{3+} phosphor, which possesses an internal quantum efficiency of ∼85%, a radiant flux of ∼95 mW, and zero thermal quenching up to 500 K. This work provides a further understanding of spectral shifts in phosphor solid solutions and in particular the application of the magentoplumbites as promising next-generation NIR phosphor host systems.
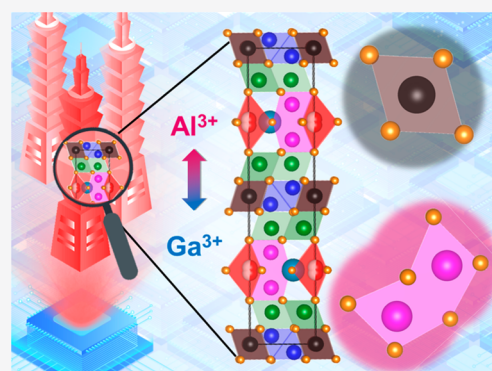
INTRODUCTION

Phosphor-converted light-emitting diodes (pc-LEDs) are widely incorporated in everyday applications as a result of their environmental friendliness, low cost, and long life stability. Advancements in solid-state lighting are facilitated by material discovery; using high-throughput approaches, structural design as informed by density functional theory calculations targeting property optimization has already reduced the size of conventional LEDs to micro and mini, enabling the visualization of colors with finer contrast for backlighting applications.[1−3] This pc-LED technology also finds use as an alternative light source for still-developing compact NIR applications including spectroscopy, health monitoring, biomodulation, bioimaging, plant growth, night vision, and anticounterfeit identification.[4−7] In such NIR devices, NIR-emitting phosphors are encapsulated over blue LEDs, with the final performance almost solely dependent on the phosphors.[8] Accordingly, NIR-emitting luminescence materials with high efficiency and good thermal properties are in increasing demand. Most NIR phosphor research is focused on garnet, borate, spinel, double-perovskite, and inverse spinel-type structures.[9−14] Notably, NIR luminescence in these materials is solely dependent on the isolated Cr^{3+} ion, as controlled through crystal-field engineering. The design of

NIR luminescence based on the Cr^{3+}−Cr^{3+} ion pair is an interesting and unexplored strategy, despite most phosphor hosts forming exchange-coupled Cr^{3+} pairs, which are weak and not detectable in ambient conditions.[15,16]

The magnetoplumbite type structures with formula $A[B_{12}]O_{19}$ offer an opportunity for a stronger Cr^{3+}−Cr^{3+} ion pair signal due to the availability of five independent crystallographic sites for the B site cation, where cation B may have valence ranging from 2+ to 5+.[17,18] Therefore, the magnetoplumbite type structure provides a versatile host system in which to tune luminescent optical properties. For example, Xu et al. reported $SrGa_{12}O_{19}$:Cr^{3+} (λ_{em} = 750 nm) for long-persistence applications,[19] while the narrowband green-emitting $SrGa_{12}O_{19}$:Mn^{2+} (λ_{em} = 505 nm) is integrated with ethyl cellulose for the latent fingerprints visualization in anticounterfeiting applications.[20] Similarly, LaMgAl$_{11}$O$_{19}$:Cr^{3+}(λ_{em} = 698 nm) is co-doped with Yb^{3+} ions for

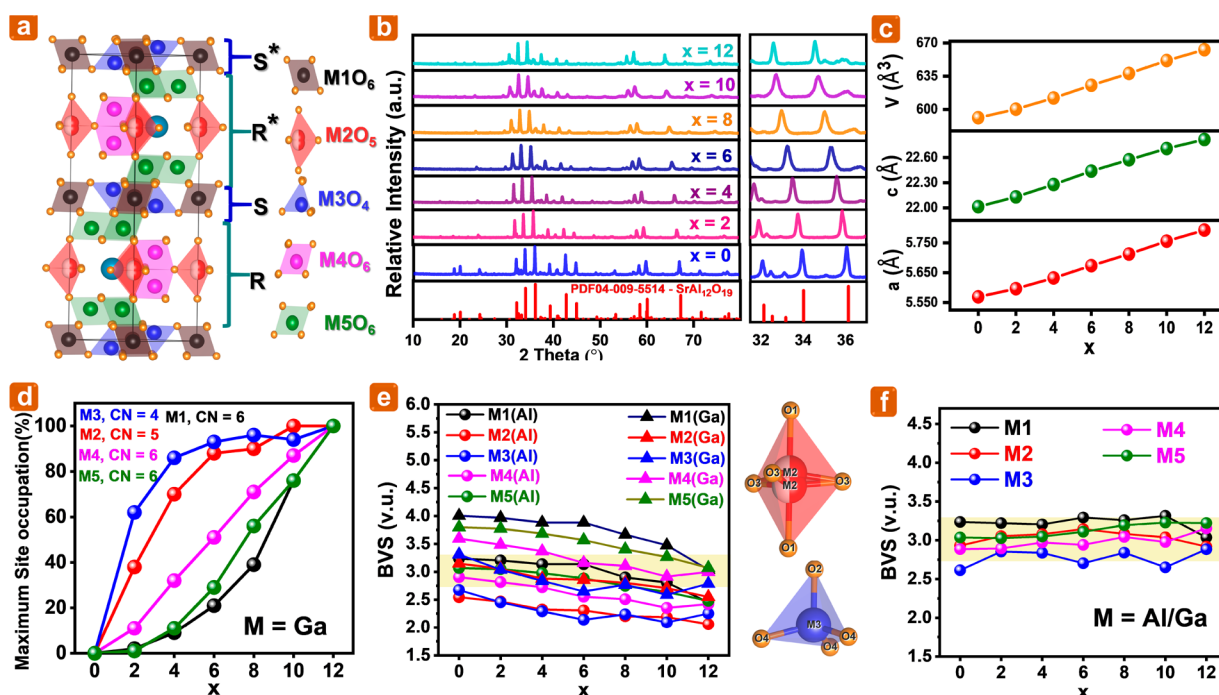**Figure 1.** Structure investigation results of $SrAl_{11.88-x}Ga_xO_{19}:0.12Cr^{3+}$ ($x = 0, 2, 4, 6, 8, 10,$ and 12). (a) The magnetoplumbite type structure. Brown, red, blue, magenta, and green spheres represent M(Al, Ga) in M1 to M5 sites, respectively, orange spheres are O. S and R basic building blocks are identified. (b) XRD data along with that calculated from the structure PDF#04-009-5514 in the range of $10-80°$ and in the region $31.5-37°$. (c) Lattice parameter obtained from joint Rietveld refinement using S-XRD and NPD data. (d) Refined % Ga at each site. (e) Bond−valence sum (BVS) of Al and Ga along with the local coordination structure of M2 and M3. (f) Occupancy-corrected BVS for mixed Ga/Al sites. Lines through points are guides to the eye.

the requirements of emission at 980 nm in solar energy conversion.[21] The quantum efficiency and thermal stability are the two critical parameters that eventually determine the phosphor host effectiveness. In 2020, Liu et al.[22] reported highly efficient NIR phosphor $LaMgGa_{11}O_{19}:Cr^{3+}$ ($\lambda_{em} = 715-800$ nm) with an internal quantum efficiency of 82.6% and excellent thermal quenching resistance. Recently, Liu et al.[23] have reported internal/external quantum efficiencies of 98%/45% in $SrGa_{12}O_{19}:Cr^{3+}$ ($\lambda_{em} = 770$ nm) through a local site-engineered strategy and also showed that the integrated PL intensity at 500 K remains 86.5% as compared with 290 K. The energy transfers among multiple Cr^{3+} sites in $LaMg-Ga_{11}O_{19}:Cr^{3+}$ and inducing symmetry changes in $SrGa_{12}O_{19}:Cr^{3+}$ are considered as the possible luminescence mechanism.[22,23] In this work, detailed structural and luminescence investigations are further carried out and explored the actual NIR luminescence center in the magentoplumbite host as a $Cr^{3+}-Cr^{3+}$ ion pair and its corresponding luminescence mechanism. In addition, the potential pc-NIR LED application of a magnetoplumbite host is also reported.

■ RESULTS AND DISCUSSION

Crystal Structure. $SrAl_{12}O_{19}$ and $SrGa_{12}O_{19}$ have a magnetoplumbite type structure and are commonly present in chondritic meteorites.[17,18] Magnetoplumbites crystallize in the hexagonal crystal system, often with the $P6_3/mmc$ space group with five unique crystallographic sites for the M^{3+} cation [M = Al, Ga] (Figure 1a). A magnetoplumbite unit cell comprises two basic building blocks stacked together along the c axis in the sequence RSR*S*, where S is a spinel block and forms a two-layer sequence, and the R block forms a three-

layer sequence. Typically, the M1 $2a$ and M3 $4f$ cation sites in the S block form a regular octahedron and a distorted tetrahedron, respectively, connected by the O atom O4. The M4 $4f$ and M5 $12k$ cation sites in the R block form dimers of trigonally distorted edge-shared octahedra, with M5 having three units (Figure S1). The atoms at M4 and M5 sites, as well as the Sr at $2d$ sites, are connected through the O atom at O5 sites. In contrast, the M2 $4e$ site is close to trigonal bipyramidal coordination but slightly displaced (split) into two statistically half-occupied, pseudotetrahedral $4e$ sites.

X-ray powder diffraction (XRD) and neutron powder diffraction (NPD) data of $SrAl_{11.88-x}Ga_xO_{19}:0.12Cr^{3+}$ ($x = 0, 2, 4, 6, 8, 10,$ and 12) samples (laboratory XRD data are shown in Figure 1b) could be indexed to a main phase isostructural to $SrAl_{12}O_{19}$ (PDF#04-009-5514), indicating the full solid solubility of Ga within the hexagonal structure. The Cr in the material could not be detected using either laboratory or synchrotron XRD (S-XRD) nor with NPD, due to the similar X-ray scattering factors and coherent neutron scattering lengths of Al^{3+} and Cr^{3+}.[24] It is expected that Cr^{3+} substitutes for Al^{3+} in the series due to their similar ionic radius and valence (six-coordinate $Al^{3+} = 0.535$ Å and $Cr^{3+} = 0.615$ Å)[25] and that Cr^{3+} in an octahedral and not tetrahedral environment will emit NIR light.[26,27] A minor amount of Al_2O_3 was found in the $x = 0$ sample, Al_2O_3 and Ga_2O_3 in the $x = 2$ sample, and Ga_2O_3 in the $x = 4$ sample (Table S1). Structural refinement of the main phase against both S-XRD and high-resolution NPD was conducted, and results are shown in Figures S2 and S3, respectively, and in Tables S1 and S2. As a typical solid solution, the lattice parameters (a and c) and cell volume (V) increase with x from 0 to 12 (Figure 1c), evidencing the successful substitution of Ga^{3+} for Al^{3+} in the structure. The
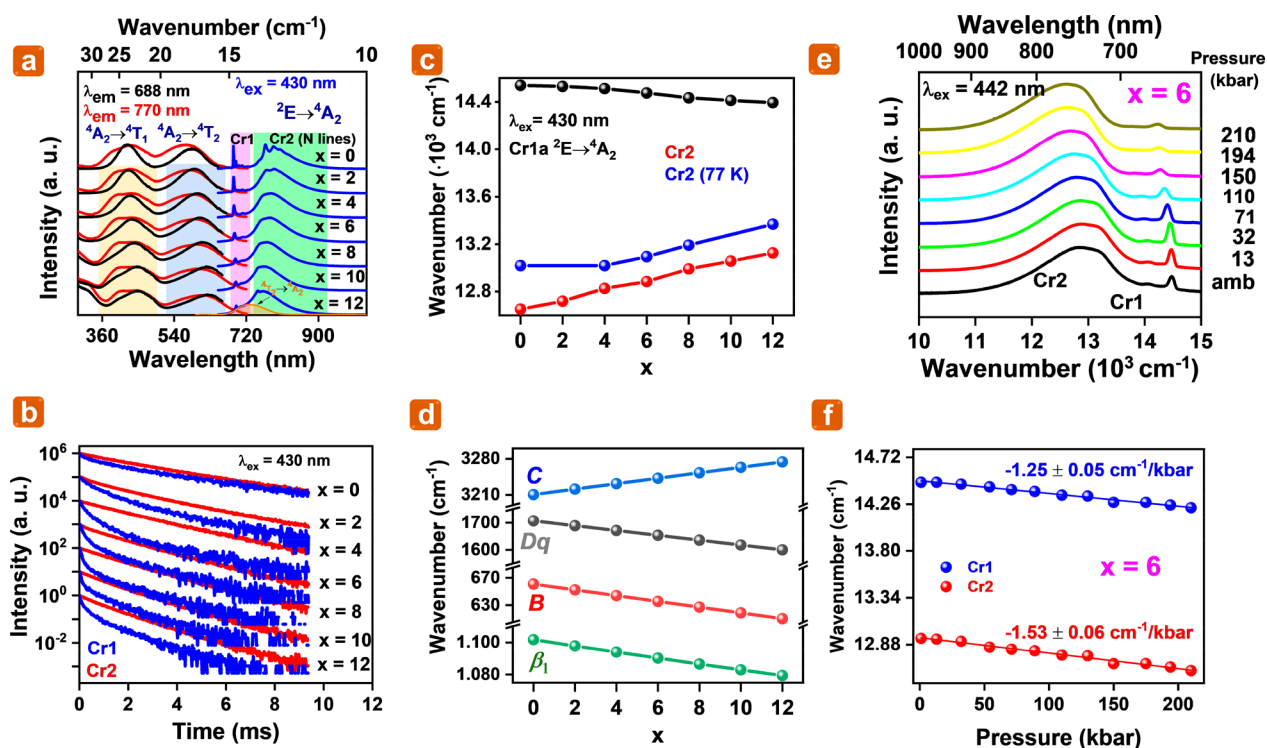
Figure 2. Luminescence analysis of $SrAl_{11.88-x}Ga_xO_{19}$:0.12Cr^{3+} (x = 0, 2, 4, 6, 8, 10, and 12). (a) PLE spectra at 688 (black line) and 760 nm (red line) and emission spectra upon excitation at 430 nm. (b) Decay profiles of Cr1 (blue line) and Cr2 (red line). (c) Position of the maximum Cr1 and Cr2 emission at room temperature and Cr2 emission at 77 K. (d) Crystal field strength parameter Dq and Racah parameters B and C together with the nephelauxetic parameter β_1. (e) Pressure-dependent PL spectra of the x = 6 sample at room temperature, and (f) pressure dependence of Cr1 and Cr2 emission for the x = 6 composition.

refined site occupancy factors for Ga and Al sites resulted in stoichiometry in good agreement with the nominal composition, noting the presence of minor impurity Al_2O_3 and Ga_2O_3 phases for some samples. The Ga content at each M1 to M4 site within the $SrAl_{11.88-x}Ga_xO_{19}$:0.12Cr^{3+} series is shown in Figure 1d. Ga^{3+} has a preferred occupancy trend for sites: M3(IV) > M2(V) > M4(VI) > M5(VI) > M1(VI). In this system, Ga^{3+} prefers tetrahedral over octahedral sites, counter to that expected for the larger Ga^{3+}. To understand this further, the bond valence sum (BVS) for each site is considered (Figure 1e).[25,28]

Bond-Valence Sum. At x = 0, Al^{3+} in the M3 site (tetrahedral) is underbonded with a BVS value less than +3 (+2.6), whereas Al^{3+} at the octahedral sites M1, M4, and M5 are within the BVS limits (+3). Hence, Ga^{3+} is incorporated into the crystal lattice by first occupying sites that bring the BVS value closer to +3, after which the higher BVS value sites M4, M5, and M1 are occupied. BVS values adjusted for Ga^{3+} and Al^{3+} content are shown in Figure 1f, where the BVS values of both tetrahedral and octahedral sites are near +3, confirming the preferred occupancy of Ga^{3+} at tetrahedral sites in the $SrAl_{11.88-x}Ga_xO_{19}$:0.12Cr^{3+} series. To further understand the substitution behavior, the bond length of Al/Ga−O at the M2 and M3 sites is compared, as shown in Figure S4. The M^{3+}(Al/Ga) atom at M3 sites is bonded to two O atoms with a bond length of 1.806−1.881 Å (M3−O2) and 1.798−1.858 Å (M3−O4), which are close to each other over the series. The M^{3+}(Al/Ga) atom at the M2 site is also bonded to two O atoms, but the apical bond lengths of 2.116 Å (M2−O1) are much larger than the M2−O3 length of 1.773−1.848 Å. The corresponding distortion index calculated based on quadratic

elongation for the M2 site is therefore much larger than that for the M3 site (Figure S5), rendering the M2 sites less favorable than M3 sites for Ga^{3+} substitution.

Photoluminescence. The photoluminescence excitation (PLE) and photoluminescence (PL) spectra of $SrAl_{11.88-x}Ga_xO_{19}$:0.12Cr^{3+} at room temperature (RT) are shown in Figure 2a. Under 442 nm excitation, two kinds of emissions are observed. The first consists of sharp lines (Cr1, denoted by a pink contour), with the most intense line at ∼688 nm. The second is a broadband emission extending from 650 to 950 nm (Cr2, denoted by a green contour). PLE spectra at 688 (black line) and 770 nm (red line) show two excitation bands typical for Cr^{3+} ions in octahedral coordination. The higher energy band (∼23 000 cm^{-1}, ∼430 nm) corresponds to the $^4A_2 \rightarrow {}^4T_1$ transition, whereas the lower energy band (∼17 000 cm^{-1}, ∼600 nm) corresponds to the $^4A_2 \rightarrow {}^4T_2$ transition of Cr^{3+}. Typically, Cr^{3+} samples exhibit a sharp line usually assigned to the spin-forbidden transition $^2E \rightarrow {}^4A_2$, whereas the broadband emission is assigned to the spin-allowed transition $^4T_2 \rightarrow {}^4A_2$. However, the decay time of Cr2 emission at 740−820 nm, as shown in Figure 2b (red curve), is within the range 1.1−2.4 ms, similar to the Cr1 emission around 680−700 nm (blue). In contrast, the $^4T_2 \rightarrow {}^4A_2$ transition is expected to have a much shorter decay time (microsecond range). Thus, the broadband emission arises from the spin-forbidden $^2E \rightarrow {}^4A_2$ transition, contrary to previous reports.[20−22] Xu et al.[20] report decay time in the ms range for the $SrGa_{12}O_{19}$:Cr^{3+} phosphor at 750 nm, although the exact decay time and absence of corresponding structural information make further comparison difficult. Similarly, a decay time of ∼2 ms is observed for the $Cr^{3+}−Cr^{3+}$ ion pair in

the Cr^{3+}-doped $LaAlO_3$ perovskite material.[29] Apart from that, the decay time in the range of ms is also observed in other magnetoplubmites, and the optical transition is assigned as spin-allowed.[22,23] The crystal structure of magnetoplumbites (Figures 1a and S1) has distorted octahedral units of M4 and M5 atoms next to each other, forming a face-sharing polyhedron independently with M4−M4 and M5−M5 distances of 2.650 and 2.756 Å, respectively. This finding suggests a strong probability of forming exchange-coupled Cr^{3+} pairs upon double substitution of M4 or M5 sites. Pair interaction strength increases with decreasing bond length,[30] and the M4−M4 is shortest, as shown in Figure S6. We note a lower possibility of forming exchange-coupled Cr^{3+} pairs among other M sites such as M4−M5, M1−M5, and M1−M3, these having longer bond lengths. The coupling of Cr^{3+} ions should lead to the splitting of energy levels and may significantly alter the luminescence of the pair compared to that of isolated ions. Hence, the broadband emission of Cr2 is ascribed to Cr^{3+}−Cr^{3+} ion pairs at the M4 site. Meanwhile, the decay profile of the Cr1 emission is nonexponential and shortens with increased Ga concentration. The $^4A_2 \rightarrow {}^4T_1$ and $^4A_2 \rightarrow {}^4T_2$ excitations red-shift (Figure S7) and overlap the Cr1 emission (Figure 2a) as a result of the incorporation of Ga^{3+}. This enhances energy transfer within the Cr ions and shortens the decay time. To summarize, Cr1 emission likely arises from isolated Cr^{3+} ions in ideal octahedral M1 sites, while the broadband Cr2 emission likely arises from Cr^{3+}−Cr^{3+} ion pairs in M4−M4 sites. The construction of the energy level diagram for the Cr^{3+}−Cr^{3+} ion pair can be useful to explore the energy level differences among the transition's nature. However, it is not possible to determine the actual Stokes shift of the Cr2 emission (even if it is broadened at RT), since the relevant PLE spectra in the 700−800 nm region are obscured by optical bands of the isolated Cr1 center. Hence, the schematic energy level diagram is not included due to the absent PLE spectra in the 700−800 nm range. With increased x, the Cr1 emission shifts toward longer wavelengths (lower energies) from 685 to 695 nm (14 500−14 400 cm^{-1}) owing to the decrease in crystal-field strength around the Cr ions (Figure 2c). Interestingly, the Cr2 emission shifts toward shorter wavelengths (higher energies) in direct contrast to the Cr1 emission. Even at 77 K, the Cr2 emission peaks shift from 790 to 760 nm (12 650−13 100 cm^{-1}). Such unusual behavior can be explained on the grounds of differences in ion distances in the lattice. For $x = 0$, the distance between the paired Cr^{3+}−Cr^{3+} ions is smaller than that for $x = 12$, increasing interaction. Meanwhile, the N-line emission (zero phonon line of the Cr^{3+} pair emission) is usually very close to the R-line emission in the case of weaker interaction.[29] Our results indicate that the stronger interaction between Cr^{3+} ion pairs (reduced Cr^{3+}−Cr^{3+} distance) results in a greater energy difference from the N-line to the R-line (a larger splitting of energy levels related to paired Cr^{3+} ions). We observe the red-shift of R-lines (Cr1) and the blue-shift of N-lines (Cr2), which result in a smaller energy difference between these with increasing x (lattice parameters increase with x, increasing Cr^{3+} ion pair distance, Figure S6). Specifically, the blue-shift of N-lines (Cr2 emission) arises from the increased distance between Cr^{3+} ions, weakening their interaction, reducing the energy level split and the energy difference between the R- and N-line emissions.

To understand the behavior of isolated Cr^{3+} ions (Cr1), the crystal-field strength parameter Dq and Racah parameters B

and C are calculated (see Supporting Information), as shown in Figure 2d. The crystal-field strength Dq decreases with increased x, as a consequence of increased lattice parameters. However, the Racah parameter B decreases, whereas C increases with x. In principle, the energy shifts of the ^2E state (nephelauxetic shift) are determined by the combined effect of the B and C parameter, noting the opposite trend of the B and C parameter shift with x. The alternative nephelauxetic parameter β_1 proposed by Brik et al.[31] decreases with increased x following the experimental values of the ^2E state. Notably, the observed changes in the energy of ^2E with x (red-shift with declining crystal-field strength Dq) contradict the ^2E state of pressure behavior (red-shift with increased Dq; Figure S8). This finding indicates that the "chemically induced pressure" (decrease in x) is combined with the reduction of Cr^{3+}−ligand covalence.

Pressure-Dependent Photoluminescence. Figure 2e shows pressure-dependent PL spectra of the $x = 6$ sample, and Figure S9 shows those for samples $x = 0$ and 12. Up to 32 kbar, the fine structure in emission spectra of Cr1 and Cr2 for $x = 0$ is well resolved, whereas both emissions are broadened at higher pressure. The pressure dependence of the energy shift of Cr1 and Cr2 emissions for the $x = 0$ and 12 samples is shown in Figure S9 and that for $x = 6$ in Figure 2f. For all tested cases $x = 0$, 6, and 12, pressure increase leads to a linear shift of Cr1 and Cr2 emissions toward lower energy (longer wavelength) at approximately −1.5 cm^{-1}/kbar. This further confirms that this emission cannot be attributed to the $^4T_2 \rightarrow {}^4A_2$ transition, which would shift toward higher energy (shorter wavelengths), typically at a much stronger rate. Moreover, both the direction and magnitude of the pressure shift are typical for a $^2E \rightarrow {}^4A_2$ transition.[32−34] This evidences the spin-forbidden transition of Cr^{3+} and Cr^{3+}−Cr^{3+} pairs. Pressure-dependent decay profiles for the $x = 0$, 6, and 12 samples and calculated decay times for Cr1 and Cr2 emissions are shown in Figures S10 and S11. The decay profile of the Cr1 emission is nonexponential, as expected for conventional PL measurements, with an average decay time of 2.2−2.7 ms until 46 kbar for $x = 0$, 1.0−3.1 ms until 170 kbar for x = 6, and 1.0−2.6 ms until 126 kbar for $x = 12$. In contrast, Cr2 emissions are nearly exponential with a decay time of 2.2−2.8 ms, 1.4−2.5 ms, and 1.1−2.4 ms for $x = 0$, $x = 6$, and $x = 12$, respectively, until 200 kbar. The lower ambient-pressure average decay time for $x = 12$, combined with a greater pressure rise, likely arises from the influence of the higher excited state $^4T_2$ on the effective decay time; that is, the thermal occupation of the spin-allowed $^4T_2$ state at ambient pressure reduces the effective decay time. The effect of pressure is a shift of the $^4T_2$ state toward higher energy. In effect, the activation energy for the thermal occupation of $^4T_2$ increases, leading to a gradually smaller occupation and thus smaller influence of $^4T_2$ on the effective decay time. When the activation energy for $^4T_2$ occupation is large; the thermal occupation effect becomes negligible; however, the $^2E \rightarrow {}^4A_2$ decay time increases with increased pressure because spin−orbit interaction strength diminishes, which determines the probability of the doublet-quartet spin-forbidden transition (the effect is described as the admixing of the $^4T_2$ state to the ^2E emitting state, which diminishes as $^4T_2$ shifts toward higher energies). This effect can explain the increase in the increase in decay time for the $x = 0$ sample, where the thermal occupation of the $^4T_2$ state is absent, as well as the increase in the ^2E decay time of the $x = 12$ sample. The decrease in Cr1 emission lifetime at the highest pressure may
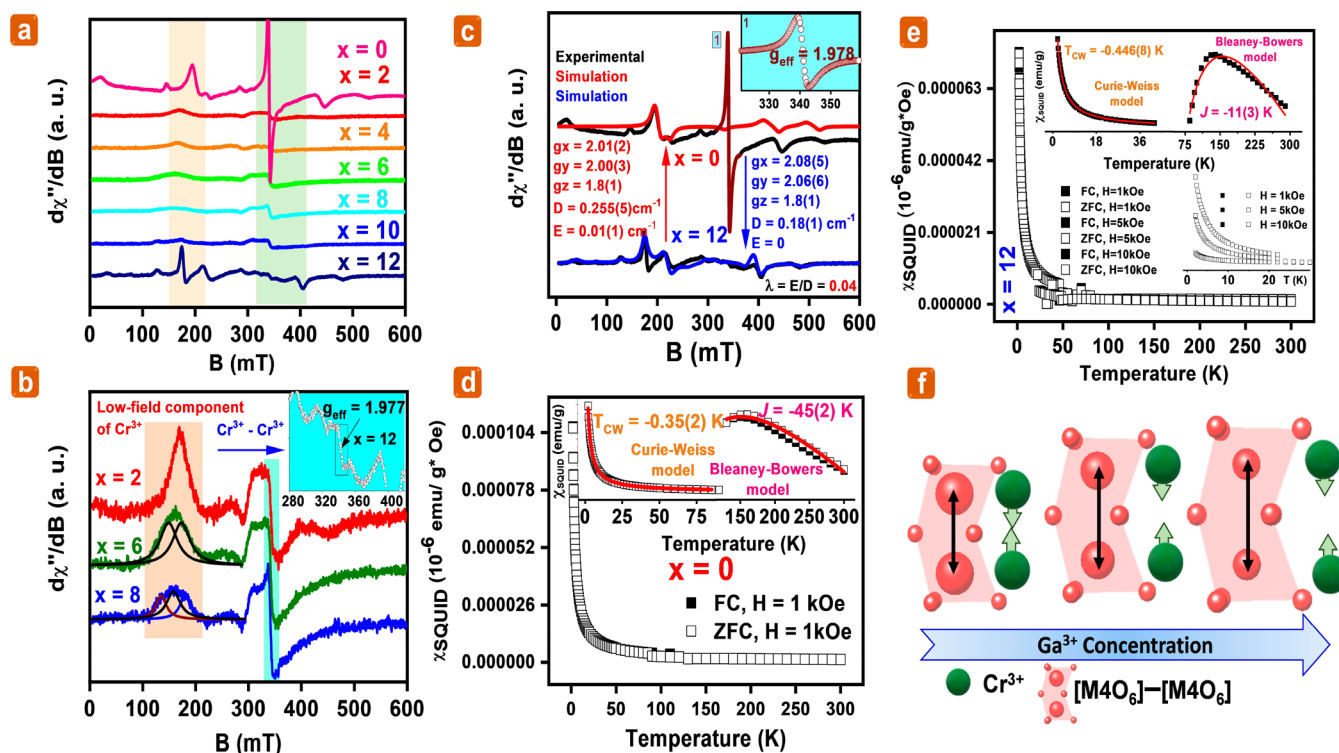
Figure 3. Local structure effects of $SrAl_{11.88-x}Ga_xO_{19}$:0.12Cr^{3+}: (a) EPR spectra of $x = 0-12$ samples over $100-600$ mT; (b) vanishing and broadening of the EPR signal from isolated Cr ions (a low component of Cr^{3+}) and Cr pairs; (c) EPR spectra and EPR/nuclear magnetic resonance simulations of $SrAl_{11.88-x}Ga_xO_{19}$ compounds $x = 0$ and $x = 12$; temperature dependence of magnetic susceptibility for (d) $x = 0$ and (e) $x = 12$; and (f) schematic of $[M4-O_6]-[M4-O_6]$ bond length and $Cr^{3+}-Cr^{3+}$ pair interactions. O atoms are red. B is the magnetic field, g is the spectroscopic splitting factor with x, y, and z tensors, and g_{eff} encompasses the zero-field interaction. D and E are axial and rhombic distortions of the octahedron, respectively.

be the effect of odd-parity distortions in the Cr^{3+} site leading to further relaxation of the parity-selection rule for the $^2E \rightarrow {}^4A_2$ parity-forbidden transition or due to the appearance of nonradiative quenching.

Local Structure. Electron paramagnetic resonance (EPR) and superconducting quantum interference device (SQUID) measurements were used to examine the paramagnetic nature of Cr^{3+} and $Cr^{3+}-Cr^{3+}$ pairs. Figure 3a shows EPR spectra of $SrAl_{11.88-x}Ga_xO_{19}$:0.12Cr^{3+} at RT. Here, g_{eff} is the spectroscopic splitting factor that encompasses the effect of zero-field interactions with x, y, and z tensors, and where D and E are the axial and rhombic distortions of the octahedron, respectively. For $x = 0$, two EPR signals are recognizable in the magnetic field range $0 \text{ mT} < B < 600 \text{ mT}$. The first signal (shaded orange in Figure 3a) represents isolated Cr^{3+} ions in an octahedral environment. The second intense signal (shaded green) with $g_{eff} = 1.9785$ (inset in Figure 3b) is assigned to the interaction within $Cr^{3+}-Cr^{3+}$ pairs after Voigt fitting with a Lorentzian contribution of 0.9. The dominant interactions are of the exchange type. Meanwhile, two isolated Cr^{3+} ions are superpositioned together in samples of $2 < x < 10$, which makes the signal less clear as a result of the inhomogeneous Cr^{3+} environment. In addition, the intensity is also reduced in this EPR signal, making it difficult to determine the parameters of the spin Hamiltonian for samples $2 < x < 10$. Interestingly, x significantly affects the interaction signal of $Cr^{3+}-Cr^{3+}$ pairs ($g_{eff} = 1.9785$). Nevertheless, the $Cr^{3+}-Cr^{3+}$ pair signal is observed until $x = 12$ (Figure 3b). The EPR spectrum is fitted using Spin−Hamilton (SH) parameters (Figure 3c), with $x = 0$: $g_x = 2.01(2)$, $g_y = 2.00(3)$, $g_z = 1.8(1)$, $D = 0.255(5) \text{ cm}^{-1}$,

and $E = 0.01(1) \text{ cm}^{-1}$. For $x = 12$: $g_x = 2.08(5)$, $g_y = 2.06(6)$, $g_z = 1.8(1)$, and $D = 0.18(1) \text{ cm}^{-1}$. The value of the SH parameter indicates that only one Cr^{3+} is centered for both compounds with some distortions in C_3 axial symmetry. Figures 3d and e show the temperature dependence of magnetic susceptibility for $x = 0$ and $x = 12$, respectively. For $x = 0$, magnetic susceptibility follows Curie−Weiss behavior with Curie−Weiss temperature $T_{CW} = -0.35$ K below 80 K. Conversely, magnetic susceptibility follows Bleaney−Bowers behavior with total angular momentum quantum number $J = -45$ K at a high temperature of about 120 K to room temperature. The negative sign indicates weak antiferromagnetic interaction of Cr^{3+} ions and $Cr^{3+}-Cr^{3+}$ pairs. Similarly, for $x = 12$, $T_{CW} = -0.45$ K ($0 < T < 45$ K) and $J = -11$ K (75 to 300 K), also indicating weak antiferromagnetic interaction of Cr^{3+} and $Cr^{3+}-Cr^{3+}$ pairs.[35] Surprisingly, another magnetic center is noted at higher magnetic fields, but unfortunately, it is undefined because of the narrow temperature range ($20 < T < 50$ K), high fields ($H = 10$ kOe), and no visible EPR signal. The strength and amount of magnetic interaction (the intensity of the EPR signal) within the $Cr^{3+}-Cr^{3+}$ pairs are much weaker in $x = 12$ than in $x = 0$. The similar symmetry Cr in both compounds makes the change in the strength of the interaction likely arise from the different $Cr^{3+}-Cr^{3+}$ center distances (Figure 3f). If the M4−M4 bond lengths increase over the range of x, then the interaction strength between paired Cr^{3+} ions decreases. This affects the broadband emission at $750-950$ nm with a blue-shift. Cr^{3+} K-edge X-ray absorption near-edge spectra reveal Cr in +3 valence in the x series (Figure S12).
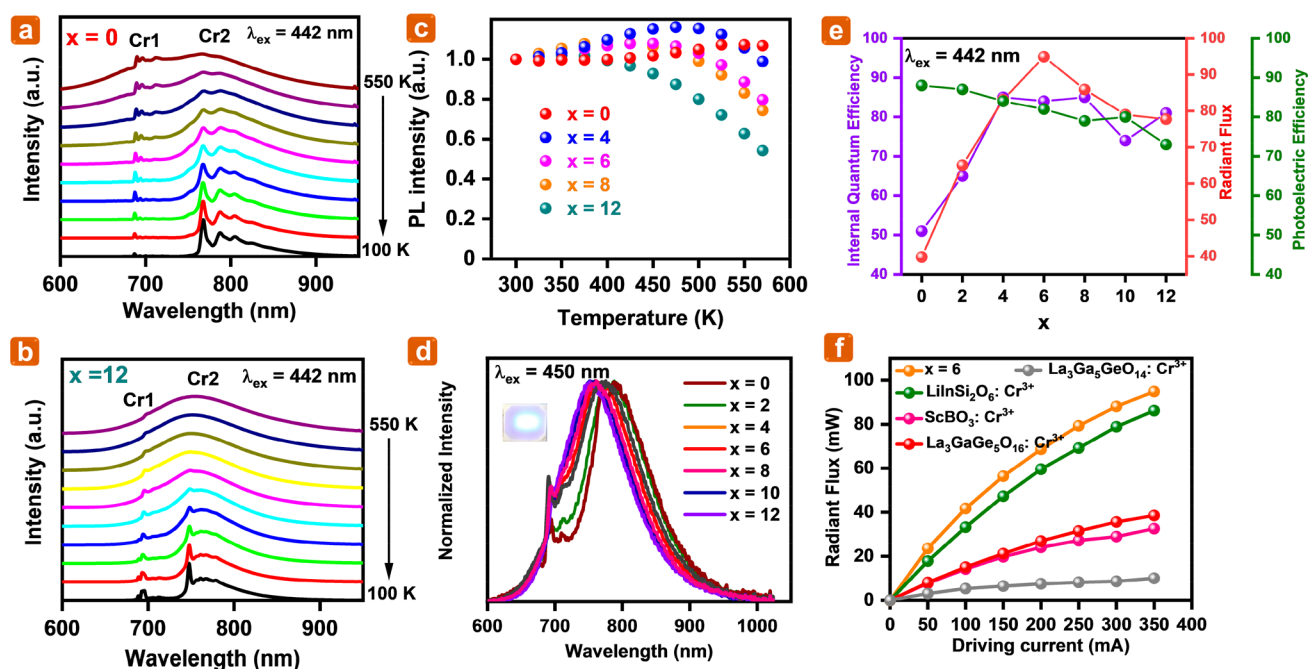
Figure 4. Temperature-dependent and prototype pc-NIR LED investigations of $SrAl_{11.88-x}Ga_xO_{19}:0.12Cr^{3+}$. Normalized temperature-dependent emission spectra for (a) $x = 0$; (b) $x = 12$; (c) integrated total emission intensity over 10−470 K at an interval of 50 K; (d) normalized electroluminescence spectra of the pc-NIR LED package fabricated using 450 nm LED as the excitation source; (e) output power of the pc-NIR LED package and internal quantum efficiency of $x = 0-12$ samples; and (f) output power of the NIR package and $LiIn_{0.94}Si_2O_6:0.06Cr^{3+}$, $Sc_{0.98}BO_3:0.02Cr^{3+}$, $La_3Ga_{0.93}Ge_5O_{16}:0.07Cr^{3+}$, and $La_3Ga_{4.95}GeO_{14}:0.05Cr^{3+}$.

Thermal Properties. Optical properties were investigated as a function of temperature for $x = 0$, 4, 6, 8, and 12. The normalized temperature-dependent emission spectra are observed until 550 K for $x = 0$ and $x = 12$ (Figure 4a,b) and $x = 4$, 6, 8 (Figure S13). A well-resolved line emission for Cr1 (680−710 nm) along with phonon sidebands and Cr2 emission (740−850 nm) with a clear zero phonon line of $Cr^{3+}-Cr^{3+}$ pairs (N-lines) is apparent for $x = 0$ and $x = 12$. However, an increase in temperature smears the profile of the Cr2 emission, especially for $x = 12$, for which the broadband emission is related to the spin-allowed $^4T_2 \rightarrow \,^4A_2$ transition. The emission profile of Cr2 is broadened even at low temperatures (77 K) for $x = 4$, 6, and 8, owing to the inhomogeneous environment of Cr^{3+}. The total intensity of emission spectra for different temperatures is obtained by the integration of non-normalized experimental data (Figure 4c).[23] The total intensity values were normalized by setting the intensity at 300 K as 1. The apparent increase of total intensity above unity seen in Figure 4c either is due to a thermally induced increase of absorption probability for the $^4A_2 \rightarrow \,^4T_1$ transition or is caused by thermally activated depopulation of electrons from electron traps associated with defects. The increase of total luminescence ceases at elevated temperatures due to the onset of nonradiative quenching (the threshold temperature for nonradiative quenching decreases with increasing x). Nonradiative quenching can also be caused by a drop in internal quantum efficiency and absorbance.[36] Nevertheless, in the operating temperature of the pc-LED device (∼400 K), the total intensity of all samples is unaffected by nonradiative quenching. To further verify the luminescent site-transition behavior, the decay profile is captured for Cr1 and Cr2 emissions within the range 30−470 K at 442 nm, with decay profiles shown in Figures S14. The decay profiles of the Cr1 emission are multiexponential and shortened with

increasing temperature. The average decay time τ_{av} is calculated using formula 1, and results are presented in Figure S15a. The decay time reduces with increased temperature for all x, but decreases fastest for the $x = 12$ composition. Notably, the increased average decay time for $x = 4$, 6, 8, and 12 is due to the overlapping Cr1 and Cr2 emissions at higher temperatures (>250 K). In contrast, the decay curve of the Cr2 emission is nearly single-exponential, and the decay time (τ) obtained using formula 2 is shown in Figure S15b. The decay time of the Cr2 emission remains constant until 200 K and starts to decrease at higher temperatures for $x = 0$ and $x = 4$. For $x = 6$, 8, and 12, the threshold temperature for decay time decrease is lower (∼100 K). Notably, the decay time shortens with increased Ga content. This effect may be ascribed to stronger agitation of odd-parity vibration modes at a higher temperature, influencing the probability of the parity-forbidden $^2E \rightarrow \,^4A_2$ transition.[37]

$$\tau_{av} = \frac{\int I(t)t \; dt}{\int I(t) \; dt} \tag{1}$$

$$I(t) = I_0 e^{-t/\tau} \tag{2}$$

where $I(t)$ is the emission intensity at time t, I_0 is the initial intensity, and τ is the decay time of the luminescence.

LED Packages. The practical viability of the as-synthesized solid-solution samples is demonstrated by pc-NIR LED fabrication with blue LED ($\lambda_{max} = 450$ nm) excitation. The normalized electroluminescence spectra of the pc-NIR LEDs are shown in Figure 4d. NIR emissions in the range 600−1000 nm are sufficiently strong to match Si detector sensitivity. As shown in Figures 4e and S16, with increased Ga content (from $x = 0$ to 12), the internal quantum efficiency and radiant flux increased until the saturation point at $x = 6$. The maximum

internal quantum efficiency and radiant flux of 84% and 96 mW (driving current = 350 mA) are achieved for $x = 6$ with a corresponding photoelectric efficiency of 82%. The external quantum efficiency was unable to be calculated for any of the samples due to limitations of the instrumentation used, which measures absorption and absolute QY. Notably, the photo-electric efficiency is also higher than 80% for all fabricated pc-NIR LEDs. Thus, the reported solid-solution tuned phosphor samples convert absorbed blue photons to NIR photons very effectively. The capability of the as-synthesized phosphor $x = 6$ for higher radiant flux is compared with well-known Cr^{3+}-doped IR phosphors (Figure 4f) such as $LiIn_{0.94}Si_2O_6:0.06Cr^{3+}$, $Sc_{0.98}BO_3:0.02Cr^{3+}$, $La_3Ga_{0.93}Ge_5O_{16}:0.07Cr^{3+}$, and $La_3Ga_{4.95}GeO_{14}:0.05Cr^{3+}$,[11,38−40] prepared following relevant literature (Figure S17). The internal quantum efficiency of the comparative samples is provided in Table S3. The $SrAl_{11.88−x}Ga_xO_{19}:Cr^{3+}$ $x = 6$ sample exhibited a higher radiant flux than all tested phosphors for driving currents between 50 and 350 mA (Figure 4f). This finding reveals the potential of magentoplumbites for application as pc-NIR LEDs.

CONCLUSIONS

In summary, the $SrAl_{11.88−x}Ga_xO_{19}:Cr^{3+}$ series of magneto-plumbites were synthesized and their crystal structure was characterized using Rietveld refinement using synchrotron X-ray and neutron powder diffraction data. Notably, Ga was found to prefer tetrahedral sites within the structure, with the M3−O bond length of the tetrahedron indicating under-bonding. Similarly, the M2−O1 bond of the trigonal bipyramidal M2 site is much longer than that of the M2−O3, inducing significant distortion. The series has broadband near-infrared luminescence in the range 650−1050 nm with the typical R line and additional broadband centered around 740−820 nm. Decay time and pressure shifts of the photoluminescent spectra indicate the broadband emission arises from spin-forbidden transitions of Cr^{3+}−Cr^{3+} pairs and not the spin-allowed $^4T_2 \rightarrow {}^4A_2$ transition. Increased Ga^{3+} concentration weakens the Cr^{3+}−Cr^{3+} ion pair and results in a blue shift of the spectrum. The construction of Cr^{3+}−Cr^{3+} pair energy levels is restricted due to the overlapping of PLE spectra in the region 700−800 nm with the optical bands of the Cr1 center. In addition, the low-temperature PL spectra also suggest the presence of prominent ZPL in the $x = 0$ and $x = 12$ samples, indicating that the Stokes shift cannot be as large as typically for $^4T_2 \rightarrow {}^4A_2$ emission. Even though the schematic energy level diagram construction for Cr^{3+}−Cr^{3+} is not possible in this case, but the attribution of the 800 nm emission to the $^4T_2 \rightarrow {}^4A_2$ transition of single Cr^{3+} centers is ruled out by the following reasons. The very large red-shift around 1500 cm^{-1} of the 800 nm emission compared to the ^2E emission would indicate the $SrAl_{11.88−x}Ga_xO_{19}:Cr^{3+}$ is a low crystal field material, in which case the $^2E \rightarrow {}^4A_2$ emission would be impossible. The pressure-induced red-shift of the 800 nm emission is inconsistent with the behavior of $^4T_2 \rightarrow {}^4A_2$ emission (strong blue-shift is expected). The luminescence decay time of the 800 nm emission is in the ms time range, which is 2 orders of magnitude longer than the $^4T_2 \rightarrow {}^4A_2$ lifetime observed in low crystal field Cr^{3+} materials. The $^4T_2 \rightarrow {}^4A_2$ emission related to the Cr1 center does appear at elevated temperature as broadband, poorly resolved emission in the 650−750 nm range. At the same time, the relation between the higher quantum efficiency and the Cr^{3+}−Cr^{3+} ion pair transition remains unexplored. Electron paramagnetic reso-

nance spectroscopy and magnetometry measurements confirm this, with two-electron paramagnetic spectroscopy signals observed and the magnetic susceptibility obeying the Bleaney−Bowers function. Significantly, the phosphor series have a high internal quantum efficiency of 95% and zero thermal quenching, demonstrating their potential for pc-NIR LED application. This study provides detailed insight into the luminescence mechanism of Cr^{3+} in the magentoplumbite-type structures that can be used to guide the future design of phosphors, revealing pathways to achieve thermal saturation and enhance the Cr^{3+}−Cr^{3+} pair strength to target perform-ance. The energy level scheme construction of the Cr^{3+}−Cr^{3+} ion pair and its microscopic energy level examination for higher quantum efficiency are the limitations of this study.

EXPERIMENTAL SECTION

Reagents. Strontium carbonate ($SrCO_3$; 99.0%) was purchased from Aldrich. Aluminum oxide (Al_2O_3; 99.99%) and gallium oxide (Ga_2O_3; 99.9%) were obtained from Gredmann. Chromium oxide (Cr_2O_3, 99.9%) was purchased from Merck.

Synthesis of $SrAl_{11.88−x}Ga_xO_{19}:0.12Cr^{3+}$ ($x = 0, 2, 6, 8, 10, 12$). Starting precursors were weighted as per stoichiometric amounts and ground well in a mortar with a pestle for 15 min. The homogeneous mixture was transferred to an alumina crucible and sintered in a muffle furnace at 1425 °C for 8 h in air. After sintering, the samples were ground well again in a mortar and pestle.

ASSOCIATED CONTENT

ⓢ Supporting Information

The Supporting Information is available free of charge at https://pubs.acs.org/doi/10.1021/jacs.1c08334.

> Details of characterization, Rietveld fit profiles along with refined structural parameters, pressure-dependent decay profiles and calculated decay time, temperature-dependent emission spectra of $x = 4$, 6, and 8 samples, and temperature-dependent decay profiles (PDF)

AUTHOR INFORMATION

Corresponding Authors

Ho Chang − *Department of Mechanical Engineering and Graduate Institute of Manufacturing Technology, National Taipei University of Technology, Taipei 106, Taiwan*; Email: f10381@ntut.edu.tw

Ru-Shi Liu − *Department of Chemistry, National Taiwan University, Taipei 106, Taiwan*; orcid.org/0000-0002-1291-9052; Email: rsliu@ntu.edu.tw

Authors

Veeramani Rajendran − *Department of Chemistry, National Taiwan University, Taipei 106, Taiwan; Department of Mechanical Engineering and Graduate Institute of Manufacturing Technology, National Taipei University of Technology, Taipei 106, Taiwan*; orcid.org/0000-0003-1479-8829

Mu-Huai Fang − *Department of Chemistry, National Taiwan University, Taipei 106, Taiwan*; orcid.org/0000-0003-1475-0200

Wen-Tse Huang − *Department of Chemistry, National Taiwan University, Taipei 106, Taiwan*

Natalia Majewska − *Institute of Experimental Physics, Faculty of Mathematics, Physics and Informatics, University of Gdańsk, 80-308 Gdańsk, Poland*; orcid.org/0000-0002-1933-0355

Tadeusz Lesniewski − *Institute of Experimental Physics, Faculty of Mathematics, Physics and Informatics, University of Gdańsk, 80-308 Gdańsk, Poland*

Sebastian Mahlik − *Institute of Experimental Physics, Faculty of Mathematics, Physics and Informatics, University of Gdańsk, 80-308 Gdańsk, Poland;* ⊙ orcid.org/0000-0002-9514-049X

Grzegorz Leniec − *Department of Technical Physics, Faculty of Mechanical Engineering and Mechatronics, West Pomeranian University of Technology Szczecin, 70-311 Szczecin, Poland*

Slawomir M. Kaczmarek − *Department of Technical Physics, Faculty of Mechanical Engineering and Mechatronics, West Pomeranian University of Technology Szczecin, 70-311 Szczecin, Poland*

Wei Kong Pang − *Institute for Superconducting and Electronic Materials, University of Wollongong, North Wollongong, New South Wales 2522, Australia;* ⊙ orcid.org/0000-0002-5118-3885

Vanessa K. Peterson − *Institute for Superconducting and Electronic Materials, University of Wollongong, North Wollongong, New South Wales 2522, Australia; Australian Centre for Neutron Scattering, Australian Nuclear Science and Technology Organisation, Sydney, New South Wales 2232, Australia;* ⊙ orcid.org/0000-0002-5442-0591

Kuang-Mao Lu − *Everlight Electronics Co., Ltd., New Taipei City 238, Taiwan*

Complete contact information is available at:
https://pubs.acs.org/10.1021/jacs.1c08334

Notes
The authors declare no competing financial interest.

■ REFERENCES

(1) Kim, M.; Singh, S. P.; Shim, S.; Park, W. B.; Sohn, K. S. Discovery of a Quaternary Sulfide, $Ba_{2-x}LiAlS_4:Eu^{2+}$, and Its Potential as a Fast-Decaying LED Phosphor. *Chem. Mater.* **2020**, *32*, 6697−6705.

(2) Kim, M.; Park, W. B.; Lee, J. W.; Lee, J.; Kim, C. H.; Singh, S. P.; Sohn, K. S. $Rb_3SiF_7:Mn^{4+}$ and $Rb_2CsSiF_7:Mn^{4+}$ Red-Emitting Phosphors with a Faster Decay Rate. *Chem. Mater.* **2018**, *30*, 6936−6944.

(3) Reuter, J. A.; Spacek, D. V.; Snyder, M. P. High-Throughput Sequencing Technologies. *Mol. Cell* **2015**, *58*, 586−597.

(4) Rateni, G.; Dario, P.; Cavallo, F. Smartphone-Based Food Diagnostic Technologies: A Review. *Sensors* **2017**, *17*, 1453.

(5) Desmet, K. D.; Paz, D. A.; Corry, J. J.; Eells, J. T.; Wong-Riley, M. T. T.; Henry, M. M.; Buchmann, E. V.; Connelly, M. P.; Dovi, J. V.; Liang, H. L.; Henshel, D. S.; Yeager, R. L.; Millsap, D. S.; Lim, J.; Gould, L. J.; Das, R.; Jett, M.; Hodgson, B. D.; Margolis, D.; Whelan, D. H. T. Clinical and Experimental Applications of NIR-LED Photobiomodulation. *Photomed. Laser Surg.* **2006**, *24*, 121−128.

(6) Beers, W. W.; Cohen, W. E.; Srivastava, A. M. Exploring Sm^{2+} Activated Phosphors as Red-Deep Red Photon Generator for Horticultural Application. *Opt. Mater. X* **2020**, *8*, 100059.

(7) Srivastava, A. M.; Brik, M. G.; Comanzo, H. A.; Beers, W. W.; Cohen, W. E.; Pocock, T. Spectroscopy of Mn^{4+} in Double Perovskites, La_2LiSbO_6 and La_2MgTiO_6: Deep Red Photon Generators For Agriculture LEDs. *ECS J. Solid State Sci. Technol.* **2018**, *7*, R3158−R3162.

(8) Rajendran, V.; Chang, H.; Liu, R. S. Recent Progress on Broadband Near-Infrared Phosphors-Converted Light Emitting Diodes for Future Miniature Spectrometers. *Opt. Mater. X* **2019**, *1*, 100011.

(9) Jia, Z.; Yuan, C.; Liu, Y.; Wang, X. J.; Sun, P.; Wang, L.; Jiang, H.; Jiang, J. Strategies to Approach High Performance in Cr^{3+}-Doped Phosphors for High-Power NIR-LED Light Sources. *Light: Sci. Appl.* **2020**, *9*, 86.

(10) Song, E.; Jiang, X.; Zhou, Y.; Lin, Z.; Ye, S.; Xia, Z.; Zhang, Q. Heavy Mn^{2+} Doped $MgAl_2O_4$ phosphor for High-Efficient Near-Infrared Light-Emitting Diode and The Night-Vision Application. *Adv. Opt. Mater.* **2019**, *7*, 1901105.

(11) Shao, Q.; Ding, H.; Yao, L.; Xu, J.; Liang, C.; Jiang, J. Photoluminescence Properties of a $ScBO_3$: Cr^{3+} Phosphor and its Applications for Broadband Near-Infrared LEDs. *RSC Adv.* **2018**, *8*, 12035−12042.

(12) Qiao, J.; Zhou, G.; Zhou, Y.; Zhang, Q.; Xia, Z. Divalent Europium-Doped Near-Infrared-Emitting Phosphor for Light-Emitting Diodes. *Nat. Commun.* **2019**, *10*, 5267.

(13) Zeng, H.; Zhou, T.; Wang, L.; Xie, R. J. Two-Site Occupation for Exploring Ultra-Broadband Near-Infrared Phosphor—Double-Perovskite La_2MgZrO_6:Cr^{3+}. *Chem. Mater.* **2019**, *31*, 5245−5253.

(14) Liu, D.; Li, G.; Dang, P.; Zhang, Q.; Wei, Y.; Lian, H.; Shang, M.; Lin, C. C.; Lin, J. Simultaneous Broadening and Enhancement of Cr^{3+} Photoluminescence in $LiIn_2SbO_6$ by Chemical Unit Cosubstitution: Night-Vision and Near-Infrared Spectroscopy Detection Applications. *Angew. Chem., Int. Ed.* **2021**, *60*, 14644−14649.

(15) Vink, A. P.; Meijerink, A. Electron−Phonon Coupling of Cr^{3+}-Pairs and Isolated Sites In α-Al_2O_3 and MgO. *Spectrochim. Acta, Part A* **1998**, *54*, 1755−1761.

(16) Derkosch, J.; Mikenda, W.; Preisinger, A. N-lines and Chromium-Pairs In The Luminescence Spectra of The Spinels $ZnAl_2O_4$:Cr^{3+} and $MgAl_2O_4$:Cr^{3+}. *J. Solid State Chem.* **1977**, *22*, 127−133.

(17) Li, J.; Medina, E. A.; Stalick, J. K.; Sleight, A. W.; Subramanian, M. A. Structural Studies of $CaAl_{12}O_{19}$, $SrAl_{12}O_{19}$, $La_{2/3+\delta}Al_{12-\delta}O_{19}$, and $CaAl_{10}NiTiO_{19}$ with the Hibonite Structure; Indications of An Unusual Type of Ferroelectricity. *Z. Naturforsch., B: J. Chem. Sci.* **2016**, *71*, 475−484.

(18) Holtstam, D.; Hålenius, U. Nomenclature of the Magnetoplumbite Group. *Mineral. Mag.* **2020**, *84*, 376−380.

(19) Xu, J.; Chen, D.; Yu, Y.; Zhu, W.; Zhou, J.; Wang, Y. Cr^{3+}:$SrGa_{12}O_{19}$: A Broadband Near-Infrared Long-Persistent Phosphor. *Chem. Asian J.* **2014**, *9*, 1020−1025.

(20) Lai, J. a.; Long, Z.; Qiu, J.; Zhou, D.; Wang, Q.; Yang, Y.; Hu, S.; Wang, Z.; Zhang, K. Novel Organic−Inorganic Hybrid Powder $SrGa_{12}O_{19}$:Mn^{2+}−Ethyl Cellulose for Efficient Latent Fingerprint Recognition via Time-Gated Fluorescence. *RSC Adv.* **2020**, *10*, 8233−8243.

(21) Luo, X.; Yang, X.; Xiao, S. Conversion of Broadband UV-Visible to Near Infrared Emission by $LaMgAl_{11}O_{19}$: Cr^{3+}, Yb^{3+} Phosphors. *Mater. Res. Bull.* **2018**, *101*, 73−82.

(22) Liu, S.; Wang, Z.; Cai, H.; Song, Z.; Liu, Q. Highly Efficient Near-Infrared Phosphor $LaMgGa_{11}O_{19}$:Cr^{3+}. *Inorg. Chem. Front.* **2020**, *7*, 1467−1473.

(23) Liu, S.; Cai, H.; Zhang, S.; Song, Z.; Xia, Z.; Liu, Q. Site Engineering Strategy Toward Enhanced Luminescence Thermostability of A Cr^{3+}-Doped Broadband NIR Phosphor and Its Application. *Mater. Chem. Front.* **2021**, *5*, 3841−3849.

(24) Sears, V. F. Neutron Scattering Lengths and Coss Sections. *Neutron News* **1992**, *3*, 26−37.

(25) Shannon, R. D. Revised Effective Ionic Radii and Systematic Studies of Interatomic Distances in Halides and Chalcogenides. *Acta Crystallogr., Sect. A: Cryst. Phys., Diffr., Theor. Gen. Crystallogr.* **1976**, *32*, 751−767.

(26) Adachi, S. Review—Photoluminescence Properties of Cr^{3+}-Activated Oxide Phosphors. *ECS J. Solid State Sci. Technol.* **2021**, *10*, 026001.

(27) Henderson, B.; Imbusch, G. F. *Optical Spectroscopy of Inorganic Solids*; Oxford University Press: Oxford, UK, 2006.

(28) Gagné, O. C.; Hawthorne, F. C. Comprehensive Derivation of Bond-Valence Parameters for Ion Pairs Involving Oxygen. *Acta Crystallogr., Sect. B: Struct. Sci, Cryst. Eng. Mater.* **2015**, *71*, 562−578.

(29) Vink, A. P.; de Bruin, M. A.; Roke, S.; Peijzel, P. S.; Meijerink, A. Luminescence of Exchange Coupled Pairs of Transition Metal Ions. *J. Electrochem. Soc.* **2001**, *148*, E313.

(30) H, G.; W, G. Short $Cr^{3+}-Cr^{3+}$ Distances in Magnetoplumbite Type $SrCr_9Ga_3O_{19}$. *Z. Kristallogr. - Cryst. Mater.* **1996**, *211*, 25−30.

(31) Brik, M. G.; Camardello, S. J.; Srivastava, A. M.; Avram, N. M.; Suchocki, A. Spin-Forbidden Transitions in the Spectra of Transition Metal Ions and Nephelauxetic Effect. *ECS J. Solid State Sci. Technol.* **2016**, *5*, R3067−R3077.

(32) Fang, M. H.; De Guzman, G. N. A.; Bao, Z.; Majewska, N.; Mahlik, S.; Grinberg, M.; Leniec, G.; Kaczmarek, S. M.; Yang, C. W.; Lu, K. M.; Sheu, H. S.; Hu, S. F.; Liu, R. S. Ultra-High-Efficiency Near-Infrared $Ga_2O_3:Cr^{3+}$ Phosphor and Controlling of Phytochrome. *J. Mater. Chem. C* **2020**, *8*, 11013−11017.

(33) Grinberg, M.; Barzowska, J.; Shen, Y.; Bray, K. L. Inhomogeneous Broadening of Cr^{3+} Luminescence in Doped $LiTaO_3$. *Phys. Rev. B: Condens. Matter Mater. Phys.* **2001**, *63*, 214104.

(34) Grinberg, M.; Barzowska, J.; Shen, Y. R.; Bray, K. L.; Dereń, P.; Hanuza, J. High-Pressure Spectroscopy Characterisation of LiSc-$(WO_4)_2$ Crystals Doped With Trivalent Chromium. *J. Lumin.* **2003**, *102*, 699−704.

(35) Basun, S. A.; Meltzer, R. S.; Imbusch, G. F. Exchange-Coupled Chromium Ion Pairs in Ruby Revisited. *J. Lumin.* **2007**, *125*, 31−39.

(36) Li, R.; Liu, Y.; Yuan, C.; Leniec, G.; Miao, L.; Sun, P.; Liu, Z.; Luo, Z.; Dong, R.; Jiang, J. Thermally Stable $CaLu_2Mg_2Si_3O_{12}:Cr^{3+}$ Phosphors for NIR LEDs. *Adv. Opt. Mater.* **2021**, *9*, 2100388.

(37) Lesniewski, T.; Mahlik, S.; Grinberg, M.; Liu, R. S. Temperature Effect on The Emission Spectra of Narrow band Mn^{4+} Phosphors for Application in LEDs. *Phys. Chem. Chem. Phys.* **2017**, *19*, 32505−32513.

(38) Xu, X.; Shao, Q.; Yao, L.; Dong, Y.; Jiang, J. Highly Efficient and Thermally Stable Cr^{3+}-Activated Silicate Phosphors for Broadband Near-Infrared LED Applications. *Chem. Eng. J.* **2020**, *383*, 123108.

(39) Rajendran, V.; Fang, M. H.; Guzman, G. N. D.; Lesniewski, T.; Mahlik, S.; Grinberg, M.; Leniec, G.; Kaczmarek, S. M.; Lin, Y. S.; Lu, K. M.; Lin, C. M.; Chang, H.; Hu, S. F.; Liu, R. S. Super Broadband Near-Infrared Phosphors with High Radiant Flux as Future Light Sources for Spectroscopy Applications. *ACS Energy Lett.* **2018**, *3*, 2679−2684.

(40) Rajendran, V.; Lesniewski, T.; Mahlik, S.; Grinberg, M.; Leniec, G.; Kaczmarek, S. M.; Pang, W. K.; Lin, Y.-S.; Lu, K. M.; Lin, C. M.; Chang, H.; Hu, S. F.; Liu, R. S. Ultra-Broadband Phosphors Converted Near-Infrared Light Emitting Diode with Efficient Radiant Power for Spectroscopy Applications. *ACS Photonics* **2019**, *6*, 3215−3224.

Chromium Ion Pair Luminescence: A Strategy in Broadband Near-Infrared Light-Emitting Diode Design

Veeramani Rajendran,[†,‡] Mu-Huai Fang,[†] Wen-Tse Huang,[†] Natalia Majewska,[§] Tadeusz Lesniewski,[§] Sebastian Mahlik,[§] Grzegorz Leniec,[&] Slawomir M. Kaczmarek,[&] Wei Kong Pang,[#] Vanessa K. Peterson,[#,φ] Kuang-Mao Lu,[⊥] Ho Chang,[*,‡] and Ru-Shi Liu[*,†]

[†]Department of Chemistry, National Taiwan University, Taipei 106, Taiwan

[‡]Department of Mechanical Engineering and Graduate Institute of Manufacturing Technology, National Taipei University of Technology, Taipei 106, Taiwan

[§]Institute of Experimental Physics, Faculty of Mathematics, Physics and Informatics, University of Gdańsk, Wita Stwosza 57, 80-308 Gdańsk, Poland

[&]Department of Technical Physics, Faculty of Mechanical Engineering and Mechatronics, West Pomeranian University of Technology Szczecin, al. Piastow 48, 70-311 Szczecin, Poland

[#]Institute for Superconducting and Electronic Materials, University of Wollongong, Squires Way, North Wollongong, New South Wales 2522, Australia

[φ]Australian Centre for Neutron Scattering, Australian Nuclear Science and Technology Organisation, Sydney, New South Wales 2232, Australia

[⊥]Everlight Electronics Co., Ltd., New Taipei City 238, Taiwan

Synthesis of Comparative Samples

$La_3Ga_{4.95}GeO_{14}$:0.05Cr^{3+}. Stoichiometric La_2O_3 (Gredmann chemicals, 99.9%), Ga_2O_3 (Gredmann chemicals, 99.9%), GeO_2 (Alfa Aesar, 99.9%), and Cr_2O_3 (Merck, 99.9%) were ground well for 15 min using a mortar and pestle. Then, the homogenous mixture was sintered at 1250 °C for 5 h in air.

$La_3Ga_{0.93}Ge_5O_{16}$:0.07Cr^{3+}. Stoichiometric La_2O_3 (Gredmann chemicals, 99.9%), Ga_2O_3 (Gredmann chemicals, 99.9%), GeO_2 (Alfa Aesar, 99.9%), and Cr_2O_3 (Merck, 99.9%) were ground well for 15 min using a mortar and pestle. Then, the homogenous mixture was sintered at 1250 °C for 5 h in air.

$LiIn_{0.94}Si_2O_6$:0.06Cr^{3+}. Stoichiometric $LiCO_3$ (Alfa Aesar, 99%), In_2O_3 (Alfa Aesar, 99.99%), SiO_2 (Aldrich, 99.99%), and Cr_2O_3 (Merck, 99.9%) were ground well for 15 min using a mortar and pestle. Then, the homogenous mixture was sintered at 1150 °C for 10 h in air.

$Sc_{0.98}BO_3$:0.02Cr^{3+}. Stoichiometric Sc_2O_3 (Gredmann Chemicals, 99.9%), H_3BO_3 (99.9%), and Cr_2O_3 (Merck, 99.9%) were ground well for 15 min using a mortar and pestle. Then, the homogenous mixture was sintered at 1250 °C for 10 h in air.

Characterization. X-ray powder diffraction (XRD) data were obtained at room temperature (RT) using a Bruker D2 phaser desktop diffractometer with CuKα radiation within the 2θ range 10−80°. RT synchrotron X-ray powder diffraction (S-XRD) data were also obtained at the wavelength 0.61993 Å using a Debye–Scherrer camera at the National Synchrotron Radiation Research Center (Taiwan) BL01C2 beamline in which the electron storage ring was operating 1.5 GeV with a beam current of 360 mA. The S-XRD wavelength was determined accurately using the LaB_6 660 National Institute of Standards and Technology (NIST) standard reference material (SRM). High-resolution neutron powder diffraction (NPD) data were obtained using the Echidna instrument at the Open Pool Australian light-water research reactor of the Australian Nuclear Science and Technology Organisation within the 2θ range 4–164° with 1.62194(5) Å neutrons as determined using the NIST $La^{11}B_6$ 660b SRM.[1] The Inorganic Crystal Structure Database structure model #ICSD69070 was used as the starting model for determination of the $SrAl_{11.88-x}Ga_xO_{19}$:0.12Cr^3 series structures and refined simultaneously against both S-XRD and NPD data using Rietveld analysis within the

academic Total Pattern Analysis Solutions software (version 5.0).[2] Lattice parameters, atomic positions, site occupancy factors, and isotropic atomic displacement parameters were all refined in the structural model. Site occupancy factors for Ga substitution at Al sites were constrained to sum to maximum, M1 = 1, M2 = 0.5, M3 = 1, M4 = 1, M5 = 1, and atomic displacement parameters constrained to be the same for the same atom site. Crystal structures were visualized using the VESTA software,[3] which was used to calculate the distortion index based on quadratic elongation that determines strain using equation S1:

$$\lambda = \frac{1}{n} \sum_{i=1}^{n} \left(\frac{l_i}{l_0}\right)^2 \qquad \text{(S1)}$$

Where l_0 is the center-to-vertex distance of a regular polyhedron, l_i is the distance from the central atom to the ith coordinating atom, l is dimensionless, giving a quantitative measure of polyhedral distortion independent of the effective size of the polyhedron.

X-ray absorption near-edge structure measurements at the Cr K-edge were acquired at the National Synchrotron Radiation Research Center (Taiwan) BL17C1 in total fluorescence yield mode using a double-crystal Si (111) monochromator. Photoluminescence excitation and emission spectra at RT were measured using a FluoroMax-4P spectrofluorometer (Horiba) equipped with a 150 W xenon lamp excitation source and an R928 Hamamatsu photomultiplier detector. Temperature and pressure-dependent luminescence spectra were measured using an Andor SR-750-D1 spectrometer equipped with a CCD camera (DU420A-OE). An Omni-Lambda 200i monochromator with a 150 W Xenon lamp or Kimmon Koha He-Cd laser at 442 nm was the excitation source. Decay profiles were obtained using a time-resolved spectroscopy apparatus, consisting of a PG 401/SH optical parametric generator pumped by a PL2251A pulsed YAG: Nd laser (EKSPLA). The detection part comprised a 2501S grating spectrometer (Bruker Optics) combined with a C4334-01 streak camera (Hamamatsu).[4] In the time-resolved luminescence measurements, samples were cooled using an APD Cryogenics closed-cycle DE-202 optical cryostat, which allowed the temperature to be varied between 30 and 470 K. For steady-state measurements, the temperature was controlled using a THMSG600 temperature controller Linkam stage combined with an LNP95 liquid nitrogen cooling pump system, allowing the temperature to be obtained within the range 77–570 K. High-pressure luminescence measurements were performed using a screw-driven Merrill–Bassett type diamond

anvil cell with 0.5 mm diameter culets.[5] The gasket for the pressure chamber was pre-indented to around 0.08 mm. A 0.2 mm diameter hole was drilled into the indentation center. $KMgF_3$:0.5%Eu^{2+} was used as a pressure sensor, and polydimethylsiloxane oil was used as a pressure transmitting medium.[6]

Electron paramagnetic resonance (EPR) spectra were recorded at RT using a conventional Bruker X-band ELEXSYS E500 CW spectrometer operated at 9.458 GHz and 2.007 mW microwave power. The magnetic induction reached 1.4 T. The first derivative of the absorption spectrum was recorded as a function of applied magnetic induction. An EPR/NMR program was applied to recognize spin Hamiltonian parameters.[7]

Magnetic measurements were performed with a superconducting quantum interference device magnetometer (Quantum Design MPMS-XL-7). Magnetic susceptibility data were obtained in the zero-field-cooled (ZFC) and field-cooled (FC) modes. Measurements were recorded for temperatures up to 300 K, and magnetic fields were varied within the range of 1–10 kOe. Magnetic susceptibility was simulated using the Curie–Weiss law at temperatures above the Curie temperature and in a weak magnetic field to satisfy the condition H/kT ≪ 1. The Bleaney–Bowers equation was applied to the simulation at higher temperatures. Susceptibility data were corrected using the diamagnetism of a sample holder and the constituent atoms by Pascal's constants.[8] To describe the EPR spectrum, a typical spin Hamiltonian for chromium in an octahedral site was used, as shown in equation S2:

$$H = \mu_B B \cdot g \cdot S + D(S^2_z - 1/3S(S+1)) + E(S^2_x + S^2_y) \qquad (S2)$$

where μ_B is the moment in Bohr magneton, B is the magnetic field induction, g is the spectroscopic splitting factor, S is electron spin, D and E are the axial and rhombic distortions of the octahedron, respectively ($\lambda = E/D$).

The internal quantum efficiency of the as-synthesized $SrAl_{11.88-x}Ga_xO_{19}$:0.12 Cr^{3+} sample was measured in a Hamamatsu Quantarus QY plus using a high-power Xe lamp at a fixed excitation wavelength of 475 ± 25 nm. It is the standard approach of calculating the external quantum efficiency using the absorption values derived from the QY machine. However, the machine's design precisely illustrates its operations, which include absorption and absolute QY measurements. There are challenges with calculating the external quantum efficiency utilizing absorption data from the QY plus instrument as per the manufacturer's design. Hence, we didn't calculate the external

quantum efficiency for our samples. A prototype phosphor-converted near-infrared (pc-NIR) light-emitting diode (LED) was constructed using a blue LED chip (450 nm) for excitation and synthesized powder phosphors as light-conversion materials. Phosphors and binders were weighed in a 2:1 ratio, mixed, and deposited over the blue-chip, which was then defoamed and cured at 150 °C for 2 h. Finally, the packaged LED was measured in an integrating sphere under a direct-current forward bias of 30–350 mA. The photoconversion efficiency specifies the ability of absorbed photons to be converted into output photons via downshifting conversion and photoconversion efficiency is calculated as the ratio of output near-infrared power to the input power.

Crystal-Field Strength Calculations

For the Cr1 optical center, the crystal-field strength parameter Dq and the Racah parameters B and C were calculated according to standard-relation equations S3 – S5.[9]

$$10Dq = E(^4A_2 \rightarrow {}^4T_2) \qquad (S3)$$

$$B = Dq\frac{\left[\frac{\Delta E}{Dq}\right]^2 - 10\frac{\Delta E}{Dq}}{15(\frac{\Delta E}{Dq} - 8)}, \qquad (S4)$$

$$C = \frac{B}{3.05}\left\{\frac{E(^2E \rightarrow {}^4A_2)}{B} - 7.9 + 1.8\frac{B}{Dq}\right\}, \qquad (S5)$$

where ΔE is the difference between the energy of the $^4A_2 \rightarrow {}^4T_1$ and $^4A_2 \rightarrow {}^4T_2$ transitions. Additionally, the nephelauxetic parameter β_1 was calculated according to equation S6.[10]

$$\beta_1 = \sqrt{\left(\frac{B}{B_0}\right)^2 + \left(\frac{C}{C_0}\right)^2} \qquad (S6)$$

Where the Racah parameters for a free Cr^{3+} ion is $B_0 = 918$ cm^{-1} and $C_0 = 3850$ cm^{-1}.
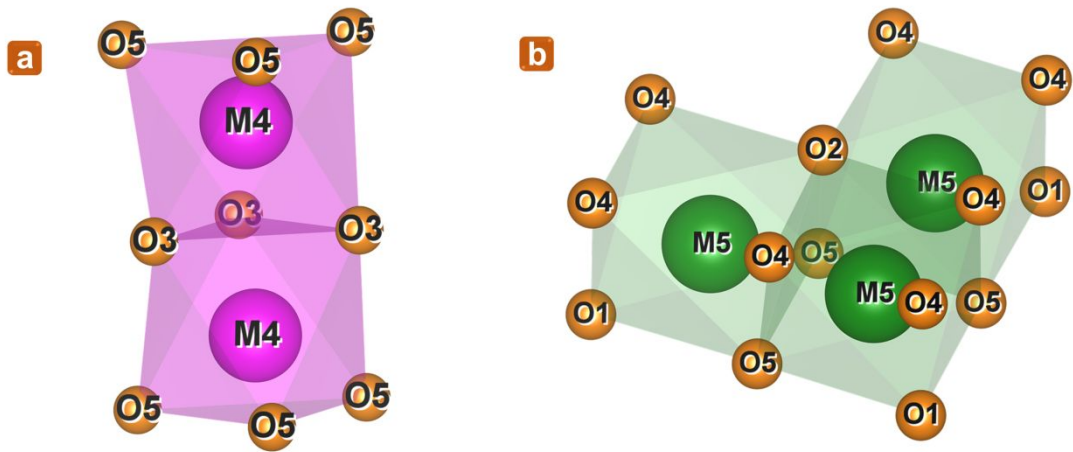
Figure S1. Local structure of the M^{3+} sites M4 and M5 in $P6_3/mmc$ magnetoplumbites. M^{3+} = (a) Al4 and (b) Al5.
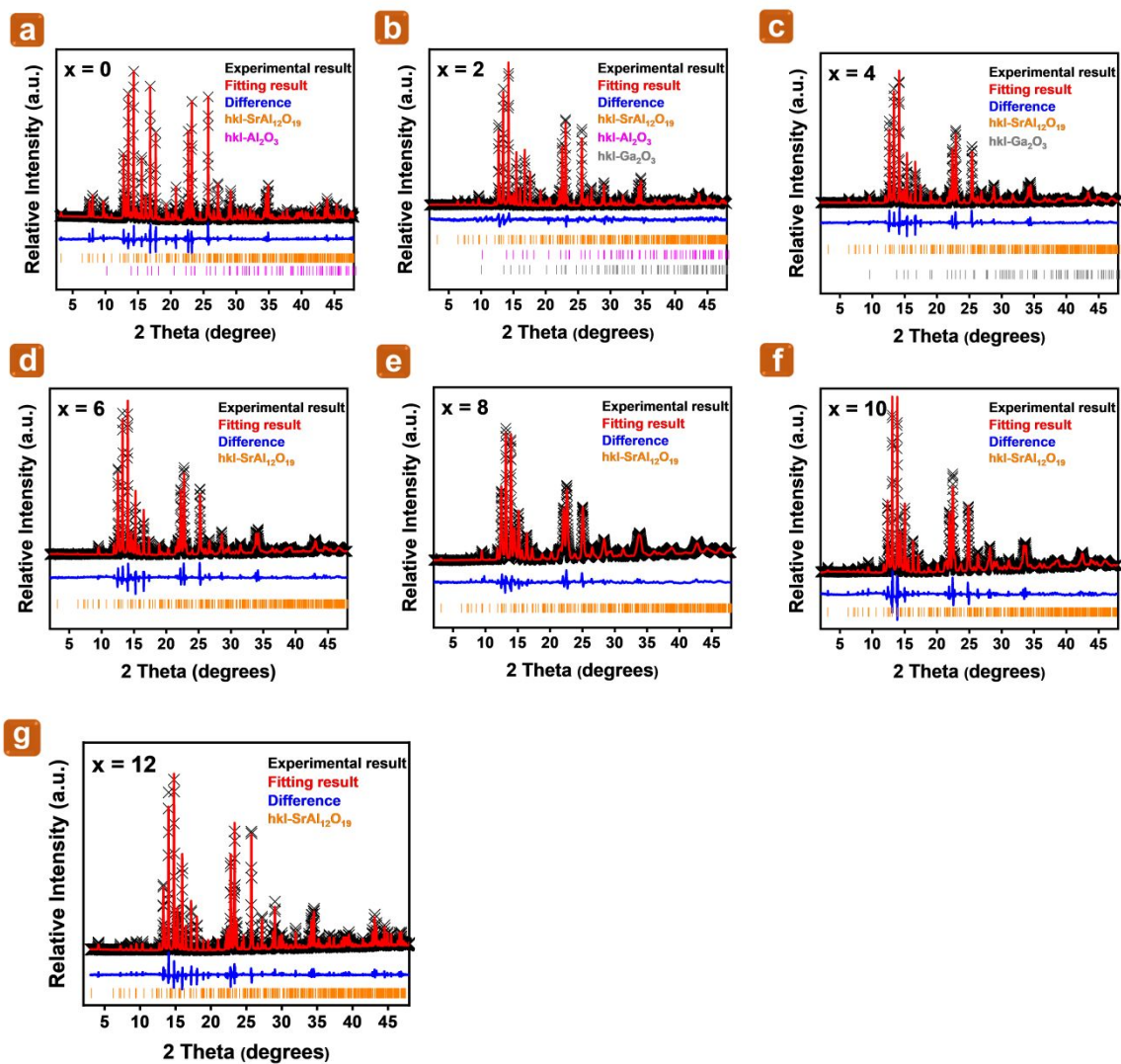
Figure S2. Joint Rietveld refinement profiles using S-XRD data for the SrAl$_{11.88-x}$Ga$_x$O$_{19}$:0.12Cr^{3+} series with (a) $x = 0$, (b) $x = 2$, (c) $x = 4$, (d) $x = 6$, (e) $x = 8$, (f) $x = 10$, and (g) $x = 12$. Refinement parameters are given in Tables S1 and S2.
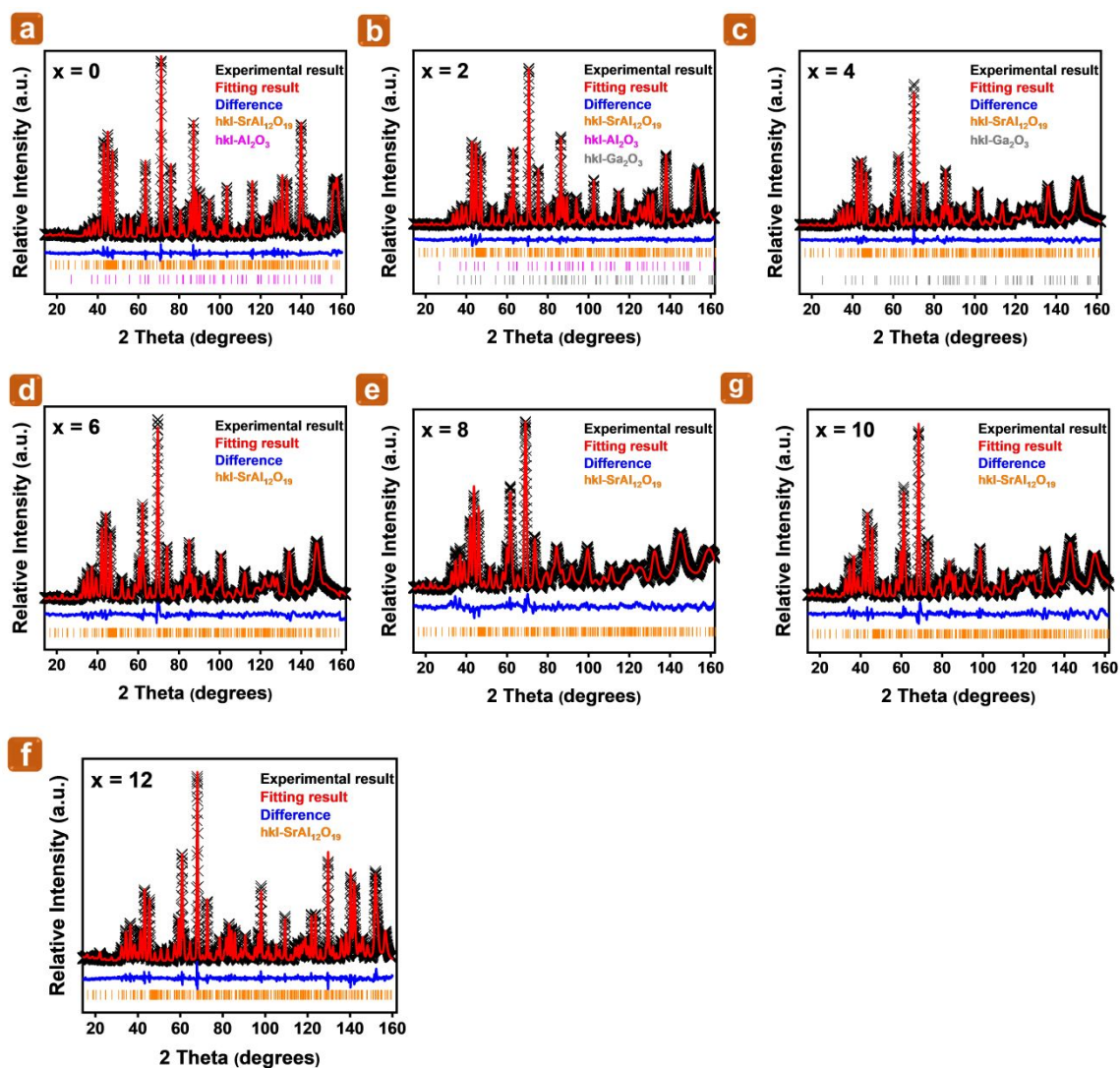
Figure S3. Joint Rietveld refinement profiles using NPD data for the SrAl$_{11.88-x}$Ga$_x$O$_{19}$:0.12Cr^3 series with (a) $x = 0$, (b) $x = 2$, (c) $x = 4$, (d) $x = 6$, (e) $x = 8$, (f) $x = 10$, and (g) $x = 12$. Refinement parameters are given in Tables S1 and S2.
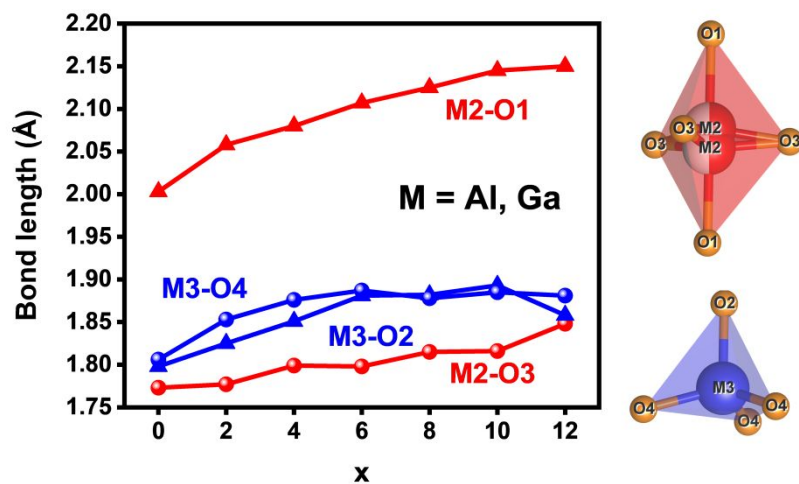
Figure S4. Bond lengths associated with M2 and M3 sites in the $SrAl_{11.88-x}Ga_xO_{19}{:}0.12Cr^3$ series, where M = Al, Ga. Lines through the points are a guide to the eye. The local environment of the M2 and M3 sites is also depicted.

Figure S5. Distortion index calculated by the quadratic elongation model for M1–M5 sites in the $SrAl_{11.88-x}Ga_xO_{19}{:}0.12Cr^3$ series where M = Al, Ga. Lines through the points are a guide to the eye. The local environment of the M2 and M3 sites is also depicted.

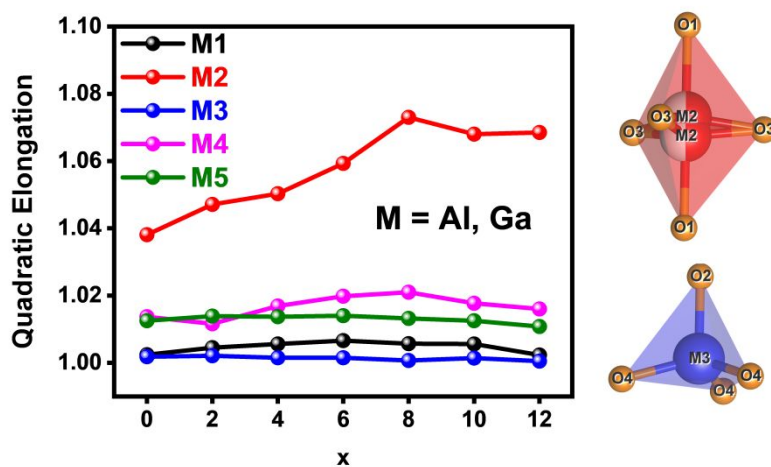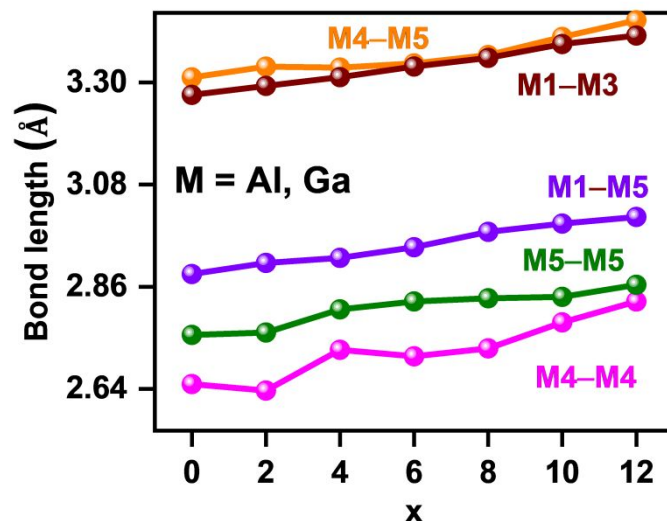Figure S6. M4–M4, M5−M5, M1−M5, M1−M3, and M4−M5 distances in the $SrAl_{11.88-x}Ga_xO_{19}$:0.12Cr^3 series, where M = Al, Ga. Lines through the points are a guide to the eye.
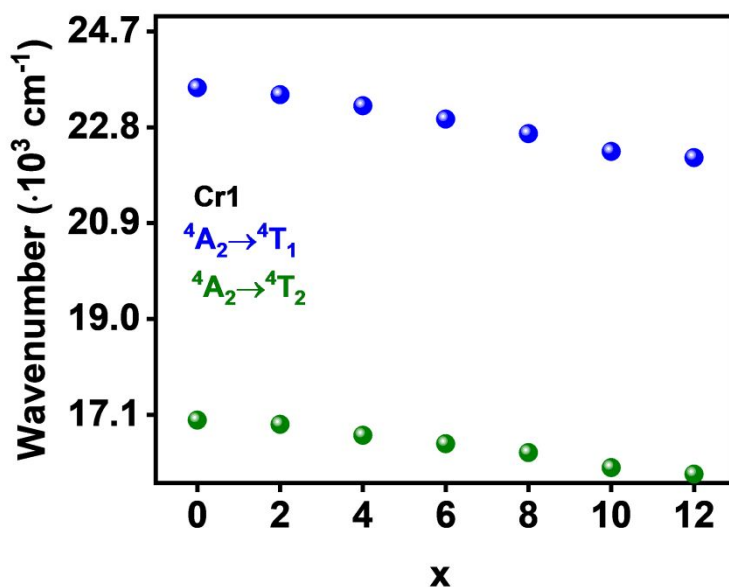

Figure S7. Position of excitation bands in the $SrAl_{11.88-x}Ga_xO_{19}$:0.12Cr^3 series.
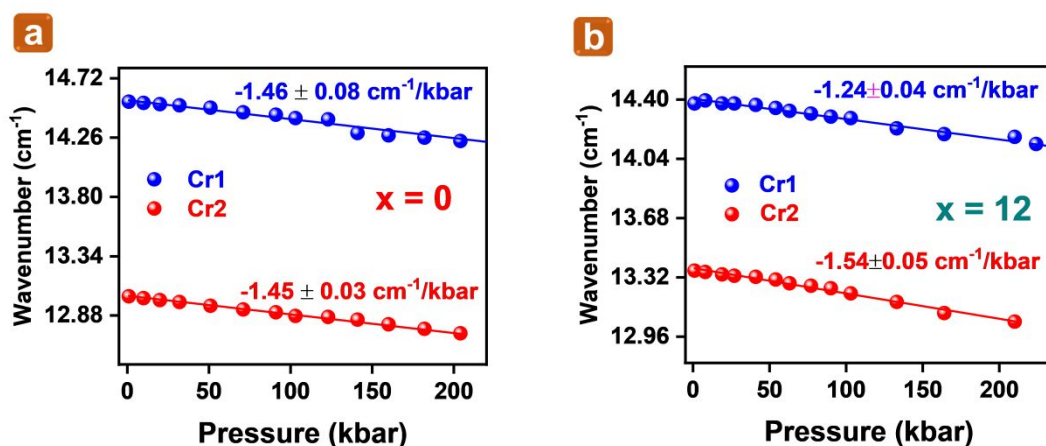
Figure S8. Pressure-dependence of the energy shift of Cr1 and Cr2 emissions for $x = 0$ (a) and $x = 12$ (b) samples.
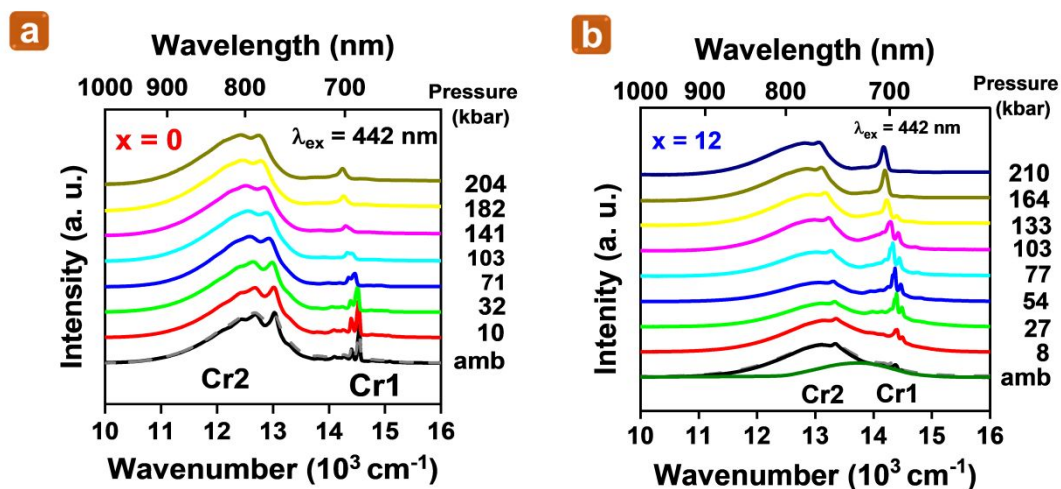
Figure S9. Room temperature pressure-dependent PL of $x = 0$ (a) and $x = 12$ (b) upon excitation at 430 nm. Ambient pressure = amb.
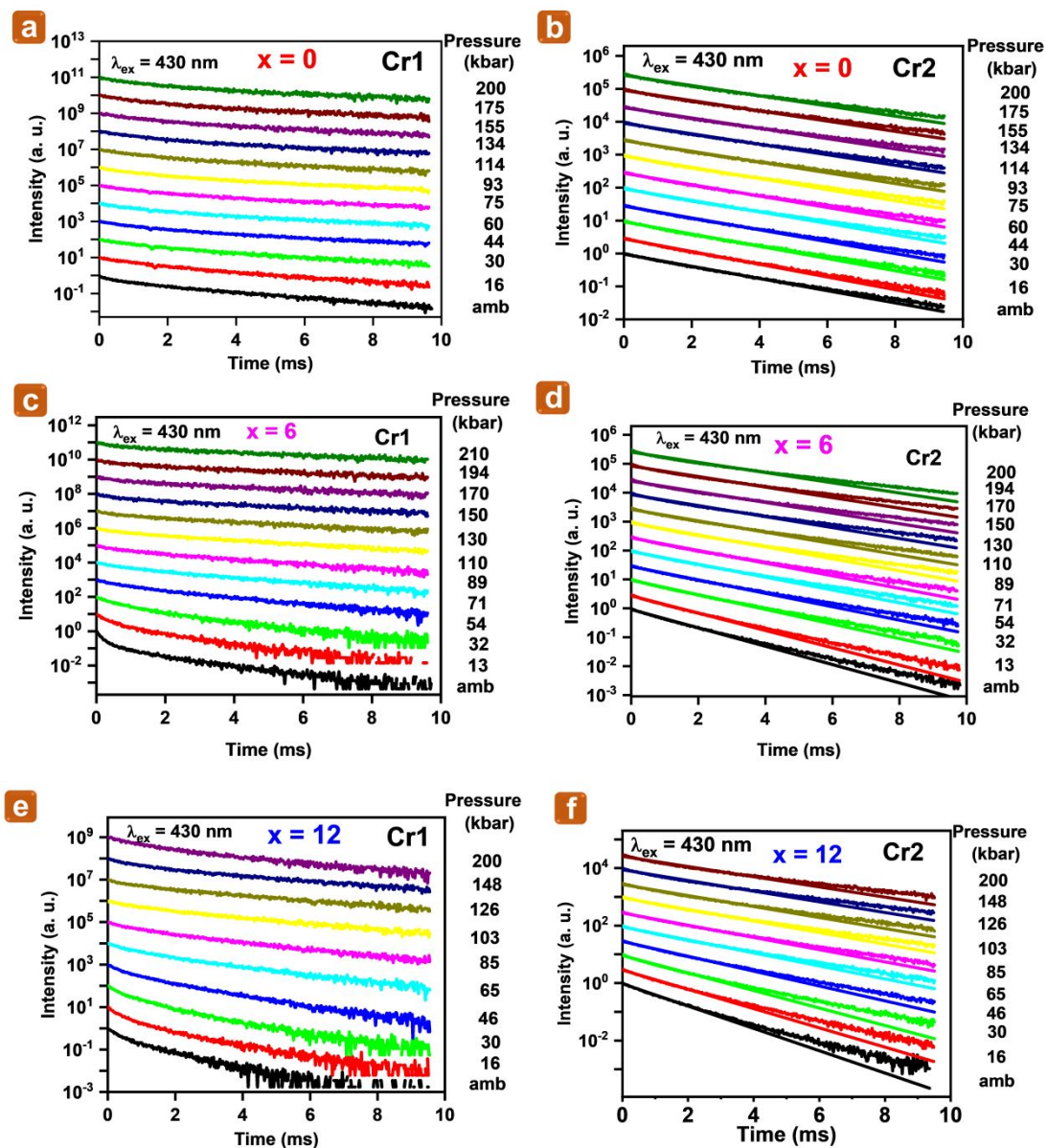
Figure S10. Pressure-dependent decay profiles of (a, c, e) Cr1 and (b, d, f) Cr2 luminescence up to 200 kbar for $x = 0, 6,$ and $x = 12$ compositions, respectively, upon excitation at 430 nm. Ambient pressure = amb. The Cr2 emission is described by a single exponential function with fits shown in (b, d, f).
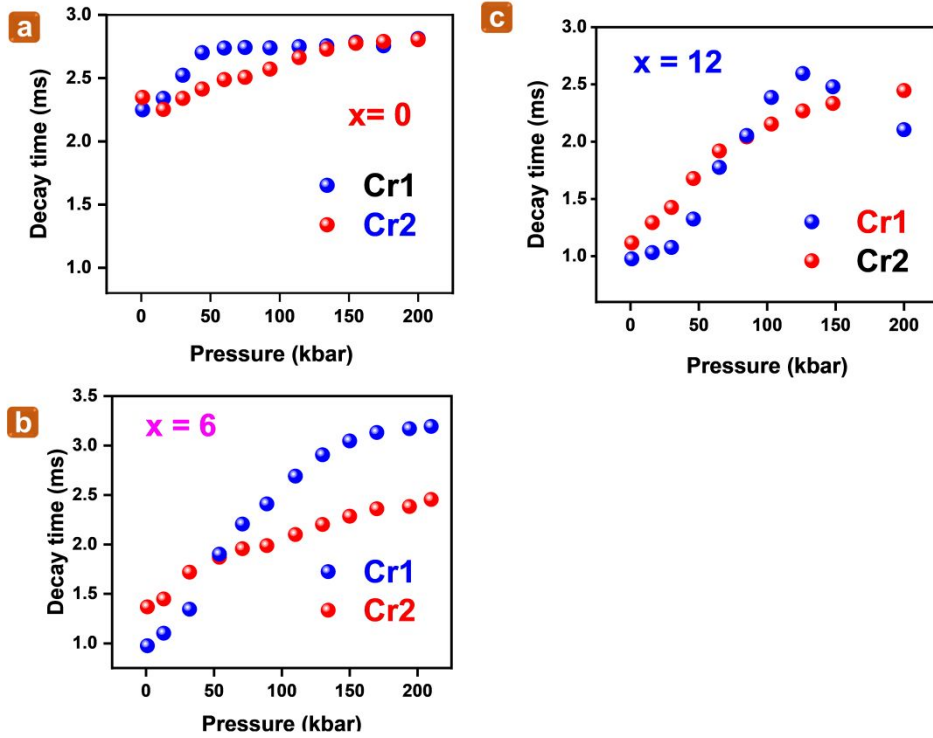
Figure S11. Calculated decay times of Cr1 (blue dots) and Cr2 (red dots) emissions of (a) $x = 0$, (b) $x = 6$, and (c) $x = 12$ samples.
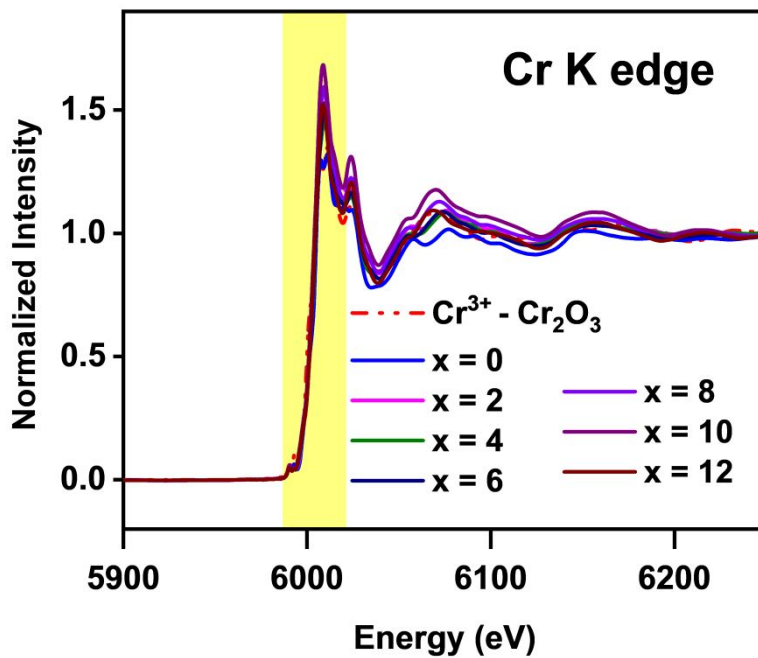
Figure S12. Cr^{3+} K-edge X-ray absorption near-edge structure spectra for $SrAl_{11.88-x}Ga_xO_{19}$:0.12Cr^3 ($x = 0$, 2, 4, 6, 8, 10, and 12) and Cr_2O_3.
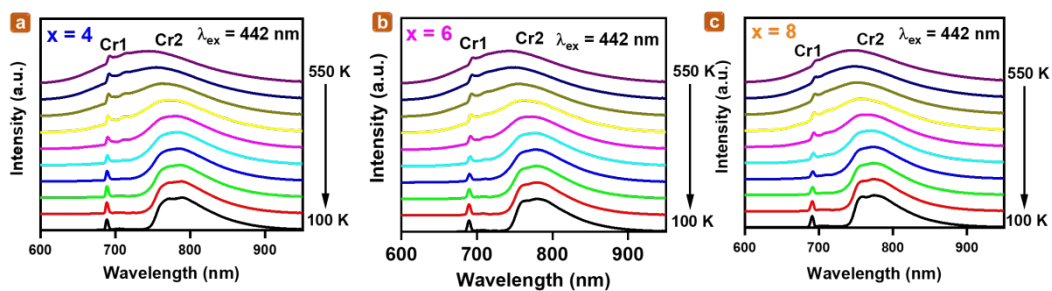
Figure S13. Temperature dependent normalized emission spectra (a) $x = 4$, (b) $x = 6$, and (c) $x = 8$ SrAl$_{11.88-x}$Ga$_x$O$_{19}$:0.12Cr^3.
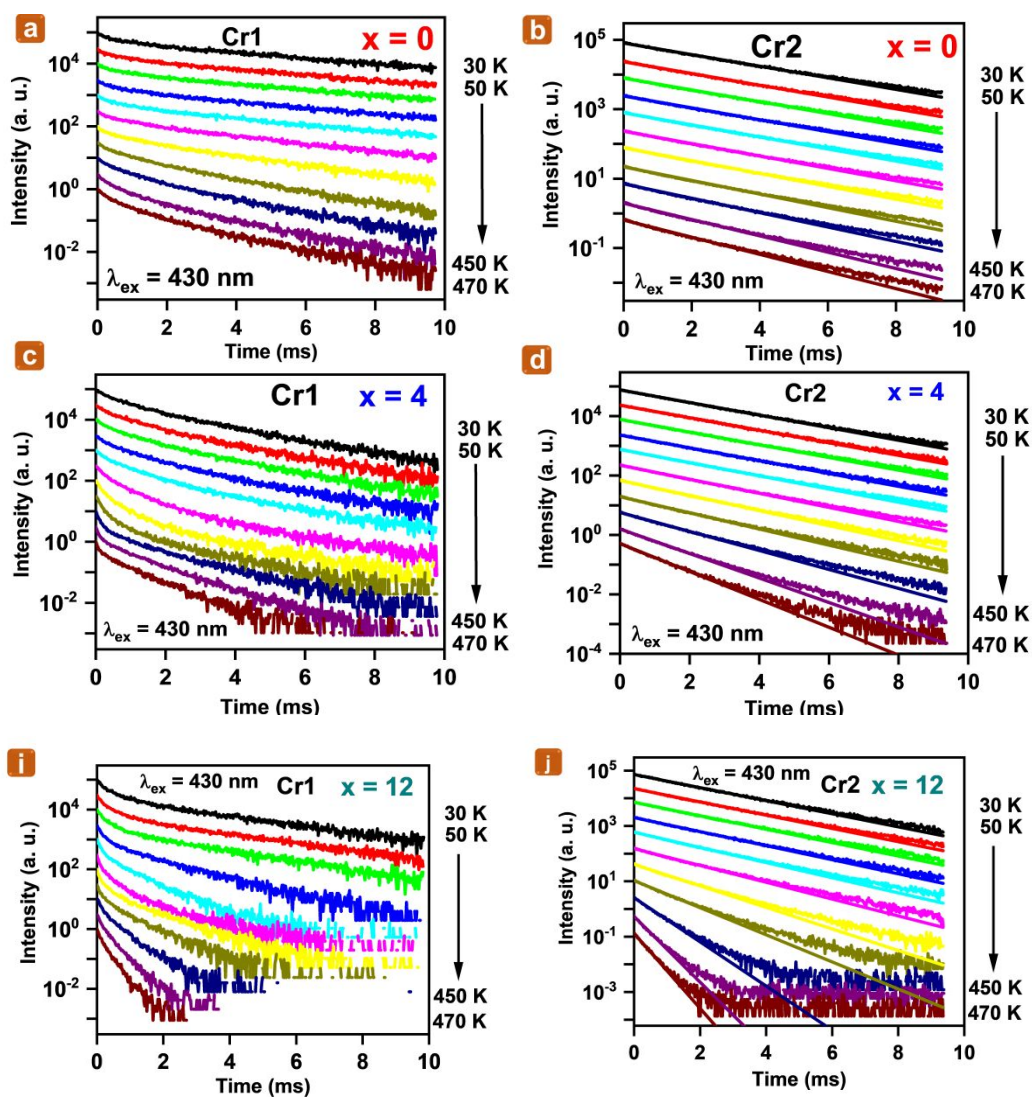
Figure S14. Temperature-dependent decay curves of (a, c, e, g) Cr1 emission and (b, d, f, h) Cr2 emission of SrAl$_{11.88-x}$Ga$_x$O$_{19}$:0.12Cr^3. The Cr2 emission is described by a single exponential function with fits shown in (b, d, j).
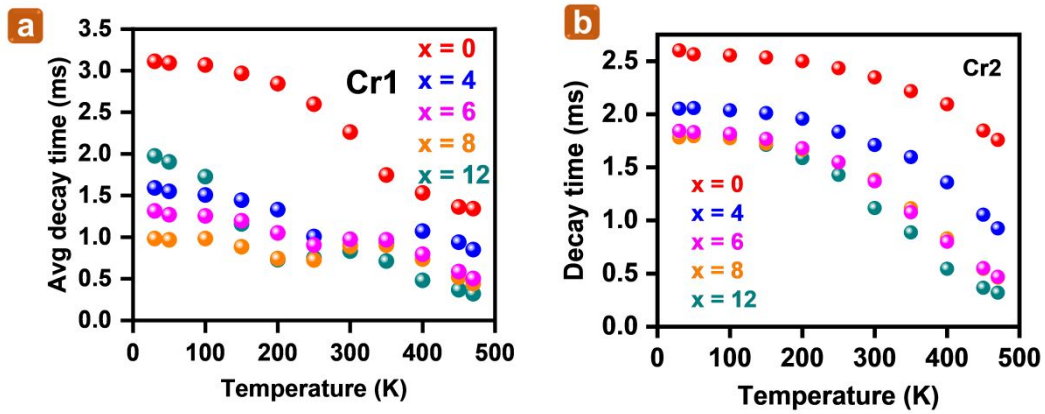
Figure S15. (a) The average decay time of Cr1 and (b) decay time of Cr2 emissions in SrAl$_{11.88-x}$Ga$_x$O$_{19}$:0.12Cr^3.
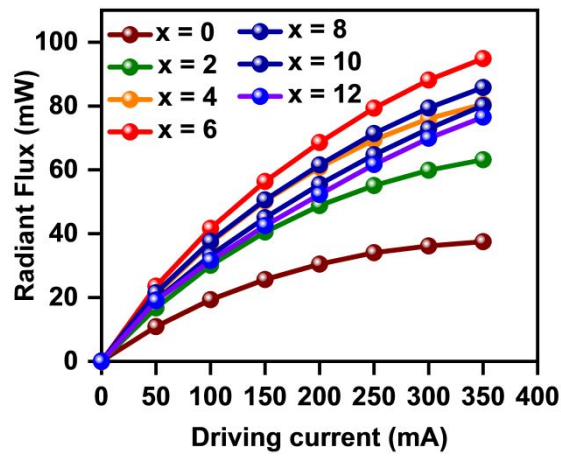
Figure S16. The output power of the pc-NIR LED package and internal quantum efficiency of SrAl$_{11.88-x}$Ga$_x$O$_{19}$:0.12Cr^3.
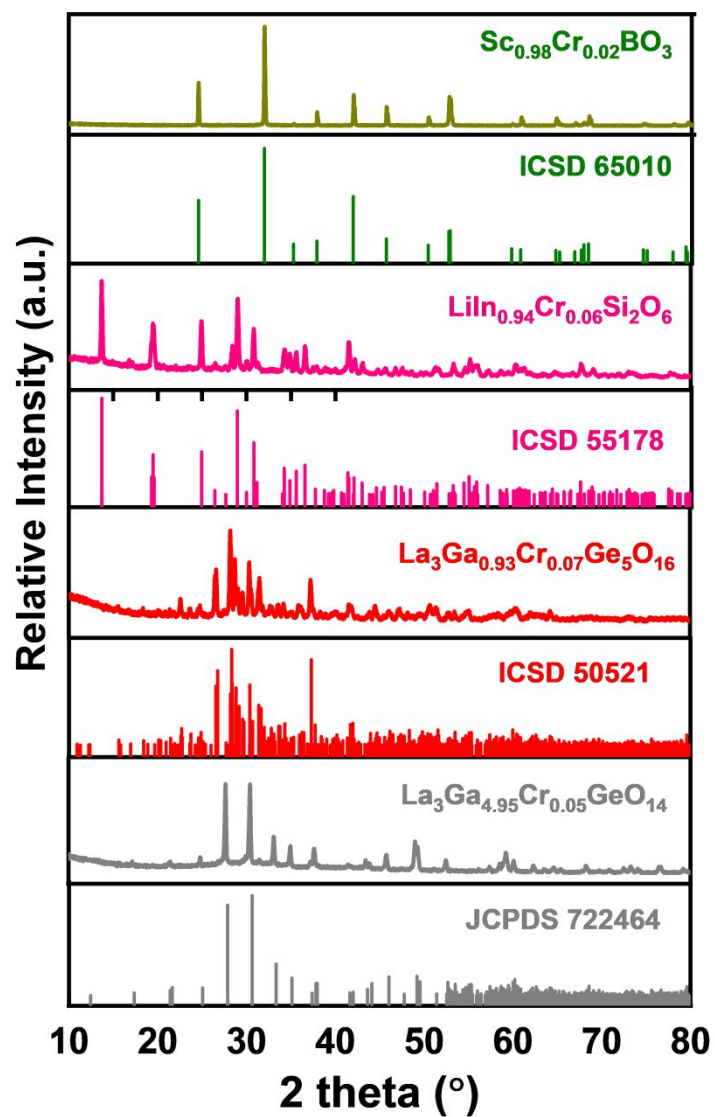
Figure S17. XRD data of $La_3Ga_{4.95}Cr_{0.05}GeO_{14}$, $La_3Ga_{0.93}Cr_{0.07}Ge_5O_{16}$, $LiIn_{0.94}Cr_{0.06}Si_2O_6$, and $Sc_{0.98}Cr_{0.02}BO_3$ along with the relevant calculated structures as indicated inset.

Table S1. Parameters from the joint Rietveld refinement of $SrAl_{11.88-x}Ga_xCr_{0.12}O_{19}$ (x = 0, 2, 4, 6, 8, 10, and 12) using S-XRD and NPD data.

x	0	2	4	6	8	10	12
a = b (Å)	5.5690(5)	5.5964(7)	5.6324(1)	5.6734(1)	5.7124(2)	5.7557(2)	5.7926(3)
c (Å)	22.0135(2)	22.1308(4)	22.2784(6)	22.4388(7)	22.5743(1)	22.7087(1)	22.8158(2)
V (Å³)	591.260(1)	600.272(18)	612.070(3)	625.490(4)	637.930(6)	651.50(5)	663.000(9)
Weighted R-profile (Rwp) and R-profile (Rp) factors for the S-XRD data histogram							
Rwp (%)	4.46	6.21	5.40	5.73	3.74	6.00	4.95
Rp (%)	2.93	3.95	3.44	3.73	2.60	3.99	3.28
Weighted R-profile (Rwp) and R-profile (Rp) factors for the NPD data histogram							
Rwp (%)	4.81	4.67	5.03	5.65	6.13	6.47	5.56
Rp (%)	3.73	3.59	3.83	4.33	4.56	4.92	4.28
GOF	1.99	2.36	2.15	2.35	2.52	2.92	2.19
Phase %							
Main Phase	95. 5(4)%	96.5(2)%	99.2(1)%	100%	100%	100%	100%
Al_2O_3	4.5(4)%	1.7(2)%	-	-	-	-	-
Ga_2O_3	-	1.8(2)%	0.8(1)%	-	-	-	-

Table S2. Atomic parameters obtained from joint Rietveld refinement of $SrAl_{11.88-x}Ga_xCr_{0.12}O_{19}$ ($x = 0$, 2, 4, 6, 8, 10, and 12) against S-XRD and NPD data. B_{eq} is constrained to be the same between atoms at the same coordinate.

$x = 0$				$SrAl_{12}O_{19}$			
Atom	x	y	z	Multiplicity & Wyckoff	Occ	Beq (Å²)	Number of Atoms
Sr1	0.6667	0.3333	0.2500	2d	1	0.25(4)	2
Al1	0	0	0	2a	1	0.55(8)	2
Al2	0	0	0.2605(3)	4e	0.5	0.10(1)	2
Al3	0.3333	0.6667	0.0278(2)	4f	1	0.10(3)	4
Al4	0.3333	0.6667	0.1897(2)	4f	1	0.10(3)	4
Al5	0.1685(3)	0.3370(5)	0.8915(6)	12k	1	0.10(2)	12
O1	0	0	0.1485(1)	4e	1	0.10(4)	4
O2	0.6667	0.3333	0.0541(1)	4f	1	0.10(4)	4
O3	0.1818(2)	0.3636(5)	0.2500	6h	1	0.10(3)	6
O4	0.1547(2)	0.3094(3)	0.0517(6)	12k	1	0.27(2)	12
O5	0.5032(2)	0.0064(5)	0.1480(5)	12k	1	0.27(2)	12

$x = 2$				$SrAl_{10.08(8)}Ga_{1.92(8)}O_{19}$			
Atom	x	y	z	Multiplicity & Wyckoff	Occ	Beq (Å²)	Atoms
Sr1	0.6667	0.3333	0.2500	2d	1	0.44(6)	2
Al1	0	0	0	2a	0.98(2)	0.43(1)	1.96(4)
Ga1	0	0	0	2a	0.02(2)	0.43(1)	0.04(4)
Al2	0	0	0.2586(4)	4e	0.31(8)	0.46(1)	1.24(3)
Ga2	0	0	0.2586(4)	4e	0.19(8)	0.46(1)	0.76(3)
Al3	0.3333	0.6667	0.0286(1)	4f	0.38(1)	0.32(4)	1.52(4)
Ga3	0.3333	0.6667	0.0286(1)	4f	0.62(1)	0.32(4)	2.48(4)
Al4	0.3333	0.6667	0.1907(2)	4f	0.89(9)	0.32(4)	3.56(4)
Ga4	0.3333	0.6667	0.1907(2)	4f	0.11(9)	0.32(4)	0.44(4)
Al5	0.1689(3)	0.3378(7)	0.8912(9)	12k	0.99(5)	0.18(4)	11.88(6)
Ga5	0.1689(3)	0.3378(7)	0.8912(9)	12k	0.01(5)	0.18(4)	0.12(6)
O1	0	0	0.1484(2)	4e	1	0.30(6)	4
O2	0.6667	0.3333	0.0551(2)	4f	1	0.35(5)	4
O3	0.1822(4)	0.3645(7)	0.2500	6h	1	0.35(5)	6
O4	0.1531(2)	0.3061(5)	0.0524(8)	12k	1	0.45(2)	12
O5	0.5031(3)	0.0062(6)	0.1479(7)	12k	1	0.45(2)	12
Al_2O_3							
Al1	0	0	0.3501(2)	12c	1.00(8)	1.40(6)	12.00(1)
O1	0.3200(3)	0	0.2500	18e	1	1.00	18
Ga_2O_3							
Ga1	0	0	0.2750(2)	12e	1.00(8)	2.90(7)	34.8(1)
O1	0.2820(4)	0	0.2500	18e	1	1.00	18

$x = 4$				SrAl$_{8.19(2)}$Ga$_{3.81(2)}$O$_{19}$			
Atom	x	y	z	Multiplicity & Wyckoff	Occ	Beq (Å^2)	Number of Atoms
Sr1	0.6667	0.3333	0.2500	2d	1	0.64(7)	2
Al1	0	0	0	2a	0.91(2)	1.19(2)	1.82(4)
Ga1	0	0	0	2a	0.09(2)	1.19(2)	0.18(4)
Al2	0	0	0.2580(4)	4e	0.15(9)	0.69(1)	0.60(4)
Ga2	0	0	0.2580(4)	4e	0.35(9)	0.69(1)	1.40(4)
Al3	0.3333	0.6667	0.0281(1)	4f	0.14(1)	0.32(4)	0.56(4)
Ga3	0.3333	0.6667	0.0281(1)	4f	0.86(1)	0.32(4)	3.44(4)
Al4	0.3333	0.6667	0.1889(2)	4f	0.68(1)	0.32(4)	2.72(4)
Ga4	0.3333	0.6667	0.1889(2)	4f	0.32(1)	0.32(4)	1.28(4)
Al5	0.1670(3)	0.3339(6)	0.8911(9)	12k	0.89(6)	0.10(4)	10.68(7)
Ga5	0.1670(3)	0.3339(6)	0.8911(9)	12k	0.11(6)	0.10(4)	1.32(7)
O1	0	0	0.1486(9)	4e	1	0.72(7)	4
O2	0.6667	0.3333	0.0561(2)	4f	1	0.24(6)	4
O3	0.1835(4)	0.3670(8)	0.2500	6h	1	0.56(6)	6
O4	0.1521(2)	0.3042(5)	0.0526(9)	12k	1	0.41(3)	12
O5	0.5040(3)	0.0080 (6)	0.1481(7)	12k	1	0.41(3)	12
Ga$_2$O$_3$							
Ga1	0	0	0.3100(9)	12e	0.48(3)	1.00	5.76(4)
O1	0.3500(4)	0	0.2500	18c	1	1.00	18

$x = 6$	SrAl$_{6.29(3)}$Ga$_{5.71(3)}$O$_{19}$						
Atom	x	y	z	Multiplicity & Wyckoff	Occ	Beq (Å²)	Number of Atoms
Sr1	0.6667	0.3333	0.2500	2d	1	0.63(8)	2
Al1	0	0	0	2a	0.79(2)	1.12(2)	1.58(4)
Ga1	0	0	0	2a	0.21(2)	1.12(2)	0.42(4)
Al2	0	0	0.2563(5)	4e	0.06(1)	1.23(1)	0.24(4)
Ga2	0	0	0.2563(5)	4e	0.44(1)	1.23(1)	1.76(4)
Al3	0.3333	0.6667	0.0278(1)	4f	0.07(1)	0.43(5)	0.28(4)
Ga3	0.3333	0.6667	0.0278(1)	4f	0.93(1)	0.43(5)	3.72(4)
Al4	0.3333	0.6667	0.1876(2)	4f	0.49(1)	0.43(5)	1.96(4)
Ga4	0.3333	0.6667	0.1876(2)	4f	0.51(1)	0.43(5)	2.04(4)
Al5	0.1671(3)	0.3343(6)	0.8911(9)	12k	0.71(6)	0.09(5)	8.52(7)
Ga5	0.1671(3)	0.3343(6)	0.8911(9)	12k	0.29(6)	0.09(5)	3.48(7)
O1	0	0	0.1498(2)	4e	1	0.86(9)	4
O2	0.6667	0.3333	0.0563(2)	4f	1	0.17(6)	4
O3	0.1824(4)	0.3649(8)	0.2500	6h	1	0.80(7)	6
O4	0.1504(2)	0.3009(5)	0.0525(1)	12k	1	0.38(3)	12
O5	0.5049(3)	0.0098(6)	0.1479(8)	12k	1	0.38(3)	12

$x = 8$				SrAl$_{4.01(1)}$Ga$_{7.99(1)}$O$_{19}$			
Atom	x	y	z	Multiplicity & Wyckoff	Occ	Beq (Å^2)	Number of Atoms
Sr1	0.6667	0.3333	0.2500	2d	1	0.27(1)	2
Al1	0	0	0	2a	0.61(2)	0.10(1)	1.22(4)
Ga1	0	0	0	2a	0.39(2)	0.10(1)	0.78(4)
Al2	0	0	0.2500(2)	4e	0.05(1)	1.01(2)	0.20(4)
Ga2	0	0	0.2500(2)	4e	0.45(1)	1.01(2)	1.80(4)
Al3	0.3333	0.6667	0.0268 (1)	4f	0.04(1)	0.31(6)	0.16(4)
Ga3	0.3333	0.6667	0.0268(1)	4f	0.96(1)	0.31(6)	3.84(4)
Al4	0.3333	0.6667	0.1874(2)	4f	0.29(1)	0.31(6)	1.16(4)
Ga4	0.3333	0.6667	0.1874(2)	4f	0.71(1)	0.31(6)	2.84(4)
Al5	0.1691(4)	0.3381(7)	0.8909(1)	12k	0.44(8)	0.47(5)	5.28(1)
Ga5	0.1691(4)	0.3381(7)	0.8909(1)	12k	0.56(8)	0.47(5)	6.72(1)
O1	0	0	0.1508(2)	4e	1	0.11(1)	4
O2	0.6667	0.3333	0.0544(3)	4f	1	0.27(9)	4
O3	0.1845(6)	0.3689(1)	0.2500	6h	1	1.08(9)	6
O4	0.1532(4)	0.3065(8)	0.0531(2)	12k	1	0.56(4)	12
O5	0.5044(5)	0.0089(1)	0.1477(1)	12k	1	0.56(4)	12

$x = 10$				SrAl$_{2.06(6)}$Ga$_{9.94(6)}$O$_{19}$			
Atom	x	y	z	Multiplicity & Wyckoff	Occ	Beq (Å^2)	Number of Atoms
Sr1	0.6667	0.3333	0.2500	2d	1	0.47(1)	2
Al1	0	0	0	2a	0.24(2)	0.93(1)	0.48(4)
Ga1	0	0	0	2a	0.76(2)	0.93(1)	1.52(4)
Al2	0	0	0.2452(1)	4e	0.00(1)	1.40(2)	0.00(4)
Ga2	0	0	0.2452(1)	4e	0.50(1)	1.40(2)	2.00(4)
Al3	0.3333	0.6667	0.0279 (2)	4f	0.06(1)	0.56(6)	0.24(4)
Ga3	0.3333	0.6667	0.0279(2)	4f	0.94(1)	0.56(6)	3.76(4)
Al4	0.3333	0.6667	0.1887(2)	4f	0.13(1)	0.56(6)	0.52(4)
Ga4	0.3333	0.6667	0.1887(2)	4f	0.87(1)	0.56(6)	3.48(4)
Al5	0.1689(3)	0.3379(6)	0.8909(8)	12k	0.24(9)	0.26(6)	2.88(1)
Ga5	0.1689(3)	0.3379(6)	0.8909(8)	12k	0.76(9)	0.26(6)	9.12(1)
O1	0	0	0.1511(2)	4e	1	0.98(1)	4
O2	0.6667	0.3333	0.0551(3)	4f	1	0.82(1)	4
O3	0.1818(6)	0.3636(1)	0.2500	6h	1	0.99(1)	6
O4	0.1521(3)	0.3042(7)	0.0527(2)	12k	1	0.37(5)	12
O5	0.5062(5)	0.0124(1)	0.1487(1)	12k	1	0.37(5)	12

$x = 12$				SrGa$_{12}$O$_{19}$			
Atom	x	y	z	Multiplicity & Wyckoff	Occ	Beq (Å^2)	Number of Atoms
Sr1	0.6667	0.3333	0.2500	2d	1	0.51(6)	2
Ga1	0	0	0	2a	1	0.29(5)	2
Ga2	0	0	0.2584(2)	4e	0.5	0.14(8)	2
Ga3	0.3333	0.6667	0.0272(1)	4f	1	0.16(2)	4
Ga4	0.3333	0.6667	0.1900(9)	4f	1	0.16(2)	4
Ga5	0.1685(2)	0.3371(4)	0.8909(5)	12k	1	0.14(2)	12
O1	0	0	0.1496(1)	4e	1	0.40(6)	4
O2	0.6667	0.3333	0.0553(2)	4f	1	0.21(6)	4
O3	0.1832(4)	0.3664(7)	0.2500	6h	1	0.39(5)	6
O4	0.1574(3)	0.3147(5)	0.0525(8)	12k	1	0.23(3)	12
O5	0.5042(3)	0.0085(6)	0.1499(7)	12k	1	0.23(3)	12

Table S3: Internal quantum efficiency of La$_3$Ga$_{4.95}$Cr$_{0.05}$GeO$_{14}$, La$_3$Ga$_{0.93}$Cr$_{0.07}$Ge$_5$O$_{16}$, LiIn$_{0.94}$Cr$_{0.06}$Si$_2$O$_6$, and Sc$_{0.98}$Cr$_{0.02}$BO$_3$.

Samples	Internal quantum efficiency
La$_3$Ga$_{4.95}$Cr$_{0.05}$GeO$_{14}$	19%
La$_3$Ga$_{0.93}$Cr$_{0.07}$Ge$_5$O$_{16}$	34%
LiIn$_{0.94}$Cr$_{0.06}$Si$_2$O$_6$	72%
Sc$_{0.98}$Cr$_{0.02}$BO$_3$	73%
SrAl$_{5.88}$Cr$_{0.12}$Ga$_6$O$_{19}$	84%

References

(1)   K. D. Liss, B. Hunter, M. Hagen, T. Noakes, S. Kennedy, *Physica B: Condensed Matter* **2006**, *385*, 1010.

(2)   A. A. Coelho, *J. Appl. Crystallogr.* **2018**, *51*, 210.

(3)   K. Momma, F. Izumi, *J. Appl. Crystallogr.* **2011**, *44*, 1272.

(4)   A. A. Kubicki, P. Bojarski, M. Grinberg, M. Sadownik, B. Kukliński, *Opt. Commun.* **2006**, *263*, 275.

(5)   L. Merrill, W. A. Bassett, *Rev. Sci. Instrum.* **1974**, *45*, 290.

(6)   J. Barzowska, T. Lesniewski, S. Mahlik, H. J. Seo, M. Grinberg, *Opt. Mater.* **2018**, *84*, 99.

(7)   M. Mombourquette, J. Weil, D. McGavin, *Department of Chemistry, University*

of Saskatchewan, Saskatoon, SK, Canada **1996**.

(8)   G. A. Bain, J. F. Berry, *J. Chem. Educ.* **2008**, *85*, 532.

(9)   B. Henderson, G. F. Imbusch, *Optical Spectroscopy of Inorganic Solids;* Oxford University Press: Oxford, UK, 2006.

(10) M. G. Brik, S. J. Camardello, A. M. Srivastava, N. M. Avram, A. Suchocki, *ECS J. Solid State Sci. Technol.* **2015**, *5*, R3067.